

## In-situ Visual Quantification of Corrosion and Corrosion Protection

Denissen, Paul

**DOI**

[10.4233/uuid:64f8f06e-5cc6-40cd-8c8d-722da6304b06](https://doi.org/10.4233/uuid:64f8f06e-5cc6-40cd-8c8d-722da6304b06)

**Publication date**

2020

**Document Version**

Final published version

**Citation (APA)**

Denissen, P. (2020). *In-situ Visual Quantification of Corrosion and Corrosion Protection*. [Dissertation (TU Delft), Delft University of Technology]. <https://doi.org/10.4233/uuid:64f8f06e-5cc6-40cd-8c8d-722da6304b06>

**Important note**

To cite this publication, please use the final published version (if applicable).  
Please check the document version above.

**Copyright**

Other than for strictly personal use, it is not permitted to download, forward or distribute the text or part of it, without the consent of the author(s) and/or copyright holder(s), unless the work is under an open content license such as Creative Commons.

**Takedown policy**

Please contact us and provide details if you believe this document breaches copyrights.  
We will remove access to the work immediately and investigate your claim.

# In-situ Visual Quantification of Corrosion & Corrosion Protection



Paul Johan Denissen

# **In-situ Visual Quantification of Corrosion and Corrosion Protection**

Dissertation

for the purpose of obtaining the degree of doctor  
at Delft University of Technology  
by the authority of the Rector Magnificus prof.dr.ir. T.H.J.J. van der Hagen  
chair of the Board for Doctorates  
to be defended publicly on  
Friday 23 October 2020 at 10:00 o'clock

by

**Paul Johan DENISSEN**

Master of Material Science and Engineering  
Technical University Delft, the Netherlands  
born in Terneuzen, the Netherlands

**This dissertation has been approved by the promotors.**

**Composition of the doctoral committee:**

|                                |  |
|--------------------------------|--|
| Rector Magnificus              | Chairperson                              |
| Dr. S.J. Garcia Espallargas    | Delft University of Technology, promotor |
| Prof. dr. ir. S. van der Zwaag | Delft University of Technology, promotor |

**Independent members:**

|                            |   |
|----------------------------|---|
| Prof.dr.ir. J.M.C. Mol     | Delft University of Technology                        |
| Prof.dr.ir. J.H.B. Sprakel | Wageningen University & Research                      |
| Dr. P. Volovitch           | École Nationale Supérieure de Chimie de Paris, France |
| Prof.dr. M.F. Montemor     | Universidade Técnica de Lisboa, Portugal              |
| Dr. E. Campazzi            | Airbus Helicopters, France                            |
| Prof.dr.ir. K. van Breugel | Delft University of Technology, reserve member        |

The research described in this thesis was carried out in the Novel Aerospace Materials group, Department of Aerospace Structures and Materials, Faculty of Aerospace Engineering.



Keywords: Optics, Electrochemistry, AA2024-T3, Cerium, Coatings

Printed by: IPSKAMP Printing B.V.

Copyright ©2020 by Paul Johan Denissen

Cover by: Marlies Dijkstra

ISBN: 978-94-6366-327-4

An electronic version of this dissertation is available at <http://repository.tudelft.nl/>

All rights reserved

Author email: [info@pauldenissen.com](mailto:info@pauldenissen.com)

## Summary

The main objective of the work described in this dissertation is to explore the route towards new anticorrosion coatings for the protection of aerospace aluminium alloys using alternative strategies that can replace the currently used toxic chromate corrosion inhibitors. As such, each chapter of this dissertation is devoted to relevant scientific and industrial challenges whereby the research on corrosion, inhibition and coating systems is combined with a newly developed in-situ optical-electrochemical technique.

*Chapter 1* gives a short introduction in the field of corrosion protection on aerospace aluminium alloys and the various methods to measure corrosion processes. Particular emphasis is put on limited prior attempts to the use of in-situ optics to monitor corrosion in parallel to electrochemical measurements. The chapter ends by defining the goals set for the research performed.

*Chapter 2* shows the development of a new in-situ optical-electrochemical technique to study corrosion and corrosion inhibition processes in real-time. The aim of this technique is to obtain optical results in a simple and inexpensive way that can be used to quantify corrosion processes and assist in the correct interpretation of complicated electrochemical signals. It combines dedicated optical analysis of images taken of a sample surface immersed in an electrolyte every 10 minutes at a resolution of 5  $\mu\text{m}$  in combination with continuous electrochemical impedance measurements using a 3-D printed electrochemical cell. The method developed is used to study the corrosion processes occurring on the surface of an AA2024-T3 alloy exposed to two NaCl concentrations and six different types of corrosion inhibitors. The optical analysis enabled identification and quantification of corrosion-features related to intermetallic corrosion (e.g. trenching and meta-stable pitting), co-operative corrosion (e.g. corrosion-rings, domes and surface-oxides) and subsurface corrosion on a spatiotemporal scale otherwise only obtained using post-mortem analysis of the samples in SEM. Furthermore, the optical analysis is used to calculate inhibition kinetics and to identify the effect of inhibitor-concentration on the corrosion behaviour. Both cerium nitrate ( $\text{Ce}(\text{NO}_3)_3$ ) and 2,5-dimercapthiadiazole (DMTD) protect the metallic surface within the first 30 minutes after immersion, even at low inhibitor concentrations,

and are defined as robust inhibitors. Low inhibitor concentrations of Lithium Carbonate ( $\text{Li}_2\text{CO}_3$ ) on the other hand do not reduce the very high corrosion rates. Interestingly, the correlation between corrosion behaviour and inhibition activity for DMTD and  $\text{Li}_2\text{CO}_3$  is easy to determine just on the basis of the recorded optical changes, but would have been quite hard to determine on the basis of the electrochemical impedance results alone. This study demonstrates the advantages of using in-situ optics of immersed corroding surfaces and improves the interpretation of electrochemical results.

*Chapter 3* is devoted to further improvements of the optical-electrochemical technique. The aim of this work is to investigate if a higher magnification combined with a more advanced image analysis can be used to obtain highly resolved information of corrosion processes, while using in essence the same simple setup as shown in chapter 2. In this case, the optical information is coupled to electrochemical noise (EN) measurements in order to explore the potential of optics to better interpret noise signals. Low magnification optical measurements are used to capture the entire exposed surface area of  $4.0 \text{ mm}^2$ . EN analysis is performed in the time-frequency domain using a continuous wavelet transform (CWT). The highly resolved data allowed the determination of time-, and space-dependent corrosion processes such as de-alloying, trenching, pit growth, co-operative and subsurface corrosion. Additional high magnification optical studies on a small part of the surface enabled the quantification of corrosion-related surface features (e.g. size, amount and nearest neighbour distance of newly appearing pits) at a  $3 \text{ pixel}/\mu\text{m}$  resolution whereby the local changes in time correspond well with the global CWT and optical analysis. For the first time ever the combination of these two techniques enabled us (i) to establish a direct relationship between EN signals and the occurrence of specific localised corrosion phenomena and (ii) to quantify local corrosion kinetics of AA2024-T3 on a sub-micron level with under immersion in-situ optics. Using this insights, we introduce a master plot that allows the direct identification of EN features to macroscopic local corrosion phenomena.

*Chapter 4* deals with the use of diatomaceous earth (DE), as powerful carriers for local inhibitor storage. DE is a readily available, naturally occurring, cheap mineral product resulting from the fossilization of nanoporous algae (diatoms) exoskeletons. These factors, together with their hollow pill-box structure and diversity in size and shapes qualifies DE as high potentials for corrosion inhibitor carriers. Epoxy coatings containing cerium loaded DE are applied onto AA2024-T3 substrates and the sustained corrosion protection under immersion conditions in presence of metal-reaching  $130 \mu\text{m}$  wide scribes is investigated. The inhibitor release and corrosion protection by loaded DE is evaluated by UV/Visible spectrometry, Raman spectroscopy and a simplified version of the optical-electrochemical setup. The results show high levels of active corrosion protection at the damage sites for at least four immersion days. The period of protection is at least four times longer than that of a coating using the same inhibitor and at the same concentration but not encapsulated in DE. The high protection levels achieved

at coating damages are due to (i) the DE shielding the cerium inhibitor from the epoxy coating thereby reducing the extent of unwanted side reactions, (ii) the relatively high inhibitor storage levels in the DE particles and (iii) the fast and sustained release of the cerium inhibitor from DE at the damaged site. Despite the obvious corrosion inhibition offered by the newly developed coatings, an even faster and more sustained inhibitor release would be beneficial to prevent the formation of all kind of localized corrosion signs (e.g. trenching) and to ensure sustained protection.

In *Chapter 5* the work on inhibitor-loaded DE microparticles is continued and several new coatings are developed to protect wide and deep scribes (up to 1 mm wide, 350  $\mu\text{m}$  deep in 75  $\mu\text{m}$  thick coatings). The DE particles are loaded with cerium nitrate and DMTD, which showed the highest levels of protection on AA2024-T3 in solution (*Chapter 2*). Different pigment volume concentrations in the coating are evaluated under continuous immersion conditions. The best performing coating was also tested under cyclic (wet/dry) conditions. The real-time optical-electrochemical setup was used in combination with two techniques that measured the local dissolved oxygen concentration in the electrolyte above the scribe and the electrochemical impedance at the exposed metal surface inside the scribe. Corroded samples were further evaluated using scanning electron microscopy in combination with energy-dispersive x-ray spectroscopy to investigate the compositional changes. The results show that corrosion protection is achieved for at least 30 days immersion in salt solution with coatings containing as little as 3.7 wt. % active inhibiting component (i.e.  $\text{Ce}^{3+}$ ). The coatings loaded with DMTD alone did not result in significant corrosion protection, possibly due to insufficient inhibitor release. Remarkably, the use of a limited amount of DMTD together with cerium leads to a synergistic increase in the efficiency and duration of the corrosion protection. The corrosion protection dropped significantly when the tests were conducted using 5 times more electrolyte volume, while keeping all other parameters constant. The wet/dry cyclic tests showed that drying steps and cumulative supply of fresh electrolyte can favor the build-up of stable inhibitor-containing layers more during the commonly performed continuous immersion testing. These results show how the coating composition and the testing conditions have a large influence on the actual degree of corrosion protection.

*Chapter 6* presents a diffusion-driven inhibitor-transport model to capture the inhibitor release from locally damaged coatings containing inhibitor-loaded particles under continuous immersion conditions. The aim of this work is to develop a simulation-based guideline that can help in the design of anticorrosion coatings. A multi-physics, finite element method is combined with kinematic and mass conservation laws to study the effect of inhibitor diffusivity, coating thickness and damage diameter on the necessary inhibitor release rate to reach the minimal required inhibitor concentrations for corrosion protection. The models are validated using a collection of coatings containing different pigment volume concentrations (PVC) of cerium-

loaded zeolite nano-carriers or micron-sized diatomaceous earth. The corrosion and inhibition activity at local through-coating damages is evaluated using the optical-electrochemical setup whereby the optical changes are combined with electrochemical noise analysis to study the corrosion and inhibition activity. The results show that inhibitors with higher diffusivity allow faster inhibition at the exposed metal surface and that the required inhibitor release rate decreases linearly with the coating thickness. Furthermore, a certain minimal particle size is found to be crucial to achieve sufficient inhibition at local damages. The experiments confirm this as coatings containing 30 PVC nano-particles are only able to protect relatively small damages of 50  $\mu\text{m}$  in diameter. Micron-sized carriers on the other hand allow sufficient release to protect larger damages of 300  $\mu\text{m}$  in diameter already at 10 PVC. Finally, the simulation and experimental results show that interconnected paths (networks) allowing for inhibitor diffusion pathways inside the coating can prolong the release and protection-time of small and large damages significantly. Experimental results show that a higher PVC around 30 will lead to this desired behaviour.

# Samenvatting

Coatings geven een uitermate goede bescherming tegen corrosie van metalen constructies. Vaak wordt er chroom-6 als effectieve maar zeer giftige corrosieremmer aan de coating toegevoegd. Het doel van het onderzoek zoals beschreven in dit proefschrift is het ontwikkelen van nieuwe chroomvrije coatings die de corrosievorming op de aluminium vliegtuiglegering AA2024-T3 tegengaan. Elk hoofdstuk in dit proefschrift gaat over één of meerdere relevante wetenschappelijke en industriële uitdagingen op het gebied van corrosieprocessen, inhibitoren en coating systemen. Hierbij wordt gebruik gemaakt van eigen ontwikkelde in-situ optische-elektrochemische technieken welke een verbindend element tussen de hoofdstukken vormt.

*Hoofdstuk 1* geeft een beknopte introductie van de verschillende manieren waarop aluminiumlegeringen beschermd kunnen worden tegen corrosie. Verschillende meetmethodes om corrosie te monitoren komen aan bod. Hierbij wordt de nog redelijk onbekende potentie van het combineren van gelijktijdige in-situ optische en elektrochemische technieken uitgebreid besproken. De resulterende doelstellingen voor het totaal onderzoek worden kort benoemd.

*Hoofdstuk 2* beschrijft de ontwikkeling van een nieuwe in-situ optische-elektrochemische techniek waarmee corrosie gemeten kan worden. De optische informatie kan worden gebruikt om corrosieprocessen eenvoudig te visualiseren. Daarnaast kan optische informatie helpen bij een betere interpretatie van gecompliceerde elektrochemische signalen. De meetopstelling maakt gebruik van een speciaal ontworpen en 3D-geprinte elektrochemische cel. Een metalen substraat wordt in de cel gemonteerd en ondergedompeld in een zoutwateroplossing. Een camera maakt beeldopnames van het substraat bij een tijdsinterval van 10 minuten en een ruimtelijke resolutie van 5  $\mu\text{m}$ . Op hetzelfde moment worden er continue elektrochemische impedantiemetingen verricht op het substraat. Voor dit onderzoek wordt het aluminiumlegering AA2024-T3 gebruikt om het effect van zes verschillende corrosieremmers te evalueren. De optische methode maakt het mogelijk om verschillende corrosieprocessen met hoge nauwkeurigheid van elkaar te onderscheiden en te kwantificeren. Dit zijn onder andere scheurgroei, pitgedrag en coöperatieve corrosie waarbij oxides neerslaan op het oppervlakte in de vorm van ringen en cirkels. Daarnaast is dezelfde meetmethode gebruikt om de effectiviteit en kinetiek van de corrosieremmers te

bepalen. Uit de optische resultaten blijkt dat 2,5-dimercapthiadiazol (DMTD) en Lithiumcarbonaat ( $\text{Li}_2\text{CO}_3$ ) goede bescherming bieden terwijl dit niet uit de elektrochemische resultaten opgemaakt kan worden. Zowel Cerium nitraat ( $\text{Ce}(\text{NO}_3)_3$ ) en DMTD geven, ook op lagere concentraties, een goede bescherming. Toevoeging van  $\text{Li}_2\text{CO}_3$  laat daarentegen een toename van de mate van corrosie zien op lage concentraties. De behaalde resultaten laten goed zien hoe in-situ optische metingen de interpretatie van elektrochemische data kunnen verbeteren.

*Hoofdstuk 3* is gericht op de verbetering van de in-situ optische-elektrochemische meetmethode. Het doel van dit werk is om te onderzoeken of een hogere optische vergroting in combinatie met geavanceerde beeldanalyse meer informatie kan geven over de mate van corrosie. Hierbij is een soortgelijke methode gebruikt als in hoofdstuk 2. In dit deelonderzoek zijn de optische metingen gecombineerd met elektrochemische ruismetingen. In de ruismeting-analyse is gebruik gemaakt van een continue wavelet-transformatie (CWT). Allereerst zijn er opnames op lage vergroting gemaakt om alle oppervlakveranderingen in kaart te brengen op  $4.0 \text{ mm}^2$ . Deze informatie maakt het mogelijk om de verschillende corrosieprocessen te volgen en te onderscheiden. Dit is bijvoorbeeld het oplossen van legeringselementen, de formatie van pitcorrosie en het optreden van coöperatieve corrosie. Vervolgens zijn er met een verhoogde resolutie (3 pixels per  $\mu\text{m}$ ) nieuwe metingen uitgevoerd op een gedeelte van het oppervlak. Deze metingen maken het mogelijk om de kenmerken van het metaaloppervlak, die relevant zijn voor de corrosie, beter te kwantificeren. Hieronder vallen de grootte, de onderlinge afstand, de totale hoeveelheid en de instabiliteit van pitcorrosie. In alle gevallen komt de optische informatie goed overeen met de resultaten van de CWT analyses. Voor de allereerste keer kan een directe relatie gelegd worden tussen elektrochemische ruismetingen en optisch waarneembare corrosieprocessen aan onbeschermd AA2024-T3 oppervlakken.

*Hoofdstuk 4* beschrijft het gebruik van diatomeënaarde (DE) voor de opslag van corrosieremmers. DE is een goed verkrijgbaar natuurlijk mineraalproduct afkomstig van het algensoort diatomeeën die als eigenschap hebben dat na fossilisatie enkel het poreuze uitwendige skelet achterblijft. In dit onderzoek zijn de holle silica deeltjes met een grootte van ongeveer  $15 \mu\text{m}$  beladen met het corrosieremmende element cerium. De beladen deeltjes zijn verwerkt in epoxy coatings en aangebracht op AA2024-T3. Vervolgens zijn de beschermende effecten van de inhibitor op de aluminiumlegering getest. Hiertoe zijn  $130 \mu\text{m}$  brede krassen in de coating gemaakt en is het substraat onderdompelt in een  $0.05 \text{ M}$  NaCl zout oplossing. Metingen zijn uitgevoerd met UV/VIS, Raman spectroscopie en een vereenvoudigde versie van de optische-elektrochemische meetopstelling gepresenteerd in Hoofdstuk 2. De resultaten laten zien dat de coatings over een periode van minstens 4 dagen bescherming bieden tegen corrosie. Dit is vier keer zo langs als coatings met dezelfde hoeveelheid corrosieremmer maar dan niet opgeslagen in de DE deeltjes. De goede bescherming is te danken aan (i) het feit dat DE de corrosieremmer afschermt van de omliggende coating en hiermee negatieve interacties met de polymere matrix

vermindert, (ii) de hoge opslagcapaciteit van de DE deeltjes waarvoor grote hoeveelheden corrosieremmers opgeslagen kunnen worden en (iii) het snelle vrijkomen van de corrosieremmer uit de DE deeltjes in de buurt van de beschadiging. Hoewel het gebruik van DE voor cerium opslag in de coating een duidelijke verbetering van de corrosiebescherming geeft, is een nog snellere en continue bescherming in de beschadiging gewenst.

*Hoofdstuk 5* gaat over de verdere ontwikkeling van coatings met inhibitor beladen DE deeltjes. In dit onderzoek zijn de DE deeltjes beladen met cerium nitraat of met DMTD. Deze twee inhibitoren geven bij lage concentraties in de zoutoplossing al een hoge bescherming (Hoofdstuk 2). Coatings met een dikte van 75  $\mu\text{m}$  zijn aangebracht op AA2024-T3 oppervlakken. Vervolgens zijn er 350  $\mu\text{m}$  diepe krassen met een breedte van 1 mm in het substraat gemaakt en zijn de preparaten ondergedompeld in zout water. De coating die de beste bescherming bij continue immersie leverde is tevens getest onder cyclische (natte/droge) omstandigheden. In dit deelonderzoek is wederom gebruik gemaakt van de optische-elektrochemische meetopstelling. Daarnaast zijn er twee nieuwe technieken gebruikt waarmee het lokale zuurstofgehalte in de zoutoplossing en de elektrochemische impedantie rondom de beschadiging gemeten kan worden. De samenstelling van het metaaloppervlakte na afloop van het corrosieexperiment is onderzocht met een elektronenmicroscop voorzien van energie dispersieve röntgenspectroscopie. De coatings met cerium beladen DE tonen een bescherming van minstens 30 dagen. Hierbij is slechts 3.7 gewichtsprocent corrosieremmer toegevoegd aan de coating. Coatings die alleen DMTD bevatten gaven geen significante bescherming. Dit komt hoogstwaarschijnlijk door een onvoldoende inhibitor-afgifte vanuit de DE. Er is wel een duidelijke synergistische verbetering in bescherming zichtbaar wanneer beide corrosieremmers samen aan de coating worden toegevoegd. De bescherming vermindert aanzienlijk wanneer het volume van de zoutoplossing met een factor 5 wordt verhoogd, terwijl alle andere parameters onveranderd blijven. De best geteste coatings laten onder cyclische (natte/droge) omstandigheden juist weer een hogere bescherming zien. Mogelijk bevorderen de sequentiële droogstappen en de herhaalde blootstelling aan zoutoplossing de opbouw van een stabiele bescherm laag. De resultaten tonen aan dat de samenstelling van de coating en de gebruikte omstandigheden een grote invloed hebben op de uiteindelijke beschermingsgraad van de coatings.

In *Hoofdstuk 6* wordt een computer-simulatie gepresenteerd die op basis van diffusie het transport van corrosieremmers vanuit beschadigingen in de coating modelleert tijdens onderdompeling. Het doel van de simulatie is het opstellen van semi-kwantitatieve richtlijnen die toegepast kunnen worden bij de ontwikkeling van corrosiebeschermende coatings. De modellen maken gebruik van eindige-elementenmethodes in combinatie met massa-conserveringswetten. Met het model kan de minimaal benodigde afgiftesnelheid van corrosieremmers uit coatings met beladen deeltjes worden bepaald. De modellen zijn gevalideerd door verscheidene coatings experimenteel te testen. Hierbij is cerium opgeslagen in zowel zeolitisch

materiaal met nanometer-afmetingen als in diatomeeënaarde met micrometer grote deeltjes. De effectiviteit van de corrosiebescherming is vervolgens getest met behulp van de optisch-elektrochemische meetopstelling beschreven in Hoofdstuk 3. De computer-simulaties en experimentele resultaten tonen aan dat corrosieremmers met een hogere diffusiecoëfficiënt sneller het metaaloppervlak bereiken en daarmee sneller bescherming bieden. Ook voorspelt het model dat de benodigde uitstroom van corrosieremmers lineair afneemt met de dikte van de coating. Daarnaast blijkt het formaat van de beladen deeltjes een cruciale rol te spelen voor het bieden van voldoende corrosieremming. Zo kan een 300  $\mu\text{m}$ -grote beschadiging enkel beschermd worden met beladen microdeeltjes, zelfs bij een lage pigmentvolumeconcentratie (PVC), en bleken beladen zeoliet nano-deeltjes ineffectief. Tot slot, de computer-simulaties en de experimenten laten zien dat er een langere beschermingstijd geleverd kan worden wanneer de microdeeltjes in de coating met elkaar in verbinding staan, zoals gebeurt bij een PVC van rond de 30. Deze langdurige bescherming geldt voor zowel kleine als grote beschadigingen.

# Contents

|   |    |
|---|----|
| Summary .....   | i  |
| Samenvatting .....  | v  |
| Contents .....  | ix |
| <b>Chapter 1. Introduction</b>  |    |
| 1.1. Aluminium AA2024-T3 and its susceptibility to corrosion .....  | 1  |
| 1.2. In-situ optical evaluation of corrosion .....  | 3  |
| 1.3. Towards Cr-free aerospace coatings .....   | 6  |
| 1.4. Thesis outline .....   | 9  |
| 1.5. References .....   | 11 |
| <b>Chapter 2. Reducing subjectivity in EIS interpretation of corrosion and corrosion inhibition processes by in-situ optical analysis</b>       |    |
| 2.1. Introduction .....   | 18 |
| 2.2. Materials and Methods .....  | 20 |
| 2.2.1. Materials .....  | 20 |
| 2.2.2. Optical and electrochemical in-situ measurement .....  | 20 |
| 2.2.3. Optical analysis .....   | 21 |
| 2.3. Results and Discussion .....   | 24 |
| 2.3.1. Identification of corrosion-related features in AA2024-T3 .....  | 24 |
| 2.3.2. Evaluation of corrosion inhibitors .....   | 30 |
| 2.4. Conclusions .....  | 36 |
| 2.5. References .....   | 37 |
| 2.6. Supporting Information .....   | 40 |
| <b>Chapter 3. Interpreting electrochemical noise and monitoring local corrosion by means of highly resolved spatiotemporal real-time optics</b> |    |
| 3.1. Introduction .....   | 48 |
| 3.2. Experimental .....   | 50 |
| 3.2.1. Optical-electrochemical setup .....  | 50 |
| 3.2.2. Electrochemical analysis .....   | 51 |
| 3.2.3. Optical analysis .....   | 51 |
| 3.2.4. Sample preparation .....   | 53 |
| 3.3. Results and Discussion .....   | 55 |
| 3.3.1. Global corrosion study (low optical magnification and EN) .....  | 55 |
| 3.3.2. Local corrosion study (high optical magnification) .....   | 61 |
| 3.3.3. Correlation between EN signals and macroscopic corrosion features from optical analysis .....  | 65 |
| 3.4. Conclusions .....  | 67 |
| 3.5. References .....   | 68 |
| 3.6. Supporting Information .....   | 70 |

## **Chapter 4. Cerium-loaded algae exoskeletons for active corrosion protection of coated AA2024-T3**

|  |     |
|--|-----|
| 4.1. Introduction.....   | 76  |
| 4.2. Materials and Preparation .....   | 78  |
| 4.2.1. Refined diatomaceous earth (DE).....  | 78  |
| 4.2.2. DE doping with cerium nitrate.....  | 78  |
| 4.2.3. Coatings preparation.....   | 79  |
| 4.2.4. Scratch damage in coated metals for corrosion inhibition evaluation.....    | 80  |
| 4.3. Testing Methods and Equipment .....   | 81  |
| 4.3.1. Diatomaceous earth particle analysis.....                                   | 81  |
| 4.3.2. Real-time inhibitor release from DE carrier.....                            | 81  |
| 4.3.3. In-situ optical-electrochemical set-up (corrosion protection studies) ..... | 81  |
| 4.3.4. Cerium interaction with the exposed AA2024-T3 metal surface.....            | 83  |
| 4.4. Results and Discussion .....  | 84  |
| 4.4.1. Particle characterization.....  | 84  |
| 4.4.2. Inhibitor-loaded particle/epoxy coating interaction .....                   | 87  |
| 4.4.3. Corrosion protection of damaged coatings .....                              | 89  |
| 4.5. Conclusions.....  | 99  |
| 4.6. References.....   | 100 |
| 4.7. Supporting Information.....   | 103 |

## **Chapter 5. Corrosion inhibition at scribed locations in coated AA2024-T3 by cerium and DMTD loaded natural silica microparticles under continuous immersion and wet/dry cyclic exposure**

|  |     |
|--|-----|
| 5.1. Introduction.....   | 116 |
| 5.2. Experimental.....   | 118 |
| 5.2.1. Materials.....  | 118 |
| 5.2.2. Inhibitor loading and coatings preparation .....                                | 118 |
| 5.2.3. Corrosion tests .....   | 120 |
| 5.3. Results and Discussion .....  | 125 |
| 5.3.1. DE loading, release and coating evaluation.....                                 | 125 |
| 5.3.2. Global electrochemistry and spatially resolved real-time optics.....            | 126 |
| 5.3.3. Spatial and temporally resolved local corrosion processes .....                 | 131 |
| 5.3.4. Effect of electrolyte volume per exposed area on the corrosion protection ..... | 137 |
| 5.3.5. Performance during wet/dry cyclic test .....                                    | 138 |
| 5.4. Conclusions.....  | 141 |
| 5.5. References.....   | 142 |
| 5.6. Supporting Information.....   | 146 |

## **Chapter 6. A simulation-based guideline for the design of anticorrosive primers based on inhibitor-loaded carriers**

|  |     |
|--|-----|
| 6.1. Introduction.....   | 152 |
| 6.2. Experimental.....   | 154 |
| 6.2.1. Damaged coating under immersion conditions used in simulation and corrosion experiments | 154 |
| 6.2.2. Diffusion-limited model for inhibitor transport in the electrolyte.....                 | 155 |
| 6.2.3. Inhibitor depletion from carriers at the primer-electrolyte interface.....              | 156 |
| 6.2.4. Materials and samples preparation for experimental validation.....                      | 158 |
| 2.2.5 Corrosion evaluation with an in-situ optical and electrochemical set-up.....             | 159 |
| 6.3. Results and Discussion .....  | 162 |
| 6.3.1. Diffusion-limited inhibitor release simulations .....                                   | 162 |
| 6.3.2. Validation through optical-electrochemical experiments.....                             | 168 |
| 6.4. Conclusions.....  | 177 |
| 6.5. References.....   | 178 |
| 6.6. Supporting Information.....   | 182 |

Acknowledgement..... 185

List of publications..... 187

About the Author..... 191

# 1

## Introduction

### 1.1. Aluminium AA2024-T3 and its susceptibility to corrosion

Aluminium alloys are classified according to the International Alloy Designation System (IADS) on the basis of their major alloying elements. In the case of AA2024 the composition is 3.8 – 4.9 wt.% Cu, 1.2 – 1.8 wt.% Mg, 0.3 – 0.9 wt.% Mn and minor constituents of Fe, Si and Zn. The alloying elements in combination with heat-treatments strengthen the material without significantly increasing its mass. The alloying elements are also responsible for the typical microstructure of AA2024-T3 (where “T3” designates the heat treatment), containing a large variety of nano-sized hardening precipitates and micron-sized dispersoid particles. This results in a high strength to weight ratio and makes copper-rich aluminium alloys widely used in the aerospace sector. However, the microparticles known as intermetallic particles (IMP), also have a different composition than the matrix and form strong local galvanic couplings between themselves and the surrounding matrix, making these alloys extremely vulnerable to corrosion.<sup>1</sup>

Corrosion of AA2024-T3 is a complex phenomenon whereby the understanding of the IMP composition and distribution plays an important role. Boag et al. suggested that the initial stage of localised corrosion occurs within the first minutes after exposure to 0.1 M NaCl through de-alloying at the anodic S-phase particles (AlCuMg), followed by trenching around the cathodic particles (e.g. AlCuFeMn and AlCuFeMnSi particles).<sup>2</sup> Hughes et al. reported that clustered IMP particles interact together and form corrosion products in the shape of domes and rings, a phenomenon also known as co-operative corrosion.<sup>3</sup> The final stage of corrosion was described by Glenn et al. as a mixed mode of intergranular attack (IGA) and grain etch-out penetrating deeper into the alloy. This subsurface corrosion process has been reported to propagate within the first hours of immersion in 0.1 M NaCl solutions. Such fast kinetics underline the need of adequate and fast acting corrosion protection strategies to prevent the loss of mechanical properties, even under mildly corrosive conditions.<sup>4</sup>

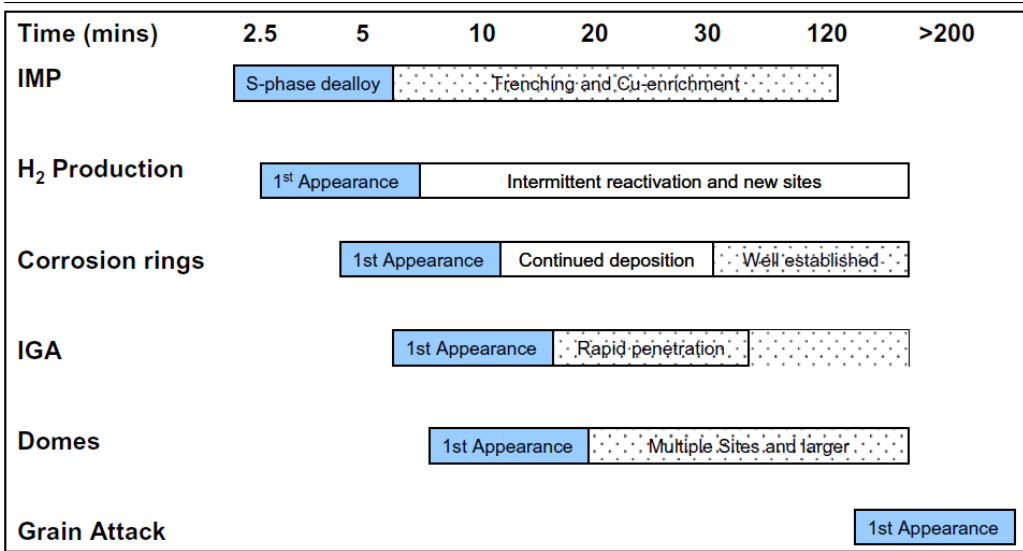


**Figure 1.1** Summary of observations for the development of corrosion processes on the surface of AA2024-T3 in 0.1 M NaCl.<sup>2</sup>

The specific features and time of occurrence for the local corrosion processes of AA2024-T3 as shown in Figure 1.1 have been obtained by visual inspection of the corroded surface after different immersion-times. A large step in accuracy and rapid screening of the results could be obtained by using in-situ optical inspection of the local surface phenomena, thereby leading to a better interpretation of corrosion-related processes. Nonetheless, corrosion studies using real-time optics are rare in literature, especially for the case of AA2024-T.

## 1.2. In-situ optical evaluation of corrosion

Scientific information on corrosion and inhibition is usually obtained through in-situ electrochemical techniques in combination with after-immersion visual inspection. Electrochemical techniques require the use of a specific cell whereby the specimen, acting as working electrode (WE), is immersed in a corrosive electrolyte. Electrochemical signals can either be imposed or measured between the WE and an auxiliary electrode (i.e. reference electrode (RE), counter electrode (CE) or a second WE) by means of a potentiostat. Electrochemical techniques can either be destructive or non-destructive for the WE. Examples of destructive techniques that promote specific redox reactions are cyclic voltammetry (CV) and linear polarisation, in which large currents or potentials are imposed to the system. Examples of non-destructive techniques are electrochemical noise (EN) and electrochemical impedance spectroscopy (EIS). In these techniques the applied signals are intentionally kept low such that no out of equilibrium conditions are imposed. EN is used to measure the fluctuations in potential (EPN) and current (ECN) at the WE as a function of time under nominally constant conditions. From this data, relevant information on both anodic and cathodic reactions can be obtained in the time and frequency domain.<sup>5,6</sup> EIS is used to measure the resistance and capacitance of materials by imposing small alternating excitations to the system over a range of frequencies while recording the currents. Especially this latter technique is well-established for the evaluation of protective coatings because EIS can give relevant information on barrier properties, barrier stability, coating-metal interfaces and electrochemical processes that take place when barrier-properties are lost.<sup>7-9</sup>

Although the above mentioned methods are accurate and highly quantitative under well-defined and very stable laboratory conditions, they reflect surface averaged behaviour and only give a global result. Thereby, a complete interpretation of the results when dealing with complicated heterogeneous systems such as AA2024-T3 or protective coating systems becomes challenging. To overcome this, local electrochemical techniques measuring electrochemical activity on a spatial scale can be used. Local techniques make use of microelectrodes that are moved over the surface of the specimen to map the local electrochemical fluctuations. The most widely used variants are scanning vibrating electrode technique (SVET),<sup>10</sup> local electrochemical impedance spectroscopy (LEIS),<sup>11,12</sup> scanning electrochemical microscopy (SECM),<sup>13</sup> and the scanning Kelvin probe (SKP).<sup>14</sup> Nevertheless, and besides the complexity of use, the relatively long scanning-times and unwanted interferences of the measurement protocol with the substrate or solution (e.g. probe-specimen interaction, electrolyte evaporation, and deposition ions on electrodes) make them less favourable as simple non-destructive real-time evaluation techniques.<sup>15</sup>

Surface characterization with spectrometric and optical techniques is usually employed before and after the electrochemical measurements. These tests provide relevant information about the

corrosion features and/or deposits (corrosion products or passive layers) and help with the correct interpretation of the electrochemical results. Most commonly used examples of such techniques are optical microscopy, SEM, FTIR, Raman spectroscopy, XPS and X-ray tomography. One of the major limitations of these ex-situ methods is the lack of relevant real-time information on surface-changes when they occur with the associated impossibility to directly correlate electrochemical events to macroscopic processes. Moreover, ex-situ measurements often require additional sample handling and changes in the environmental conditions that can influence the studied surfaces. To overcome these limitations Tokuda and Ives reported on the use of in-situ optical microscopy in the field of corrosion back in 1971. In their early work, they showed that scratches and grain-boundaries are active sites for pitting.<sup>16</sup> The number of in-situ optical studies started to increase slightly after the introduction of the digital microscope in 1986, as it facilitated the recording of optical changes and enabled more extensive analysis over continuous time-domains. Despite the progress in optics, only a limited number of works have been able to couple this information directly to electrochemical signals.

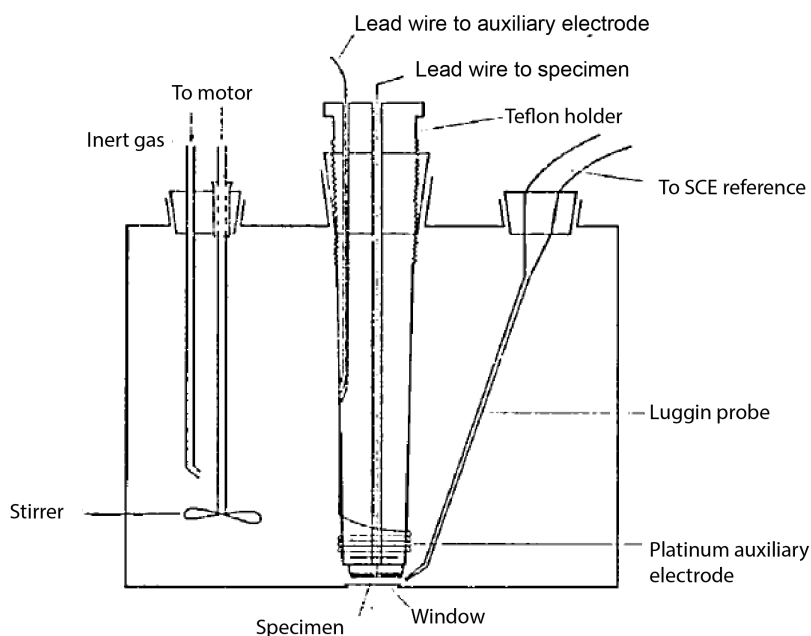


**Figure 1.2** One of the first electrochemical cells used for in-situ optical inspection.<sup>16</sup>

Figure 1.2 shows the schematics of one of the first published electrochemical cells aiming at simultaneously obtaining optical images and electrochemical signals. To do this, firstly and most importantly, the optical path between the specimen and optical detector needs to remain free from obstacles and within the working distance of the microscope. This can be achieved by using a transparent window controlling the distance to the sample and the amount of electrolyte

between the microscope and the specimen. Secondly, the lighting conditions on the specimen are important, whereby either coherent light (i.e. monochromatic lasers) or incoherent light can be used. Examples of coherent light methods are interferometry,<sup>17-21</sup> holographic microscopy,<sup>22-24</sup> reflection anisotropy spectroscopy,<sup>19,20</sup> ellipsometry,<sup>19,20,23</sup> Raman microscopy,<sup>25,26</sup> and speckle techniques.<sup>27-29</sup> These methods allow the quantification of corrosion products with high precision, but also require complicated or expensive optical systems. Incoherent light is mainly used for traditional surface inspection by optical microscopy,<sup>29-43</sup> and is often combined with contrast-enhancement techniques.<sup>37,41,44</sup> Methods based on incoherent light are inexpensive and very simple to use, making them the ideal method to be combined with traditional electrochemistry.

Besides the setup to allow for in-situ optical analysis, image processing procedures are also required to obtain relevant and quantitative information. This includes background removal by either thresholding using image segmenting or by means of subtraction using predefined models.<sup>33,42</sup> Image stabilization can be achieved using image repositioning algorithms to compensate for vibrations, drift and misalignments. Automated data analysis can then be performed on a single or a stack of images to obtain quantitative information. The obtained quantitative information can be used to determine the size, shape and number density distributions of corrosion products. Time resolved analysis involves tracking the differences between two or more images over a period of time. This allows the reconstruction of dynamic and kinetic activity that can then be used to follow corrosion processes over time (e.g. pit growth and the formation of corrosion products). Although these real-time optical analysis techniques in combination with processing algorithms have been used in other fields (e.g. biomedical<sup>45</sup> and radiography<sup>46</sup>), they are still relatively unexplored for the evaluation of corrosion processes and protective coatings.

### 1.3. Towards Cr-free aerospace coatings

The use of protective coatings is the most common strategy to prevent corrosion on metallic structures. Especially in the aerospace field, the demands on the coating performance and reliability are very high because inaccessible structural parts should remain corrosion-free over a period of at least 30 years.<sup>47</sup> To achieve this, a typical aerospace coating consists of several individual layers. The layer closest to the metal surface is a 10–60 nm thick inorganic conversion coating that provides corrosion protection and improved adhesion between the metal surface and the primer. The next layer, the primer, is a pigmented organic coating with a thickness between 5 and 100  $\mu\text{m}$  and its primary function is to provide active corrosion protection through the use of inhibitors or sacrificial particles and passive protection by offering a barrier to aggressive substances. This protection should be kept also at macroscopic local damages that directly expose the metal surface to the environment. In this case the corrosion inhibitors should leach towards the freshly exposed metal to create a new protective layer. The primer often contains other additives as well, such as colouring pigments, hardening agents, stabilising agents, surface activating compounds and dispersion agents. All additives affect the overall barrier performance, making primer coatings very complex systems. Finally, the outer layer of the aerospace coatings (topcoat) acts as barrier against external conditions (i.e. climate conditions, ultraviolet rays, and aerospace fluids) and offers other aesthetic properties such as colour.<sup>48</sup>

Chromium based salts, such as strontium chromate, have been used as corrosion inhibitors in primers since at least 1908.<sup>49,50</sup> Chromates are particularly interesting for the protection of AA2024-T3, as it has the tendency to rapidly passivate the surface, followed by the formation of a dense  $\text{CrO}_3$  layer that remains stable over a broad pH range.<sup>51</sup> Nevertheless, national and international agencies have imposed severe restrictions and bans on the use of chromates due to its toxicity and carcinogenic nature.<sup>52,53</sup> For this reason, a significant amount of research has devoted effort to find alternative corrosion inhibitors at least since the 1980s.<sup>54</sup> Lanthanide-based (i.e. Ce, Y, La, Pr and Nd) compounds belong to the most promising alternatives<sup>55,56</sup> together with organic inhibitors (i.e. DMTD, 2-MBT and DEDTC). Most of the proposed inhibiting alternatives act as chelating agents or create adsorption layers on either anodic or cathodic locations or on the entire metal surface (mixed-type inhibitors).<sup>57–60</sup> Furthermore, recent developments gave new insights on the potential use of lithium compounds as passivating agents of aluminium alloys such as AA2024-T3 when locally exposed to alkaline conditions. This protection mechanism is different than that of traditional corrosion inhibitors as it primarily leads to the in-situ formation of lithium containing pseudo-boehmite and layered double hydroxides that passivates the metal surface.<sup>61–66</sup>

The biggest challenge for most alternative corrosion inhibitors showing as good inhibiting power as chromates in solution is the loss of their protective efficiency when they are incorporated in

primers.<sup>48,60</sup> This is mainly due to insufficient inhibitor leaching from the primer or inhibitor deactivation. These are caused by insufficient diffusion paths for large molecules inside the primer and by unwanted side-reactions between the inhibitor and the surrounding coating matrix which either prevent inhibitor release or lead to the (partial) deactivation of the inhibitor.<sup>67–69</sup> The side-reactions can negatively affect the coating performance as well, resulting in local crosslinking variations, blistering and delamination. To find suitable alternatives one should therefore not only look at the inhibitor reactivity itself, but also study the inhibitor-coating interactions and the overall corrosion protection of the coating-metal system under different corrosion conditions (e.g. immersion or cyclic wet-dry exposure) using different evaluation strategies.

In order to decrease the unwanted inhibitor-coating interactions encapsulation strategies can be used wherein the anticorrosive species can be released from the capsule in a controlled manner (e.g. diffusion,<sup>70</sup> pH,<sup>71</sup> or ion-exchange<sup>72</sup>). The first encapsulation concepts were based on the use of 2D inorganic nanoparticles (e.g. bentonites,<sup>73</sup> hydrotalcites<sup>74</sup> and montmorillonites<sup>75</sup>) followed by the use of (3D) inorganic nanocarriers (e.g. zeolites<sup>76</sup> and halloysites<sup>77</sup>). Particle sizes between tenths to several hundreds of nm have been reported to allow for an effective inhibitor storage up to 0.6 gram of inhibitor per gram of particle, thereby yielding to sufficient protection of small damages in primers and sol-gels (<100  $\mu\text{m}$  width scratches).

Even though new developments are being made towards the replacement of Cr(VI), current testing and certification of protective coatings systems are still largely based on their traditional working-principles based on chromates. This makes the correct understanding and implementation of alternative protective mechanisms even more challenging.<sup>78–80</sup> For this reason the development of new inhibitor systems should go hand-in-hand with the development of new corrosion evaluation methods and modelling as shown in Figure 1.3. This philosophy was implemented during this PhD work and will be shown in the subsequent chapters of this dissertation.



## 1.4. Thesis outline

Chapter 2 introduces an in-house developed hyphenated optical and electrochemical method for the in-situ and real-time study of corrosion and corrosion inhibition processes. This set-up is applied to study the corrosion and inhibition of AA2024-T3 exposed to two NaCl concentrations and six corrosion inhibitors. During testing, 5  $\mu\text{m}$  resolution optical images of the exposed surface are obtained in parallel to EIS measurements using a newly designed 3D-printed electrochemical cell. This method allowed obtaining both optical and electrochemical information of the studied surface with high time correlation. A protocol for automated data analysis of the optical images was established and used as improvement on the understanding of EIS signals. The analysis allowed the identification and quantification of surface corrosion features on a wide spatiotemporal scale from seconds to hours. In addition, the study of the corrosion inhibition of six inhibitors at concentrations ranging from  $10^{-3}$  M to  $10^{-6}$  M allowed quantifying inhibition kinetics as well as identifying differences in the inhibition mechanisms as function of inhibitor type and concentration.

Chapter 3 describes an improved version of the real-time hyphenated setup and analysis protocol. In this occasion the highly resolved optical analysis was used to help interpreting electrochemical noise signals (EN). The concept is presented for the case of AA2024-T3 under immersion in various NaCl concentrations. EN analysis was performed in the time-frequency domain using continuous wavelet transform (CWT). Correlations between the two procedures were used to identify the succession of corrosion processes as a function of exposure time, such as de-alloying, etching, pitting and subsurface corrosion. Besides this, optical measurements at higher magnifications were used to analyse a smaller section of the exposed metal with a spatial resolution below 1  $\mu\text{m}$ . As a final result, a potentially universal plot was obtained allowing the direct relation of EN signals to the dominance of a specific corrosion phenomenon.

Chapter 4 focuses on studying the potential use of micron sized nanoporous diatom algae exoskeletons (diatomaceous earth) as corrosion inhibitor carriers for epoxy based primers. In this concept the algae exoskeleton allows internal inhibitor loading to limit the unwanted interaction between the cerium and the epoxy/amine coating and to allow for diffusion-controlled release of the inhibitor when needed. The inhibitor release (cerium salts) and corrosion protection of AA20204-T3 was evaluated by UV/Vis spectrometry, Raman spectroscopy and by using a simplified version of the optical-electrochemical analysis using EIS.

Chapter 5 builds on the knowledge gained in the previous chapters on corrosion inhibitors and the diatomite carrier system. In this case the study focused on the potential of these inhibitor-loaded algae exoskeletons to protect wide and deep scribes (up to 1 mm wide and 300  $\mu\text{m}$  below the coating) in long-time immersion testing and during cyclic (wet/dry) conditions. For this study, cerium nitrate and 2,5-dimercaptothiadiazole (DMTD) were used as inorganic and organic

corrosion inhibitors. The corrosion protection was studied using the real-time optical-electrochemical method as well as two individual local techniques measuring oxygen concentration and electrochemical impedance (LEIM) at the scribe. SEM/EDS was used to analyse the samples after exposure.

Chapter 6 introduces a diffusion-driven model to predict the inhibitor release from locally damaged coatings under immersion conditions. The effect of the inhibitor diffusivity, coating thickness and damage diameter are simulated and used to determine the inhibitor release rate necessary to reach the minimum required inhibitor concentrations allowing for corrosion protection at a circular damage. Kinematic and mass conservation laws are used as a first-order approximation to study the effect of Cerium-loaded nano- and micro-particles on the inhibitor-release. The modelled results were validated experimentally using cerium loaded zeolites and diatomite in epoxy primers. Circular damages of 50 and 300  $\mu\text{m}$  diameter were created and monitored using the real-time opto-electrochemical setup. Optics and electrochemical potential noise were used to evaluate the level of protection achieved.

## 1.5. References

- 1 A. E. Hughes, N. Birbilis, J. M. C. Mol, S. J. Garcia, X. Zhou, and G. E. Thompson, "High Strength Al-Alloys: Microstructure, Corrosion and Principles of Protection," *Recent Trends Process. Degrad. Alum. Alloy.*, pp. 223–262, 2011, doi: 10.5772/18766.
- 2 A. Boag, A. E. Hughes, A. M. Glenn, T. H. Muster, and D. McCulloch, "Corrosion of AA2024-T3 Part I: Localised corrosion of isolated IM particles," *Corros. Sci.*, vol. 53, no. 1, pp. 17–26, 2011, doi: 10.1016/j.corsci.2010.09.009.
- 3 T. G. Harvey *et al.*, "The effect of inhibitor structure on the corrosion of AA2024 and AA7075," *Corros. Sci.*, vol. 53, no. 6, pp. 2184–2190, 2011, doi: 10.1016/j.corsci.2011.02.040.
- 4 A. M. Glenn *et al.*, "Corrosion of AA2024-T3 Part III: Propagation," *Corros. Sci.*, vol. 53, no. 1, pp. 40–50, 2011, doi: 10.1016/j.corsci.2010.09.035.
- 5 A. Aballe, M. Bethencourt, F. J. Botana, and M. Marcos, "Using wavelets transform in the analysis of electrochemical noise data," *Electrochim. Acta*, vol. 44, no. 26, pp. 4805–4816, 1999, doi: 10.1016/S0013-4686(99)00222-4.
- 6 A. M. Homborg *et al.*, "Novel time-frequency characterization of electrochemical noise data in corrosion studies using Hilbert spectra," *Corros. Sci.*, vol. 66, pp. 97–110, 2013, doi: 10.1016/j.corsci.2012.09.007.
- 7 D. D. MacDonald, "Reflections on the history of electrochemical impedance spectroscopy," *Electrochim. Acta*, vol. 51, no. 8–9, pp. 1376–1388, 2006, doi: 10.1016/j.electacta.2005.02.107.
- 8 W. Tait, K. Handrich, S. Tait, and J. Martin, "Analyzing and Interpreting Electrochemical Impedance Spectroscopy Data from Internally Coated Steel Aerosol Containers," in *Electrochemical Impedance: Analysis and Interpretation*, J. Scully, D. Silverman, and M. Kendig, Eds. West Conshohocken: ASTM International, 2009, pp. 428–428–10.
- 9 E. L. Ferrer, A. P. Rollon, H. D. Mendoza, U. Lafont, and S. J. Garcia, "Double-doped zeolites for corrosion protection of aluminium alloys," *Microporous Mesoporous Mater.*, vol. 188, pp. 8–15, Apr. 2014, doi: Doi 10.1016/J.Micromeso.2014.01.004.
- 10 M. G. Taryba, M. F. Montemor, and S. V. Lamaka, "Quasi-simultaneous Mapping of Local Current Density, pH and Dissolved O<sub>2</sub>," *Electroanalysis*, vol. 27, no. 12, pp. 2725–2730, 2015, doi: 10.1002/elan.201500286.
- 11 V. Shkirskiy, P. Volovitch, and V. Vivier, "Development of quantitative Local Electrochemical Impedance Mapping: an efficient tool for the evaluation of delamination kinetics," *Electrochim. Acta*, vol. 235, pp. 442–452, 2017, doi: 10.1016/j.electacta.2017.03.076.
- 12 M. W. Wittmann, R. B. Leggat, and S. R. Taylor, "Detection and mapping of defects in organic coatings using local electrochemical impedance methods," *J. Electrochem. Soc.*, vol. 146, no. 11, pp. 4071–4075, 1999, doi: 10.1149/1.1392593.
- 13 J. C. Seegmiller, J. E. Pereira Da Silva, D. A. Buttry, S. I. Córdoba De Torresi, and R. M. Torresi, "Mechanism of action of corrosion protection coating for AA2024-T3 based on poly(aniline)-poly(methylmethacrylate) blend," *J. Electrochem. Soc.*, vol. 152, no. 2, p. B45, 2005, doi: 10.1149/1.1839472.
- 14 A. Nazarov, N. Le Bozec, and D. Thierry, "Assessment of steel corrosion and deadhesion of epoxy barrier paint by scanning Kelvin probe," *Prog. Org. Coatings*, vol. 114, no. July 2017, pp. 123–134, 2018, doi: 10.1016/j.porgcoat.2017.09.016.
- 15 A. C. Bouali, A. C. Bastos, S. V. Lamaka, M. Serdechnova, M. G. S. Ferreira, and M. L. Zheludkevich, "Evaporation of Electrolyte during SVET Measurements: The Scale of the Problem and the Solutions," *Electroanalysis*, vol. 31, no. 11, pp. 2290–2298, Nov. 2019, doi: 10.1002/elan.201900435.
- 16 T. Tokuda and M. B. Ives, "Pitting corrosion of Ni," *Corros. Sci.*, vol. 11, no. 5, pp. 297–306, 1971, doi: 10.1016/S0010-938X(71)80063-X.
- 17 G. N. Frantziskonis, L. B. Simon, J. Woo, and T. E. Matikas, "Characterization of Pitting Corrosion Damage Through Multiscale Analysis," *Nondestruct. Eval. Aging Mater. Compos. III*, vol. 3585, no. March, pp. 48–58, 1999, doi: 10.1117/12.339869.
- 18 J. Chmiel, A. Cieszyzyk-Chmiel, and J. Matysik, "Use of interferometry in corrosion investigations," *Corrosion*, 1990, doi: 10.5006/1.3585140.
- 19 C. Punckt and H. Hinrich Rotermond, "Optical imaging of pattern formation: Reflection

- anisotropy microscopy applied to globally coupled oscillatory CO-oxidation,” *Phys. Chem. Chem. Phys.*, vol. 9, no. 27, pp. 3635–3640, 2007, doi: 10.1039/b701530p.
- 20 H. H. Rotermund, “Real time imaging of catalytic reactions on surfaces: Past, present and future,” *Surf. Sci.*, vol. 603, no. 10–12, pp. 1662–1670, Jun. 2009, doi: 10.1016/j.susc.2008.11.048.
- 21 C. Merola *et al.*, “Nanometer Resolved Real Time Visualization of Acidification and Material Breakdown in Confinement,” *Adv. Mater. Interfaces*, vol. 6, no. 10, May 2019, doi: 10.1002/admi.201802069.
- 22 D. Courjon and J. Bulabois, “Real time holographic microscopy using a peculiar holographic illuminating system and rotary shearing interferometer,” *J. Opt.*, vol. 10, no. 3, pp. 125–128, 1979, doi: 10.1088/0150-536X/10/3/004.
- 23 P. E. Klages, M. K. Rotermund, and H. H. Rotermund, “Simultaneous holographic, ellipsometric, and optical imaging of pitting corrosion on SS 316LVM stainless steel,” *Corros. Sci.*, vol. 65, pp. 128–135, Dec. 2012, doi: 10.1016/j.corsci.2012.08.023.
- 24 B. Yuan, Z. Li, S. Tong, L. Li, and C. Wang, “In situ monitoring of pitting corrosion on stainless steel with digital holographic surface imaging,” *J. Electrochem. Soc.*, vol. 166, no. 11, pp. C3039–C3047, 2019, doi: 10.1149/2.0061911jes.
- 25 E. S. M. Sherif, R. M. Erasmus, and J. D. Comins, “In situ Raman spectroscopy and electrochemical techniques for studying corrosion and corrosion inhibition of iron in sodium chloride solutions,” *Electrochim. Acta*, vol. 55, no. 11, pp. 3657–3663, Apr. 2010, doi: 10.1016/j.electacta.2010.01.117.
- 26 A. Maltseva, V. Shkirskiy, G. Lefèvre, and P. Volovitch, “Effect of pH on Mg(OH) 2 film evolution on corroding Mg by in situ kinetic Raman mapping (KRM),” *Corros. Sci.*, vol. 153, pp. 272–282, Jun. 2019, doi: 10.1016/j.corsci.2019.03.024.
- 27 C. Babu Rao and R. A. J. Baldev, “Study of engineering surfaces using laser-scattering techniques,” *Sadhana - Acad. Proc. Eng. Sci.*, vol. 28, no. 3–4, pp. 739–761, 2003, doi: 10.1007/bf02706457.
- 28 U. Kamachi Mudali, C. Babu Rao, and B. Raj, “Intergranular corrosion damage evaluation through laser scattering technique,” *Corros. Sci.*, vol. 48, no. 4, pp. 783–796, 2006, doi: 10.1016/j.corsci.2005.02.027.
- 29 V. Nascov, C. Samoilă, and D. Ursuțiu, “Corrosion monitoring by optical inspection with coherent and incoherent light,” *Optoelectron. Adv. Mater. Rapid Commun.*, vol. 8, no. 11–12, pp. 1005–1012, 2014.
- 30 T. Dunford and B. Wilde, “The use of quantitative microscopy in studying the localized corrosion of aluminum 7075,” *F. Metallogr. Fail. Anal. Metallogr.*, pp. 263–272, 1987.
- 31 A. Chiba, I. Muto, Y. Sugawara, and N. Hara, “Microelectrochemical investigation of pit initiation and selective dissolution between MnS and stainless steel,” *ECS Trans.*, vol. 50, no. 47, pp. 15–23, 2012, doi: 10.1149/05047.0015ecst.
- 32 A. Chiba, I. Muto, Y. Sugawara, and N. Hara, “A Microelectrochemical System for in Situ High-Resolution Optical Microscopy: Morphological Characteristics of Pitting at MnS Inclusion in Stainless Steel,” *J. Electrochem. Soc.*, vol. 159, no. 8, pp. C341–C350, 2012, doi: 10.1149/2.054208jes.
- 33 A. M. Zimer, M. A. S. De Carra, E. C. Rios, E. C. Pereira, and L. H. Mascaro, “Initial stages of corrosion pits on AISI 1040 steel in sulfide solution analyzed by temporal series micrographs coupled with electrochemical techniques,” *Corros. Sci.*, vol. 76, pp. 27–34, Nov. 2013, doi: 10.1016/j.corsci.2013.04.054.
- 34 A. M. Zimer, M. A. S. De-Carra, L. H. Mascaro, and E. C. Pereira, “Temporal series of micrographs coupled with electrochemical techniques to analyze pitting corrosion of AISI 1040 steel in carbonate and chloride solutions,” *Electrochim. Acta*, vol. 124, pp. 143–149, Apr. 2014, doi: 10.1016/j.electacta.2014.02.023.
- 35 R. Bonzom and R. Oltra, “Droplet cell investigation of intergranular corrosion on AA2024,” *Electrochem. commun.*, vol. 81, no. June, pp. 84–87, 2017, doi: 10.1016/j.elecom.2017.06.011.
- 36 C. M. Liao, J. M. Olive, M. Gao, and R. P. Wei, “In-Situ Monitoring of Pitting Corrosion in Aluminum Alloy 2024,” *Corrosion*, vol. 54, no. 6, pp. 451–458, 1998, doi: 10.5006/1.3284873.
- 37 C. Punckt *et al.*, “Sudden onset of pitting corrosion on stainless steel as a critical phenomenon,” *Science (80- )*, vol. 305, no. 5687, pp. 1133–1136, 2004, doi: 10.1126/science.1101358.

- 38 J. W. J. Silva, A. G. Bustamante, E. N. Codaro, R. Z. Nakazato, and L. R. O. Hein, "Morphological analysis of pits formed on Al 2024-T3 in chloride aqueous solution," *Appl. Surf. Sci.*, vol. 236, no. 1–4, pp. 356–365, 2004, doi: 10.1016/j.apsusc.2004.05.007.
- 39 K. Y. Choi and S. S. Kim, "Morphological analysis and classification of types of surface corrosion damage by digital image processing," *Corros. Sci.*, vol. 47, no. 1, pp. 1–15, Jan. 2005, doi: 10.1016/j.corsci.2004.05.007.
- 40 K. V. Rybalka, L. A. Beketaeva, V. S. Shaldaev, L. V. Kasparova, and A. D. Davydov, "Development of pitting corrosion on 20Kh13 steel," *Russ. J. Electrochem.*, vol. 45, no. 11, pp. 1217–1225, 2009, doi: 10.1134/S1023193509110019.
- 41 A. S. Mikhailov, J. R. Scully, and J. L. Hudson, "Nonequilibrium collective phenomena in the onset of pitting corrosion," *Surf. Sci.*, vol. 603, no. 10–12, pp. 1912–1921, Jun. 2009, doi: 10.1016/j.susc.2008.08.045.
- 42 A. M. Zimer *et al.*, "Investigation of AISI 1040 steel corrosion in H<sub>2</sub>S solution containing chloride ions by digital image processing coupled with electrochemical techniques," *Corros. Sci.*, vol. 53, no. 10, pp. 3193–3201, Oct. 2011, doi: 10.1016/j.corsci.2011.05.064.
- 43 R. J. Power and J. Shirokoff, "Techniques for Studying In Situ Corrosion and Related Surface and Interfacial Phenomena," *Recent Patents Corros. Sci.*, vol. 1, no. 1, pp. 38–55, 2011, doi: 10.2174/2210683911101010038.
- 44 C. Merola *et al.*, "In situ nano- to microscopic imaging and growth mechanism of electrochemical dissolution (e.g., corrosion) of a confined metal surface," *Proc. Natl. Acad. Sci. U. S. A.*, vol. 114, no. 36, pp. 9541–9546, Sep. 2017, doi: 10.1073/pnas.1708205114.
- 45 D. Huang *et al.*, "Optical coherence tomography," *Science (80- )*, vol. 254, no. 5035, pp. 1178–1181, Nov. 1991, doi: 10.1126/science.1957169.
- 46 H. Nguyen Thi *et al.*, "In situ and real-time analysis of TGZM phenomena by synchrotron X-ray radiography," *J. Cryst. Growth*, vol. 310, no. 11, pp. 2906–2914, May 2008, doi: 10.1016/j.jcrysgro.2008.01.041.
- 47 G. Biepwagen--North, "Aircraft Coatings."
- 48 R. L. Twite and G. P. Bierwagen, "Review of alternatives to chromate for corrosion protection of aluminum aerospace alloys," *Prog. Org. Coatings*, vol. 33, no. 2, pp. 91–100, 1998, doi: 10.1016/S0300-9440(98)00015-0.
- 49 A. S. Cushman, "The corrosion of iron," *Science*, vol. 27, no. 695. p. 666, 1908, doi: 10.1126/science.27.695.666.
- 50 D. Chidambaram, M. J. Vasquez, G. P. Halada, and C. R. Clayton, "Studies on the repassivation behavior of aluminum and aluminum alloy exposed to chromate solutions," *Surf. Interface Anal.*, vol. 35, no. 2, pp. 226–230, 2003, doi: 10.1002/sia.1507.
- 51 M. Kendig, S. Jeanjaquet, R. Addison, and J. Waldrop, "Role of hexavalent chromium in the inhibition of corrosion of aluminum alloys," *Surf. Coatings Technol.*, vol. 140, no. 1, pp. 58–66, 2001, doi: 10.1016/S0257-8972(01)01099-4.
- 52 E. Eichinger, J. Osborne, and T. Van Cleave, "Hexavalent chromium elimination: An aerospace industry progress report," *Met. Finish.*, 1997, doi: 10.1016/S0026-0576(97)86771-2.
- 53 Surface Engineering Association, "REACH and the impact of Hexavalent Chromium," *Surface Engineering Association*, 2019.
- 54 O. Gharbi, S. Thomas, C. Smith, and N. Birbilis, "Chromate replacement: what does the future hold?," *npj Mater. Degrad.*, vol. 2, no. 1, pp. 23–25, 2018, doi: 10.1038/s41529-018-0034-5.
- 55 M. A. Jakab, F. Presuel-Moreno, and J. R. Scully, "Critical concentrations associated with cobalt, cerium, and molybdenum inhibition of AA2024-T3 corrosion: Delivery from Al-Co-Ce(-Mo) alloys," *Corrosion*, vol. 61, no. 3, pp. 246–263, 2005, doi: 10.5006/1.3280634.
- 56 H. Shi, E. H. Han, and F. Liu, "Corrosion protection of aluminium alloy 2024-T3 in 0.05M NaCl by cerium cinnamate," *Corros. Sci.*, vol. 53, no. 7, pp. 2374–2384, Jul. 2011, doi: 10.1016/j.corsci.2011.03.012.
- 57 D. Chadwick and T. Hashemi, "Electron spectroscopy of corrosion inhibitors: Surface films formed by 2-mercaptobenzothiazole and 2-mercaptobenzimidazole on copper," *Surf. Sci.*, vol. 89, no. 1–3, pp. 649–659, 1979, doi: 10.1016/0039-6028(79)90646-0.
- 58 W. Chen, H. Q. Luo, and N. B. Li, "Inhibition effects of 2,5-dimercapto-1,3,4-thiadiazole on the corrosion of mild steel in sulphuric acid solution," *Corros. Sci.*, vol. 53, no. 10, pp. 3356–3365,

- 2011, doi: 10.1016/j.corsci.2011.06.013.
- 59 G. Williams, A. J. Coleman, and H. N. McMurray, "Inhibition of Aluminium Alloy AA2024-T3 pitting corrosion by copper complexing compounds," *Electrochim. Acta*, vol. 55, no. 20, pp. 5947–5958, Aug. 2010, doi: 10.1016/j.electacta.2010.05.049.
- 60 D. Snihirova, S. V. Lamaka, P. Taheri, J. M. C. Mol, and M. F. Montemor, "Comparison of the synergistic effects of inhibitor mixtures tailored for enhanced corrosion protection of bare and coated AA2024-T3," *Surf. Coatings Technol.*, vol. 303, no. Part B, pp. 342–351, 2016, doi: 10.1016/j.surfcoat.2015.10.075.
- 61 J. Gui and T. M. Devine, "Influence of lithium on the corrosion of aluminum," *Scr. Metall.*, vol. 21, no. 6, pp. 853–857, 1987, doi: 10.1016/0036-9748(87)90336-X.
- 62 C. M. Rangel and M. A. Travassos, "The passivation of aluminium in lithium carbonate/bicarbonate solutions," *Corros. Sci.*, vol. 33, no. 3, pp. 327–343, 1992, doi: 10.1016/0010-938X(92)90064-A.
- 63 R. G. Buchheit, M. D. Bode, and G. E. Stoner, "Corrosion-resistant, chromate-free talc coatings for aluminum," *Corrosion*, vol. 50, no. 3, pp. 205–214, 1994, doi: 10.5006/1.3293512.
- 64 C. D. Dieleman, P. J. Denissen, and S. J. Garcia, "Long-Term Active Corrosion Protection of Damaged Coated-AA2024-T3 by Embedded Electrospun Inhibiting Nanonetworks," *Adv. Mater. Interfaces*, vol. 5, no. 12, 2018, doi: 10.1002/admi.201800176.
- 65 P. Visser, M. Meeusen, Y. Gonzalez-Garcia, H. Terryn, and J. M. C. Mol, "Electrochemical evaluation of corrosion inhibiting layers formed in a defect from lithium-leaching organic coatings," *J. Electrochem. Soc.*, vol. 164, no. 7, pp. C396–C406, 2017, doi: 10.1149/2.1411707jes.
- 66 J. S. Laird, P. Visser, S. Ranade, A. E. Hughes, H. Terryn, and J. M. C. Mol, "Li leaching from Lithium Carbonate-primer: An emerging perspective of transport pathway development," *Prog. Org. Coatings*, vol. 134, pp. 103–118, Sep. 2019, doi: 10.1016/j.porgcoat.2019.04.062.
- 67 D. G. Shchukin, "Container-based multifunctional self-healing polymer coatings," *Polym. Chem.*, vol. 4, no. 18, pp. 4871–4877, 2013, doi: 10.1039/c3py00082f.
- 68 D. Borisova, H. Möhwald, and D. G. Shchukin, "Influence of embedded nanocontainers on the efficiency of active anticorrosive coatings for aluminum alloys part I: Influence of nanocontainer concentration," *ACS Appl. Mater. Interfaces*, vol. 4, no. 6, pp. 2931–2939, 2012, doi: 10.1021/am300266t.
- 69 Y. Peng *et al.*, "Leaching Behavior and Corrosion Inhibition of a Rare Earth Carboxylate Incorporated Epoxy Coating System," *ACS Appl. Mater. Interfaces*, vol. 11, no. 39, pp. 36154–36168, 2019, doi: 10.1021/acsami.9b13722.
- 70 E. Javierre, S. J. Garcia, J. M. C. Mol, F. J. Vermolen, C. Vuik, and S. van der Zwaag, "Tailoring the release of encapsulated corrosion inhibitors from damaged coatings: Controlled release kinetics by overlapping diffusion fronts," *Prog. Org. Coatings*, vol. 75, no. 1–2, pp. 20–27, 2012, doi: 10.1016/J.Porgcoat.2012.03.002.
- 71 M. L. Zheludkevich, D. G. Shchukin, K. A. Yasakau, H. Möhwald, and M. G. S. Ferreira, "Anticorrosion coatings with self-healing effect based on nanocontainers impregnated with corrosion inhibitor," *Chem. Mater.*, vol. 19, no. 3, pp. 402–411, 2007, doi: 10.1021/cm062066k.
- 72 M. Abdolah Zadeh, J. Tedim, M. Zheludkevich, S. van der Zwaag, and S. J. Garcia, "Synergistic active corrosion protection of AA2024-T3 by 2D- anionic and 3D-cationic nanocontainers loaded with Ce and mercaptobenzothiazole," *Corros. Sci.*, vol. 135, pp. 35–45, 2018, doi: 10.1016/j.corsci.2018.02.018.
- 73 S. Bohm, H. N. McMurray, D. A. Worsley, and S. M. Powell, "Novel environment friendly corrosion inhibitor pigments based on naturally occurring clay minerals," *Mater. Corros.*, vol. 52, no. 12, pp. 896–903, 2001, doi: 10.1002/1521-4176(200112)52:12<896::aid-maco896>3.0.co;2-8.
- 74 R. G. Buchheit, S. B. Mamidipally, P. Schmutz, and H. Guan, "Active corrosion protection in Ce-modified hydrotalcite conversion coatings," *Corrosion*, vol. 58, no. 1, pp. 3–14, 2002, doi: 10.5006/1.3277303.
- 75 L. V. Gorobinskii, G. Y. Yurkov, and D. A. Baranov, "Production of high porosity nanoparticles of cerium oxide in clay," *Microporous Mesoporous Mater.*, vol. 100, no. 1–3, pp. 134–138, 2007, doi: 10.1016/j.micromeso.2006.09.047.
- 76 E. L. Ferrer, A. P. Rollon, H. D. Mendoza, U. Lafont, and S. J. Garcia, "Double-doped zeolites for

- 
- corrosion protection of aluminium alloys,” *Microporous Mesoporous Mater.*, vol. 188, pp. 8–15, 2014, doi: Doi 10.1016/J.Micromeso.2014.01.004.
- 77 D. Fix, D. V. Andreeva, Y. M. Lvov, D. G. Shchukin, and H. Möhwald, “Application of inhibitor-loaded halloysite nanotubes in active anti-corrosive coatings,” *Adv. Funct. Mater.*, vol. 19, no. 11, pp. 1720–1727, 2009, doi: 10.1002/adfm.200800946.
- 78 Y. L. Cheng *et al.*, “A study of the corrosion of aluminum alloy 2024-T3 under thin electrolyte layers,” *Corros. Sci.*, vol. 46, no. 7, pp. 1649–1667, 2004, doi: 10.1016/j.corsci.2003.10.005.
- 79 B. S. Skerry and C. H. Simpson, “Corrosion and Weathering of Paints for Atmospheric Corrosion Control,” *Corrosion*, vol. 49, no. 8, pp. 663–674, 1993, doi: 10.5006/1.3316098.
- 80 K. R. Baldwin and C. J. E. Smith, “Accelerated corrosion tests for aerospace materials: current limitations and future trends,” *Aircr. Eng. Aerosp. Technol.*, vol. 71, no. 3, pp. 239–244, 1999, doi: 10.1108/00022669910270718.



# 2

## Reducing subjectivity in EIS interpretation of corrosion and corrosion inhibition processes by in-situ optical analysis

*An in-situ hyphenated optical and electrochemical method for the real-time study of corrosion and corrosion inhibition processes is presented and validated for the case of AA2024-T3 exposed to two NaCl concentrations and six inhibitors. During testing, 5 μm resolution optical images of the exposed surface are obtained in parallel to electrochemical impedance measurements using a home-made 3D printed electrochemical cell. This method allowed obtaining both optical and electrochemical information of the studied surface with high time correlation. A data treatment analysis of the optical images was established thereby allowing the identification and quantification of corrosion-features related to intermetallic corrosion (e.g. trenching and meta-stable pitting) and co-operative corrosion (e.g. corrosion-rings, domes and surface-oxides) on a spatiotemporal scale, generally only observed through the use of ex-situ methods such as SEM. In addition, the study of the long-term corrosion inhibition of six inhibitors at concentrations ranging from 10<sup>-3</sup> M to 10<sup>-6</sup> M allowed quantifying inhibition kinetics as well as identifying different inhibitor and concentration dependent mechanisms (e.g. Cerium and DEDTC vs. Lithium) and decreasing incongruences between impedance and inhibition behaviour (e.g. DMTD). As a result, the use of quantifiable in-situ optical analysis is confirmed as a powerful tool to better interpret electrochemical signals or monitor electrochemical-dependent surface phenomena.*

This chapter has been published as:

P. J. Denissen, S. J. Garcia, Reducing subjectivity in EIS interpretation of corrosion and corrosion inhibition processes by in-situ optical analysis, *Electrochimica Acta* 2019.

## 2.1. Introduction

Electrochemical Impedance Spectroscopy (EIS) is a well-established technique broadly used to monitor corrosion processes and monitor coating properties.<sup>1</sup> The foundation for EIS dates back to the end of the 19th century by Oliver Heaviside who applied Laplace transformations to frequency dependent electrical circuits, thereby enabling the conversion of integro-differentials to simple algebraic equations.<sup>2</sup> His paper, published in 1872, was heavily criticized because the theorem could not be proven mathematically until the following century.<sup>3</sup> It was not until the 1980s that EIS awoke the general interest of scientists working on coatings, corrosion and batteries, rapidly growing from around 30 annual publications in 1980 to more than 6000 in 2017.<sup>1</sup> Despite the ever increasing literature, effective interpretation of EIS data is not always evident for complicated systems that require mathematical skills and good understanding of the involved physical processes.<sup>4</sup>

As a natural evolution, EIS data is often interpreted through electrical equivalent circuits (EECs) whereby a successful fit is described as proof that the presented physical model is correct, while in fact many different models within the same accuracy will represent the data equally well.<sup>5</sup> The correctness of the EECs can only be truly confirmed by applying a dataset of infinite accuracy to the model, which is clearly an unrealistic presumption. Part of the problem lies in the fact that electrochemical processes are often complex and are influenced by many different parameters such as composition, porosity, interphases, environmental conditions and sample geometry, as well as the time superposition of different phenomena.<sup>6-9</sup> These factors increase subjectivity and risk of misinterpretations difficult to identify. In the case of corrosion and coating studies, a common approach to interpret electrochemical data is to perform analysis by means of optical microscopy<sup>10</sup> and other surface analysis techniques such as TEM,<sup>11</sup> SEM-EDS,<sup>12</sup> Raman<sup>13</sup> and FTIR<sup>14</sup>. Despite informative, this approach requires the sample to be extracted from the electrolyte, analysed and in some cases brought back to the electrochemical test, thereby missing the time-dependent information relevant to interpret time-evolution of electrochemical signals as well as their correlation to macroscopic phenomena simultaneously. Alternatively, multiple samples can be collected and analysed after different immersion times but raise concerns on the influence of the different intermetallic (IM) distribution or composition between the samples on the optical analysis and electrochemical signals.<sup>15</sup> As an alternative to these traditional approaches some authors working on coatings and corrosion have coupled electrochemical measurements to other techniques (e.g. X-ray micro-tomography,<sup>16,17</sup> Atomic Emission Spectroelectrochemistry<sup>18</sup> and Raman Spectroscopy<sup>19</sup>) to monitor corrosion phenomena in real time. Despite offering powerful information about corrosion processes and delamination of coatings, such techniques remain scarcely used due to their limited availability, complexity and high costs.

In this paper we propose a simple and inexpensive method to obtain real-time electrochemical and optical information of the corrosion process of metals immersed in electrolyte. The hyphenated optical and electrochemical setup and the data analysis protocol here presented allow obtaining a full set of characteristic parameters to monitor and study the evolution of surface-related macroscopic phenomena and their correlation to electrochemical data with spatio-temporal resolution. The setup and data processing protocol are defined and validated by studying the corrosion behaviour of aluminium alloy 2024-T3 exposed to 0.05 M and 0.5 M NaCl solutions. For this, the electrochemical changes observed in the EIS spectra are related to the corresponding macroscopic surface changes observed with the optical component and the interpretation validated by means of previous works on the corrosion process of AA2024-T3.<sup>20-36</sup> Subsequently, the optical-electrochemical setup is employed to study the time-dependent inhibiting efficiency of six corrosion inhibitors for AA2024-T3 alternative to chromates at inhibitor concentrations ranging from  $10^{-3}$  M to  $10^{-6}$  M. The six inhibitors were selected based on their nature, protection efficiency, and reportedly different inhibiting mechanisms. Cerium Nitrate ( $\text{Ce}(\text{NO}_3)_3$ ) and Lithium Carbonate ( $\text{Li}_2\text{CO}_3$ ) were selected as efficient inorganic corrosion inhibitors, while Sodium diethyldithiocarbamate trihydrate (DEDTC), 2,5-dimercapto-1,3,4-thiadiazolate (DMTD), 2-mercaptobenzothiazole (2MBT), and 8-hydroxyquinoline (8HQ) were selected as organic corrosion inhibitors. While the inhibitor mechanism for  $\text{Ce}$ <sup>37</sup> and  $\text{Li}$ <sup>38,39</sup> are known, this remains an ongoing debate for the selected organic inhibitors. These have been reported to act as insoluble chelating reagents, specifically at cathodic copper-rich regions,<sup>40</sup> or work as mixed type inhibitors that chemisorb<sup>41</sup> over the entire surface. This paper shows the validity of the optical-electrochemical in-situ evaluation as a powerful approach to visualize and quantify surface phenomena related to the corrosion or/and inhibition processes normally observed by ex-situ post-mortem SEM studies, leading to a better interpretation of corrosion-related processes.

## 2.2. Materials and Methods

### 2.2.1. Materials

Commercial 2 mm thick bare AA2024-T3 sheets were obtained from Kaizer Aluminium and cut into coupons of 25x50 mm. The native oxide layer was removed by Scotch Brite 3M followed by degreasing with acetone and rinsing with demineralised water prior to clamping in the optical-electrochemical cell and exposure to NaCl electrolyte solutions with and without corrosion inhibitors.

Analytical grade corrosion inhibitors were purchased from Sigma-Aldrich and used as received: Cerium Nitrate Hexahydrate ( $\text{Ce}(\text{NO}_3)_3$ , >99%), Lithium Carbonate ( $\text{Li}_2\text{CO}_3$ , >99%), Sodium diethyldithiocarbamate trihydrate (DEDTC, >97%), 2,5-dimercapto-1,3,4-thiadiazolate (DMDT >99%), 2-mercaptobenzothiazole (2-MBT, >98%), and 8-hydroxyquinoline (8HQ, >99%). Sodium chloride (NaCl, >98%) was purchased from VWR Chemicals. Aqueous solutions at 0.05 and 0.5 M NaCl were prepared using Milipore® Elix 3 UV filtered water. The inhibitors were then added to the 0.05 M NaCl aqueous solution to obtain varying corrosion inhibitor concentrations in the range  $10^{-3}$  M to  $10^{-6}$  M.

### 2.2.2. Optical and electrochemical in-situ measurement

A potentiostat Metrohm PGSTAT 302 fitted with FRA32M and MUX.MULTI.4 modules was used to perform the Electrochemical Impedance Spectroscopy (EIS) and Open Circuit Potential (OCP) measurements. A three-electrode set up was employed consisting of a silver/silver-chloride (Ag/AgCl) reference electrode (RE), 6.6 mm diameter graphite rod as counter electrode (CE) and the metallic coupons subject of study acting as the working electrodes (WE). The frequency range of study was  $10^{-2}$ - $10^5$  Hz at 10 points per decade, with applied amplitude of 10 mV root mean square (RMS) over OCP to minimize the influence of the test on the metal-coating system while still obtaining a reliable response. The potentiostat was controlled with a USB interface through the software package NOVA V1.11.1 to allow for automatic EIS measurements every hour. For the optical measurement an inexpensive and commercially available USB Celestron handheld digital microscope camera with 5.0 megapixel resolution and equipped with an adjustable 8-led ring-light was used. The camera was programmed to take a picture every 10 minutes in parallel with the EIS measurements.

A home-made cell was produced from polycarbonate using an Ultimaker 2+ 3D printer for the real time optical and electrochemistry studies as shown in Figure 2.1 and supporting information (SI-2.1).

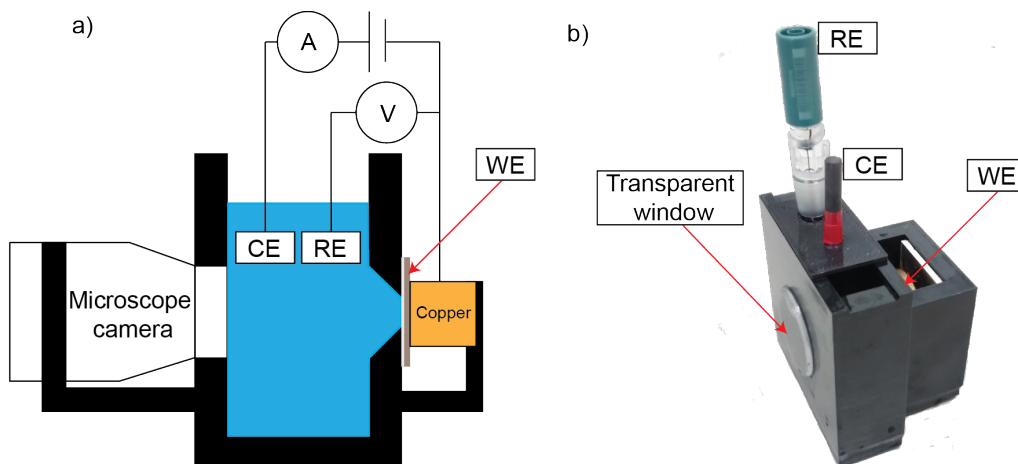


**Figure 2.1** Schematic illustration of the cell for the optical and electrochemical studies (a). Scheme shows the three-electrode set up and the position of the microscope optical camera with respect to the working electrode target of the study. Photography of the optical-electrochemical cell used in this study (b).

The cell shown in Figure 2.1b was subsequently cleared of printing defects and coated with epoxy/amine coating to avoid leakage. A 3 mm thick transparent polymethylmethacrylate (PMMA) lid was attached to the previously manufactured aperture of 40 mm diameter to act as window for the optical camera placement. The metallic coupons subject of study (in this case AA2024-T3) were then placed, with the help of a copper block, against an 9.5 mm diameter hole at the opposite side of the window for the optical analysis. The optical camera and ring-light was then aligned against the PMMA window focusing it to the metal surface. Both the camera and the electrochemical cell were placed inside a fully closed Faraday cage to avoid external electrochemical and optical interferences. Right before immersion of the three-electrode setup the cell was filled with 100 mL electrolyte solution.

### 2.2.3. Optical analysis

Quantitative information extracted from the in-situ optical analysis was obtained through an automated image analysis procedure as shown in Figure 2.2.

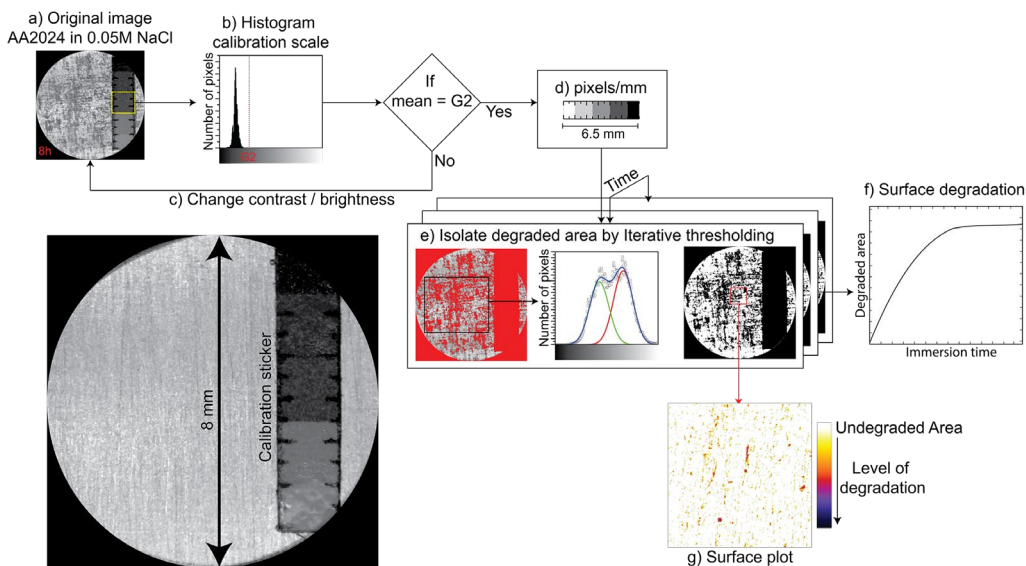


**Figure 2.2** Block-diagram of the image analysis procedure.

The camera-software recorded and automatically stored images in 8-bit format (256 bin grey-scale, bin 0 for black and bin 255 for white) right from the start of the measurement. In order to compensate for changes in contrast/brightness caused by differences in lighting and auto-exposure settings of the camera between images a calibration sticker containing 5 grey standards including a scale bar was attached to the metal surface prior to immersion as shown in Figure 2.2a. In order to obtain quantifiable information from the images an evaluation protocol was established. A Macro scripting protocol was used to automatically analyse the images in ImageJ open source software (SI-2.2). The calibration-script measures the grey-value on the calibration sticker for each individual image (Figure 2.2b) and adjusts iteratively the contrast/brightness of the image until the grey-value of the calibration sticker matches their predefined calibrated standard value (Figure 2.2c), thereby also correcting the corresponding metal surface to any optically imposed external interference. The scale-bar on the calibration sticker was further used by the script to accurately determine the magnification of the images (Figure 2.2d), which was around  $5 \mu\text{m}$  per pixel for all the measurements. For easier processing, all images corresponding to one test were stacked together and the averaged 8-bit histogram over the entire exposure-time was calculated (Figure 2.2e). This allowed obtaining a double-Gaussian distribution whereby the peak in the light regime is attributed to the pixels corresponding to non-corroded aluminium surface (background) and the peak in the dark regime (foreground) to the pixels corresponding to optically detectable macroscopic phenomena related to the corrosion processes (e.g. pitting corrosion, intergranular corrosion and deposits on the surface which are darker than the background such as oxides). To separate the signals corresponding to the corrosion-related optically detectable features from the unaffected background an iterative thresholding algorithm

developed by Ridler and Calvard<sup>42</sup> was implemented to deconvolute the two peaks in the histogram, as expressed by Equation (2.1) and the procedure described here below;

$$\theta_i = \frac{m_{f,i-1} + m_{b,i-1}}{2} \quad \text{until } \theta_i = \theta_{i-1} \quad (2.1)$$

where ( $\theta$ ) is the starting grey value at half of the dynamic range used as threshold to segment the total histogram into two parts. Then, the mean grey values were computed for both parts, namely the foreground ( $m_{f,0}$ ) and background ( $m_{b,0}$ ). The average of these two parts represents the new threshold and the entire calculation process is repeated 'i' number of times until the threshold converges to its optimal value. For each individual image the pixels with grey-values below this threshold were assigned as corresponding to the unaffected background and converted to white. The image was then reconstructed into 8-bit whereby the optically-detectable time dependent surface features receive a grey-value between 1 and 255. These now highlighted areas are then used to quantify what is here presented as the degraded area (Figure 2.2f). The degree and type of degradation processes was further analysed by constructing a colour-plot whereby the grey-value of each pixel was transposed to a colour-gradient (Fire-LUT) in which the pixels related to no corrosion (white) are coloured white and the pixels related to high degradation (black) are coloured purple (Figure 2.2g). Such an approach allowed identifying in a first order approximation surface features as pits or as oxides depending on the colour scale.

## 2.3. Results and Discussion

### 2.3.1. Identification of corrosion-related features in AA2024-T3

#### 2.3.1.1. Global temporally-resolved evaluation

Figure 2.3 shows the electrochemical (Bode plots) and optical greyscale images obtained with the optical-electrochemical set-up for AA2024-T3 panels after 1 h, 3 h, 9 h and 15 h immersion in 0.05 M NaCl and 0.5 M NaCl solutions.

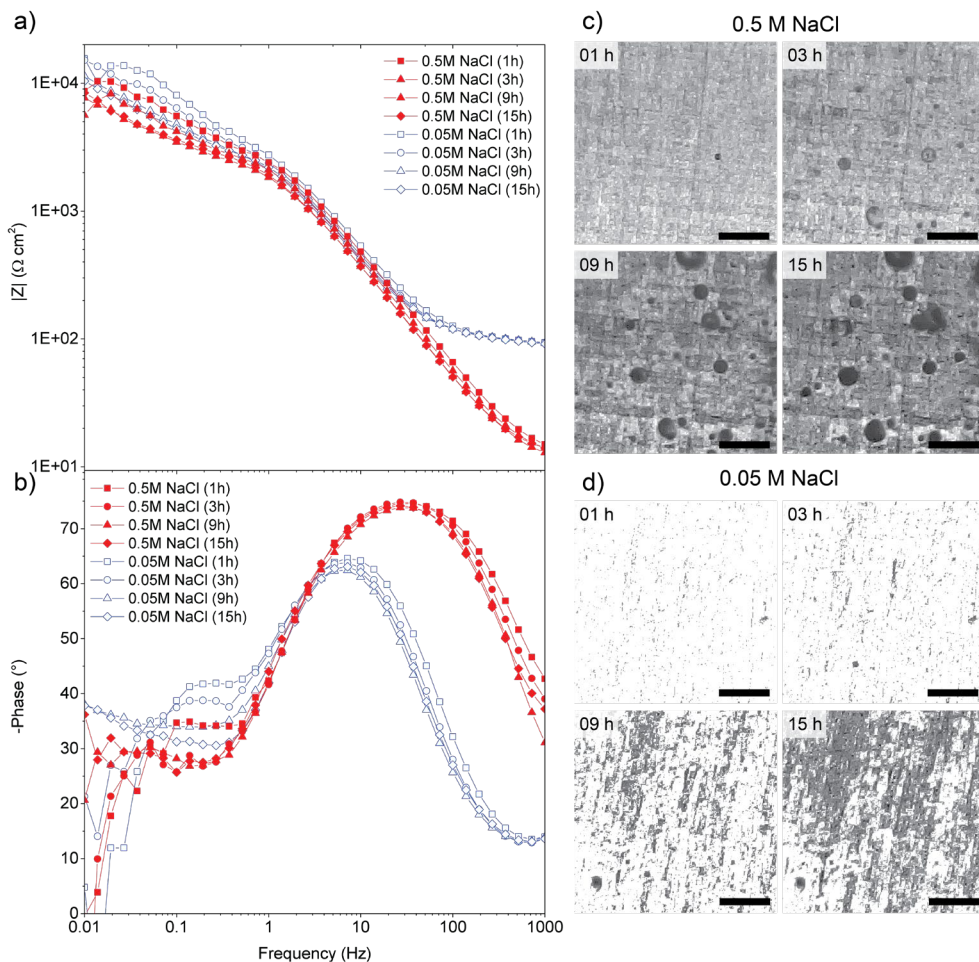


**Figure 2.3** Bode plots of AA2024-T3 exposed to 0.5 M and 0.05 M NaCl and corresponding optical images where (a) shows the total impedance  $|Z|$  and (b) the phase angle after 1 h, 3 h, 9 h and 15 h immersion. (c) and (d) show the corresponding optical images to the selected EIS times for 0.5 M and 0.05 M NaCl, respectively. Scale bar represents 500  $\mu\text{m}$ .

The effect of the salt concentration is clearly visible both electrochemically and optically (Figure 2.3) while the time-dependent effects are only clearly visible in the optical results. At high

frequencies between 100 and 1000 Hz the influence of fast electron-transfer results in a lower total impedance and higher phase for the highest salt concentration as expected for higher electrolyte conductivity.<sup>20</sup> At frequencies between 1 Hz and 0.01 Hz the total impedance and phase shift can be attributed to electrochemical processes near the metal surface (e.g. oxide layers).<sup>21,29,30</sup> Kramers-Kronig residual errors on the data (shown in SI-2.3) confirmed the systems instability during the first 2 to 6 hours of immersion at frequencies below 1 Hz. Such electrochemical instabilities are also related to large OCP fluctuations as a result of pitting, causing unrealistic EIS data.<sup>31</sup> The unprocessed greyscale images for the first immersion hours could also not confirm the presence of such surface-changes due to a lack of resolution in the current setup. After the first hours of immersion the fluctuations below 0.05 Hz become lessened together with an increasing negative phase angle. This, combined with the reduction of the total impedance at 0.01 Hz indicates the appearance of another time constant below the investigated frequency region and correspond to the mass-transfer diffusion processes located at the pits.<sup>32</sup>

In order to obtain more detailed and quantifiable information of the surface-related corrosion processes, the electrochemical and optical data were further analysed as explained in the methods section. The impedance values at 0.01 Hz were selected for the comparison as this frequency highlights the on-going processes at the metal surface related to corrosion phenomena.<sup>43</sup> Figure 2.4 shows the time-evolution in electrolyte of: (a, b) the total impedance  $|Z|$  at a frequency of 0.01 Hz for AA2024-T3; and (c, d) the calculated optically-detectable degraded area in percentage.

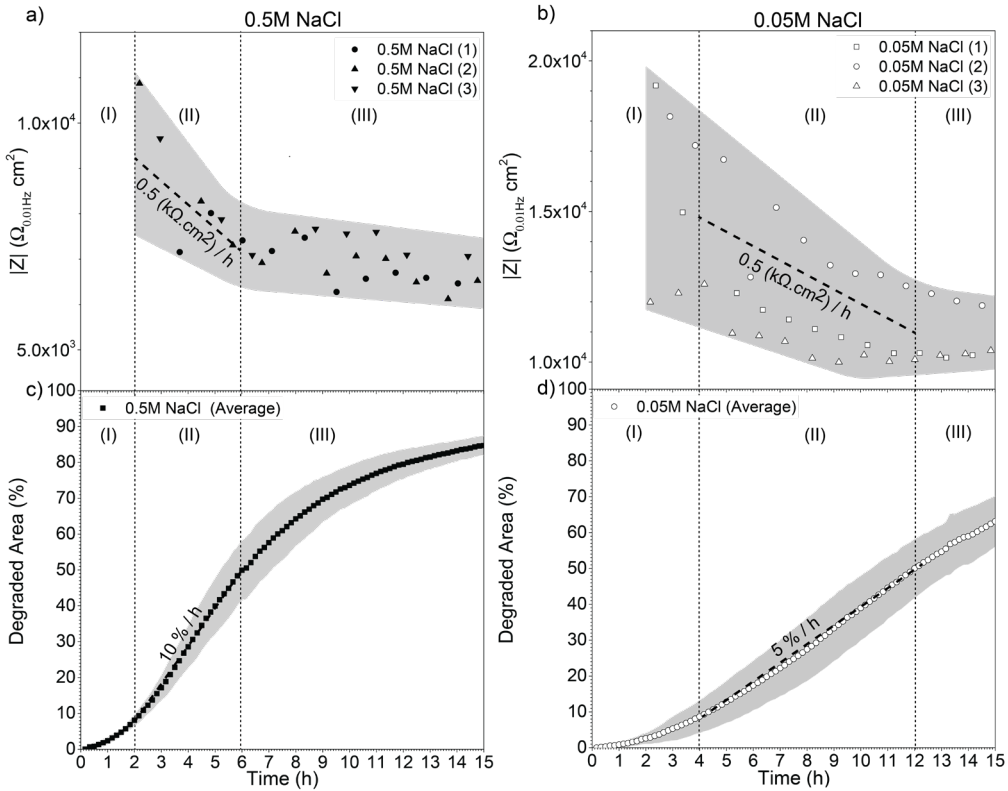


**Figure 2.4** Processed optical and electrochemical data into quantifiable information for AA2024-T3 immersed in 0.5 M and 0.05 M NaCl. (a, b) shows the time-evolution of the stable total impedance  $|Z|$  at a frequency of 0.01 Hz in and with negative phase angle; and (c, d) time-evolution of the optically detectable degradation area. Note: greyscale bands show the error bars related to three repeated tests, and the numbers relate to the different stages of the corrosion process.

From Figure 2.4 a clear increase of the degraded area and decrease of the total impedance with the immersion time can be observed for both electrolyte salt concentrations. The evolution in total impedance shows a high degree of scatter between the repeating tests and is fairly similar at both salt concentrations. Contrarily, the surface degradation quantified from the optical images evolves significantly faster at higher salt concentrations (0.5 M NaCl) and shows good reproducibility by the narrower error-band. Three different stages of the surface corrosion process can be identified and related to the corrosion features reported in literature for AA2024-T3 as a first order approximation:

- (I) First 2 and 4 hours of immersion in 0.5 M and 0.05 M NaCl, respectively: slow increase of the degraded area until it reaches 7% degraded area (Figure 2.4c and Figure 2.4d) combined with a limited amount of stable total impedance measurements at 0.01 Hz (unstable unreliable data with negative phase angle and in accordance to large Kramers-Kronig residual errors (SI-2.3) are not shown). This is in agreement with the first stages

of the corrosion process where chloride ions break down the visually undetectable natural oxide layer<sup>33</sup> explaining the higher impedance measured during the initial hours of immersion followed by the decrease over time as shown in Figure 2.4a. While the optical changes during the first hours of immersion were difficult to detect from the unprocessed grey-scale images (Figure 2.3), the optical analysis procedure used to calculate the surface-changes (Figure 2.4c and Figure 2.4d) clearly shows an increase of degraded-area due to localised pitting corrosion occurring first at isolated S-phase intermetallic (IM) particles followed by AlCuFeMn and  $(\text{AlCu})_x(\text{FeMn})_y\text{Si}$  (IM) particles.<sup>15</sup> The reason for the initiation at the S-phase is due to their lower OCP compared to other IM particles and matrix, making them anodically active thereby undergoing dissolution and trenching.<sup>34,35</sup> Several studies report that this corrosive attack occurs during the first minutes of immersion at the sub-micron level in the form of dissolution and copper enrichment of the S-phase until they switch to cathodic sites, resulting in the dissolution of hydrated aluminium oxide products.<sup>15,22,36</sup> Boag et al. also illustrate in their work that these oxides might appear on the S-phase and form a homogeneous layer with limited lifetime over the entire IM/matrix interface during the first hours of immersion, which can electrochemically isolate the IM particle remnants. Even if many of these individual corrosion-processes take place below detection-limit of the current optical setup, the total accumulation of degraded-area around 7% is in good correlation with trenching, pit-initiation, and the formation of an oxide products on and around the IM particles that cover roughly 3% of the total area on AA2024.<sup>23</sup>

- (II) From 2 to 6 h and 4 to 12 h immersion in 0.5 M and 0.05 M NaCl, respectively: comparable decrease of total impedance of roughly  $0.5 \text{ (k}\Omega\cdot\text{cm}^2) / \text{h}$  (Figure 2.4a and Figure 2.4b) for the two salt concentrations, combined with an increase in degraded area of 10 %/h for 0.5 M NaCl and 5 %/h for 0.05 M NaCl (Figure 2.4c and Figure 2.4d). This second stage of surface corrosion corresponds to co-operative corrosion or severe corrosion attack reported in literature.<sup>24,25</sup> This process involves a number of particles, as the name indicates, and describes the broader interaction of IM particles with themselves, the wider matrix or both.
- (III) From 6 and 12 h onwards in 0.5 M and 0.05 M NaCl, respectively: decrease of the degraded area growth kinetics (less visible for 0.05 M) combined with stagnation of the total impedance in the case of 0.5 M. The final stabilization of total impedance and decrease of the degradation rate is most likely caused by the decrease of surface corrosion combined with the propagation to subsurface corrosion attack as reported in literature.<sup>10</sup>

### 2.3.1.2. Local spatial-resolved evaluation

In order to shed some extra light on the local surface corrosion phenomena, colour-plots of the optical images were derived as for the 0.05 M NaCl solution in Figure 2.5.

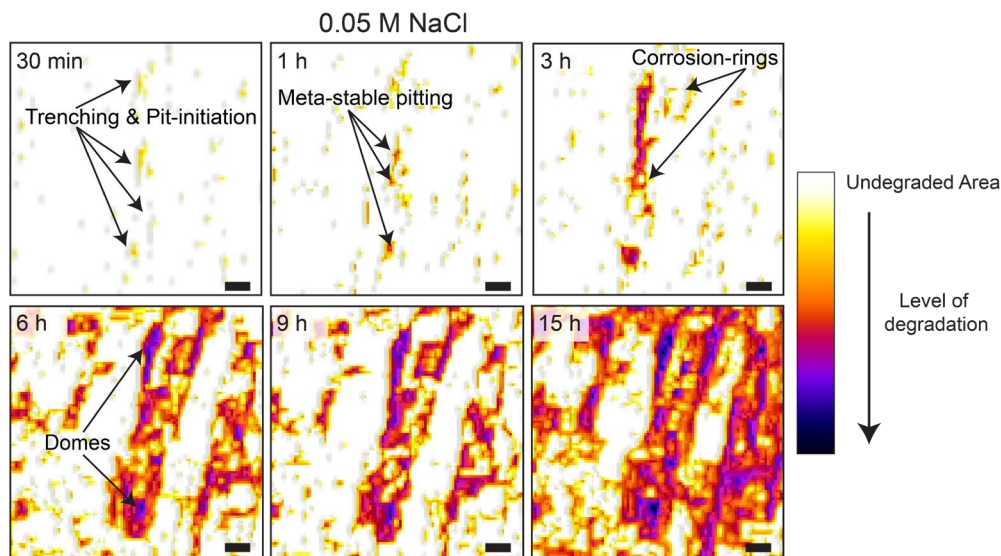


**Figure 2.5** Colour-plots of the micrographs of the same region after different immersion-times in 0.05 M NaCl. Scale bars represent 50  $\mu\text{m}$ .

Multiple yellow spots of 5 to 20  $\mu\text{m}$  diameter appear during the first 30 min immersion and are related to pit initiation involving trenching. The size and distribution of these spots are in good agreement with the reported average size for IM particles found in AA2024, which are evenly distributed and have cross-sectional diameters between 1 to 30  $\mu\text{m}$ .<sup>26</sup> Between 1 and 3 h immersion the growth of these spots is in good agreement with further IM dissolution and trenching. The thin yellow border around grey areas (IMs) suggests higher depth and a higher degree of degradation related to the propagation of meta-stable pits possibly caused by the deposition of the thin copper layer around the pits and trenching sites.<sup>27</sup> Besides the growth, the micrographs show that the active locations start interconnecting to each-other to form faint rings of corrosion-products with a size between 50 and 200  $\mu\text{m}$  and coincide with the descriptions made for early-stage co-operative corrosion.<sup>28</sup> After 3 h the local surface-degradation at the meta-stable pits and corrosion-rings start to coalesce into dense circular spots that appear purple in colour which can be typified as domes of corrosion products as indicated in Figure 2.5 (6 h).<sup>28</sup> The surface around the domes has degraded significantly as well, suggesting an increase of oxide-deposits at the surface. After 6 h of immersion the amount of oxide-deposits continues to increase (presence of domes), suggesting the propagation to subsurface corrosion under the domes<sup>28</sup> besides the propagation of surface corrosion attack.

The detection of surface-related features in time under immersion conditions as obtained here and their relation to reported local corrosion activity around the IM particles and co-operative sites can be summarised as shown in Figure 2.6 for AA2024-T3 in 0.05 M NaCl. Figure 2.6 shows that the in-situ spatiotemporal optical analysis makes it possible to observe and identify several different corrosion-features typically only identified by SEM or ex-situ optical microscopy studies.<sup>11,15,24,36</sup> While the current optical setup with 5  $\mu\text{m}$  pixel resolution does not allow the observation of early-stage etching, quantification of the IM composition or sub-surface related processes (e.g. subsurface intergranular attack), the different features related to corrosion around IM particles (i.e. trenching and meta-stable pitting) and co-operative corrosion (i.e. corrosion rings, domes, and surface oxide-deposits) can easily be identified and quantified based on their time-evolved kinetics and colour map of the optical images while the electrochemical signals are of more difficult correlation to macroscopic phenomena.

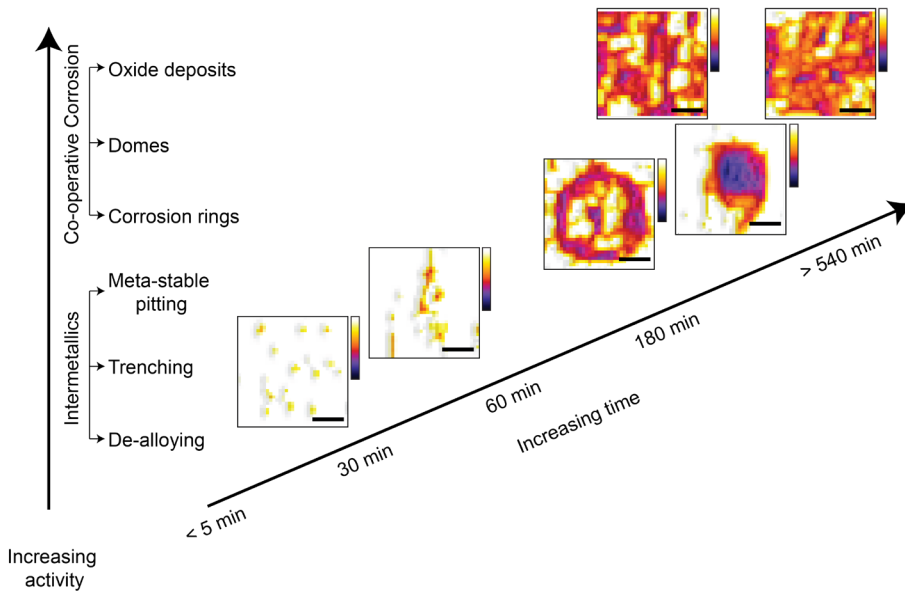


**Figure 2.6** Summary of the optical observations for the evolution of intermetallic and co-operative corrosion on the surface of AA2024-T3 in 0.05 M NaCl. Scale bars represent 50  $\mu\text{m}$ .

## 2.3.2. Evaluation of corrosion inhibitors

### 2.3.2.1. Global temporally-resolved evaluation

The corrosion protection potential of AA2024-T3 by six different salts at concentrations ranging from  $10^{-3}$  M to  $10^{-6}$  M was studied with the optical-electrochemical setup. The Nyquist and Bode plots of six different inhibitors in 0.05 M NaCl solutions after 15 h of immersion can be found in SI-2.4. While each inhibitor shows a particular trend depending on their concentration and inhibition mechanism, information on the degree of protection remains difficult to obtain. Moreover, inhibition effects are often identified by the impedance values at low frequencies (e.g. 0.01 Hz) as inhibition is often related to the suppression of electron transfer due to the formation of a passivation layer on the metal surface or IM locations.<sup>37</sup> As a consequence we propose the combination of optical and electrochemical data as presented in Figure 2.7, showing the total impedance  $|Z|$  at a frequency of 0.01 Hz together with the calculated optically-detectable degraded area in percentage for an easier interpretation and quantification of the inhibition effects.

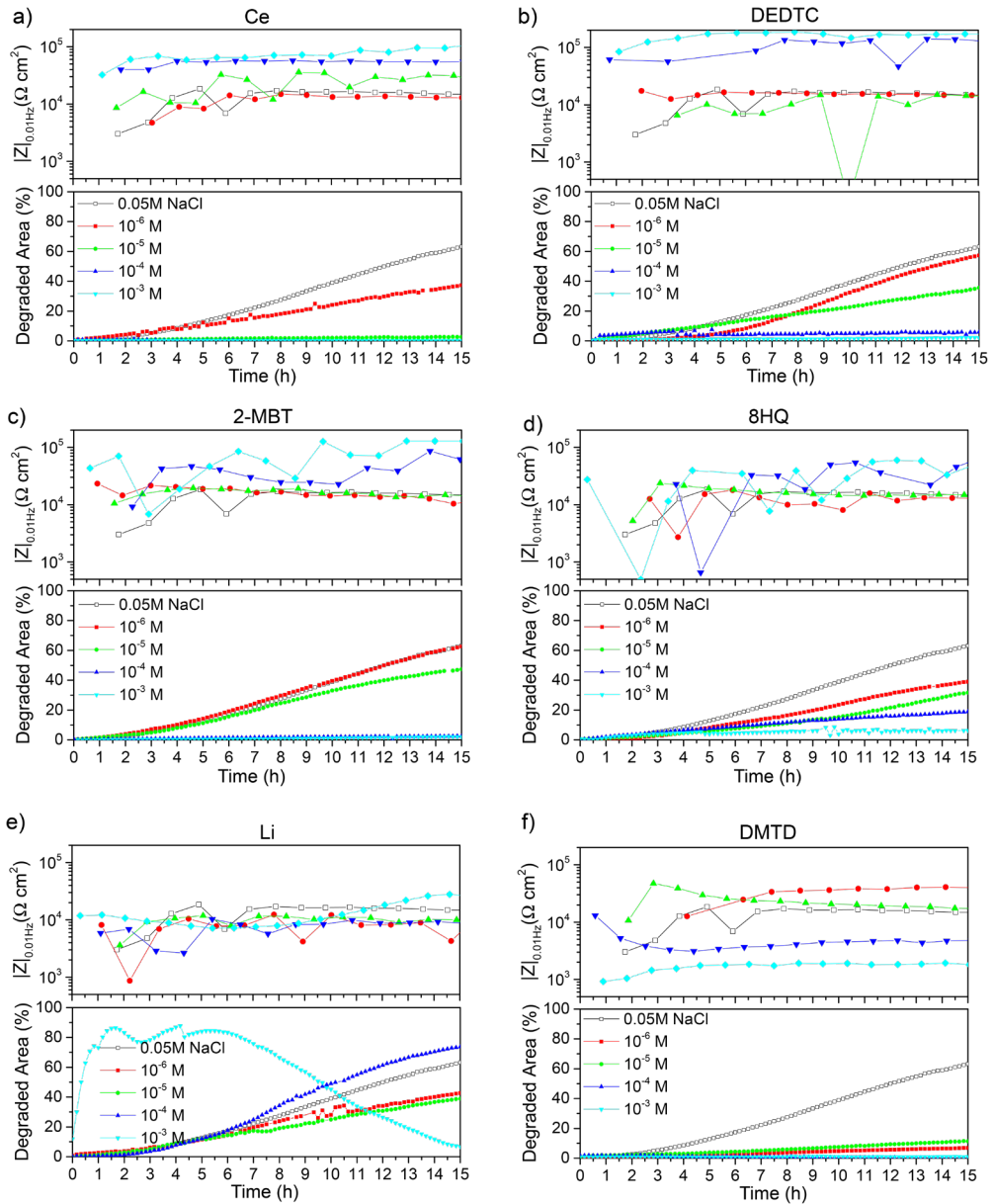


**Figure 2.7** Time evolution of the total impedance  $|Z|$  at a frequency of 0.01 Hz and the calculated optically-detectable degraded area in percentage for AA2024-T3 during 15 h immersion in 0.05 M NaCl electrolyte containing different concentrations of inhibitor Ce (a), DEDTC (b), 2-MBT (c), and 8HQ (d), Li (e), DMTD (f).

Figure 2.7 shows that the total impedance values at 0.01 Hz remain relatively similar during 15 h of immersion, while the optical degradation shows either no changes or a clear increase over time depending on the degree of inhibition. Three different overall inhibitor behaviours can be identified based on their impedance and degraded area time evolution: (i) Ce, DEDTC, 2MBT and 8HQ; (ii) Li; and (iii) DMTD. Inhibitors Ce, DEDTC, 2MBT and 8HQ at concentrations between  $10^{-3}$ M and  $10^{-4}$ M show higher  $|Z|_{0.01\text{Hz}}$  than the non-inhibited sample (named 0.05 NaCl). This coincides with less than 1 %/h degraded area evolution during 15 h of immersion. At  $10^{-5}$  M inhibitor concentration only Ce continues the trend of high impedance and low degraded area (Figure 2.7a) thereby still showing good protection and inhibitor robustness. At such inhibitor concentrations the three organic inhibitors (DEDTC, 2MBT and 8HQ) show similar/lower impedance values at 0.01 Hz than the non-inhibited sample combined with an increase of the degraded surface-area between 2 %/h and 5 %/h, similar to the values shown for the non-inhibited sample in Figure 2.4d, thereby suggesting a loss of their inhibiting power at low concentrations (Figure 2.7 b-d).

Li inhibitor on the other hand shows an abrupt transition in the impedance time evolution as function of the inhibitor concentrations at around  $10^{-3}$ M (Figure 2.7e). In this case, the impedance values at 0.01 Hz for all the tested concentrations are close to the values for the non-inhibited sample suggesting high local corrosion attack. Interestingly, at  $10^{-3}$  M the degradation profile changes and shows a very fast overall corrosion attack (almost complete surface degradation) within one hour which is kept during the first 6 hour of immersion to start decaying afterwards. This suggests a significant loss of material, followed by a second transition after 6 hours whereby the surface gradually becomes comparable (optically) to its initial state suggesting a passivation of the surface. These results can be related to observations found in literature for this particular inhibitor.<sup>38,39</sup> The initial surface-degradation during the first 6 hours can be related to massive surface etching of the aluminium surface, whereby the presence of Li-inhibitor promotes the corrosion processes at the surface and results in the dissolution of aluminium into an amorphous  $\text{Al}(\text{OH})_3$ . This is further supported by the low-frequency impedance values comparable to those of the non-inhibited sample suggesting no passivation-layer has been formed yet during this period. After 6 h the amount of degraded area decreases along with a slight increase of impedance (Figure 2.7b). This suggests that an electrochemically passive barrier is being developed and is in good agreement with the reported works showing the formation of a protective hydrated lithium/aluminium layer.<sup>38,39</sup> From the results in Figure 2.7b it can be seen that this protective barrier layer is not formed when lower inhibitor concentrations are used ( $< 10^{-3}$  M) and might in some cases lead to massive local degradation of the exposed surface.

In the case of DMTD, low concentrations ( $10^{-5}$  and  $10^{-6}$  M) show higher impedance values than the reference non-inhibited solution accompanied by very low surface degradation (below 1 %/h). Nevertheless, high concentrations ( $10^{-3}$  and  $10^{-4}$  M) show similarly low surface

degradation but lower impedance values than the reference non inhibited sample suggesting an incongruence between the two results. The misleading low impedance values can be attributed to the so called pseudo-inductance process ascribed to the relaxation effects of ionic adsorption/desorption phenomena at the electrode surface which become more prominent at high concentrations.<sup>44</sup> The Nyquist plot for DMTD ( $10^{-3}$  and  $10^{-4}$  M) as shown in SI-2.4 confirms that this pseudo-inductance occurs for this inhibitor by the depressed semicircle at low frequencies suggesting that impedance alone might not always be enough to evaluate inhibition and highlighting the need for in situ optical-electrochemical analysis as proposed here.

In order to compare the inhibiting classification given by the electrochemical and optical analysis the total impedance at 0.01 Hz can be plot against the degraded area surface coverage for a given immersion time. Figure 2.8 shows such a plot at 15 h immersion in 0.05 M NaCl with all the inhibitor concentrations studied ( $10^{-3}$  M up to  $10^{-6}$  M).

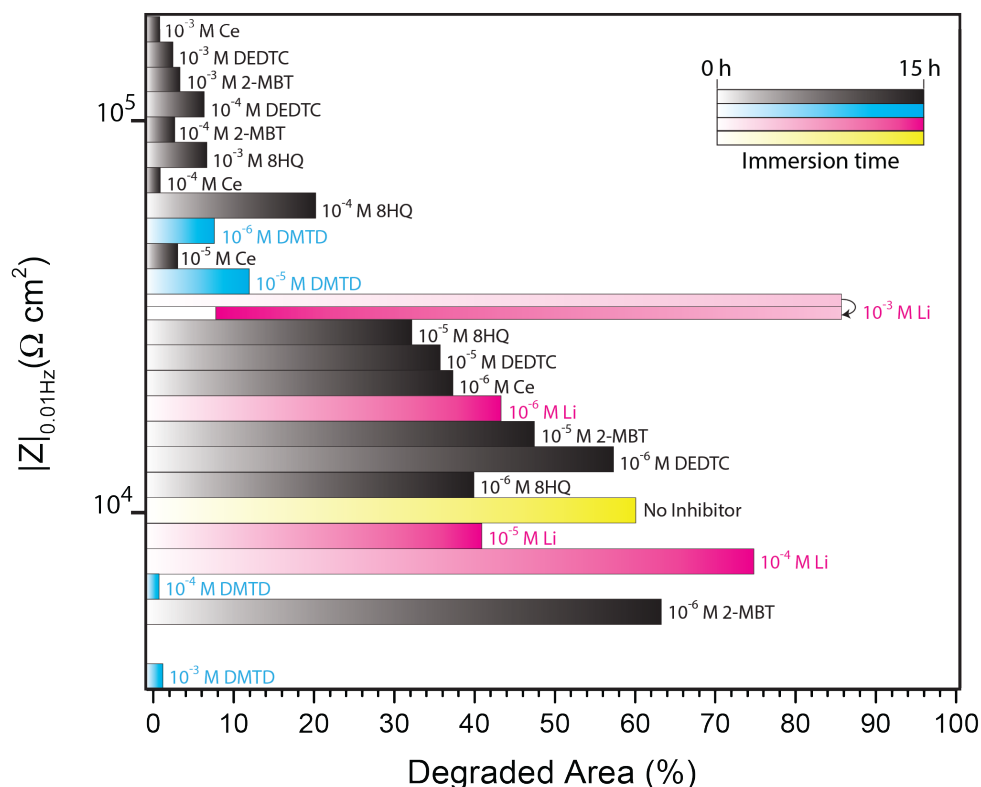


**Figure 2.8** Time-evolution of the degradation area of AA2024-T3 in 0.05 M NaCl solutions containing corrosion inhibitors against the total impedance at 0.01 Hz categorized per decade. The three overall inhibitor groups are indicated for Ce, DEDTC, 2MBT and 8HQ (black), Li (Magenta), and DMTD (Cyan) and additionally the non-inhibited sample (Yellow).

From Figure 2.8 it becomes evident that inhibitors showing a high total impedance at 0.01 Hz are always accompanied by a low degraded area, indicating good corrosion-protection both electrochemically and optically. On the contrary, inhibitors that show a lower total impedance lower than the non-inhibited system do not necessarily result in a high degraded area, as is the case for DMTD. Based on these results it can be concluded that the optical analysis and quantification of the degraded area evolution is a powerful tool to identify and quantify corrosion inhibiting while the electrochemical impedance analysis can result in subjective interpretations as function of the inhibitor type.

### 2.3.2.2. Local spatial-resolved evaluation

Figure 2.9 shows the colour plots of AA2024-T3 immersed for 15 h in 0.05 M NaCl containing inhibitors at different concentrations.

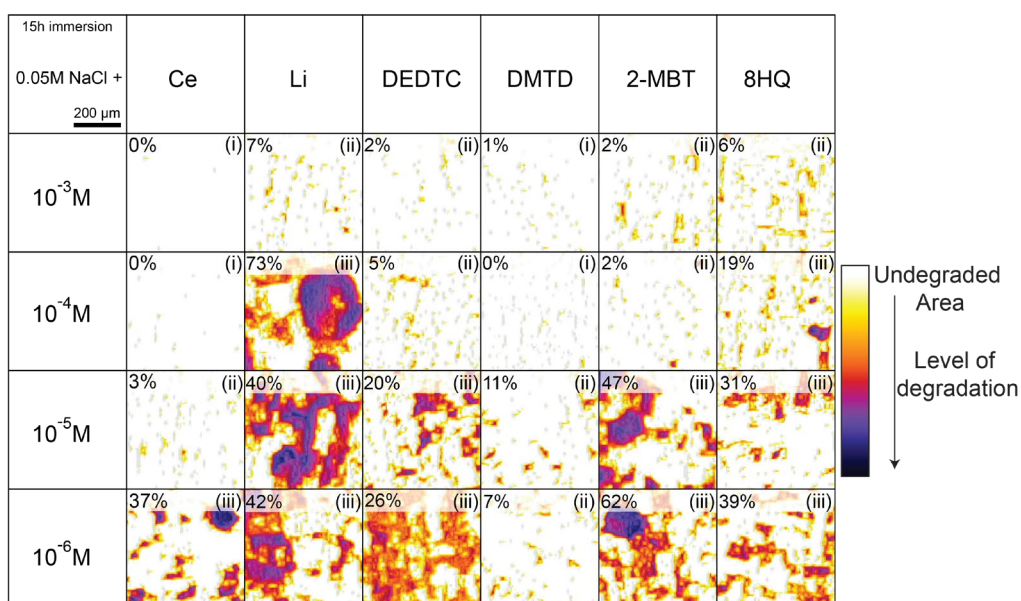


**Figure 2.9** Colour plots of the micrographs obtained from the optical analysis for AA2024 after 15 h immersion in 0.05 M NaCl containing corrosion inhibitors at different concentrations. The values in the micrographs represent the total degraded area in percentage, and the presence of (i) no visual surface-features, (ii) red spots between 5 and 30  $\mu$ m in diameter, and (iii) purple domes and oxide-deposits.

In Figure 2.9 surface features related to local corrosion processes can be seen whereby the total degraded area given in the upper left corner is calculated over a 2 mm<sup>2</sup> exposed surface corresponding to the values shown in Figure 2.7 and Figure 2.8 after 15 h immersion. The micrographs for the 2 mm<sup>2</sup> exposed surface can be found in SI-2.5. Based on the type and amount of surface-degradation, the degree of inhibition can be related to the corrosion-features typically identified on non-inhibited AA2024-T3 in 0.05 M NaCl (Figure 2.6). The inhibitor-concentration micrographs marked with an (i) in Figure 2.9 show the absence of corrosion-related surface

features. This suggests that the inhibitors (Ce and DMTD) are able to stop the corrosion-processes within the first 30 minutes of immersion, preventing trenching and pit-initiation during the next 15 h of immersion. The inhibitor-concentration micrographs marked with a (ii) in Figure 2.9 show moderate degrees of surface degradation whereby the features are similar to those observed for meta-stable pit-formation (red spots between 5 and 30  $\mu\text{m}$ ) combined with a total degraded surface between 2% and 11%. Although these features can be related to the local deposition of inhibitor-products at the surface, the disappearance of features related to co-operative corrosion generally detected after several hours of immersion as seen in Figure 2.5 (purple domes and oxide-deposits) suggests that local corrosion processes have been significantly suppressed in those inhibitor-concentration combinations marked with (i) and (ii). The inhibitor-concentration micrographs marked with (iii) in Figure 2.9 show surface features generally taking place after several hours immersion without the presence of inhibition (Figure 2.5) thereby suggesting the appearance of co-operative corrosion processes or, in the case of Li, massive surface-etching even in the presence of inhibitor.

## 2.4. Conclusions

A combined optical-electrochemical technique is proposed as inexpensive and simple method for the evaluation of corrosion and corrosion inhibition. For the proof of concept the data collection and analysis protocol were developed and used to study corrosion and corrosion inhibition of AA2024-T3. Three different corrosion stages were identified using time-dependent surface variations quantified by optical analysis and low frequency total impedance. Further analysis of the optical micrographs enabled the visualization and identification of time-dependent surface-related corrosion features corresponding to intermetallic corrosion (e.g. trenching and meta-stable pitting) and co-operative corrosion (e.g. corrosion-rings, domes and surface-oxides) typically only identified by SEM or ex-situ optical microscopy studies. The same optical-electrochemical technique and protocol was used to study six corrosion inhibitors. The optical analysis protocol allowed calculating inhibition kinetics, identifying three different inhibitor-concentration dependent behaviours and visualizing the presence or absence of local corrosion features depending on the level of inhibition with high spatial and temporal resolution. In terms of inhibitor behaviour it was found that both  $Ce(NO_3)_3$  and DMTD are robust inhibitors showing little concentration dependency and able to prevent the initiation of early-stage corrosion within 30 minutes of immersion as well as long term immersion. The use of optical analysis with high local resolution allowed determining the high level of protection by DMTD despite its low impedance values.  $Li_2CO_3$  on the other hand showed a very high concentration and time dependency up to the point that short immersion times and low concentrations lead to high degradation levels as measured with the optical evaluation. The results highlight the high potential of in-situ optical analysis under immersion combined with electrochemical analysis. In essence, the optical analysis could be used as a complementary technique to clarify EC models for corrosion and inhibitor action. Although the measurements have been performed on aluminium alloy AA2024-T3 with the used of EIS, the used opto-electrochemical setup and protocol analysis can easily be adapted to improve the interpretation of electrochemical signals from other electrochemical tests such as electrochemical noise as well as to follow surface related phenomena on other metal substrates with high spatio-temporal resolution without the need of extensive post-mortem analysis.

## 2.5. References

- 1 M. E. Orazem and B. Tribollet, "History of Impedance Spectroscopy," in *Electrochemical Impedance Spectroscopy*, 2nd ed., John Wiley & Sons, Incorporated, 2017, pp. xlii–xlvii.
- 2 H. Griffiths, "Oliver Heaviside," *Hist. Wirel.*, vol. 6, no. 1, pp. 229–246, 2006, doi: 10.1002/0471783021.ch6.
- 3 I. Yavetz, *From Obscurity to Enigma*, 1st ed. Basel: Birkhäuser Basel, 1995.
- 4 D. D. MacDonald, "Reflections on the history of electrochemical impedance spectroscopy," *Electrochim. Acta*, vol. 51, no. 8–9, pp. 1376–1388, 2006, doi: 10.1016/j.electacta.2005.02.107.
- 5 W. Tait, K. Handrich, S. Tait, and J. Martin, "Analyzing and Interpreting Electrochemical Impedance Spectroscopy Data from Internally Coated Steel Aerosol Containers," in *Electrochemical Impedance: Analysis and Interpretation*, J. Scully, D. Silverman, and M. Kendig, Eds. West Conshohocken: ASTM International, 2009, pp. 428–428–10.
- 6 E. L. Ferrer, A. P. Rollon, H. D. Mendoza, U. Lafont, and S. J. Garcia, "Double-doped zeolites for corrosion protection of aluminium alloys," *Microporous Mesoporous Mater.*, vol. 188, pp. 8–15, 2014, doi: Doi 10.1016/J.Micromeso.2014.01.004.
- 7 T. H. Muster *et al.*, "A combinatorial matrix of rare earth chloride mixtures as corrosion inhibitors of AA2024-T3: Optimisation using potentiodynamic polarisation and EIS," *Electrochim. Acta*, vol. 67, pp. 95–103, Apr. 2012, doi: 10.1016/j.electacta.2012.02.004.
- 8 F. Fabregat-Santiago, J. Bisquert, G. Garcia-Belmonte, G. Boschloo, and A. Hagfeldt, "Influence of electrolyte in transport and recombination in dye-sensitized solar cells studied by impedance spectroscopy," *Sol. Energy Mater. Sol. Cells*, vol. 87, no. 1–4, pp. 117–131, 2005, doi: 10.1016/j.solmat.2004.07.017.
- 9 F. El-Taib Heakal and S. Haruyama, "Corrosion Science, Vol. 20, lap. 887 to 898 Pergamon Press Ltd. 1980. Printed in Great Britain.," *Corrosion*, vol. 20, no. September 1979, pp. 887–898, 1980.
- 10 A. M. Glenn *et al.*, "Corrosion of AA2024-T3 Part III: Propagation," *Corros. Sci.*, vol. 53, no. 1, pp. 40–50, 2011, doi: 10.1016/j.corsci.2010.09.035.
- 11 S. R. K. Malladi *et al.*, "Quasi in situ analytical TEM to investigate electrochemically induced microstructural changes in alloys: AA2024-T3 as an example," *Corros. Sci.*, vol. 69, pp. 221–225, 2013, doi: 10.1016/j.corsci.2012.12.006.
- 12 S. J. Garcia, T. A. Markley, J. M. C. Mol, and A. E. Hughes, "Unravelling the corrosion inhibition mechanisms of bi-functional inhibitors by EIS and SEM-EDS," *Corros. Sci.*, vol. 69, pp. 346–358, 2013, doi: 10.1016/j.corsci.2012.12.018.
- 13 P. J. Denissen and S. J. Garcia, "Cerium-loaded algae exoskeletons for active corrosion protection of coated AA2024-T3," *Corros. Sci.*, vol. 128, no. September, pp. 164–175, Nov. 2017, doi: 10.1016/j.corsci.2017.09.019.
- 14 D. Snihirova, S. V. Lamaka, P. Taheri, J. M. C. Mol, and M. F. Montemor, "Comparison of the synergistic effects of inhibitor mixtures tailored for enhanced corrosion protection of bare and coated AA2024-T3," *Surf. Coatings Technol.*, vol. 303, no. Part B, pp. 342–351, 2016, doi: 10.1016/j.surfcoat.2015.10.075.
- 15 A. Boag, A. E. Hughes, A. M. Glenn, T. H. Muster, and D. McCulloch, "Corrosion of AA2024-T3 Part I: Localised corrosion of isolated IM particles," *Corros. Sci.*, vol. 53, no. 1, pp. 17–26, 2011, doi: 10.1016/j.corsci.2010.09.009.
- 16 S. M. Ghahari *et al.*, "In situ synchrotron X-ray micro-tomography study of pitting corrosion in stainless steel," *Corros. Sci.*, vol. 53, no. 9, pp. 2684–2687, 2011, doi: 10.1016/j.corsci.2011.05.040.
- 17 S. J. Garcia, X. Wu, and S. Van Der Zwaag, "A combined electrochemical impedance spectroscopy and x-ray-computed tomography study of the effect of a silyl ester on delamination and underfilm pit formation in a coated AA7050 sample," *Corrosion*, vol. 70, no. 5, pp. 475–482, 2014, doi: 10.5006/0966.
- 18 V. Shkirskiy *et al.*, "Revisiting the electrochemical impedance spectroscopy of magnesium with online inductively coupled plasma atomic emission spectroscopy," *ChemPhysChem*, vol. 16, no. 3, pp. 536–539, 2015, doi: 10.1002/cphc.201402666.
- 19 E. S. M. Sherif, R. M. Erasmus, and J. D. Comins, "In situ Raman spectroscopy and electrochemical techniques for studying corrosion and corrosion inhibition of iron in sodium

- chloride solutions,” *Electrochim. Acta*, vol. 55, no. 11, pp. 3657–3663, Apr. 2010, doi: 10.1016/j.electacta.2010.01.117.
- 20 M. L. Zheludkevich, R. Serra, M. F. Montemor, K. A. Yasakau, I. M. M. Salvado, and M. G. S. Ferreira, “Nanostructured sol-gel coatings doped with cerium nitrate as pre-treatments for AA2024-T3 Corrosion protection performance,” *Electrochim. Acta*, vol. 51, no. 2, pp. 208–217, Oct. 2005, doi: 10.1016/j.electacta.2005.04.021.
- 21 S. J. Xia, R. Yue, R. G. Rateick, and V. I. Birss, “Electrochemical Studies of AC/DC Anodized Mg Alloy in NaCl Solution,” *J. Electrochem. Soc.*, vol. 151, no. 3, pp. B179–B187, 2004, doi: 10.1149/1.1646139.
- 22 M. Shao, Y. Fu, R. Hu, and C. Lin, “A study on pitting corrosion of aluminum alloy 2024-T3 by scanning microreference electrode technique,” *Mater. Sci. Eng. A*, vol. 344, no. 1–2, pp. 323–327, 2003, doi: 10.1016/S0921-5093(02)00445-8.
- 23 R. G. Buchheit, R. P. Grant, P. F. Hlava, B. Mckenzie, and G. L. Zender, “Local dissolution phenomena associated with S phase (Al<sub>2</sub>CuMg) particles in aluminum alloy 2024-T3,” *J. Electrochem. Soc.*, vol. 144, no. 8, pp. 2621–2628, 1997, doi: 10.1149/1.1837874.
- 24 A. E. Hughes *et al.*, “Corrosion of AA2024-T3 Part II: Co-operative corrosion,” *Corros. Sci.*, vol. 53, no. 1, pp. 27–39, 2011, doi: 10.1016/j.corsci.2010.09.030.
- 25 C. M. Liao, J. M. Olive, M. Gao, and R. P. Wei, “In-Situ Monitoring of Pitting Corrosion in Aluminum Alloy 2024,” *Corrosion*, vol. 54, no. 6, pp. 451–458, 1998, doi: 10.5006/1.3284873.
- 26 C. M. Liao and R. P. Wei, “Galvanic coupling of model alloys to aluminum - a foundation for understanding particle-induced pitting in aluminum alloys,” *Electrochim. Acta*, vol. 45, no. 6, pp. 881–888, 1999, doi: 10.1016/S0013-4686(99)00299-6.
- 27 N. Dimitrov, J. A. Mann, M. Vukmirovic, and K. Sieradzki, “Dealloying of Al<sub>2</sub>CuMg in alkaline media,” *J. Electrochem. Soc.*, vol. 147, no. 9, pp. 3283–3285, 2000, doi: 10.1149/1.1393896.
- 28 A. Hughes *et al.*, “Co-operative corrosion phenomena,” *Corros. Sci.*, vol. 52, no. 3, pp. 665–668, 2010, doi: 10.1016/j.corsci.2009.10.021.
- 29 H. Yasuda, Q. S. Yu, and M. Chen, “Interfacial factors in corrosion protection: An EIS study of model systems,” *Prog. Org. Coatings*, vol. 41, no. 4, pp. 273–279, 2001, doi: 10.1016/S0300-9440(01)00142-4.
- 30 L. Wen, Y. Wang, Y. Zhou, L. Guo, and J. H. Ouyang, “Microstructure and corrosion resistance of modified 2024 Al alloy using surface mechanical attrition treatment combined with microarc oxidation process,” *Corros. Sci.*, vol. 53, no. 1, pp. 473–480, 2011, doi: 10.1016/j.corsci.2010.09.061.
- 31 G. O. Ilevbare, “Inhibition of pitting corrosion on aluminum alloy 2024-T3: Effect of soluble chromate additions vs chromate conversion coating,” *Corrosion*, vol. 56, no. 3, pp. 227–242, 2000, doi: 10.5006/1.3287648.
- 32 D. Battocchi, A. M. Simões, D. E. Tallman, and G. P. Bierwagen, “Electrochemical behaviour of a Mg-rich primer in the protection of Al alloys,” *Corros. Sci.*, vol. 48, no. 5, pp. 1292–1306, 2006, doi: 10.1016/j.corsci.2005.04.008.
- 33 K. A. Yasakau, M. L. Zheludkevich, S. V. Lamaka, and M. G. S. Ferreira, “Mechanism of corrosion inhibition of AA2024 by rare-earth compounds,” *J. Phys. Chem. B*, vol. 110, no. 11, pp. 5515–5528, Mar. 2006, doi: 10.1021/jp0560664.
- 34 A. Boag *et al.*, “Stable pit formation on AA2024-T3 in a NaCl environment,” *Corros. Sci.*, vol. 52, no. 1, pp. 90–103, 2010, doi: 10.1016/j.corsci.2009.08.043.
- 35 N. Birbilis and R. G. Buchheit, “Investigation and discussion of characteristics for intermetallic phases common to aluminum alloys as a function of solution pH,” *J. Electrochem. Soc.*, vol. 155, no. 3, p. C117, 2008, doi: 10.1149/1.2829897.
- 36 F. M. Queiroz, M. Magnani, I. Costa, and H. G. de Melo, “Investigation of the corrosion behaviour of AA 2024-T3 in low concentrated chloride media,” *Corros. Sci.*, vol. 50, no. 9, pp. 2646–2657, 2008, doi: 10.1016/j.corsci.2008.06.041.
- 37 R. L. Twite and G. P. Bierwagen, “Review of alternatives to chromate for corrosion protection of aluminum aerospace alloys,” *Prog. Org. Coatings*, vol. 33, no. 2, pp. 91–100, 1998, doi: 10.1016/S0300-9440(98)00015-0.
- 38 C. M. Rangel and M. A. Travassos, “The passivation of aluminium in lithium carbonate/bicarbonate solutions,” *Corros. Sci.*, vol. 33, no. 3, pp. 327–343, 1992, doi:

- 10.1016/0010-938X(92)90064-A.
- 39 P. Visser, M. Meeusen, Y. Gonzalez-Garcia, H. Terryn, and J. M. C. Mol, "Electrochemical evaluation of corrosion inhibiting layers formed in a defect from lithium-leaching organic coatings," *J. Electrochem. Soc.*, vol. 164, no. 7, pp. C396–C406, 2017, doi: 10.1149/2.1411707jes.
- 40 G. Williams, A. J. Coleman, and H. N. McMurray, "Inhibition of Aluminium Alloy AA2024-T3 pitting corrosion by copper complexing compounds," *Electrochim. Acta*, vol. 55, no. 20, pp. 5947–5958, Aug. 2010, doi: 10.1016/j.electacta.2010.05.049.
- 41 M. Finšgar and D. Kek Merl, "An electrochemical, long-term immersion, and XPS study of 2-mercaptobenzothiazole as a copper corrosion inhibitor in chloride solution," *Corros. Sci.*, vol. 83, pp. 164–175, 2014, doi: 10.1016/j.corsci.2014.02.016.
- 42 T. W. Ridler and S. Calvard, "Picture Thresholding Using an Iterative Selection Method.," *IEEE Trans. Syst. Man Cybern.*, vol. SMC-8, no. 8, pp. 630–632, 1978, doi: 10.1109/tsmc.1978.4310039.
- 43 S. K. Poznyak *et al.*, "Novel inorganic host layered double hydroxides intercalated with guest organic inhibitors for anticorrosion applications," *ACS Appl. Mater. Interfaces*, vol. 1, no. 10, pp. 2353–2362, 2009, doi: 10.1021/am900495r.
- 44 W. Chen, H. Q. Luo, and N. B. Li, "Inhibition effects of 2,5-dimercapto-1,3,4-thiadiazole on the corrosion of mild steel in sulphuric acid solution," *Corros. Sci.*, vol. 53, no. 10, pp. 3356–3365, 2011, doi: 10.1016/j.corsci.2011.06.013.

## 2.6. Supporting Information

### SI-2.1. Optical-electrochemical cell

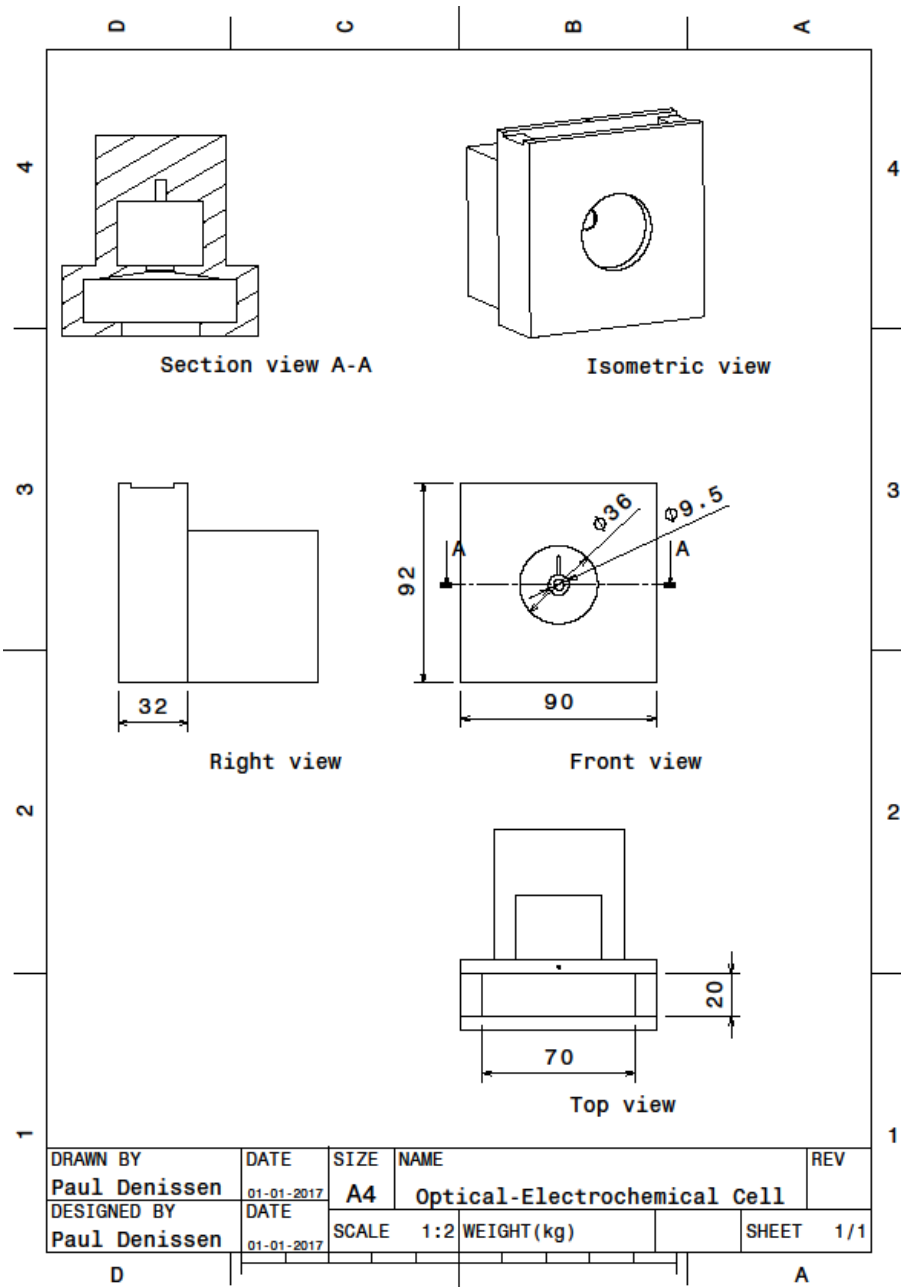


Figure SI-2.1 optical electrochemical cell.

**SI-2.2. ImageJ macro protocol for ImageJ***Calibration*

```

k=25
if (mean<=g)
{k=255;
  for (i=1; i<k; i++)
  {run("Select All");
  run("Brightness/Contrast...");
  setMinAndMax(0,255-i);
  run("Apply LUT");
  makeRectangle(x,y,w,h);
  getRawStatistics(n, mean, min, max, std, hist);
  if (mean<=g)
  {close();
  open(dir1+list[m]);
  }
  else
  {i=k;}}
else
{  setMinAndMax(i,255);}

```

*Iterative thresholding*

```

for (i=0; i<list.length; i++) {
  setAutoThreshold("Default stack");
  getThreshold(lowerTh, upperTh);}
id1 = getImageID();
id2 = getImageID();
imageCalculator("Add create", id1,id2);}

```

*Degraded area*

```

for (i=0; i<list.length; i++) {
  run("Invert");
  run("Create Selection");
  run("Measure");}

```

*Surface-plot*

```

for (i=0; i<list.length; i++) {
  getDimensions(widthCurrent, heightCurrent, channelsCurrent, slicesCurrent,
  framesCurrent);
  run("Brightness/Contrast...");
  setMinAndMax(lowerTh, upperTh);
  run("Interactive 3D Surface Plot", "plotType=1 colorType=4 drawAxes=0 drawLines=0
  drawText=0 drawLegend=0 grid=1024 smooth=10 perspective=0 light=0.2
  isEqualxyzRatio=0 invertZ=0 rotationX=0 rotationZ=0 scale=1.5 scaleZ=0 max=100
  min=0 snapshot=1 backgroundColor=FFFFFF");
  run("Size...", "width=0 height=heightCurrent constrain average `
  interpolation=Bilinear");}

```

SI-2.3. Kramers-Kroning residual errors

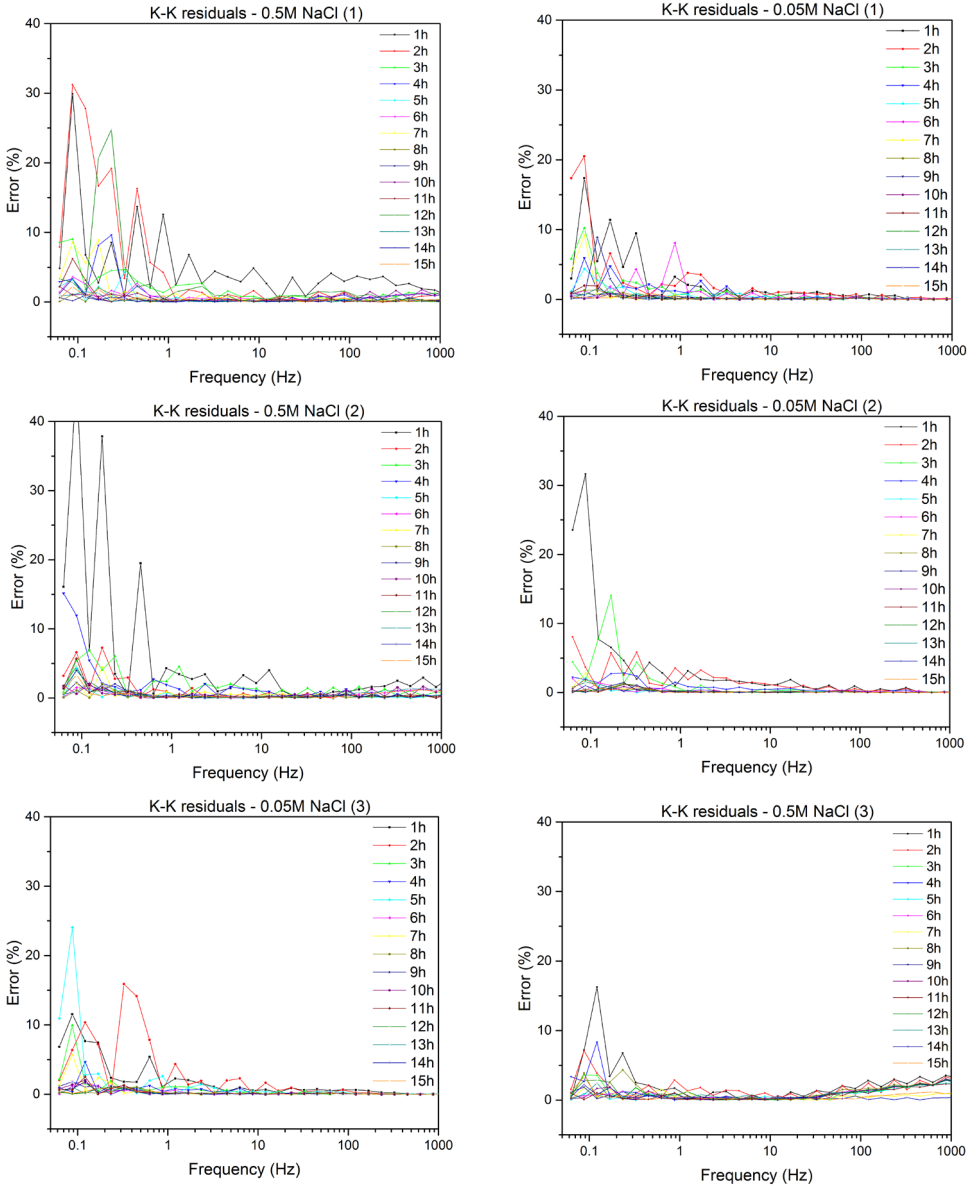
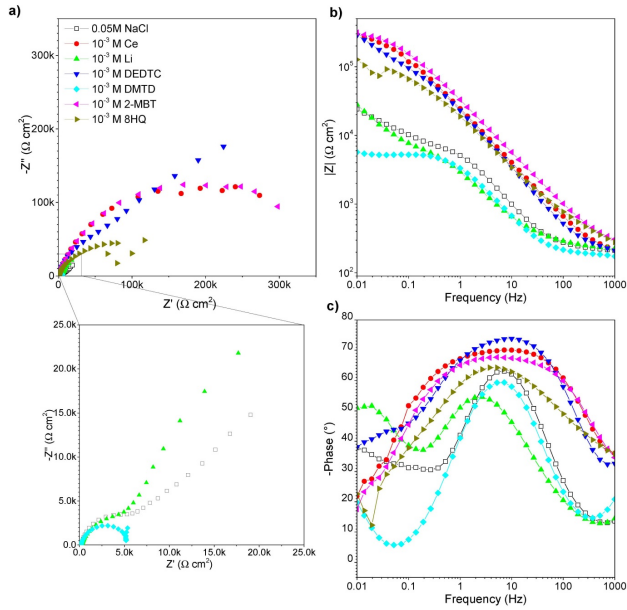
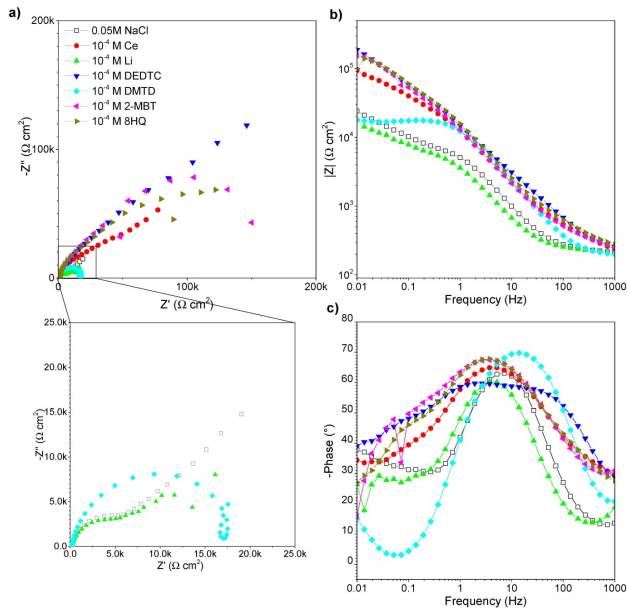


Figure SI 2.2 Kramers-Kroning residual errors.

**SI-2.4. Nyquist and Bode plots of six different inhibitors in 0.05 M NaCl solutions after 15 h immersion**



**Figure SI 2.3** 0.05 M NaCl containing  $10^{-3}$  M inhibitor concentration after 15 h immersion.



**Figure SI 2.4** 0.05 M NaCl containing  $10^{-4}$  M inhibitor concentration after 15 h immersion.

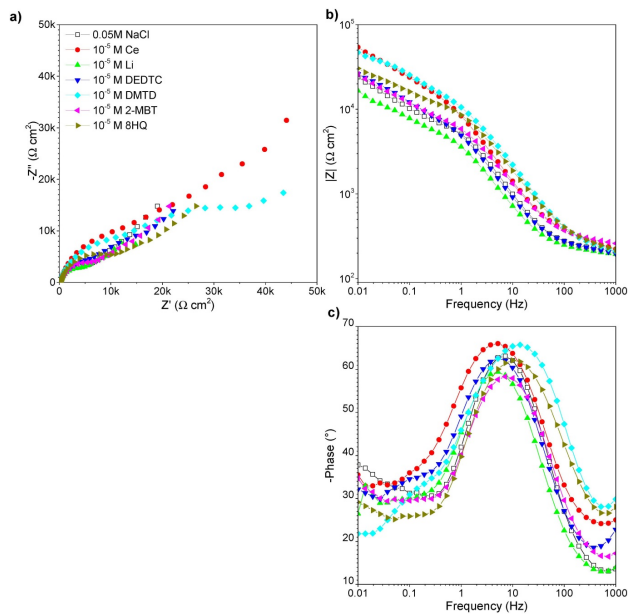


Figure SI 2.5 0.05 M NaCl containing  $10^{-5}$  M inhibitor concentration after 15 h immersion.

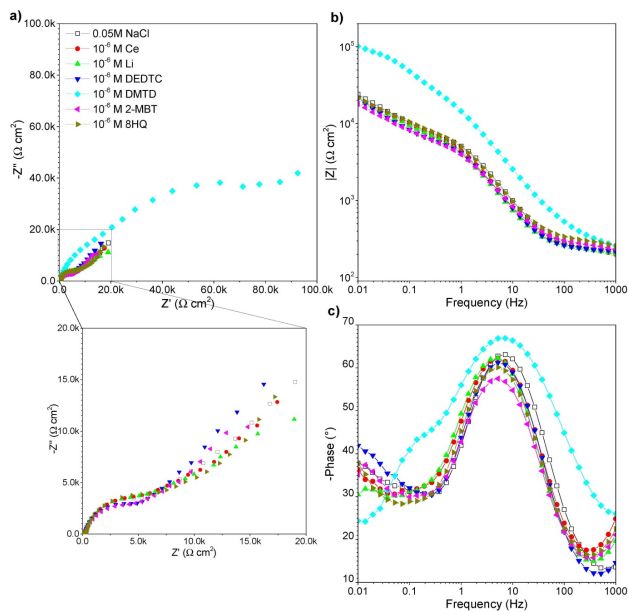
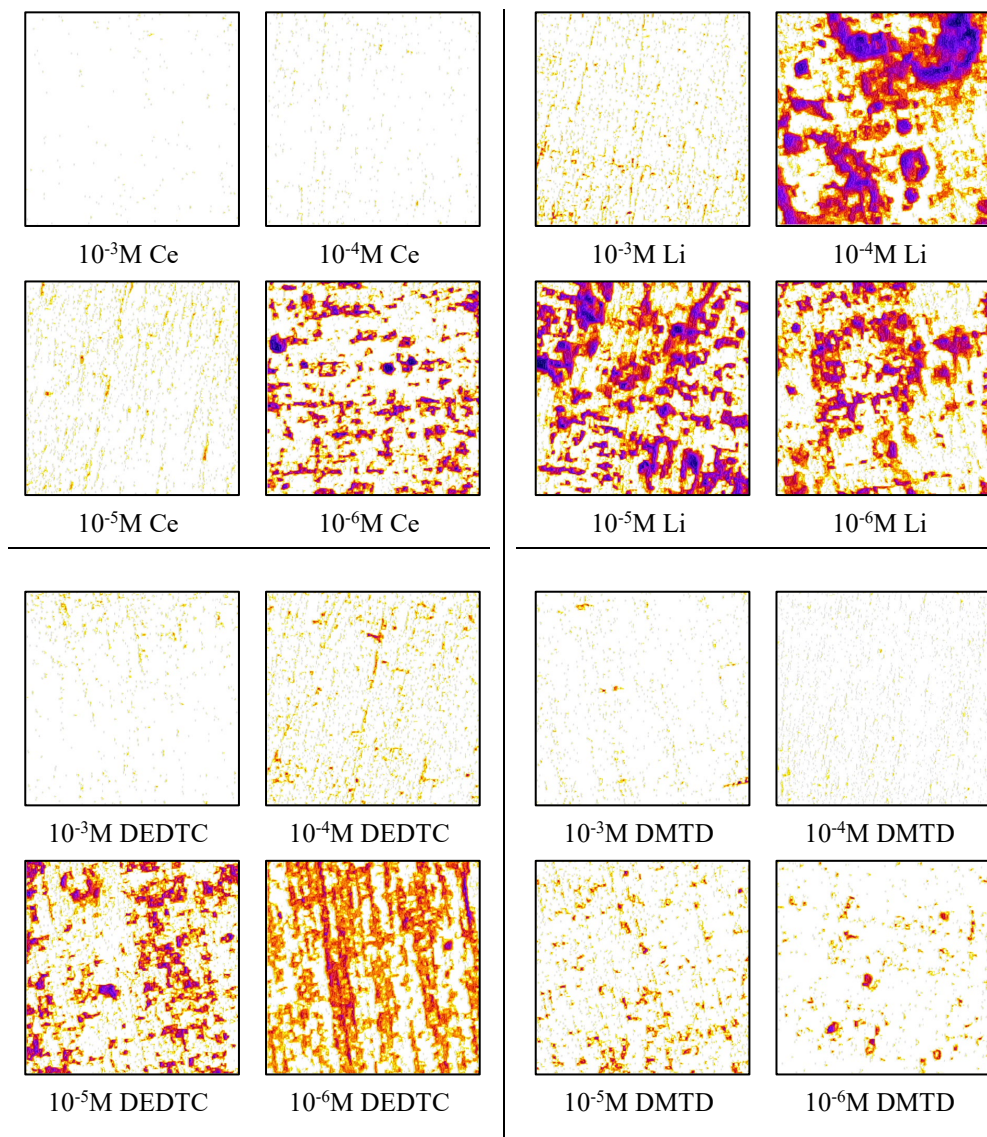
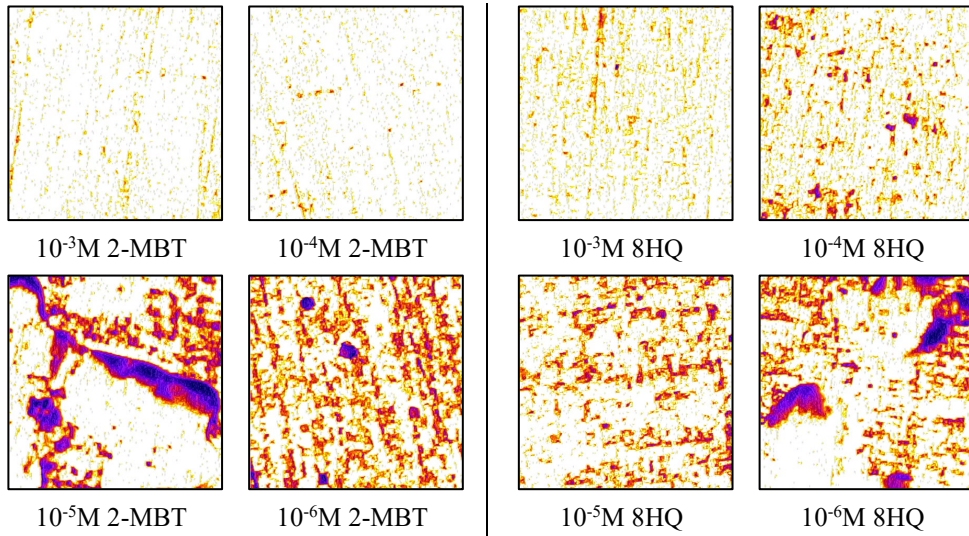


Figure SI 2.6 0.05 M NaCl containing  $10^{-5}$  M inhibitor concentration after 15 h immersion.

**SI-2.5. Colour-plots of the full micrographs (2 mm<sup>2</sup>) for AA2024 after 15 h immersion in 0.05 M NaCl containing corrosion inhibitors at different concentrations**





**Figure SI 2.7** AA2024 after 15 h immersion in 0.05 M NaCl containing inhibitors.

# 3

## **Interpreting electrochemical noise and monitoring local corrosion by means of highly resolved spatiotemporal real-time optics**

*Real-time optical analysis is used to improve the interpretation of electrochemical noise signals (EN). The concept is presented for the case of AA2024-T3 under immersion in various NaCl concentrations. An in-house developed optical-electrochemical technique allowed for high spatiotemporal resolution and was used to visualise and quantify surface changes in parallel with monitoring EN signals. EN analysis was performed in the time-frequency domain using continuous wavelet transform (CWT). Correlations between the two procedures enabled the identification of corrosion processes in time, such as de-alloying, etching, pitting and subsurface corrosion. Besides this, optical measurements at higher magnification were used to analyse a smaller section of the exposed metal with a spatial resolution below 1  $\mu\text{m}$ . This enabled the quantification on the size, number and nearest neighbour distance of local corrosion events, such as pits and corrosion rings. The set-up and optical protocol allowed for the first time (i) to establish a direct relationship between EN signals and the occurrence of specific localised corrosion phenomena and (ii) an in-situ highly-resolved monitoring of local corrosion processes. As a final result of the optical analysis we introduce a straightforward illustration that allows the direct identification of EN features to macroscopic local corrosion phenomena.*

This chapter has been published as:

P. J. Denissen, A. M. Homborg, S. J. Garcia, Interpreting Electrochemical Noise and Monitoring Local Corrosion by Means of Highly Resolved Spatiotemporal Real-Time Optics, Journal of The Electrochemical Society, 2019

### 3.1. Introduction

In wet corrosion studies, prior knowledge of the evaluated systems normally plays a crucial role when aiming at a correct interpretation of the measured electrical signals during immersion. Back in the 90s Hugh Isaacs already emphasised the difficulty of correlating current and potential fluctuations, defined as electrochemical noise (EN), to local corrosion processes.<sup>1</sup> Despite the attempts, this remains a largely unsolved issue, typically only addressed in the past by optical inspection after the corrosion activity has occurred.

Individual electrochemical phenomena that are localized in time generate singularities, or transients, in the EN signal. These transients are characterized by a distinct energy distribution over a (set of) timescale(s) which are different than the rest of the EN signal, providing them a specific shape and duration. Nevertheless, these EN transients are often superimposed in time, making it difficult to correctly interpret the signals in the time domain. Deconvolution of the transients can be achieved by analysing the EN data in the time-frequency domain, allowing a more robust description of their appearance. For instance, Aballe et al. used discrete wavelet transforms in the late 90s<sup>2</sup> to analyse EN, while Homborg et al. introduced the Hilbert-Huang transform to relate specific domains in the time-frequency spectra to different types of corrosion processes based on their transient characteristics.<sup>3-6</sup> One of the most recent works proposes the use of continuous wavelet transform (CWT) to analyse EN in relation to corrosion processes.<sup>7</sup> The CWT procedure operates in the time-frequency domain by the scaling and translation of a wavelet at a number of timescales. The energy distribution of the EN signal over the different timescales can in turn be attributed to the occurrence of processes primarily under either activation, diffusion or mixed control.<sup>2,8-11</sup> Nevertheless, complementary measurements after the corrosion test such as optical microscopy,<sup>12</sup> SEM/EDS,<sup>13</sup> and Raman,<sup>14</sup> are still required. While this approach can be used to obtain information on the final type of degradation, it does not provide any real-time information on the corrosion process in relation to the electrochemistry. Time-resolved information can only be achieved by combining electrochemistry with a supplementary techniques such as in-situ XRD<sup>15</sup> or optical microscopy in real-time.<sup>16-18</sup> In the particular case of EN, gathering information on the corrosion processes that can be directly related to the EN signals would boost the potential use and robustness of this technique.

In previous works we introduced how the in-situ combination of real-time optics and electrochemistry can be used as an inexpensive and straightforward method to correlate electrochemical impedance spectroscopy to macroscopic corrosion-related phenomena of metals and coatings in corrosive media.<sup>17,18</sup> In this work we go one step further with an improved setup that shows how real-time optics with high spatiotemporal resolution and image analysis can be combined with EN to follow local corrosion processes. To demonstrate the concept we analysed the corrosion processes of AA2024-T3 immersed in salt solutions at different concentrations. Optical measurements were performed using a low magnification setup with a pixel density of

---

0.33 pixels per micron and a high magnification setup with 2.7 pixels per micron using two different cameras. The lower magnification enables the identification of all surface-related processes occurring at a macroscopic scale ( $<5\ \mu\text{m}$  resolution), while the high magnification allows a more detailed sub-micron view of a smaller surface area. The use of a newly developed image analysis procedure allows the isolation of the pixels changing in time (i.e. affected by the corrosion process) from the unchanged pixels (i.e. not affected). This process enabled the visualization of the corrosion processes normally non-detectable with microscopy images at the same resolution. The higher magnification approach also allowed the clear identification in time and quantification of corrosion-related features, such as the amount, size and nearest neighbour distance of pits and oxide rings, which have previously only been observed by post-immersion inspection by SEM. The electrochemical potential noise (EPN) monitored in parallel with the optical analysis serves as a basis for the time-frequency electrochemical analysis using CWT as previously shown for steel.<sup>19</sup> The in-situ combination of optical and electrochemical analysis allowed for the first time to directly assign electrochemical signals to specific corrosion processes (e.g. de-alloying, trenching, pitting and oxide formation). As a result, a plot correlating the optical and electrochemical analysis to corrosion processes is introduced.

## 3.2. Experimental

### 3.2.1. Optical-electrochemical setup

Figure 3.1 shows the improved optical-electrochemical setup used in this work derived from our previous studies.<sup>17,18</sup>

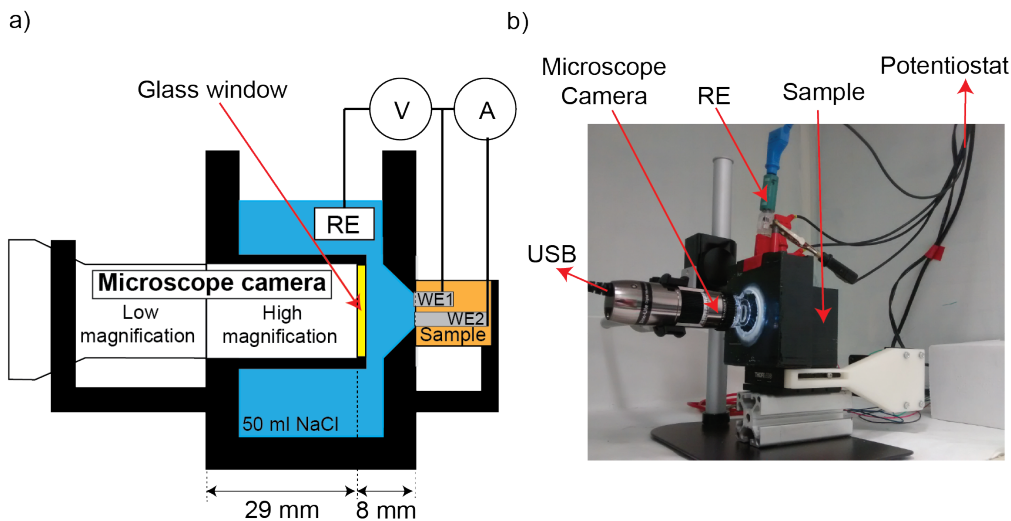


**Figure 3.1** a) Schematic illustration of the cell used for the optical and electrochemical measurements. The scheme shows the two-electrode setup and the varying positions of the two microscope cameras (for high or low magnification studies) with respect to the two AA2024-T3 working electrodes (WE1 and WE2). b) Image of the optical-electrochemical cell used in this study in the Faraday cage.

The current and potential signals for EN were recorded with an Ivium Compactstat using IviumSoft V2.86. The electrochemical current noise (ECN) was measured between the two parallel working electrodes (see sample preparation) with the Compactstat acting as zero resistance ammeter (ZRA). The electrochemical potential noise (EPN) was measured between the two working electrodes and a Metrohm double-junction (Ag/AgCl/sat. KCl) reference electrode (RE). The required sampling frequency to record faster occurring fluctuations was set to 20 Hz, combined with a low-pass filter of 10 Hz (Nyquist frequency at this sampling rate). The maximum range of the ZRA was automatically determined depending on the local dynamic range of the ECN signal, with a lower limit of 100 nA and an upper limit of 1  $\mu$ A. The maximum range of the potentiometer was set at a lower limit of 100 mV and an upper limit of 400 mV. The EN data, processed using Matlab from MathWorks, showed that the potential signals from EN provided all relevant information for this study and therefore the current signals, despite initially analysed, were not further used.

Compared to the setup used in our previous works,<sup>18</sup> a new geometry of the optical-electrochemical cell was used for the alignment of the high-resolution microscope. Two different magnification cameras from Dino-Lite with a 5.0 megapixel CMOS sensor (2592x1944 pixels)

were used. For the low magnification (60x) an AM7915MZTL camera combined with an adjustable 8-LED ring for bright-field lighting was used. This enabled a pixel density of 0.33 pixels per micron at a working distance of 37 mm. For high magnification measurements (420x) an AM7515MT4A camera in coaxial lighting mode was used. This enabled a pixel density of 2.7 pixels per micron at a working distance of 8 mm. The cameras were controlled with DinoCapture 2.0 and programmed to record an image every 10 seconds simultaneously with the electrochemical measurements. Quantitative optical information was obtained through an automated image analysis procedure in ImageJ which can be found in the supplementary information (SI-3.1).

The optical-electrochemical setup was placed inside a Faraday cage to avoid external electrochemical and optical interferences.

### 3.2.2. Electrochemical analysis

The electrochemical analysis as described in this work uses the CWT approach in the time-frequency domain. An analytic Morlet wavelet was applied to calculate the CWT spectrum. The CWT was calculated using 10 voices per octave, which implies that 10 logarithmically spaced frequencies were calculated for each factor of two frequency range. Following established protocols,<sup>20</sup> a symmetric extension of the EN signal at the beginning and at the end by reflection ('symmetric padding') was applied to mitigate boundary effects in the CWT spectrum. The choice whether or not to apply padding, and if so, which method to apply has a significant effect on the artefacts that may arise at the edges of the spectrum.

The CWT spectrum shows the distribution of the energy in the EN signal over time and range. In order to facilitate the interpretation of features visible in the CWT spectrum, in the present work those scales are transferred into instantaneous frequencies. Although transients containing relatively high instantaneous frequencies (i.e. above  $10^{-1}$  Hz) are present in the EN signals, the CWT spectra of the entire signals are dominated by relatively low instantaneous frequencies, in many cases around  $10^{-2}$  Hz and lower. In this frequency domain, local maxima in the CWT spectrum are correlated with optical observations. Those represent large timescale processes that last from several hundreds up to one thousand seconds.

### 3.2.3. Optical analysis

In order to obtain higher resolved quantitative information on the corrosion processes our recently introduced optical analysis protocol of corroding surfaces<sup>17</sup> was improved as presented here. The cameras used in this work are equipped with controllable exposure time and automated magnification determination. This significantly simplifies the optical analysis and eliminates the need of calibration and compensation in contrast/brightness of the images. The analysis is further improved by performing a recursive repositioning procedure on the images to remove

misalignments occurring during the measurement due to movements of the camera or electrochemical cell. This alignment procedure enables the possibility to remove the optical features visible at the beginning of the immersion for each individual pixel, which was not possible with our previous protocol.<sup>17</sup> The algorithm is based on the work of P. Thévenaz et al., whereby each image is used as template with respect to the next one in time, so that the repositioning proceeds by propagation.<sup>21</sup> The first image is used as anchor to reference all other images. The allowed transformations are based on the rigid-body approach, whereby the mapping of coordinates takes the form shown in equation (3.1):

$$x, y = \{\{\cos \theta, -\sin \theta\}, \{\sin \theta, \cos \theta\}\} \cdot u + \Delta u \quad (3.1)$$

This procedure allows both translational and rotational transformations of the images. The background removal is done by subtracting the initial intensity ( $i_0$ ) of each pixel in  $x$  and  $y$  of the first image, from the intensity of all subsequent images ( $i_n$ ) as shown in equation (3.2) and illustrated in Figure 3.2.

$$i_{Difference}(x, y) = |i_n(x, y) - i_0(x, y)| \quad (3.2)$$

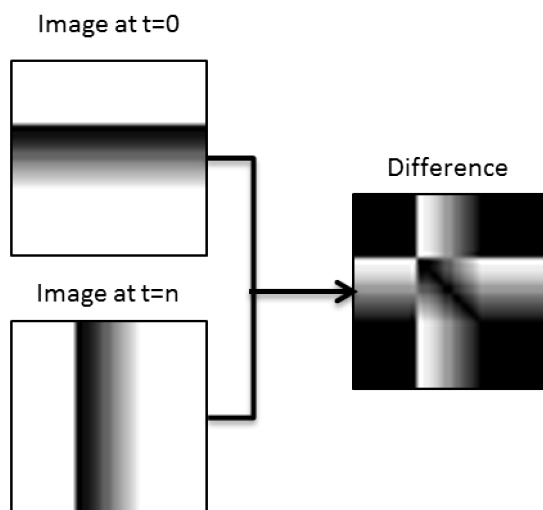


**Figure 3.2** Background removal procedure subtracting the initial intensity of each pixel in  $x$  and  $y$  of the first image from the intensity of all subsequent images.

With this procedure, a pixel that becomes either lighter or darker compared to its initial intensity is taken observed as a “changed pixel”, whereby the difference in intensity with the initial pixel ( $t=0$ ) is translated to an increase in intensity. All processed images are converted to 8-bit (256 bin grey-scale, bin 0 for black and bin 255 for white). This allows obtaining a half-normal intensity distribution in the greyscale histogram attributed to the pixels corresponding to the

optically changed area. In order to calculate the changed surface area, the high intensity signals corresponding to the corrosion-related optically detectable features (e.g. pitting corrosion, intergranular corrosion and deposits on the surface) are isolated from the low intensity background (unchanged surface) using a static thresholding with a lower bin limit of 30. This step is necessary to remove random statistical fluctuations (shot noise) recorded by the photodetector when the charge carriers (photons) traverse a gap. The total changed surface area ( $S_{\text{changed}}$ ) is calculated using equation (3.3):

$$S_{\text{changed}}(\%) = \frac{N_p}{w_p * h_p} * 100 \% \quad (3.3)$$

Where  $N_p$  is the number of changed pixels,  $w_p$  the width resolution and  $h_p$  the height resolution in pixels.

### 3.2.4. Sample preparation

A single 3 mm thick commercial bare AA2024-T3 sheet provided by Kaizer Aluminium served as working electrode.  $2 \times 2 \text{ mm}^2$  pillars were milled out from this sheet and connected to a copper wire using copper adhesive tape. One sample was prepared by embedding two pillars using epoxy casting resin as shown schematically in Figure 3.3.

a) Global corrosion study

b) Local corrosion study

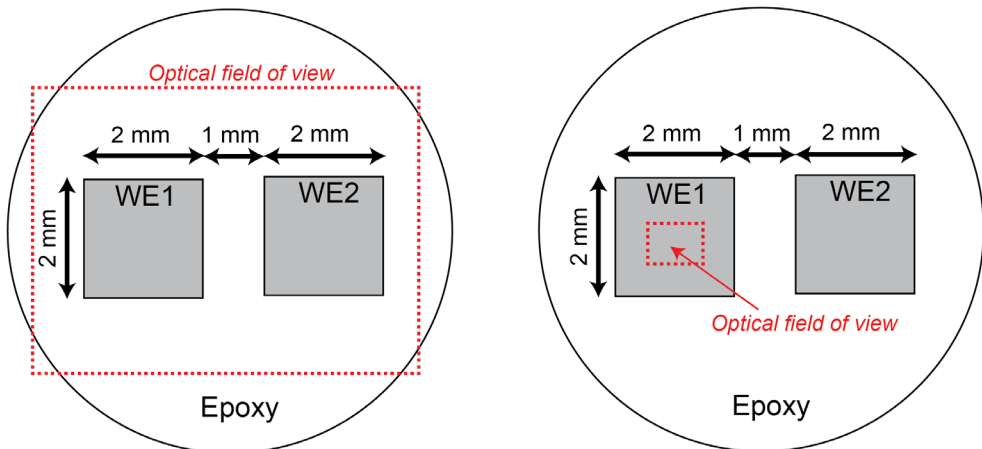


**Figure 3.3** Sample containing two AA2024-T3 working electrodes (WE1 and WE2) embedded in an epoxy casting resin indicating the optical field of view for a) the global corrosion study with low magnification camera and b) the local corrosion study with high magnification camera.

The surface of the sample was freshly prepared 30 min prior to immersion by grinding up to grit 4000 with SiC paper and polishing to a final roughness of  $1 \mu\text{m}$ , This was followed by ultrasonic

cleaning in ethanol and drying with compressed air. The global and the local measurements were performed using the same sample, but after re-polishing between the tests. The global corrosion study used a low magnification camera (see optical-electrochemical setup), recording all optical changes at both working electrodes simultaneously (Figure 3.3a). The local corrosion study used a high magnification camera, allowing only a part of WE1 to be optically monitored (Figure 3.3b).

A similar sample was prepared using two high purity (5N) aluminium rods with a diameter of 3.2 mm for the verification of the experimental data. The reference results, showing an optically and electrochemically stable system, can be found in the supporting information (SI-3.2). All measurements were performed in Milipore® Elix 3 UV filtered water containing 0.5 M, 0.05 M or 0.005 M NaCl at an ambient temperature of  $20\pm 2^\circ\text{C}$  and were repeated at least two times for each salt concentration. Before the start of each measurement, the opto-electrochemical cell was filled with 50 ml electrolyte solution.

### 3.3. Results and Discussion

The results are divided in three sections in order to present on the analysed of the data obtained with the optical-electrochemical setup. In the first section the electrochemical noise (EN) data are analysed in relation to the global (low magnification) optical data analysis. In the second section a more detailed local optical analysis is performed on a new measurement using the high magnification camera to identify the phenomena not captured in the low magnification optical analysis. In the third section we introduce a final plot summarizing the correlation between the EN signals to the different macroscopic corrosion phenomena identified with the optical analysis.

#### 3.3.1. Global corrosion study (low optical magnification and EN)

Figure 3.4 shows the combined EN and optical results from the global corrosion study on AA2024-T3 immersed in 0.05 M NaCl. Figure 3.4a-f shows the raw EPN signal and corresponding CWT spectrum at different immersion time windows:  $t=0-1800$  s (a, d),  $t=200-1800$  s (b, e), and  $t=1800-10000$  s (c, f). The immersion time ( $t$ ) is indicated on the x-axis, the instantaneous frequencies ( $f$ ) of the EPN signal on the y-axis, and the local amplitudes of the wavelets by the colour bar and z-axis for the CTW spectrum. The first 200 s or 1800 s are removed from Figure 3.4e and Figure 3.4f, respectively, to magnify the visualization of the instantaneous frequencies appearing at lower amplitudes. It is also important to note that in Figure 3.4d the edge-effect is present at the beginning of the measurement (described in the method section and clearly observable in the reference measurement on high purity aluminium in SI-3.2). This edge-effect is not related to any occurring corrosion processes, but is a result of the boundary conditions which play a significant role at the beginning and the end of the measurement when the signals have a low amplitude. Enlargements of the raw EPN data and CWT spectrum can be found in SI-3.3. Figure 3.4g shows the real-time raw images, recorded during the EPN measurement, whereby differences in intensity of the pixels are caused by surface features (e.g. sample roughness, lightning condition and corrosion processes). Figure 3.4h shows the processed optical images after the analysis of removing the background as explained in the methods section. Figure 3.4i-j shows the optically changed surface area as calculated from the analysed images at short and long immersion times of  $t=0-1800$  s (i) and  $t=0-10000$  s (j) and can be used to investigate the kinetics of the optically detectable time-dependent processes.

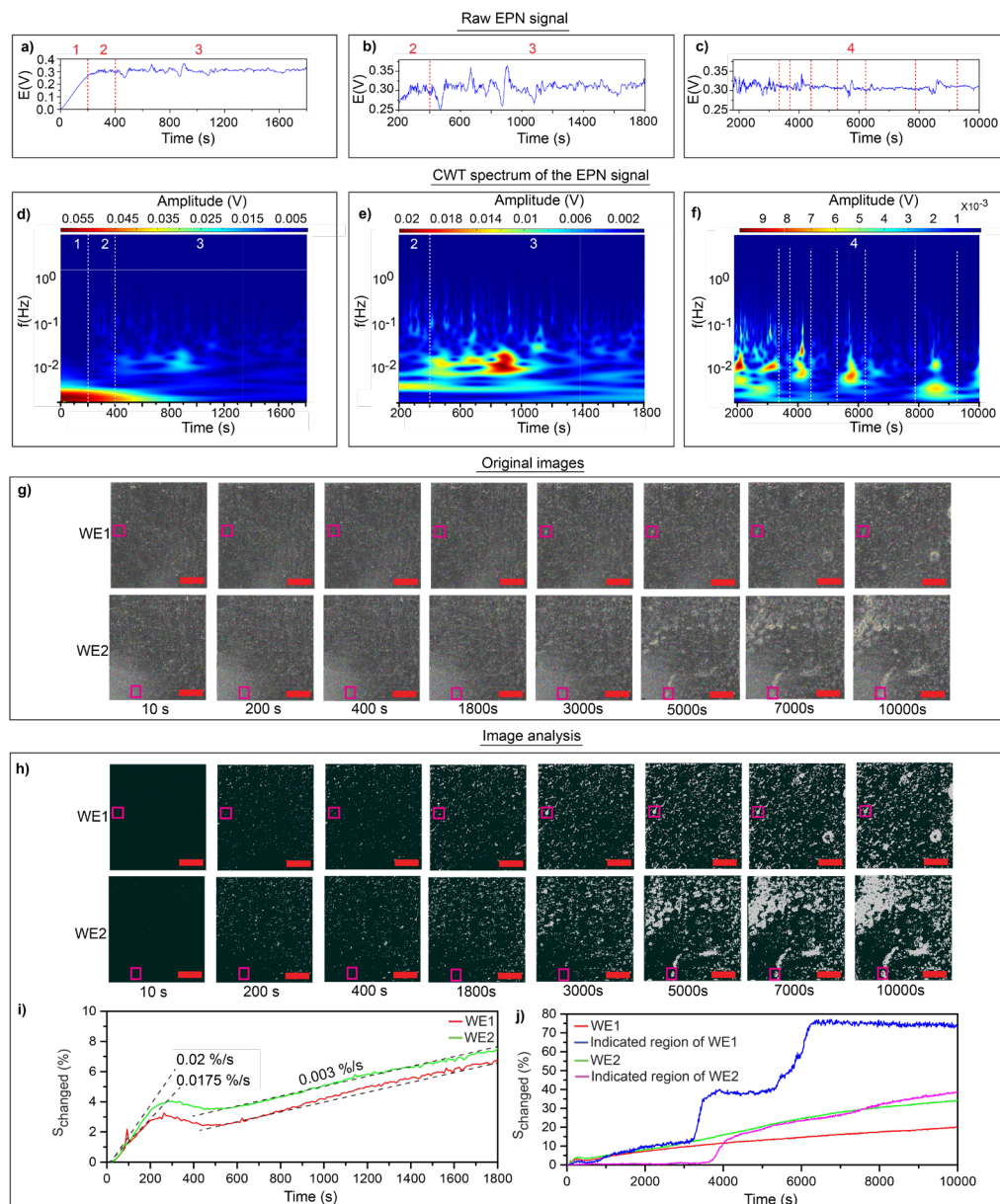


**Figure 3.4** Combined optical-electrochemical results for AA2024-T3 immersed in 0.05 M NaCl. 4a-c show the raw EPN signal and 4d-f the corresponding CWT spectrum for the entire exposed surface at different immersion time periods of  $t=0-1800$  s,  $t=200-1800$  s, and  $t=1800-10000$  s, respectively. 4g-h show the real-time optical raw images (g), processed images (h) showing unchanged (black) and changed pixels (white) in time and the extracted quantitative information of the optically detectable surface changes for short (i) and long immersion times (j). Scalebar represents 0.5 mm.

Four different time-dependent stages of activity can be observed according to the raw EPN signal and CWT spectrum as marked with the numbers 1-4 in Figure 3.4a-c and discussed here below:

- (1) From  $t=0$  s to  $t=200$  s the EPN signal (Figure 3.4a) increases with 300mV and the CWT spectrum (Figure 3.4d) shows no significant amplitudes of instantaneous frequencies above  $10^{-2}$  Hz, indicated by the absence of colours other than the dark-blue low amplitude background. In addition, there is a large low-frequency contribution, below  $10^{-2}$  Hz, indicated in red. The raw optical images (Figure 3.4g) show several features at  $t=10$  s due to surface scratches, compositional differences, and glare caused by the ring-light (e.g. bottom of WE1 and bottom left of WE2). Nevertheless, no new optical features were detected in the first 200 s with this magnification and prior to image treatment. Figure 3.4h on the other hand, shows that after implementing our image processing protocol, removing all initial features at  $t=0$ . Now surface changes do occur during the first 200 s immersion, despite the relatively low magnification. These surface-changes can be explained by the occurrence of individual corrosion events that take place at a dimension below the resolution of the microscope which become detectable after accumulation of these single events using the global image analysis. Figure 3.4i shows the calculated surface area variation with time. From  $t=0$  s to  $t=200$  s the surface rapidly changes with a rate of  $0.0175\%s^{-1}$  and  $0.02\%s^{-1}$  for WE1 and WE2, respectively leading to a total surface change of 3-4 % at 200 s immersion. The optical results indicate that during the first 200 s immersion a relatively high surface activity has taken place at specific locations leading to detectable surface changes (pixels becoming darker or lighter). This period corresponds with the significant increase of the EPN signal (Figure 3.4a) combined with the largest energy contribution in the CWT spectrum (Figure 3.4d). These optically observable features, electrochemically expressed as high energetic processes (CWT) with a strong increase of the EPN signal,<sup>22</sup> can be related to local anodic and cathodic processes Intermetallic (IM) particles leading to, amongst others, de-alloying of copper-rich S-phase and  $\theta$ -phases resulting in early-stage pitting and the formation of oxide caps at the IM sites,<sup>13</sup> The low frequency signal in the CWT spectrum is thereby attributed to de-alloying, which is a relatively slow surface diffusion controlled process at the IM particles.
- (2) From  $t=200$  s to  $t=400$  s the EPN signal (Figure 3.4b) reaches a steady-state stage and shows many high frequency fluctuations with a relatively small amplitude, resulting in a CWT spectrum (e) dominated by short time-scale processes with an instantaneous frequency ranging from approximately  $4 \cdot 10^{-2}$  Hz to 1 Hz. Figure 3.4i shows that the surface changed increases but at lower kinetics between  $t=200$  s and  $t=250$  s. This is then followed by a drop of the surface changed of approximately 0.5 % at  $t=400$  s. To understand this decrease in surface changes with respect to the first image it is important to clarify that the changed surface is calculated from the analysed images after removing all the optical effects observed at  $t=0$  s. In other words, a pixel has optically changed when it becomes either lighter or darker in time with respect to its original state ( $t=0$  s). This can therefore be explained by pixels that became darker during the first 250 s and turned lighter again between  $t=250$  s and

$t=400$  s (or vice versa), until the pixel matches its original state. We attribute this process to the transition from one corrosion process to another at the very same location (pixel). Interestingly, this optically detectable transition takes place when the EPN signal stabilised and the CWT spectrum shows a shift from low frequency to high frequency transients. By combining the EPN signal with the quantified surface changes it is argued that new corrosion processes take place after  $t=200$  s whereby the formed oxide caps on the IM phases start to dissolve, resulting in a decrease of changed surface area, combined with the initiation of new (meta)stable pits and trenching. This is in good agreement with SEM/EDS studies on AA2024-T3 after a similar immersion times.<sup>13</sup>

- (3) From  $t=400$  s to  $t=1800$  s the EPN signal (Figure 3.4b) shows fluctuations with a larger amplitude than in stage 2. Simultaneously, the CWT spectrum (Figure 3.4e) shows concurrent processes on a larger timescale in the frequency range from approximately  $4 \cdot 10^{-3}$  Hz to  $4 \cdot 10^{-2}$  Hz, with the largest local maxima between  $7 \cdot 10^{-3}$  Hz and  $3 \cdot 10^{-2}$  Hz. Figure 3.4i shows that the surface changes increases again but at a much slower rate compared to stage 1 ( $0.003 \text{ \% s}^{-1}$  for both working electrodes). This indicates that at around  $t=400$  s a different corrosion process dominates (instead of dealloying and pit initiation in stage 1-2). From the analysed images (Figure 3.4h) it can be seen that the (white) spots seem to grow in size after  $t=400$  s at the same time as new smaller spots appear. These observations suggest that a slower corrosion process, such as oxygen diffusion-controlled corrosion processes, take place at the IM particles after pit-initiation (i.e. pit growth<sup>23</sup>). As time progresses the number of large transients in the EPN signal and fast occurring fluctuations in the CWT spectrum reduces, indicating that fewer initiation events are taking place. This process is combined with a shift to lower frequency and amplitude. We attribute these to composition and size differences between individual IM particles which are attacked at different moments in time. The reduction in high frequency transients over time is attributed here to a decrease in the number of new pits.
- (4) After  $t=1800$  s the EPN signal (Figure 3.4c) further stabilizes while the CWT spectrum (Figure 3.4f) shows a further decrease of instantaneous frequencies, indicating a change from localized smaller time scale processes to larger time scale processes. This is further accompanied by several local maxima, as indicated in Figure 3.4f, with instantaneous frequencies between  $10^{-3}$  Hz and  $10^{-1}$  Hz ( $t=1800\text{-}3600$  s,  $t=3800\text{-}4200$  s,  $t=5300\text{-}6200$  s, and  $t=7900\text{-}9100$  s). Figure 3.4g shows that, even without image analysis, the raw images clearly show surface changes after  $t=3000$  s. The treated images (Figure 3.4h) show that such surface changes take place already in the period 1800-3000 s and appear as white spots growing in size, clustering or appearing as new. This process proceeds over time until at  $t=5000$  s several large spots with a diameter beyond  $50 \text{ }\mu\text{m}$  become visible. Considering that IM phases on AA2024 are generally reported to be smaller than  $50 \text{ }\mu\text{m}$  in diameter and only cover approximately 3 % to 4 % of the surface<sup>24,25</sup> and that these values are largely surpassed

after 1800 s according to the image analysis, we attribute the largest amount of changes after  $t=1800$  s to heavy subsurface corrosion (e.g. intergranular corrosion) leading to thick oxides deposition on the surface. When measuring the surface changes over the whole exposed area (Figure 3.4j) it appears that these changes grow gradually over time, at a relatively lower kinetics than in stage 3 and with WE1 (indicated in red) being slightly less active after  $t=3000$  s than WE2 (indicated in green). Nevertheless, when a small area is analysed (squares in Figure 3.4h and blue and magenta lines in 4j) clear jumps in start to appear for the changes surface. Oxide deposits appear on the WE1 selected area after roughly  $t=3000$  s, after which it stabilizes to grow further after  $t=6000$  s, whereas the oxides at the selected location of WE2 appear after  $t=4000$  s and keeps on growing. This local analysis on selected areas of the surface was performed on several other locations with high surface changes (SI-3.3). As a result we found that the changes starts to appear at specific moments in time (i.e. around  $t=2000$  s,  $t=3000$  s,  $t=4000$  s,  $t=6000$  s, and  $t=8700$  s). Although the appearance of these oxides coincide with the four local maxima in the CWT spectrum (indicated in Figure 3.4c), oxides do not start appearing and stop growing at the exact same periods. This mismatch in time indicates that the formation of surface oxides is the result of earlier occurring electrochemical corrosion processes underneath the surface and, in some cases, lags behind the corresponding electrochemical charge transfer.

In order to confirm the observations sketched above as well as the robustness of the protocol we repeated the tests and analysis at different salt concentrations. Figure 3.5 shows the combined EN and optical results for the global corrosion study on AA2024-T3 using 0.005 M NaCl. The same measurements for 0.5 M can be found in SI-3.4, A close analysis to this Figure 3.5 allows identifying exactly the same stages (numbered also 1-4) as discussed above for Figure 3.4 but delayed in time, at different amplitudes and with lower surface kinetics, as expected for lower salt concentrations.

Although this low-magnification optical analysis gave a significant fundamental insight on the interpretation of EN and the corrosion processes, a high-magnification study was followed to better identify local corrosion processes as will be discussed here onwards.

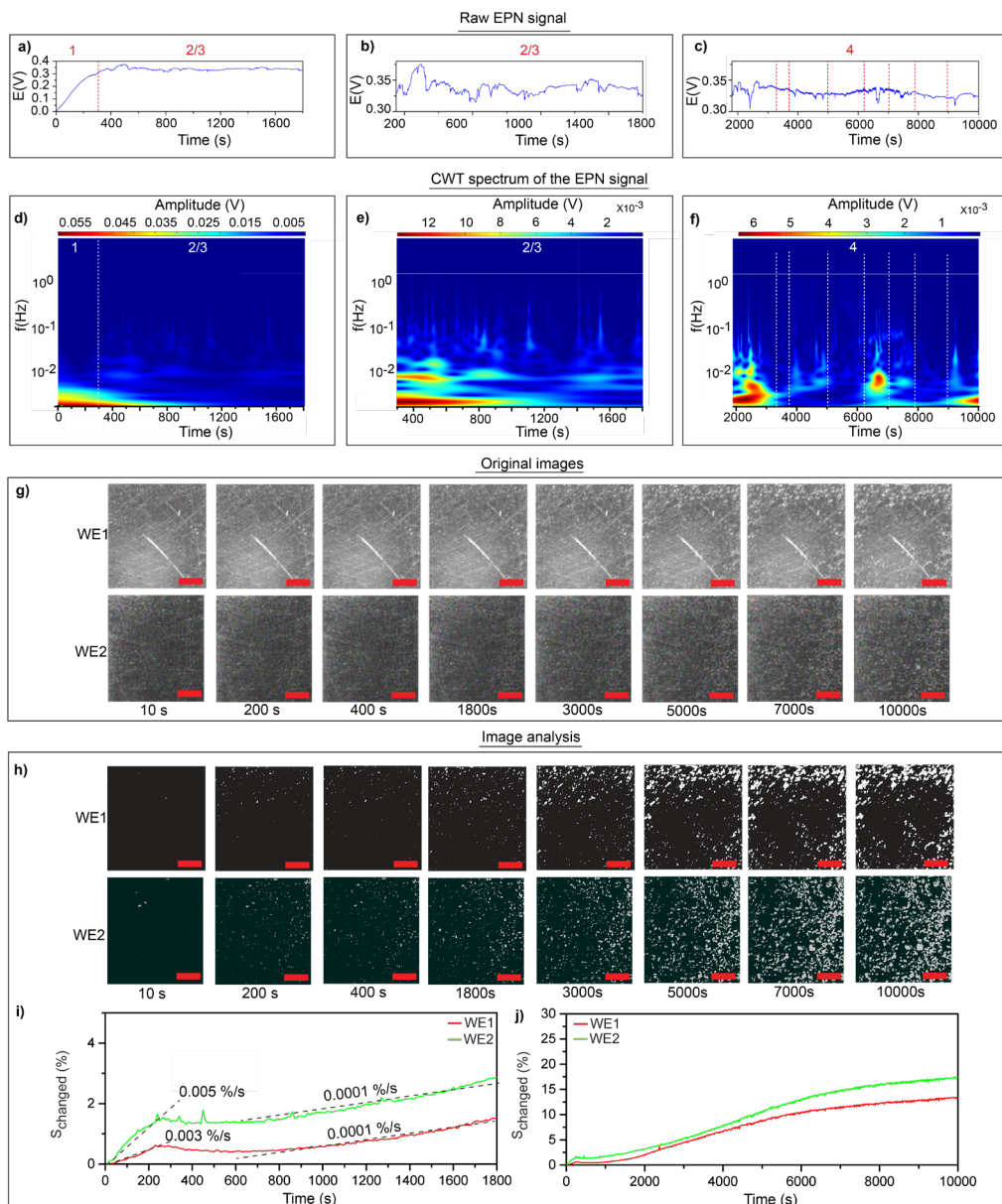
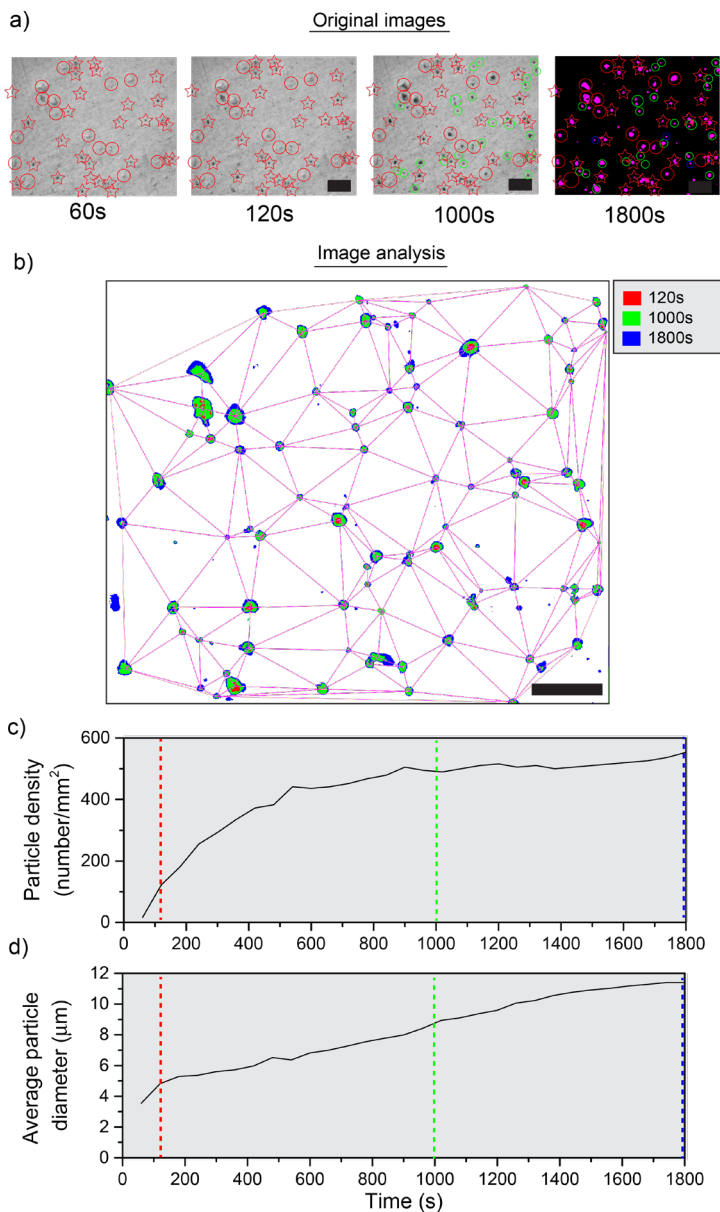


**Figure 3.5** Combined optical-electrochemical results for AA2024-T3 immersed in 0.005 M NaCl. 4a-c show the raw EPN signal and 4d-f the corresponding CWT spectrum for the entire exposed surface at different immersion time periods of  $t=0-1800$  s,  $t=200-1800$  s, and  $t=1800-10000$  s, respectively. 4g-h show the real-time optical raw images (g), processed images (h) showing unchanged (black) and changed pixels (white) in time and the extracted quantitative information of the optically detectable surface changes for short (i) and long immersion times (j). Scalebar represents 0.5 mm.

### 3.3.2. Local corrosion study (high optical magnification)

The high-magnification optical tests were also performed in parallel with EN. As seen in the SI3.4, the EN features and analysis is comparable to the one discussed above. Nevertheless, as a result of the higher magnification (and impossibility to make smaller samples) the optical analysis is only performed on a small area as shown in the experimental section. For this reason, not all the observed electrochemical signals can be correlated to the optical changes as shown in the previous section and the analysis will primarily be based on optics.

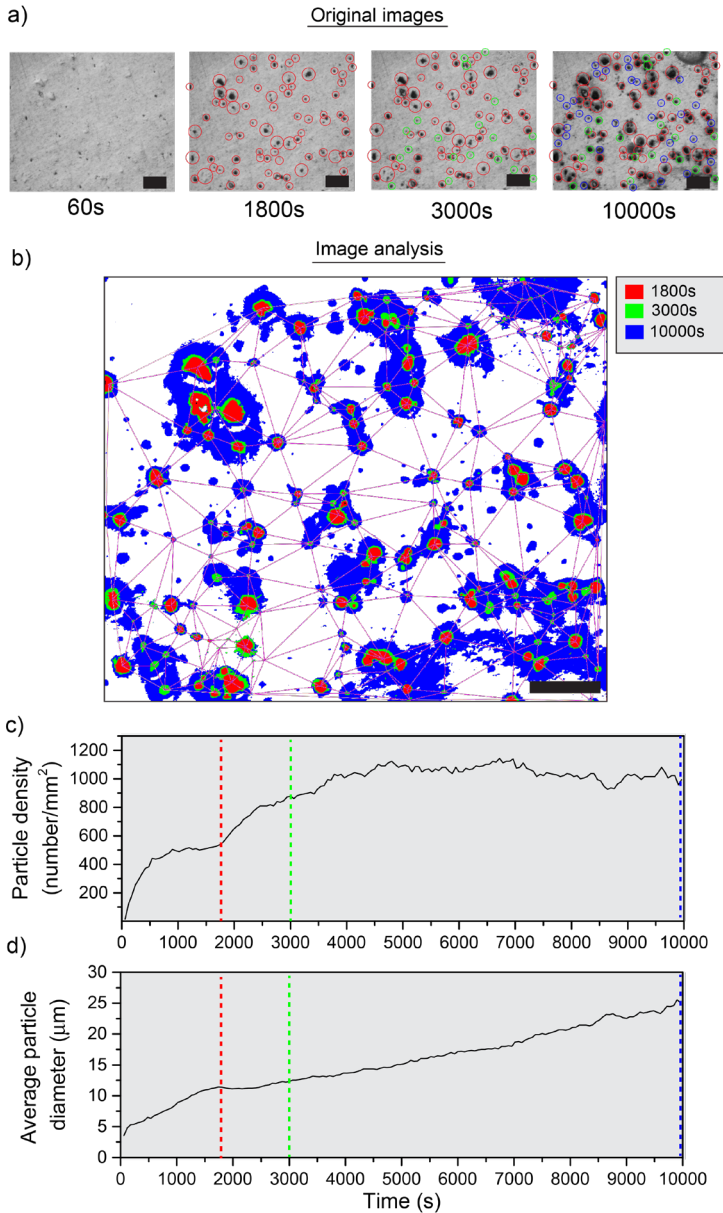
Figure 3.6 shows the optical results between  $t=60$  s and  $t=1800$  s for AA2024-T3 immersed in 0.05 M NaCl. While Figure 3.6a shows the raw images with defects (corrosion features) evolving in time (coloured circles), Figure 3.6b shows a time-overlapped analysed image. This Figure 3.6 allows identifying the location and appearance of individual particles (IMs, corrosion spots), their time of growth and the distance to their nearest neighbours. These calculations were possible due to the higher pixel density of the high magnification camera and were performed using the automated particle analysis from ImageJ, combined with Delaunay triangulations on nearest neighbour distances<sup>26</sup>. This approach also enabled the calculation of the particle density (Figure 3.6c) and average particle size (Figure 3.6d) in each image.



**Figure 3.6** High magnification optical results for AA2024-T3 immersed in 0.05 M NaCl between  $t=60$  s and  $t=1800$  s. The original images are shown in (a) including red, green and blue markings (circles and stars) related to particle appearance over time at  $t=60$  s,  $t=1000$  s, and  $t=1800$  s, respectively. (b) shows the time-evolution of the detected particles using identical colour code as in (a). (c) and (d) show the particle density and average particle size evolution with time respectively. Scale bar represents 50 microns.

From the original images shown in Figure 3.6a it becomes clear that there are already surface features visible after  $t=60$  s of immersion. Due to different lighting conditions compared to the low-magnification study (Figure 3.4), the intensity of the reflected light in this case reduces with the surface roughness (i.e. darker when rougher). Several dark spots with a diameter smaller than  $10\ \mu\text{m}$  (marked with stars in red in Figure 3.6a) are visible right after immersion. These were not visible right after polishing (optical image before corrosion test can be found in SI-3.5). This indicates that these locations are revealed within the first 60 s immersion (no optical data could be obtained between 0 and 60 s). In addition to these black spots, there are also lighter particles with a diameter larger than  $10\ \mu\text{m}$  visible after  $t=60$  s (circled in red in Figure 3.6a). Contrary to the black spots, these were already observed prior to the immersion experiment (SI-3.5). Their appearance can be explained by local compositional differences, resulting in a different surface roughness after polishing<sup>27</sup>. After  $t=120$  s, the black spots continued to increase in size while the lighter particles started to etch away (became darker). The image particle-analysis allowed quantifying such changes in time (Figure 3.6c and Figure 3.6d). This revealed that the number of particles increases towards 100 particles/ $\text{mm}^2$ , and  $5\ \mu\text{m}$  average particle diameter in the first 120 s exposure. This average size is similar to the mean IM particle diameter being reported to be between 2 and  $5\ \mu\text{m}$  based on compositional analysis on AA2024-T3<sup>28</sup>. We therefore suggest that the black spots here detected are related to pitting at IM particles during the first 120 s. It should be highlighted that this observation was not possible with EN, low-magnification analysis, and SEM/EDS studies after similar immersion-times<sup>13</sup>. After 1000 s pits grow further in size (marked in red in Figure 3.6a) and new pits appeared (circled in green in Figure 3.6a), reaching a total of 490 particles/ $\text{mm}^2$  (Figure 3.6c) with an average particle diameter of  $8\ \mu\text{m}$  (Figure 3.6d). From the graphical representation (Figure 3.6b) it can be seen that the particles have a circular shape and that they are distributed within an average nearest neighbouring distance of  $55\ \mu\text{m}$ . The total number of pits after  $t=1000$  s is close to the expected IM particle density, which was reported to be between 270 and 530 particles/ $\text{mm}^2$ .<sup>24,27,29</sup> These findings suggest that most IM particles are being attacked within the first 1000 s. This corresponds to the highest activity (largest amplitudes) in the instantaneous frequency range between  $4 \cdot 10^{-2}$  Hz and 1 Hz in this time-period visible in the CWT spectrum (AI-3.4). After  $t=1000$  s, the number of pits remains remarkably stable until  $t=1800$  s, while the diameter of the particles increases further to stabilize at  $11\ \mu\text{m}$ . From the graphical representation in Figure 3.6b it can be confirmed that the pits at  $t=1000$  s (in green) to  $t=1800$  s (in blue) have grown in size and only a small number of new particles has emerged. This consequently results in comparable average nearest neighbour distance of  $52\ \mu\text{m}$ . The CWT spectrum in SI-3.5 also shows a decreased activity in the instantaneous frequency range between  $4 \cdot 10^{-2}$  Hz and 1 Hz, whereas the instantaneous frequencies below  $10^{-2}$  Hz remain active in this region. This corresponds well with the optical analysis relating this to relatively stable, long timescale, pit growth.

Figure 3.7 shows the optical results on the local corrosion study between  $t=60$  s and  $t=10000$  s for AA2024-T3 immersed in 0.05 M NaCl.



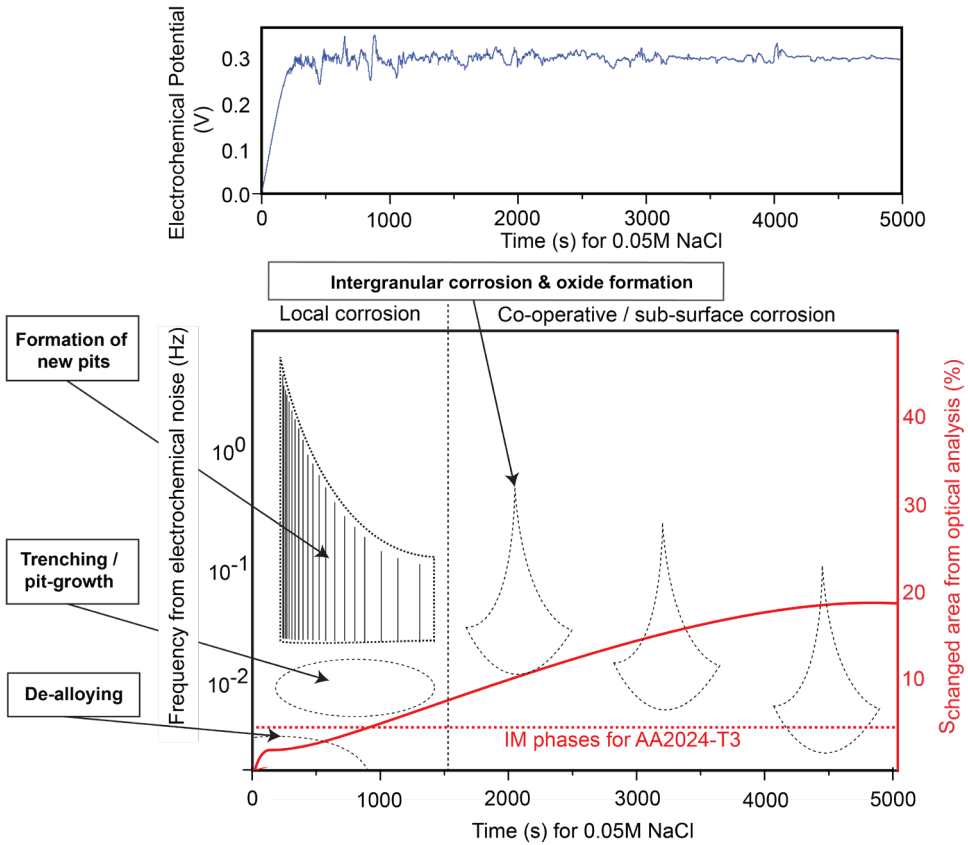
**Figure 3.7** High magnification optical results for AA2024-T3 immersed in 0.05 M NaCl between  $t=60$  s and  $t=10,000$  s. The original images are shown in (a) including red, green, and blue circles related to particle appearance over time at  $t=1800$  s,  $t=3000$  s, and  $t=10,000$  s, respectively. (b) shows the time-evolution of the detected particles using identical colour code as in (a). (c) and (d) show the particle density and average particle size evolution with time respectively. Scale bar represents 50 microns.

Figure 3.7a shows that after 1800 s the number and size of particles increases again (indicated in green in Figure 3.7a) so that, at around  $t=3000$  s, there are 977 particles/ $\text{mm}^2$  with an average particle diameter of 12  $\mu\text{m}$  (Figure 3.7c-d). From the graphical representation (Figure 3.7b) it becomes obvious that the newly appeared particles remain relatively small, while the particles that are already present have significantly grown in size. This is in line with the deductions from the CWT spectrum in this period (SI-3.5), highlighting the same localized corrosion processes. After  $t=3000$  s the particle density grows until 900-1100 particles/ $\text{mm}^2$ , while the average particle diameter remains increasing, towards 25  $\mu\text{m}$  at  $t=10,000$  s. At this stage, both the density and average diameter of the particles are significantly larger compared to the reported IM particle size and density, indicating that trenching and sub-surface corrosion processes have resulted in the deposition of oxides on the surface. From the graphical representation (Figure 3.7b) it becomes clear that at  $t=10,000$  s (indicated in blue) particles are clustered together while new locations have emerged in between the clusters. This results in a sudden drop of the nearest neighbour distance to 36  $\mu\text{m}$ . This indicates that, besides the formation of oxides around the pits, more complicated co-operative corrosion processes take place (e.g. coupling of neighbouring IM particles by “cross-talk” between activation and passivation processes leading to corrosion rings<sup>30</sup>). Although corrosion processes were clearly visible from CWT- as well as global optical analysis, the quantification of surface features from pitting up to the formation of corrosion rings over time have previously only be observed by optical and SEM analysis after the sample had been removed from the electrolyte.

### 3.3.3. Correlation between EN signals and macroscopic corrosion features from optical analysis

Figure 3.8 shows a summary of the observed features for AA2024-T3 (both as EPN signal and CWT spectrum) coupled to macroscopic corrosion processes observed with and quantified by real-time optical inspection. This Figure 3.8 serves to illustrate the interpretation of corrosion information by integration of the electrochemical and optical technique. In the first stage de-alloying takes place, which can be observed electrochemically by a large drift in the EPN signal by the and by a significantly high low-frequency contribution below  $10^{-2}$  Hz in the CWT spectrum. In the optical analysis this de-alloying manifests itself by a sudden increase of surface changes. This is followed by the formation of pits, observable in the EPN signal and CWT spectrum by high frequency fluctuations, combined with trenching and pith growth on a larger timescale in the frequency range around  $10^{-2}$  Hz in the CWT spectrum. Optically, the transition from de-alloying to trenching and pit formation is observed by a shift to slower surface changes over time (stage 2). Subsequently, co-operative and sub-surface corrosion processes start to appear and are visible in the EPN signal by a relatively stable signal with a few large fluctuations, and in the CWT spectrum by local maxima at large timescales In the optical analysis these phenomena become apparent by the total amount of surface changes exceeding the percentage

of covered area by IM phases, combined with a stabilisation of the surface coverage at later stages. Experiments at different salt concentrations show comparable electrochemical and optical characteristics, however the respective phenomena occur earlier in time for higher salt concentrations, and additionally with a different intensity.



**Figure 3.8** Correlation of characteristics in the EPN signal and CWT spectrum with macroscopic local corrosion phenomena for the case of AA2024-T3 as a result of real-time optical analysis.

### 3.4. Conclusions

Real-time optical analysis of the corrosion process is presented in this work as a powerful approach to improve the readability of electrochemical fluctuations in EN and their correlation to macroscopic corrosion phenomena and time evolution. An in-house optical-electrochemical setup was developed to simultaneously capture both optical changes and electrochemical fluctuations that appear on the metal substrate under immersion. In this work, the corrosion processes and stages of AA2024-T3 have been investigated at different salt concentrations whereby detailed optical analysis served as a basis for the interpretation of the raw EPN signal and the EPN signal analysed in the time-frequency domain using CWT. Low magnification optical measurements (60x) allowed capturing all the surface changes appearing on the exposed metal surface with a 3  $\mu\text{m}$  resolution. Image analysis was developed for the removal of surface features that were not related to corrosion (e.g. scratches, compositional differences and glare) and enabled the detection of local surface changes that could not be observed in the raw images. The highly resolved data, obtained from the different types of analyses, allowed the collective determination of time- and space- dependent corrosion processes such as de-alloying, trenching, pit growth, co-operative and subsurface corrosion. A second measurement was performed at higher magnification (420x), capturing only a small section of the exposed metal, but at a much higher optical resolution ( $<1 \mu\text{m}$ ). This, together with the use of our optical analysis protocol, enabled a time-resolved quantification of corrosion-related surface features (e.g. size, amount and nearest neighbour distance of newly appearing pits) whereby the local changes in time corresponded well with the global CWT- and optical analysis. Finally, an integrated optical and EN illustration was created to simplify the interpretation of the raw EPN signal, as well as the CWT spectrum, while allowing the detection of different corrosion processes over time. The results illustrate the robustness of using real-time optical microscopy to visualise and quantify the corrosion processes while they take place, thereby improving the interpretation of electrochemical signals, such as EN, in a straightforward way.

### 3.5. References

- 1 H. S. Isaacs, "The localized breakdown and repair of passive surfaces during pitting," *Corros. Sci.*, vol. 29, no. 2–3, pp. 313–323, 1989, doi: 10.1016/0010-938X(89)90038-3.
- 2 A. Aballe, M. Bethencourt, F. J. Botana, and M. Marcos, "Wavelet transform-based analysis for electrochemical noise," *Electrochem. commun.*, vol. 1, no. 7, pp. 266–270, 1999, doi: 10.1016/S1388-2481(99)00053-3.
- 3 A. M. Homborg *et al.*, "Transient analysis through Hilbert spectra of electrochemical noise signals for the identification of localized corrosion of stainless steel," *Electrochim. Acta*, vol. 104, pp. 84–93, 2013, doi: 10.1016/j.electacta.2013.04.085.
- 4 A. M. Homborg, C. F. Leon Morales, T. Tinga, J. H. W. De Wit, and J. M. C. Mol, "Detection of microbiologically influenced corrosion by electrochemical noise transients," *Electrochim. Acta*, vol. 136, pp. 223–232, 2014, doi: 10.1016/j.electacta.2014.05.102.
- 5 A. M. Homborg *et al.*, "Application of transient analysis using Hilbert spectra of electrochemical noise to the identification of corrosion inhibition," *Electrochim. Acta*, vol. 116, pp. 355–365, Jan. 2014, doi: 10.1016/j.electacta.2013.11.084.
- 6 A. M. Homborg *et al.*, "Novel time-frequency characterization of electrochemical noise data in corrosion studies using Hilbert spectra," *Corros. Sci.*, vol. 66, pp. 97–110, 2013, doi: 10.1016/j.corsci.2012.09.007.
- 7 R. A. Cottis, A. M. Homborg, and J. M. C. Mol, "The relationship between spectral and wavelet techniques for noise analysis," *Electrochim. Acta*, vol. 202, pp. 277–287, 2016, doi: 10.1016/j.electacta.2015.11.148.
- 8 A. Aballe, M. Bethencourt, F. J. Botana, and M. Marcos, "Using wavelets transform in the analysis of electrochemical noise data," *Electrochim. Acta*, vol. 44, no. 26, pp. 4805–4816, 1999, doi: 10.1016/S0013-4686(99)00222-4.
- 9 A. M. Lafront, F. Safizadeh, E. Ghali, and G. Houlachi, "Study of the copper anode passivation by electrochemical noise analysis using spectral and wavelet transforms," *Electrochim. Acta*, vol. 55, no. 7, pp. 2505–2512, 2010, doi: 10.1016/j.electacta.2009.12.006.
- 10 C. Cai, Z. Zhang, F. Cao, Z. Gao, J. Zhang, and C. Cao, "Analysis of pitting corrosion behavior of pure Al in sodium chloride solution with the wavelet technique," *J. Electroanal. Chem.*, vol. 578, no. 1, pp. 143–150, 2005, doi: 10.1016/j.jelechem.2004.12.032.
- 11 J. A. Wharton, R. J. K. Wood, and B. G. Mellor, "Wavelet analysis of electrochemical noise measurements during corrosion of austenitic and superduplex stainless steels in chloride media," *Corros. Sci.*, vol. 45, no. 1, pp. 97–122, 2003, doi: 10.1016/S0010-938X(02)00140-3.
- 12 A. M. Glenn *et al.*, "Corrosion of AA2024-T3 Part III: Propagation," *Corros. Sci.*, vol. 53, no. 1, pp. 40–50, 2011, doi: 10.1016/j.corsci.2010.09.035.
- 13 A. Boag, A. E. Hughes, A. M. Glenn, T. H. Muster, and D. McCulloch, "Corrosion of AA2024-T3 Part I: Localised corrosion of isolated IM particles," *Corros. Sci.*, vol. 53, no. 1, pp. 17–26, 2011, doi: 10.1016/j.corsci.2010.09.009.
- 14 F. H. Scholes, S. A. Furman, A. E. Hughes, and T. A. Markley, "Corrosion in artificial defects. I: Development of corrosion," *Corros. Sci.*, vol. 48, no. 7, pp. 1812–1826, 2006, doi: 10.1016/j.corsci.2005.05.050.
- 15 J. Wang, B. M. Ocko, A. J. Davenport, and H. S. Isaacs, "In situ x-ray-diffraction and -reflectivity studies of the Au(111)/electrolyte interface: Reconstruction and anion adsorption," *Phys. Rev. B*, vol. 46, no. 16, pp. 10321–10338, 1992, doi: 10.1103/PhysRevB.46.10321.
- 16 C. Punckt *et al.*, "Sudden onset of pitting corrosion on stainless steel as a critical phenomenon," *Science (80-. )*, vol. 305, no. 5687, pp. 1133–1136, 2004, doi: 10.1126/science.1101358.
- 17 P. J. Denissen and S. J. Garcia, "Cerium-loaded algae exoskeletons for active corrosion protection of coated AA2024-T3," *Corros. Sci.*, vol. 128, no. September, pp. 164–175, Nov. 2017, doi: 10.1016/j.corsci.2017.09.019.
- 18 P. J. Denissen and S. J. Garcia, "Reducing subjectivity in EIS interpretation of corrosion and corrosion inhibition processes by in-situ optical analysis," *Electrochim. Acta*, vol. 293, pp. 514–524, 2019, doi: 10.1016/j.electacta.2018.10.018.
- 19 A. M. Homborg, P. J. Ooninx, and J. M. C. Mol, "Wavelet transform modulus maxima and holder exponents combined with transient detection for the differentiation of pitting corrosion using

- electrochemical noise,” *Corrosion*, vol. 74, no. 9, pp. 1001–1010, 2018, doi: 10.5006/2788.
- 20 A. M. Homborg, R. A. Cottis, and J. M. C. Mol, “An integrated approach in the time, frequency and time-frequency domain for the identification of corrosion using electrochemical noise,” *Electrochim. Acta*, vol. 222, pp. 627–640, 2016, doi: 10.1016/j.electacta.2016.11.018.
- 21 P. Thévenaz, U. E. Ruttimann, and M. Unser, “A pyramid approach to subpixel registration based on intensity,” *IEEE Trans. Image Process.*, vol. 7, no. 1, pp. 27–41, 1998, doi: 10.1109/83.650848.
- 22 M. Curioni, R. A. Cottis, and G. E. Thompson, “Application of electrochemical noise analysis to corroding aluminium alloys,” in *Surface and Interface Analysis*, 2013, vol. 45, no. 10, pp. 1564–1569, doi: 10.1002/sia.5173.
- 23 Y. Shi, Z. Zhang, J. Su, F. Cao, and J. Zhang, “Electrochemical noise study on 2024-T3 Aluminum alloy corrosion in simulated acid rain under cyclic wet-dry condition,” *Electrochim. Acta*, vol. 51, no. 23, pp. 4977–4986, 2006, doi: 10.1016/j.electacta.2006.01.050.
- 24 A. Boag *et al.*, “How complex is the microstructure of AA2024-T3?,” *Corros. Sci.*, vol. 51, no. 8, pp. 1565–1568, 2009, doi: 10.1016/j.corsci.2009.05.001.
- 25 R. G. Buchheit, R. P. Grant, P. F. Hlava, B. Mckenzie, and G. L. Zender, “Local dissolution phenomena associated with S phase (Al<sub>2</sub>CuMg) particles in aluminum alloy 2024-T3,” *J. Electrochem. Soc.*, vol. 144, no. 8, pp. 2621–2628, 1997, doi: 10.1149/1.1837874.
- 26 R. Loisy, “Sur la forme des courbes [voir pdf],” *J. Phys. le Radium*, vol. 12, no. 7, pp. 735–739, 1951, doi: 10.1051/jphysrad:01951001207073500.
- 27 G. S. Chen, M. Gao, and R. P. Wei, “Microconstituent-Induced Pitting Corrosion in Aluminum Alloy 2024-T3,” *Corros.*, vol. 52, no. 1, pp. 8–15, 1996, doi: 10.5006/1.3292099.
- 28 A. E. Hughes, N. Birbilis, J. M. C. Mol, S. J. Garcia, X. Zhou, and G. E. Thompson, “High Strength Al-Alloys: Microstructure, Corrosion and Principles of Protection,” *Recent Trends Process. Degrad. Alum. Alloy.*, pp. 223–262, 2011, doi: 10.5772/18766.
- 29 A. E. Hughes and A. Boag, “Statistical Approach to Determine Spatial and Elemental Correlations of Corrosion Sites on Al-Alloys,” in *Aluminium Surface Science and Technology Conference Beaune, France, ATB Metallurgie, 45 (1-4)*, 2006, pp. 551–556.
- 30 A. E. Hughes *et al.*, “Corrosion of AA2024-T3 Part II: Co-operative corrosion,” *Corros. Sci.*, vol. 53, no. 1, pp. 27–39, 2011, doi: 10.1016/j.corsci.2010.09.030.

## 3.6. Supporting Information

### SI-3.1. Automated image analysis protocol for ImageJ

#### Recursive Repositioning

1. for (i=listDone.length; i<list.length; i++)
2. {
3. open(dir+list[1]);
4. open(dir+list[i]);
5. run("Images to Stack", "name=Stack title=[] use")
6. run("StackReg ", "transformation=[Rigid Body]");
7. run("Delete Slice");
8. saveAs(format, dir2+list[i]);
9. }

#### Background removal

1. for (i=0; i<list.length; i++)
2. {
3. open(dir+list[0]);
4. open(dir+list[i]);
5. imageCalculator("Difference create", list[i],list[0]);
6. saveAs(dir2+list1[i])
7. }

#### Lower limit thresholding

1. for (i=0; i<list.length; i++)
2. {
3. open(dir+list[i]);
4. setThreshold(30, 255);
5. setOption("BlackBackground", false);
6. run("Convert to Mask");
7. run("Invert");
8. saveAs(dir2+list[i])
9. }

### SI-3.2. High purity (5N) Aluminium optical-electrochemical results

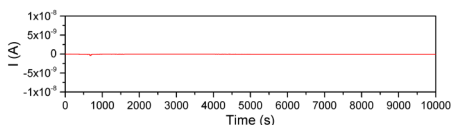


**Figure SI 3.1** raw current data for high purity 5N Aluminium immersed in 0.05 M NaCl between  $t=0$  s and  $t=10.000$  s.

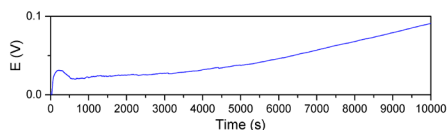


**Figure SI 3.2** raw potential data for high purity 5N Aluminium immersed in 0.05 M NaCl between  $t=0$  s and  $t=10.000$  s.

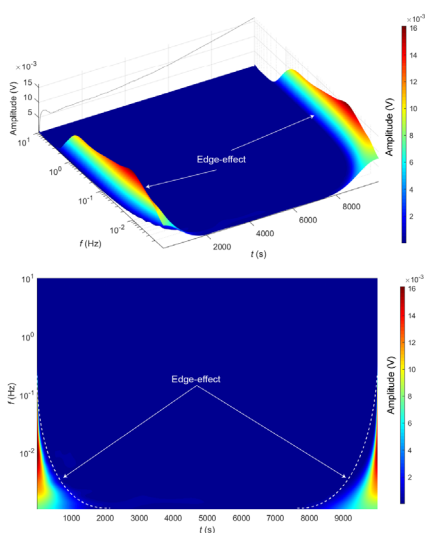


**Figure SI 3.3** CWT spectrum of the EPN signal for high purity 5N Aluminium immersed in 0.05 M NaCl between  $t=0$  s to  $t=10000$  s.

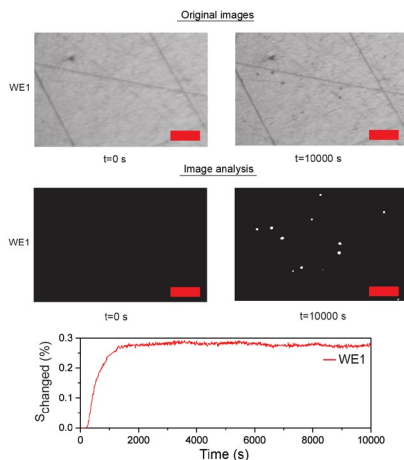


**Figure SI 3.4** optical analysis for 5N Aluminium immersed in 0.05 M NaCl between  $t=0$  s and  $t=10000$  s. Scalebar represents 50  $\mu$ m.

### SI-3.3. Global corrosion study at 0.05M NaCl

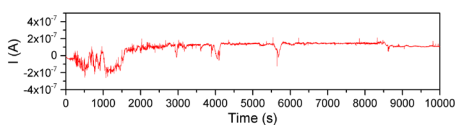


**Figure SI 3.5** raw current data for the global corrosion study on AA2024-T3 immersed in 0.05 M NaCl between  $t=0$  s and  $t=10.000$  s.

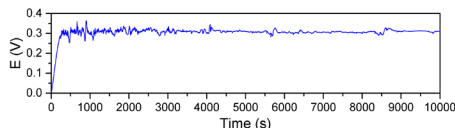


**Figure SI 3.6** Raw potential data for the global corrosion study on AA2024-T3 immersed in 0.05 M NaCl between  $t=0$  s and  $t=10.000$  s.

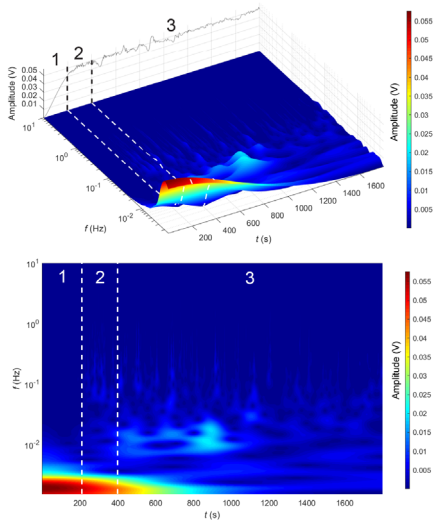


**Figure SI 3.7** CWT spectrum of the EPN signal for the global corrosion study on AA2024-T3 immersed in 0.05 M NaCl between  $t=0$  s and  $t=1800$  s.

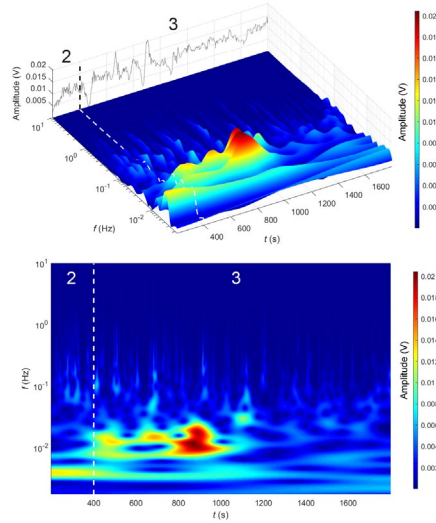


**Figure SI 3.8** CWT spectrum of the EPN signal for the global corrosion study on AA2024-T3 immersed in 0.05 M NaCl between  $t=200$  s and  $t=1800$  s.

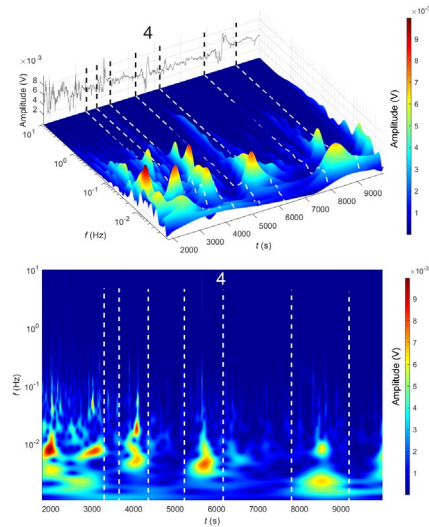


**Figure SI 3.9** CWT spectrum of the EPN signal for the global corrosion study on AA2024-T3 immersed in 0.05 M NaCl between  $t=1800$  s and  $t=10000$  s.

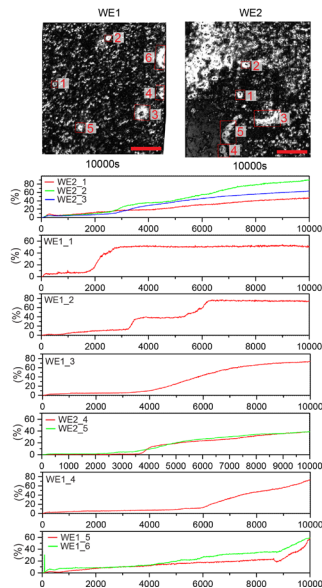


**Figure SI 3.10** Optical results for AA2024-T3 immersed in 0.05 M NaCl from  $t=0$  s to  $t=10000$  s, showing the analysed images for unchanged (black) and changed (white) pixels at  $t=10000$  s together the percentage of changed pixels at the indicated locations. Scale bar represents 0.5 mm.

## SI-3.4. Global Corrosion Study at 0.5 M

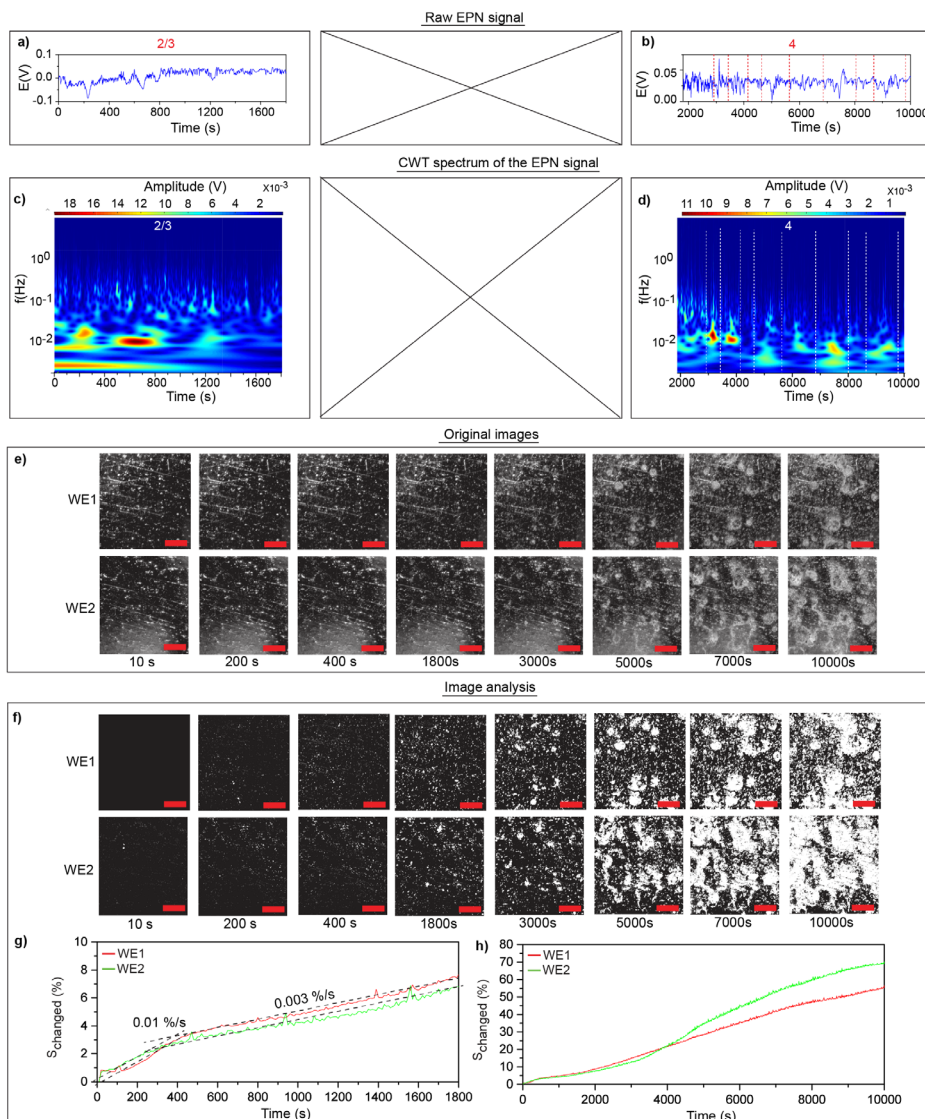


**Figure SI 3.11** Combined optical-electrochemical results for AA2024-T3 immersed in 0.5 M NaCl. 4a-b show the raw EPN signal and 4c-d show the CWT spectrum of the EPN signal for whole exposed surface at different immersion time periods of  $t=0-1800$  s and  $t=1800-10000$  s respectively. 4e-f show the real-time optical raw images (e), treated images (f) showing unchanged (black) and changed pixels (white) in time and the extracted quantitative information of the optically detectable surface changes for short (g) and long immersion times (h). Scalebar represents 0.5 mm.

### SI-3.5. Local corrosion study

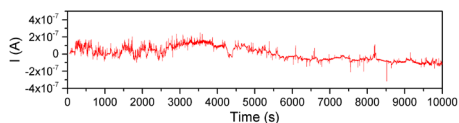


**Figure SI 3.12** raw current data for the local corrosion study on AA2024-T3 immersed in 0.05 M NaCl between  $t=0$  s and  $t=10,000$  s.

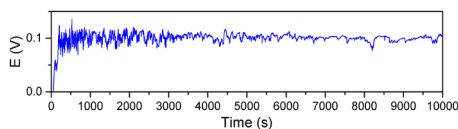


**Figure SI 3.13** raw potential data for the local corrosion study on AA2024-T3 immersed in 0.05 M NaCl between  $t=0$  s and  $t=10,000$  s.

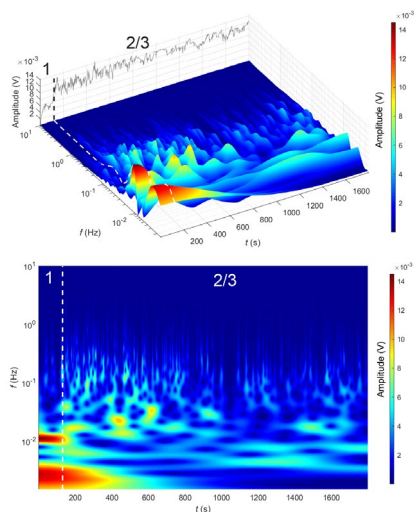


**Figure SI 3.14** CWT spectrum of the EPN signal for the local study on AA2024-T3 immersed in 0.05 M NaCl between  $t=0$  s and  $t=1800$  s.

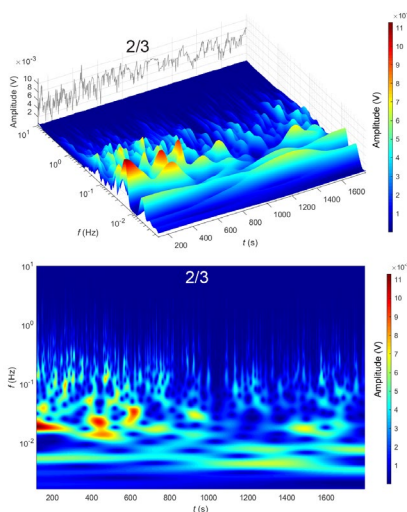


**Figure SI 3.15** CWT spectrum of the EPN signal for the local study on AA2024-T3 immersed in 0.05 M NaCl between  $t=120$  s and  $t=1800$  s.

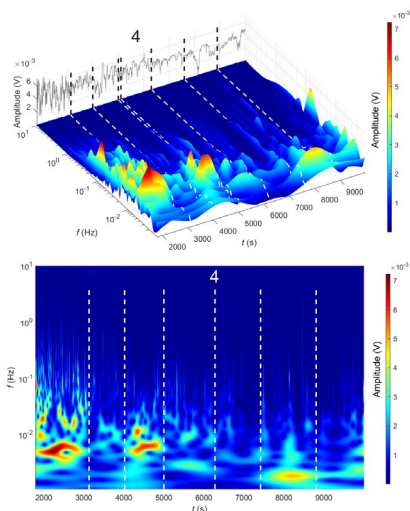


**Figure SI 3.16** CWT spectrum of the EPN signal for the local study on AA2024-T3 immersed in 0.05 M NaCl between  $t=1800$  s and  $t=10,000$  s.

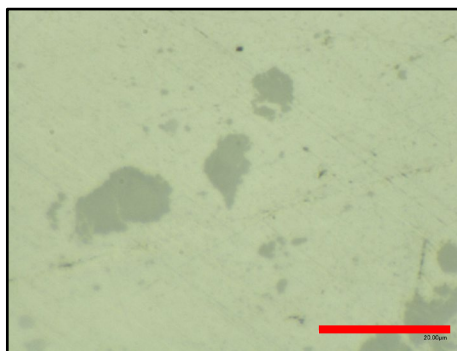


**Figure SI 3.17** Polished AA2024-T3 before immersion. Scale bar represents 20  $\mu\text{m}$ .

# 4

## **Cerium-loaded algae exoskeletons for active corrosion protection of coated AA2024-T3**

*The use of micron sized nanoporous diatom algae exoskeletons for inhibitor storage and sustained corrosion protection of coated aluminium structures upon damage is presented. In this concept the algae exoskeleton allows local inhibitor loading, limits the interaction between the cerium and the epoxy/amine coating and allows for diffusion-controlled release of the inhibitor when needed. The inhibitor release and corrosion protection by loaded exoskeletons was evaluated by UV/Vis spectrometry, a home-built optical-electrochemical setup, and Raman spectroscopy. Although this concept has been proven for a cerium-epoxy-aluminium alloy system the main underlying principle can be extrapolated to other inhibitor-coating-metal systems*

This chapter has been published as:

P. J. Denissen, S. J. Garcia, Cerium-loaded algae exoskeletons for active corrosion protection of coated AA2024-T3, Corrosion Science, 2017.

## 4.1. Introduction

Two of the major challenges faced by scientists replacing toxic and carcinogenic hexavalent chromium (CrVI)-based corrosion inhibitors by environmentally friendly ones are (i) the reduction of the negative inhibitor-coating matrix interactions that limit the new inhibitors efficiency, and (ii) the control over the release of the inhibitor in time.<sup>1</sup> For this reason several encapsulation methods have been proposed in the last decade. The most common and successful concepts use 2 dimensional (2D) inorganic nanoparticles (e.g. montmorillonites,<sup>2</sup> bentonites<sup>3</sup> and hydrotalcites<sup>4</sup>) and since more recently 3 dimensional (3D) inorganic nanocarriers (e.g. zeolite<sup>5,6</sup> and halloysites<sup>7</sup>). Such carriers allow controlling the inhibitor release by different mechanisms (e.g. diffusion, pH, redox, ion exchange) while at the same time prevent unwanted inhibitor reactions with the surrounding polymer matrix and too fast inhibitor release leading to blistering.<sup>1</sup> Despite the significant progress and reported evidence for nanocarriers yielding protection of small damages (<100  $\mu\text{m}$  width scratches) for short periods of immersion time, their long-term protection of relatively large damages is constantly under question. This, together with their limited versatility, often synthesis complexity and insufficient local release capacity motivates the constant search for alternatives. In this work we introduce the use of diatom algae exoskeletons as carriers for corrosion inhibitors allowing lower inhibitor-matrix interactions, high local inhibitor storage and time-based release leading to sustained protection at damaged coated metals under immersion in salt solution.

Diatoms are a major group of unicellular algae with the unique feature of forming highly ordered hollow nanoporous silica exoskeletons (named frustules). Each of the estimated 100.000 extant species as well as the species found as mineral (diatomaceous earth) has a distinctive frustule (typically two symmetric sides hold together) which varies in size (from 2  $\mu\text{m}$  to 4 mm), shape (star, cylinder, disk, oval, etc) and nanopore distribution and size.<sup>8</sup> For their characteristics the diatom exoskeletons are described as forming “pill-box” structures.<sup>9</sup> The availability, morphological characteristics and potential application of the bio-based diatom exoskeletons as carriers has recently attracted significant attention in the biomedical field where their use as drug delivery systems in fluid media has been studied.<sup>10–18</sup> Nevertheless, to the best of our knowledge, no dedicated studies of such silica based structures for corrosion inhibition have been reported in the scientific literature.

The proof of concept is here demonstrated for an epoxy-amine coating on an aerospace aluminium alloy AA2024-T3 system. Cerium nitrate was used as the model corrosion inhibitor for two reasons: (i) trivalent cerium ( $\text{Ce}^{3+}$ ) ions are known for being excellent corrosion inhibitors in copper-rich aluminium alloys as AA2024-T3, and (ii) the industrial application of cerium containing inhibitors is highly limited by its reactivity with the surrounding coating matrix.<sup>19,20</sup> Cerium nitrate was here stored into refined diatomaceous earth (DE) and its loading, release kinetics and corrosion inhibition efficiency of bare AA2024-T3 in salt solution studied

by real-time UV/VIS spectroscopy, scanning electron microscopy (SEM), energy-dispersive X-ray spectroscopy (EDS) and Raman spectroscopy. The active corrosion protection of the cerium-loaded DE particles (Ce-DE) was then evaluated in a particle-loaded epoxy coating by a home-made in-situ optical-electrochemical setup after creating highly controlled scratches of 130  $\mu\text{m}$  width at the bottom of the scratch. The results obtained are compared to those obtained for an unloaded epoxy coating and two epoxy coatings directly loaded with cerium nitrate and potassium dichromate respectively. Although potassium dichromate is not typically used in coating systems due to its high solubility leading to blistering, the very fast action and high efficiency to protect large damages after short immersion times makes it a very useful model inhibitor to compare to and was therefore used in this study. The in-situ optical-electrochemical approach allowed obtaining real-time optical and electrochemical information on the corrosion/protection processes. This approach decreased the subjectivity and difficulty of interpreting traditional electrochemical signals of damaged corrosion inhibiting coatings. The analysis of the results showed a significant delay of the on-set and kinetics of the degradation process when the Ce-DE were used compared to the protection achieved by the direct addition of cerium nitrate to the coating. The role of the cerium ions on the corrosion inhibition was further confirmed by a post-mortem analysis of the damaged site by SEM-EDS and Raman spectroscopy. While the protection offered by the inhibiting species was detected with both techniques, the higher spatial resolution of the Raman signal at the scratch gained additional information on the interaction between cerium species and copper-rich intermetallic phases. The results here presented prove the high potential of the use of diatom exoskeletons to encapsulate corrosion inhibitors to avoid coating-inhibitor negative interactions and improve active corrosion protection in coated systems.

## 4.2. Materials and Preparation

Diatomaceous earth Diafil 525 mainly consisting of cylinder shaped diatom exoskeletons was supplied by Profiltra Customized Solutions (The Netherlands, NL). The as-received diatomaceous earth consists of 89.0 wt. % amorphous silica ( $\text{SiO}_2$ ), a tapped powder bulk density of  $0.42 \text{ g/cm}^3$  and a mean particle size of  $12 \mu\text{m}$ . Cerium nitrate hexahydrate ( $\text{Ce}(\text{NO}_3)_3 \cdot 6\text{H}_2\text{O}$ ) and Potassium dichromate ( $\text{K}_2\text{Cr}_2\text{O}_7$ ) with >99 % purity were purchased from Sigma-Aldrich. Commercial 2 mm thick bare AA2024-T3 sheet obtained from Kaizer Aluminium was used as metallic substrate. Commercially available bisphenol-A based epoxy resin (Epikote™ 828) and amine crosslinker (Ancamine®2500) were supplied by AkzoNobel (NL) and used as received to form the coating binder.<sup>21</sup> Xylene with a purity of 99 % was used as epoxy solvent. All aqueous solutions for the particle doping, corrosion and release studies were prepared using Milipore® Elix 3 UV filtered water.

### 4.2.1. Refined diatomaceous earth (DE)

In order maximize the amount of intact diatom exoskeletons and reduce the impurities content (i.e. non-silica) a refining process was applied based on the work of Zhang et al.<sup>22</sup> Figure 4.1 shows the schematic illustration of the refining process whereby 8.0 g of as-received diatomaceous earth was suspended in 120 ml demineralized water and sonicated for 30 min. This was left in unstirred condition for 30 min to allow the silica intact exoskeletons to settle down. The supernatant (containing the impurities and small diatom parts) was discarded with the help of a glass pipette. This settling process was repeated 5 times (without sonication). Finally the settled particles were filtered using a Whatman® grade 595 paper filter and dried in a vacuum oven at  $60 \text{ }^\circ\text{C}$  for 24 h. The refined diatomaceous earth, named DE for simplicity across the manuscript, was used in the rest of the study as the corrosion inhibitor carrier.

### 4.2.2. DE doping with cerium nitrate

For the doping procedure as illustrated in Figure 4.2, a powder mixture of 0.85 g refined DE and 0.15 g cerium nitrate hexahydrate was added to 2.0 ml demineralized water. The mixture was then placed on a shaking table at 320 rpm for 24 h followed by complete drying in an oven at  $80 \text{ }^\circ\text{C}$  under ambient atmosphere for another 24 h. As a result of the process a DE powder containing 15 wt. % of cerium nitrate was obtained. The loaded powder was then screened through a stainless steel sieve of  $50 \mu\text{m}$  aperture to reduce agglomerates and conform the here on called cerium-doped DE (Ce-DE).

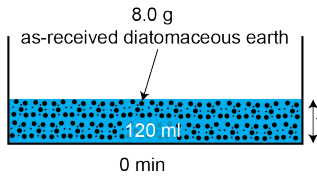


**Figure 4.1** schematic illustration of the refining process of the diatomaceous earth.

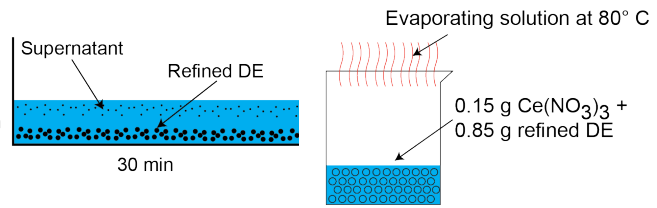


**Figure 4.2** schematic illustration of the DE doping process leading to Ce-DE particles.

### 4.2.3. Coatings preparation

The AA2024-T3 metal sheets were cut into pieces of 25x50 mm prior to surface modification and coating application. The metal surface preparation followed previously reported procedures<sup>6</sup> consisting of the following sequential steps: (i) removal of native oxide layer and surface chemistry homogenization using SiC sandpapers down to grit 320; (ii) surface roughness formation by Scotch Brite 3M “Clean N Finish grade AVFN”; (iii) degreasing with acetone; and (iv) immersion in a 2M sodium hydroxide (NaOH) aqueous solution for 10 seconds followed by rinsing with distilled water and air drying in order to increase the surface hydroxide (OH) fraction and therefore adhesion with the subsequent organic coating.

The organic coatings were prepared using a mixture of Epikote™ 828, Ancamine®2500 and Xylene (2.70:1.57:1 weight ratio) as reported elsewhere.<sup>21</sup> Five coating systems (named Epoxy, DE, Ce, Ce-DE and Cr) were formulated as summarized in Table 4.1.

**Table 4.1** overview of the coatings compositions, sample coding and relevant coating parameters.

| Sample Coding | Particle content (wt. %) <sup>1</sup> | Thickness (μm) | PVC (%) | Active inhibitor content (moles/kg binder) |
|---------------|---------------------------------------|----------------|---------|--|
| <b>Epoxy</b>  | 0 <sup>2</sup>                        | 110±20         | 0       | 0  |
| <b>DE</b>     | 12 <sup>3</sup>                       | 80±20          | 25      | 0  |
| <b>Ce</b>     | 2 <sup>4</sup>                        | 80±20          | 0.5     | 0.04                                       |
| <b>Ce-DE</b>  | 14 <sup>5</sup>                       | 110±20         | 25      | 0.04                                       |
| <b>Cr</b>     | 2 <sup>6</sup>                        | 100±20         | 0.8     | 0.06                                       |

<sup>1</sup>  $M_{\text{inhibiting particles}} / M_{\text{epoxy-amine coating}}$ ; where M is mass.

<sup>2</sup> coating Epoxy contains no particles (epoxy-amine clear-coat)

<sup>3</sup> coating DE contains 12 wt.% refined diatomaceous earth (DE) particles

<sup>4</sup> coating Ce contains 2 wt.% cerium nitrate hexahydrate ( $\text{Ce}(\text{NO}_3)_3 \cdot 6\text{H}_2\text{O}$ )

<sup>5</sup> coating Ce-DE contains 14 wt.% refined diatomaceous earth (DE) doped with cerium nitrate hexahydrate ( $\text{Ce}(\text{NO}_3)_3 \cdot 6\text{H}_2\text{O}$ )

<sup>6</sup> coating Cr contains 2 wt.% potassium dichromate ( $\text{K}_2\text{Cr}_2\text{O}_7$ )

In all cases the epoxy-amine-xylene mixture was first high-shear mixed for 5 minutes at 2500 rpm in a high-speed mixer. In order to reduce possible side reactions with the epoxy/amine matrix the mixtures were then let pre-cure at ambient conditions for 30 min before the corrosion inhibiting components (cerium nitrate powder, DE, Ce-DE or potassium dichromate) were added. The mixtures were then manually stirred to form a homogeneous mixture, applied on the AA2024-T3 coupons by a 100  $\mu\text{m}$  spiral bar coater and cured at 60°C for 24 h as reported elsewhere to achieve complete crosslinking.<sup>6</sup> After curing the coated panels were stored in a desiccator until 30 min before testing. The final pigment volume concentration (PVC) in the dry coatings was calculated using equation (4.1).

$$PVC(\%) = \frac{V_{inhibitor} + V_{DE}}{V_{inhibitor} + V_{DE} + V_{epoxy/amine}} * 100\% \quad (4.1)$$

Where  $V_{inhibitor}$  is the volume of cerium nitrate powder,  $V_{DE}$  is the volume of refined DE, and  $V_{epoxy/amine}$  is the volume of the epoxy-amine binder in the system. It should be noted that the amount of active species in weight was kept constant as shown in Table 4.1, resulting in a lower molar content of cerium compared to the molar content of chromium calculated as shown in the supporting information (SI-4.1).

#### 4.2.4. Scratch damage in coated metals for corrosion inhibition evaluation

Reproducible and controlled 5 mm long and 130  $\mu\text{m}$  wide scratches (at the bottom of the scratch) were created on the coated panels with a CSM Microscratch tester using a 100  $\mu\text{m}$  Rockwell C diamond tip in multi-pass mode. For this, the tip was programmed to give 5 passes at each load of 5N, 10N and 15N at the same location until the AA2024-T3 substrate was reached.

### 4.3. Testing Methods and Equipment

#### 4.3.1. Diatomaceous earth particle analysis

A JEOL SJM-840 scanning electron microscope coupled with energy dispersive X-ray spectroscopy (SEM-EDS) was used to analyse the topological and elemental composition of the diatomaceous earth powders. Images were recorded at 5 kV accelerating voltage. Samples were coated with a 15 nm gold layer before SEM examination.

A Malvern Mastersizer 2000 particle size distribution analyser (PSD) was used to evaluate the effect of the refining process of the as-received diatomaceous earth. The effect of the cerium doping on the crystalline structure of the exoskeletons was monitored with a Bruker D8 advanced X-ray diffractometer (XRD) using Cu-K $\alpha$  radiation ( $\lambda=1.54\text{\AA}$ ) with scattering angles ( $2\theta$ ) of 5-130 $^\circ$ .

#### 4.3.2. Real-time inhibitor release from DE carrier

Cerium inhibitor release was studied in real immersion time with a PerkinElmer LAMBDA 35 UV/VIS spectrometer. For the real-time release studies the UV/VIS cuvette was modified as shown in the S.I. (Figure SI 4.1) allowing for measurements without the need of aliquot extraction. Samples containing Ce(NO<sub>3</sub>)<sub>3</sub> salt and Ce-doped DE were placed inside a cone-shaped Whatman<sup>®</sup> grade 1 paper filter on top of the cuvette filled with demineralized water. UV-Vis spectra were taken every second. In order to ensure an even inhibitor dispersion in the cuvette and to avoid false measurements the solution was constantly magnetically stirred at 1400 rpm. Both samples were analysed in threefold. Cerium inhibitor release was followed by the variation in the 252 nm wavelength signal corresponding to Ce III as shown in the S.I. (Figure SI 4.2) and reported in literature.<sup>23,24</sup> For the inhibitor concentration quantification from the UV signal a linear calibration curve was constructed with an R<sup>2</sup> of 0.999 over 10 predefined inhibitor concentrations in the range 10<sup>-3</sup> M to 10<sup>-5</sup> M, as shown in the S.I (Figure SI 4.3). The UV/VIS calibration curve was validated with a PerkinElmer Optima 3000DV inductively coupled plasma analyser (ICP). An acceptable margin of error on the final cerium concentration of around 10 % was measured probably due to small weighting variations and hygroscopic effect of the cerium nitrate.

#### 4.3.3. In-situ optical-electrochemical set-up (corrosion protection studies)

The corrosion protection behaviour of the scratched coatings was monitored with a home-built in-situ optical-electrochemical set-up during immersion in 0.05 M sodium chloride (NaCl) aqueous solution. A minimum of two repeats per coating system was performed. The set-up consisted of a three-electrode electrochemical cell coupled to a microscope camera allowing for real-time electrochemical and surface optical analysis at the damaged site. A schematic

illustration of the set-up is shown in Figure 4.3 and a photo of the set up for more clarity can be found the S.I. (Figure SI 4.4).

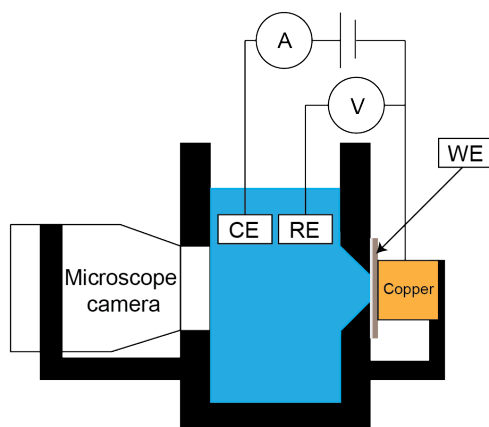


**Figure 4.3** schematic illustration of the optical-electrochemical set-up used in the study. The microscope camera is visible on the left hand of the image and the analysed sample (working electrode) on the right hand.

A potentiostat Metrohm PGSTAT 302 and a universal serial bus (USB) Celestron handheld digital microscope camera with 1.2 megapixel (Mpx) resolution were used for the electrochemical tests and optical monitoring respectively. The coated sample was placed vertically in the electrochemical cell by clamping it with a copper block to a hole made on one side of the electrochemical cell as reported elsewhere.<sup>25</sup> Opposite to the studied sample, a hole closed with a transparent Plexiglas window allowed aligning the handheld digital microscope to the exposed sample thereby optically monitoring the immersed sample. Both the camera and the three-electrode electrochemical cell were placed inside a Faraday cage to avoid external interferences. During immersion Electrochemical Impedance Spectroscopy (EIS) and Open Circuit Potential (OCP) measurements were performed. The three-electrode electrochemical cell consisted of a silver/silver-chloride (Ag/AgCl) reference electrode (RE), 6.6 mm diameter graphite rod as counter electrode (CE) and the coated and damaged AA2024-T3 samples as working electrode (WE). The frequency range of study was  $10^5$ - $10^{-2}$  Hz, with applied amplitude of 10 mV root mean square (RMS) over OCP to minimize the influence of the test on the metal-coating system while still obtaining a reliable response. The potentiostat was controlled with a USB interface through the software package NOVA V1.11.1.

The microscope camera and the potentiostat were programmed to take an optical image and an EIS measurement every hour so that the optical images correspond to the moment of the EIS analysis. It should be here noted that all the relevant surface variations were found within a 0.9 mm lateral distance from the centre of the scratch as well as from scratch ends as shown in the S.I. (Figure SI 4.5). The absence of optical variations outside that area confirmed the good barrier

properties of the coatings during the studied immersion time. The optical images were then converted to 8-bit greyscale files and processed with the use of ImageJ free software as shown in in the S.I. (Figure SI 4.6-4.10). Once the images were converted to 8-bit, the lighter background corresponding to the undamaged area was removed using a bimodal threshold method. The increase of the dark area over time with reference to the initial dark areas is caused by the degradation of the system ( $\Delta A_{\text{degraded}}$ ) and can be calculated using equation (4.2):

$$\Delta A_{\text{degraded}}(\%) = \frac{A_t - A_0}{A_s} * 100\% \quad (4.2)$$

Where  $A_t$  is the increased dark area (degraded area) at time  $t$ ,  $A_0$  the initial dark area (e.g. caused by scratch) and  $A_s$  the total studied area of 12 mm<sup>2</sup>.

#### 4.3.4. Cerium interaction with the exposed AA2024-T3 metal surface

In order to confirm the involvement of cerium in the active corrosion protection at damage sites both SEM-EDS and Raman spectroscopy analysis were performed at the bottom of the scribe (i.e. metal surface) of the damaged coated samples used in the optical-electrochemical study. For the Raman analysis a Renishaw inVia reflex microscope equipped with a research-grade Leica microscope objective at 50 $\times$  magnification and numerical aperture of 0.55 was used. A 532-nm laser light with an effective laser power of 32mW in 1 second excitation measurements was employed. Control tests were performed on a copper block, cerium oxide precipitates, and on bare AA2024-T3 exposed to inhibited and non-inhibiting solutions, which are included in the support information.

## 4.4. Results and Discussion

### 4.4.1. Particle characterization

Figure 4.4 shows a set of SEM images and EDS spectra of the diatom exoskeletons before (4a and 4c) and after (4b and 4c) the refining process. Figure 4.4 shows the effect of the refining process on the particle size distribution. From the SEM images it becomes clear that the refining process significantly reduced the amount of broken diatoms and other impurities of the as received diatomaceous earth as intended.

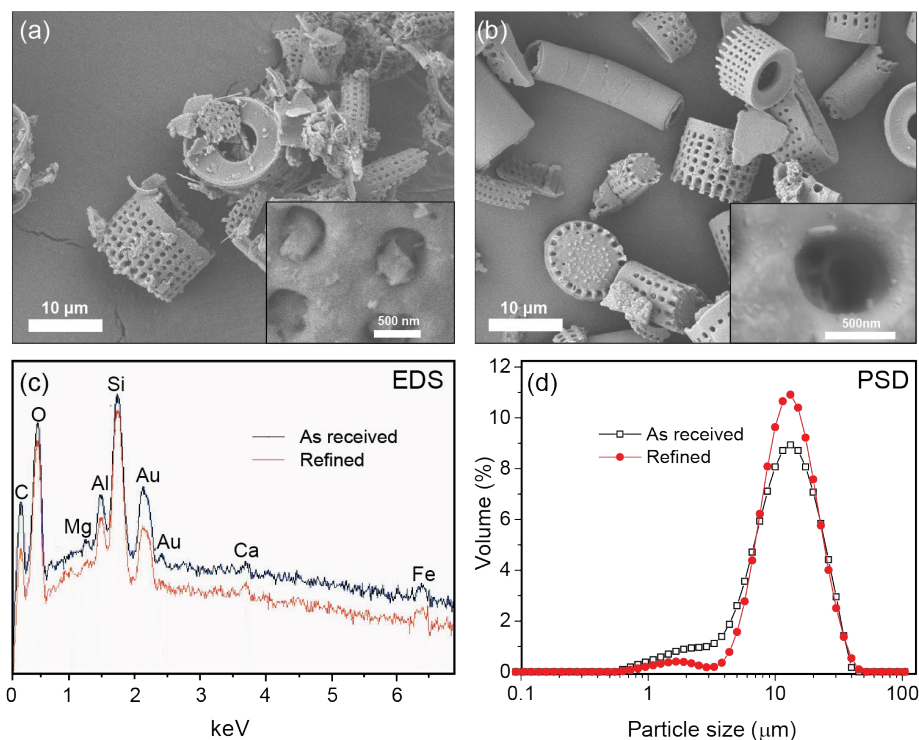


**Figure 4.4** SEM images of diatom exoskeletons and their open porous structure (insets) for as-received (a) and refined (b) diatomaceous earth. Energy dispersive spectroscopy (EDS) spectrum and particle size distribution of the two samples are shown in (c) and (d) respectively.

The SEM inserts in Figure 4.4a and Figure 4.4b further confirm the removal of very small particles blocking the nano-pores in the as-received exoskeletons. The particle size analysis showed a near Gaussian-shaped size distribution with an increased peak centred at 12  $\mu\text{m}$  (Figure 4.4d) as well as a drop of the small fraction particles after the refining process. A detailed SEM image analysis of the refined diatomaceous earth (DE) allowed recognising exoskeletons of four clearly different diatom species whereby the, by far, most abundant one was identified as *sp.*

*Aulacoseira* with exoskeletons similar to those reported in literature having a cylindrical pill-box structure with nanopores of around 500nm evenly distributed around the exoskeleton wall.<sup>11</sup>

EDS analysis (Figure 4.4c) was used to determine the effect of the refining process on the removal of the chemical species other than the silica of the diatom shell. Figure 4.4c shows the predominance of silicon (Si) and oxygen (O) constituents as expected for diatom silica ( $\text{SiO}_2$ ) exoskeletons. Small traces of aluminium (Al), Iron (Fe), Calcium (Ca) and Magnesium (Mg) were also detected and assigned to impurity oxides ( $\text{Al}_2\text{O}_3$ ,  $\text{Fe}_2\text{O}_3$ ,  $\text{CaCO}_3$ ,  $\text{CaO}$ , and  $\text{MgO}$ ) as reported in previous studies.<sup>12</sup> The presence of the same constituent elements in the refined diatomaceous earth as in the as received ones revealed that the refining process used was not capable of removing, at least not fully, the oxide impurities. The presence of the impurities in the clean DE did nevertheless not have an effect on the ulterior cerium doping when the doping procedure proposed in this work was employed. This was proven by a further study on the chemical treatments of the DE with alkali and acidic solutions leading to the disappearance of the impurity oxides but no significant difference in the Ce-uptake as shown in the S.I (Figure SI 4.11 and S12; section 4.4). As the impurities did not have a significant effect in the doping it was decided to skip the acid and alkali post-treatments to simplify the process.

Diatom exoskeleton loading with corrosion inhibitors was confirmed by SEM and XRD analysis (Figure 4.5).

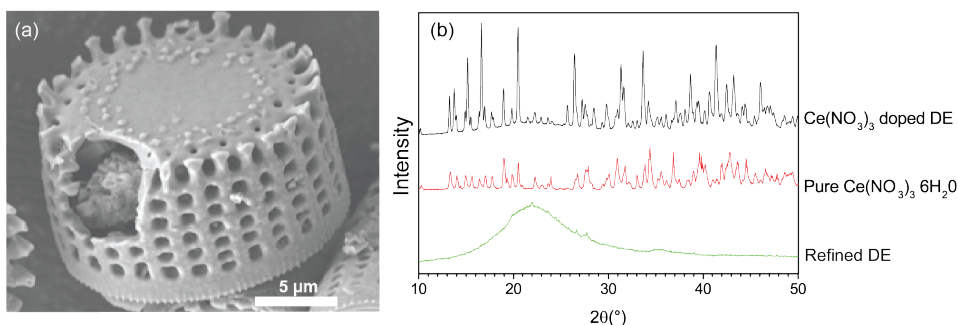


**Figure 4.5** (a) SEM image of a single fractured diatom exoskeleton after corrosion inhibitor. (b) Comparative XRD spectra of refined DE,  $\text{Ce}(\text{NO}_3)_3 \cdot 6\text{H}_2\text{O}$  corrosion inhibitor salt, and Ce-DE.

The XRD spectra in Figure 4.5b show that the DE (refined diatomaceous earth) primarily consisted of amorphous silica with some minor diffraction peaks at  $22.0^\circ$  and  $26.6^\circ$  corresponding to crystalline structures of quartz and cristobalite. The XRD spectra for the Ce-DE (cerium doped DE) shows the amorphous silica baseline combined with crystalline peaks corresponding to  $\text{Ce}(\text{NO}_3)_3$ . The increased intensity of the peaks compared to pure  $\text{Ce}(\text{NO}_3)_3 \cdot 6\text{H}_2\text{O}$  is presumably caused by the decrease of water in the crystal lattice due to drying and localized deposition on the diatom silica surface. The results confirm that, during the doping

process, the cerium inhibitor did not change its crystalline structure and remained as an inorganic salt primarily inside the diatom exoskeletons body space and nanopores, thereby confirming the success of the developed doping procedure.

Figure 4.6 shows the difference in the release behaviour (dissolution and diffusion) of the  $\text{Ce}(\text{NO}_3)_3$  salt directly placed in the paper filter of the UV-Vis system as shown in the S.I. (Figure SI 4.1) and that of the cerium salt contained in the Ce-DE particles.

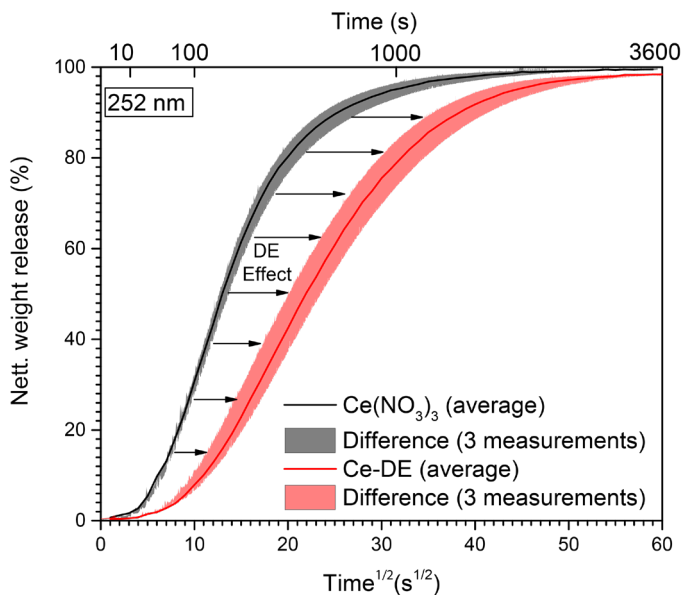


**Figure 4.6** cerium release kinetics of cerium nitrate from the salt powder (black) and from cerium-loaded DE particles (Ce-DE) (red) obtained with a real-time UV/VIS spectroscopy from the 252nm wavelength.

By analysing the release plots it can be seen that the inhibitor is fully dissolved after one hour in both cases, which is in line with the diffusion coefficients of the ionic species in aqueous media.<sup>26</sup> The release response for both systems is comparable whereby the release at the beginning increases exponentially due to the high solubility of  $\text{Ce}(\text{NO}_3)_3$  and ends asymptotically due to the equal distribution of  $\text{Ce}(\text{NO}_3)_3$  in the UV/VIS cuvette. Interestingly, the release curve for the Ce-DE particles is slower than that of the cerium salt over the entire time domain. Such a delay can be attributed to the chemical or topological trapping of the cerium included in the DE exoskeleton structure together with the delay due to diffusion through the porous walls of the diatom exoskeletons. Furthermore, the increasing separation in time between the two release curves plotted against  $t^{1/2}$  shows the entire release spectrum of Ce from DE is delayed between 10 and  $10^3$  seconds with respect to the cerium salt in the filter. These results confirmed that the cerium inhibitor loaded in the DE structure was able to come out by a time diffusion controlled process in aqueous solution as intended.

The active corrosion protection by the release of cerium from the Ce-DE particles in solution was studied by a detailed SEM/EDS and Raman study on bare AA2024-T3 immersed in 0.05 M NaCl solutions (SI.; section 4.5 Figure SI 4.13 and section 4.6 Figure SI 4.14-4.17 respectively). Despite the delay with respect to the salt observed with UV-VIs, the results confirmed that the cerium is released from the DE particles at a sufficient rate to prevent local corrosion by the formation of protective cerium precipitates at copper-rich phases.

#### 4.4.2. Inhibitor-loaded particle/epoxy coating interaction

The presence of cerium inhibitor in the coating matrix and a validation of its active state when Ce-DE particles were used was monitored by SEM and colour changes (yellowing). Figure 4.7 shows the SEM-EDS micrograph of a fractured epoxy coating containing Ce-DE particles. The fractured plane shows a DE cylindrical particle (from the top) embedded in the epoxy matrix. The EDS analysis further confirmed the presence of high cerium concentrations inside the exoskeleton with a low carbon signal of the polymeric matrix. This confirms that the cerium inhibitor remained in the inner volume of the DE during the particle mixing with the epoxy coating and is therefore available for local release as intended.

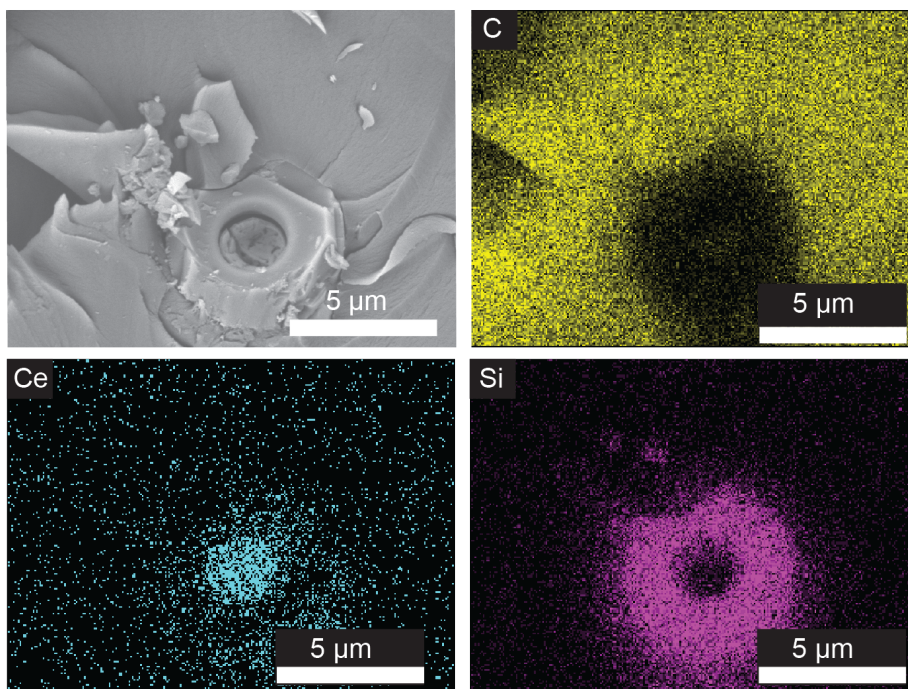


**Figure 4.7** SEM and EDS micrographs for C, Ce and Si of the fractured plane of an epoxy coating loaded with Ce-DE. The SEM/EDS analysis confirms the presence of high Ce-concentrations in the diatom frustule after mixing with the epoxy-amine coating.

When the coatings were prepared a fast deep yellowing was observed in the case of the Ce coating (Cerium nitrate salt directly added to the epoxy-amine coating). This yellowing can be seen in the S.I. (Section 7; Figure SI 4.18) when the amine was added directly to the cerium nitrate salt after one hour (Figure SI 4.18a, b). Such yellowing has been well reported and indirectly attributed to the oxidation of Ce III to Ce IV by the amines.<sup>27–30</sup> Although this reaction does not lead to any significant changes in the overall mechanical properties of the epoxy-amine matrix it has been reported as one of the factors leading to lower inhibition efficiencies than expected in Ce-rich epoxy coatings.<sup>29</sup> A reduction in the yellowing is therefore desired as it indicates a lower matrix-inhibitor reaction and therefore an increase of the expected inhibition power in the Ce-loaded coating systems. When the amine was added to the Ce-DE particles (Figure SI 4.18c and d) a significant decrease in the yellowing was observed during the 1 h test. Such a result is in agreement with the intended isolation of the Cerium inhibitor from the epoxy-amine matrix by means of the silica diatom exoskeleton thereby leaving higher amounts of Ce III available in the interior of the particles ready to act as corrosion inhibitors.

### 4.4.3. Corrosion protection of damaged coatings

Figure 4.8 shows selected EIS Bode plots ( $|Z|$  and phase) for the scratched coatings after 3 h (8a and 8c) and 90 h (8b and 8d) immersion.

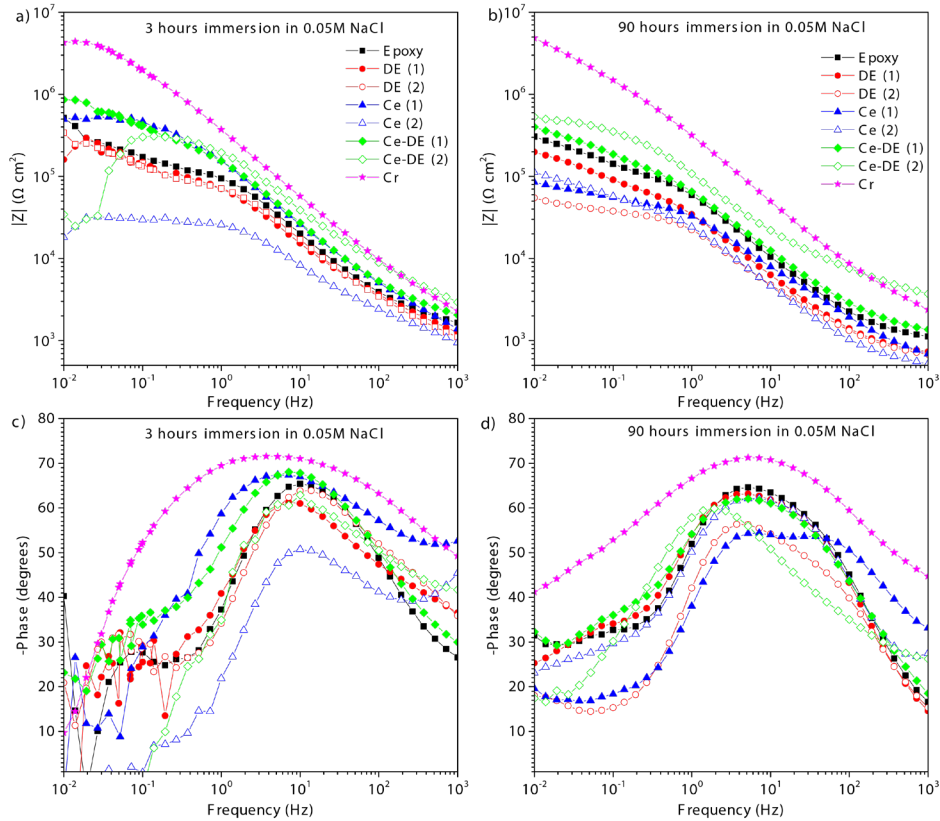


**Figure 4.8** bode plots showing the total impedance (a and b ) and phase (c and d) EIS plots for the coatings (1x Epoxy, 2x DE, 2x Ce, 2x Ce-DE and 1x Cr) after 3 h (a and b) and 90 h (c and d) immersion in 0.05 M NaCl.

At 3 h immersion it becomes clear that the Cr coating shows the highest total impedance ( $|Z|$ ) and phase shift of all coatings, particularly in the low frequency range. Such high impedance in the Cr coating indicates a fast active corrosion protection due to the inhibitor high solubility and its high inhibiting power. On the other hand, the observed instabilities for the other coatings at short immersion times highlight the high activity at the scribe. After 90 h of immersion all coating systems are more stable and differences amongst them become more clear. Three coatings showed a total impedance increase from 3 h to 90 h: Cr, CE (2) and Ce-DE (2). Although the increase over time is often used to confirm sufficiently protecting systems,<sup>31</sup> it remains unlikely to be the case for Ce (2) due to its lower initial and final total impedance value compared to the non-inhibiting Epoxy reference coating. On the other hand, the Cr and the two Ce-DE

coatings show higher total impedance values than the Epoxy, DE and Ce coatings. Such higher impedance and the absence of clear signs in the phase related to pit formation seem to suggest an active corrosion protection in the case of the Cr and Ce-DE systems. Due to the complexity of the degradation processes at and around the scribes impedance analysis are generally complemented with other post-mortem studies. Yet this allows only to identify the final degradation state and not to undoubtedly relate impedance observations with degradation processes. To gain more information of the on-going degradation in time the optical images during the electrochemical measurements were analysed with the optical-electrochemical setup described in the experimental section and the support information.

Figure 4.9 shows selected optical microscopy images of the scratched coatings after 3 h and 90 h of immersion taken during the electrochemical measurements.

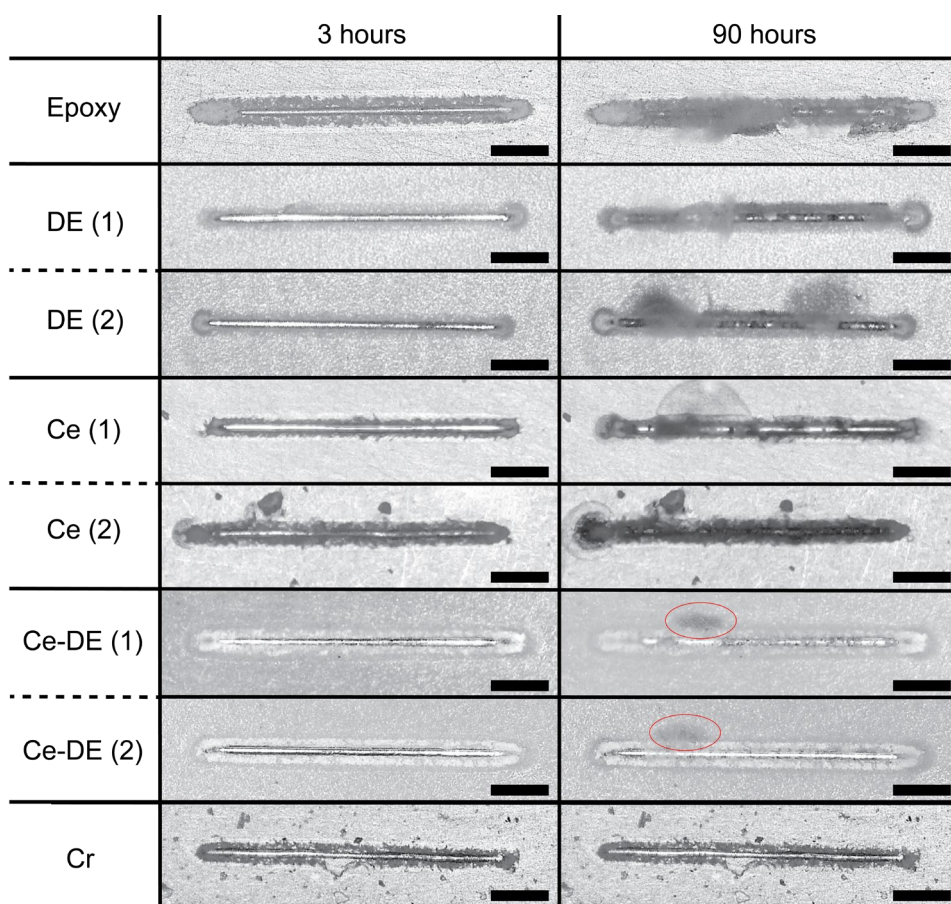


**Figure 4.9** optical microscopy images obtained with the optical-electrochemical setup for the coatings (1x Epoxy, 2x DE, 2x Ce, 2x Ce-DE and 1x Cr) after 3 and 90 h immersion in 0.05 M NaCl. The red oval in the Ce-DE marks the formation and development of a dark area under the Ce-DE coating.

The formation of delaminated areas, corrosion products (grey “clouds”) and local corrosion sites (dark spots) can clearly be seen at the scribe of the non-inhibited coatings (Epoxy and DE). Similar features can be observed in the case of the Ce coatings (cerium salt added to the coating matrix) although up to a minor extent. These optical observations point at the low or non-corrosion protection offered by the Epoxy, DE and Ce coatings. On the other hand, both Ce-DE coatings and the Chromium containing coating (Cr) do not show significant variations with the immersion time at the scribe, which remains bright in both cases, thereby indicating a clear active corrosion protection of the damaged site. For the two Ce-DE coatings a dark area under the coating appeared next to the scratch (indicated with the red oval in Figure 4.9). Interestingly, the two dark areas appeared at a similar location, are of about the same size, and they both grew slowly in size and colour intensity after their first appearance until stabilization. Although the degradation phenomenon that caused this process is not yet clear it seems clear that the process was somehow controlled by the inhibitors in the coating. The presence of these degradation areas could justify the relatively low impedance values of the Ce-DE coatings compared to the epoxy, DE and Ce coatings despite the clear bright scribes indicating no corrosion.

A dedicated image analysis of the images taken with the in-situ optical-electrochemical setup followed the EIS study. In the analysis the degraded area at and around the scratch with immersion time was calculated and represented by the parameter  $\Delta A_{\text{degraded}}$ . This parameter is obtained after a sequential image analysis of the micrographs by converting the images into grey scale, removing the lighter background and calculating the increase of the degraded area in time as explained in the experimental section and the support information. In this work the ‘degraded area’ is identified as darkening and is related to corrosion signs such as oxide formation, localized corrosion (e.g. pits) and delamination. When plotting the  $\Delta A_{\text{degraded}}$  parameter in % against the immersion time both the on-set time of the optically-detectable ‘degradation processes’ and the kinetics of the degradation process itself (slope after the on-set time) can be obtained. A more detailed description of the quantification process can be found in the S.I. (section 3). Figure 4.10 shows the degraded area around the scratch for the two DE, Ce and Ce-DE coatings. The two non-inhibiting DE coatings show a stable period with no visible degradation during the first 30 h followed by a fast propagation of the degraded area at similar kinetics of 0.13 and 0.20 % per hour. On the other hand in the Ce coatings first signs of degradation start short after immersion but grow at a much lower pace of 0.08 and 0.07 % per hour, thereby highlighting the moderate corrosion inhibiting effect of Ce. Based on the detail image analysis, the initial stable period seen in the DE coatings was attributed to a higher adhesion strength between the coating and the metal substrate compared to the Ce coatings. Such interphase improvement leads to a delay of the delamination on-set but not to a decrease in the delamination growth kinetics as there is no inhibiting effect, A different result was found for the Ce-DE inhibited samples. In this case, the samples remain stable with no visible degradation

during the first 70 h, at which some degradation is detected around the scribe (red oval in Figure 4.9) and propagate at a degradation growth kinetics of around 0.002 % per hour.

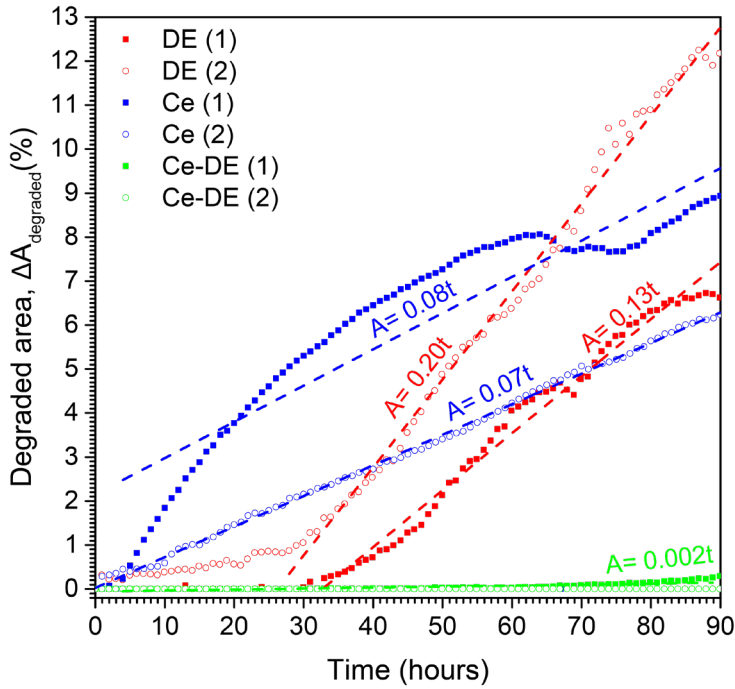


**Figure 4.10** optical variation of the degraded area ( $\Delta A_{\text{degraded}}$ ) including regressions after the on-set time obtained from the processed optical images for coating systems CE, DE and Ce-DE during immersion in 0.05 M NaCl.

In order to facilitate the reading of the impedance results in relation to degradation and protection Figure 4.11 was developed.

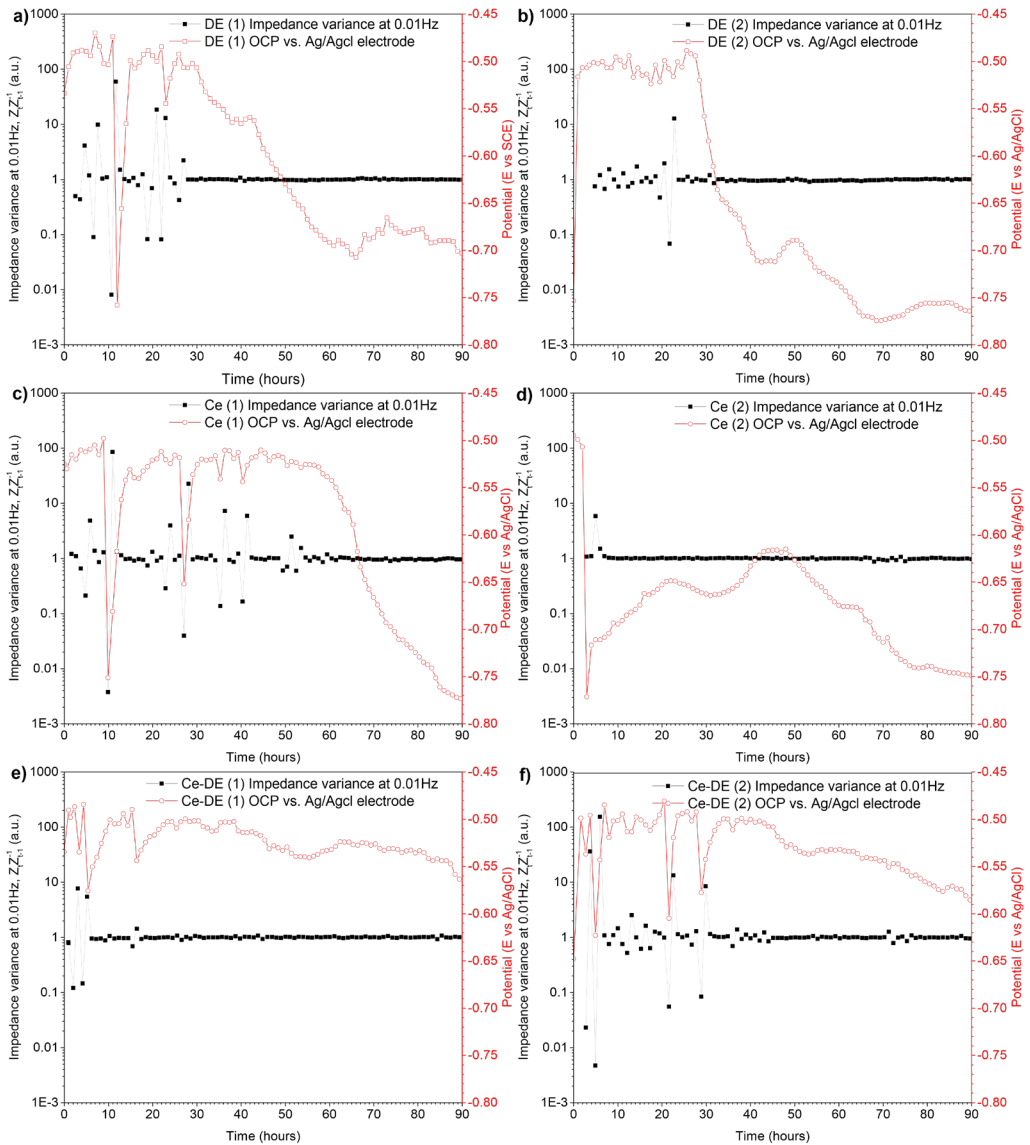


**Figure 4.11** Open circuit potential (OCP) and the impedance variance  $Z_t/Z_{t-1}$  at 0.01Hz evolving over time for (a) DE (1), (b) DE (2), (c) Ce (1), (d) Ce (2), (e) Ce-DE (1), and (f) Ce-DE (2).

In Figure 4.11 the variation of the total impedance at a given frequency (0.01 Hz) between two consecutive time measurements (i.e.  $Z_t/Z_{t-1}$ ) and the OCP are plot against immersion time. The normalizing of the impedance to the previous measurement was used to filter out possible effects of initial coating properties, delamination, and changes in barrier protection. Impedance at 0.01Hz and OCP time evolution were chosen for the comparison between samples as this frequency highlights the on-going processes at the metal surface related to corrosion or

protection phenomena<sup>32</sup> and the OCP also relates to delaminations and other underfilm corrosion processes.<sup>33,34</sup> Results for the variation in impedance obtained at other frequencies (e.g. 0.014 and 0.1 Hz) did not lead to trend or interpretation changes but show less enhanced signals as shown in the S.I. (Figure SI 4.24).

Figure 4.11a and Figure 4.11b show the impedance variation and OCP evolution over time for the two non-inhibited coatings DE (1) and DE (2), respectively. Both systems show instabilities and high impedance jumps during the first 27 h of immersion. Such a behaviour is in good agreement with initial local corrosion such as pitting, dealloying and replating processes typical observed on non-inhibited AA2024-T3.<sup>20</sup> After 30 h the impedance for both systems stabilize and the OCP dropped from -0.5 V until it reached a plateau at -0.7 V for coating DE (1) and -0.75 V for DE (2). This drop is in agreement with values reported in literature for dealloyed AA2024-T3<sup>20</sup> and is in agreement with the onset of delamination and underfilm corrosion optically observed and plot in Figure 4.10. Figure 4.11c and Figure 4.11d show the impedance variation and OCP evolution over time for the Ce containing coatings, Ce (1) and Ce (2), respectively. Ce (1) shows impedance instabilities until 60 h with two very strong impedance jump events at 10 and 27 h. These two impedance jumps are accompanied by a sudden drop in OCP followed by a slow recovery back to -0.5 V during the consecutive hours. This recovery can be related to the passivation of the metallic surface by cerium species (i.e. inhibiting event) as is not observed in non-inhibited samples. At 60 h (two times longer than the non-inhibited system) the impedance stabilizes and the OCP drops, indicating that the dealloying has been reduced but not stopped and that delaminations take place as can also be seen by the change in degradation kinetics shown in Figure 4.10 after 60 h. On the other hand, coating Ce (2) only shows one single instability after 3 h coupled to a sudden OCP drop down to -0.77 V, indicating a fast degradation and no (significant) inhibition effect of the contained cerium. This trend is also in good agreement with the high amount of corrosion attack visible in Figure 4.9 and the stable degradation kinetics in Figure 4.10 directly after immersion. The big differences between the two Ce coating systems clearly show that adding  $\text{Ce}(\text{NO}_3)_3$  salt pigments directly to the epoxy binder results in uncontrolled behaviour with high scatter in the level of corrosion protection achieved probably due to differences in inhibitor dispersion degree as well as reactivity of the cerium with the epoxy matrix as indicated by the strong yellowing of the coating. Figure 4.11e and Figure 4.11f show the impedance variation and OCP evolution over time for the coatings containing cerium doped DE particles, Ce-DE (1) and Ce-DE (2) respectively. In both cases the OCP remains between -0.5 V and -0.6 V over the whole exposure time. Sudden drops in OCP are again coupled to impedance instabilities which are slowly recovered with the immersion time. These trends are in agreement with the slow degradation growth kinetics of 0.002 % area increase per hour (Figure 4.10) as well as the absence of features related to abundant oxide formation (grey clouds) and local corrosion sites (dark spots) at the scribe observed in the other samples (Figure 4.9). When compared to the Ce-coating, the behaviour of

the Ce-DE coating suggests that the new encapsulation concept allowed, as intended, for a fast and sufficient local cerium release during the first immersion hours followed by a sustained inhibitor supply capable of maintaining the overall corrosion protection level for the studied time. Yet the presence of lateral delaminations shown in Figure 4.9 and the undoubtful better results with the chromated system highlight the room for improvement of this new concept despite the initial promising results.

In order to identify any direct relationship between the observed inhibition at the scribe and the inhibitor release a detailed optical, SEM-EDS and Raman spectroscopy analysis was performed at the scribe at the end of the immersion time. Figure 4.12 shows the optical and SEM micrographs of the DE, Ce and Ce-DE damaged coatings after 4 days of immersion.

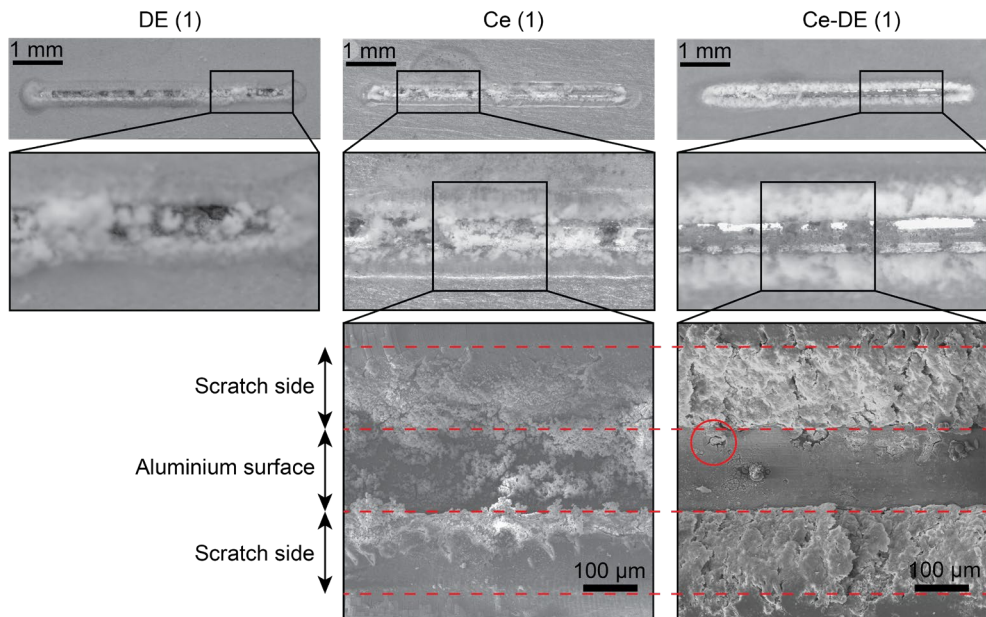


**Figure 4.12** Optical microscopy and SEM low secondary electron image (LEI) at the damaged sites of the DE (1), Ce (1) and Ce-DE (1) coatings after 4 days immersion in 0.05 M NaCl. The red circle indicates trenching around IM particles at the scribe of the Ce-DE (1) coating system.

It can clearly be seen that the corrosion products completely block the exposed aluminium surface at the scratch in the case of the DE and, to a minor extent, the Ce coating. On the other hand, the metal surface remains clearly visible and partially shiny in the case of the Ce-DE (1) coating. Despite the clear lack of oxide products and measured protection in the Ce-DE coating, trenching could be observed (red oval in Figure 4.12) and assigned to localized corrosion attack around intermetallic sites as reported elsewhere for non-inhibited AA2024-T3 during the first hours of immersion.<sup>35</sup> In the same sample, signs of oxide cracking as observed in AA2024-T3 directly exposed to Cerium ions was also observed. The low presence of features possibly related

to aluminium oxides and subsurface attack confirms the local action of the released cerium ions from the coating and its interaction with the intermetallic compounds (IMs). The presence of cerium at the scribe was confirmed by SEM-EDS analysis (Figure 4.13).

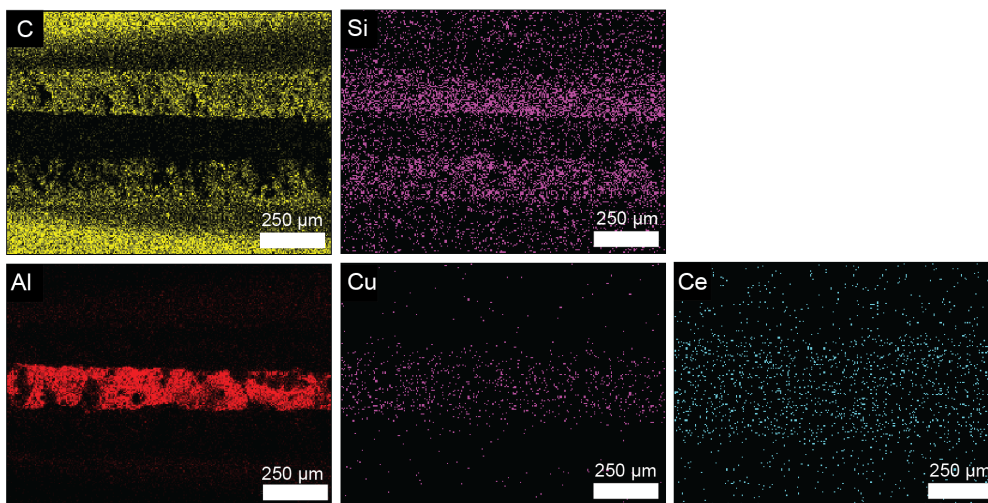


**Figure 4.13** EDS elemental mapping for the Ce-DE (1) coating showing: the location of the organic coating (C map), the diatom exoskeletons (Si map), the metallic substrate (Cu, Al maps) and the cerium (Ce map).

In this image it can be seen how the diatom exoskeletons remain in the coating (Si signal) while the cerium is located primarily at the scribe (metal surface) confirming the cerium was released from the coating. It should be noted that similar cerium signals were detected in the case of the Ce-coating. However, EDS is highly sensitive to Ce but quantification is not possible. It is therefore assumed that even if some cerium was released from the Ce-coating, the amount was not sufficient or was released too slowly to lead to any significant corrosion protection of the damaged site.

As SEM-EDS was not capable of identifying the exact location of cerium ions the scribe was further analysed by Raman spectroscopy. For the purpose, detailed analysis was performed on some control samples; a copper block and cerium oxide precipitates on a glass substrate to establish the wavelengths of the characteristic peaks related to cerium oxides and copper sites (S.I.; section 6, Figure SI 4.14, Figure SI 4.15). Two main characteristic sharp peaks were then detected: (i) a  $625\text{cm}^{-1}$  peak assigned to  $\text{Cu}_2\text{O}$ ; and (ii) a peak at the  $\text{F}_{2g}$  Raman active mode at  $463\text{ cm}^{-1}$  attributed to the symmetrical stretching of the Ce-8O vibrational units as reported elsewhere,<sup>36-40</sup> and confirmed by the presence of  $\text{CeO}_2$  precipitates on glass. Subsequently the interaction of cerium ions with the AA2024-T3 substrate was studied for Ce-DE particles and  $\text{Ce}(\text{NO}_3)_3$  in solution (S.I.; section 6, Figure SI 4.16 and Figure SI 4.17). It was then observed that the cerium peak signal was always detected at the same locations where the copper oxide

peak signal was found being thus possible to determine the location of Cu-rich IMs and Cerium deposition. Finally a Raman analysis of the scribe of the Ce-DE coated sample was performed. Figure 4.14 shows the Raman shift region of interest.

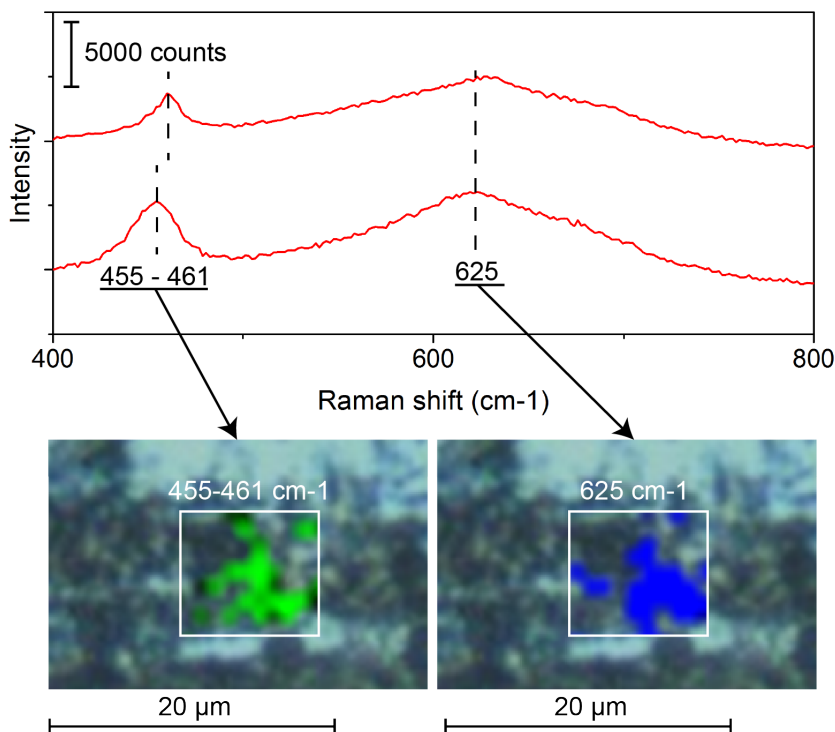


**Figure 4.14** Raman spectrum for Ce-DE (1) at the damaged sites of the coatings after 4 days of immersion and the Raman shift intensity plots at 455-461  $\text{cm}^{-1}$  and 625  $\text{cm}^{-1}$ . Image clearly shows the preferential deposition of Ce (455-461  $\text{cm}^{-1}$ ) at Cu-rich sites (625  $\text{cm}^{-1}$ ) for two random locations.

Again the two characteristic peaks were found at the same locations on the metallic surface although the Raman shift corresponding to the  $\text{CeO}_2$  was found to be broader than that of the  $\text{CeO}_2$  precipitates (Figure SI 4.15; SI) and having a maximum peak located at Raman shifts ranging from 455 to 461  $\text{cm}^{-1}$  depending on the location. Such a variation can be explained by the disorder of the oxygen sublattice, changes in the valence band, or grain-size induced effects.<sup>36,39</sup> The Raman analysis at the scribe clearly shows the interaction of the Ce ions at Cu-rich sites thereby confirming that the observed inhibiting effect of the Ce-DE coatings with the optical-electrochemical setup can be related to sufficient release of cerium at the damage site followed by its interaction preferentially at cathodic Cu-rich sites. The use of the different optical-electrochemical techniques and local analysis of inhibitor-metal interaction at the scribe site with Raman spectroscopy confirmed the appropriateness of using diatom exoskeletons to encapsulate efficient inhibitors that otherwise cannot be used due to their tendency to react with

the surrounding matrix. Such an approach opens the path for the development of more efficient Cr-free technologies based on inhibitor release from organic coatings.

## 4.5. Conclusions

The potential use of bio based algae exoskeleton as powerful carriers for local inhibitor storage leading to high active protection at damaged sites in coated metals is presented. The concept, based on the use of diatom algae silica exoskeletons, has been proven for the protection of AA2024-T3 structures by cerium nitrate corrosion inhibitor. In order to evaluate the corrosion protection at damaged sites a home-made optical-electrochemical set-up was used. High levels of active corrosion protection at damage sites were obtained for at least 4 immersion days; this being about 4 more times than coatings using the same inhibitor without the diatom shell. The high protection levels achieved are due to the isolation of the cerium inhibitor by the silica algae cage from the epoxy coating reducing unwanted reactions, the elevated inhibitor storage in the silica cages and the fast and sustained release of the cerium inhibitor at the damaged site. The study also shows the feasibility of developing protective systems based on fast release and inhibition at damaged sites followed by a time-sustained or on-demand release of corrosion inhibitors supplied at a sufficient concentration to ensure the long term protection. Despite the obvious corrosion inhibition offered by the newly developed Ce doped diatomaceous earth particles a faster and sufficient inhibitor release during the first immersion hours would be beneficial to prevent the formation of all kind of localized corrosion signs (e.g. trenching) and ensure long-time protection. The use of inhibitor loaded algae exoskeleton particles for sustained corrosion inhibition here presented is not restricted to cerium and epoxy coatings on aluminium substrates but should be regarded as a generic concept with high versatility and potential for developing environmentally friendly active corrosion protection in coated metals.

## 4.6. References

- 1 H. R. Fischer and S. J. Garcia, "Active Protective Coatings : Sense and Heal Concepts for Organic Coatings," in *Active Protective Coatings: New-Generation Coatings for Metals*, A. E. Hughes, J. M. C. Mol, M. L. Zheludkevich, and R. G. . Buchheit, Eds. Dordrecht: Springer Netherlands, 2016, pp. 139–156.
- 2 M. G. Hosseini, M. Jafari, and R. Najjar, "Effect of polyaniline-montmorillonite nanocomposite powders addition on corrosion performance of epoxy coatings on Al 5000," *Surf. Coatings Technol.*, vol. 206, no. 2–3, pp. 280–286, 2011, doi: 10.1016/j.surfcoat.2011.07.012.
- 3 S. Bohm, H. N. McMurray, D. A. Worsley, and S. M. Powell, "Novel environment friendly corrosion inhibitor pigments based on naturally occurring clay minerals," *Mater. Corros.*, vol. 52, no. 12, pp. 896–903, 2001, doi: 10.1002/1521-4176(200112)52:12<896::aid-maco896>3.0.co;2-8.
- 4 R. G. Buchheit, S. B. Mamidipally, P. Schmutz, and H. Guan, "Active corrosion protection in Ce-modified hydrotalcite conversion coatings," *Corrosion*, vol. 58, no. 1, pp. 3–14, 2002, doi: 10.5006/1.3277303.
- 5 R. Cai and Y. Yan, "Corrosion-resistant zeolite coatings," *Corrosion*, vol. 64, no. 3, pp. 271–278, 2008, doi: 10.5006/1.3278471.
- 6 E. L. Ferrer, A. P. Rollon, H. D. Mendoza, U. Lafont, and S. J. Garcia, "Double-doped zeolites for corrosion protection of aluminium alloys," *Microporous Mesoporous Mater.*, vol. 188, pp. 8–15, 2014, doi: Doi 10.1016/J.Micromeso.2014.01.004.
- 7 D. Fix, D. V. Andreeva, Y. M. Lvov, D. G. Shchukin, and H. Möhwald, "Application of inhibitor-loaded halloysite nanotubes in active anti-corrosive coatings," *Adv. Funct. Mater.*, vol. 19, no. 11, pp. 1720–1727, 2009, doi: 10.1002/adfm.200800946.
- 8 E. Theriot, D. Herbarium, F. E. Round, R. M. Crawford, and D. G. Mann, *The Diatoms. Biology and Morphology of the Genera.*, vol. 41, no. 1. Cambridge University Press, 1992.
- 9 Y. Wang, J. Cai, Y. Jiang, X. Jiang, and D. Zhang, "Preparation of biosilica structures from frustules of diatoms and their applications: Current state and perspectives," *Appl. Microbiol. Biotechnol.*, vol. 97, no. 2, pp. 453–460, 2013, doi: 10.1007/s00253-012-4568-0.
- 10 M. S. Aw, M. Bariana, Y. Yu, J. Addai-Mensah, and D. Losic, "Surface-functionalized diatom microcapsules for drug delivery of water-insoluble drugs," *J. Biomater. Appl.*, vol. 28, no. 2, pp. 163–174, 2013, doi: 10.1177/0885328212441846.
- 11 M. S. Aw, S. Simovic, J. Addai-Mensah, and D. Losic, "Silica microcapsules from diatoms as new carrier for delivery of therapeutics," *Nanomedicine*, vol. 6, no. 7, pp. 1159–1173, 2011, doi: 10.2217/nmm.11.29.
- 12 M. S. Aw, S. Simovic, Y. Yu, J. Addai-Mensah, and D. Losic, "Porous silica microshells from diatoms as biocarrier for drug delivery applications," *Powder Technol.*, vol. 223, pp. 52–58, 2012, doi: 10.1016/j.powtec.2011.04.023.
- 13 M. Bariana, M. S. Aw, and D. Losic, "Tailoring morphological and interfacial properties of diatom silica microparticles for drug delivery applications," *Adv. Powder Technol.*, vol. 24, no. 4, pp. 757–763, 2013, doi: 10.1016/j.apt.2013.03.015.
- 14 M. Milovic, S. Simovic, D. Losic, A. Dashevskiy, and S. Ibric, "Solid self-emulsifying phospholipid suspension (SSEPS) with diatom as a drug carrier," *Eur. J. Pharm. Sci.*, vol. 63, pp.

- 226–232, 2014, doi: 10.1016/j.ejps.2014.07.010.
- 15 H. Zhang *et al.*, “Diatom silica microparticles for sustained release and permeation enhancement following oral delivery of prednisone and mesalamine,” *Biomaterials*, vol. 34, no. 36, pp. 9210–9219, 2013, doi: 10.1016/j.biomaterials.2013.08.035.
- 16 P. Gnanamoorthy, S. Anandhan, and V. A. Prabu, “Natural nanoporous silica frustules from marine diatom as a biocarrier for drug delivery,” *J. Porous Mater.*, vol. 21, no. 5, pp. 789–796, 2014, doi: 10.1007/s10934-014-9827-2.
- 17 I. Ruggiero *et al.*, “Diatomite silica nanoparticles for drug delivery,” *Nanoscale Res. Lett.*, vol. 9, no. 1, pp. 1–7, 2014, doi: 10.1186/1556-276X-9-329.
- 18 T. Todd *et al.*, “Iron oxide nanoparticle encapsulated diatoms for magnetic delivery of small molecules to tumors,” *Nanoscale*, vol. 6, no. 4, pp. 2073–2076, 2014, doi: 10.1039/c3nr05623f.
- 19 K. A. Yasakau, M. L. Zheludkevich, S. V. Lamaka, and M. G. S. Ferreira, “Mechanism of corrosion inhibition of AA2024 by rare-earth compounds,” *J. Phys. Chem. B*, vol. 110, no. 11, pp. 5515–5528, Mar. 2006, doi: 10.1021/jp0560664.
- 20 S. J. Garcia, T. A. Markley, J. M. C. Mol, and A. E. Hughes, “Unravelling the corrosion inhibition mechanisms of bi-functional inhibitors by EIS and SEM-EDS,” *Corros. Sci.*, vol. 69, pp. 346–358, 2013, doi: 10.1016/j.corsci.2012.12.018.
- 21 M. Abdolaz Zadeh, S. van der Zwaag, and S. J. García, “Assessment of healed scratches in intrinsic healing coatings by AC/DC/AC accelerated electrochemical procedure,” *Surf. Coatings Technol.*, vol. 303, pp. 396–405, 2016, doi: 10.1016/j.surfcoat.2015.11.001.
- 22 D. Zhang, Y. Wang, J. Pan, and J. Cai, “Separation of diatom valves and girdle bands from *Coscinodiscus* diatomite by settling method,” *J. Mater. Sci.*, vol. 45, no. 21, pp. 5736–5741, 2010, doi: 10.1007/s10853-010-4642-x.
- 23 S. Joshi, E. A. Kulp, W. G. Fahrenholtz, and M. J. O’Keefe, “Dissolution of cerium from cerium-based conversion coatings on Al 7075-T6 in 0.1M NaCl solutions,” *Corros. Sci.*, vol. 60, pp. 290–295, 2012, doi: 10.1016/j.corsci.2012.03.023.
- 24 E. G. Heckert, A. S. Karakoti, S. Seal, and W. T. Self, “The role of cerium redox state in the SOD mimetic activity of nanoceria,” *Biomaterials*, vol. 29, no. 18, pp. 2705–2709, 2008, doi: 10.1016/j.biomaterials.2008.03.014.
- 25 S. J. Garcia *et al.*, “The influence of pH on corrosion inhibitor selection for 2024-T3 aluminium alloy assessed by high-throughput multielectrode and potentiodynamic testing,” *Electrochim. Acta*, vol. 55, no. 7, pp. 2457–2465, 2010, doi: 10.1016/j.electacta.2009.12.013.
- 26 F. Martelli, S. Abadie, J. P. Simonin, R. Vuilleumier, and R. Spezia, “Lanthanoids(III) and actinoids(III) in water: Diffusion coefficients and hydration enthalpies from polarizable molecular dynamics simulations,” *Pure Appl. Chem.*, vol. 85, no. 1, pp. 237–246, 2013, doi: 10.1351/PAC-CON-12-02-08.
- 27 C. Wang, F. Jiang, and F. Wang, “The characterization and corrosion resistance of cerium chemical conversion coatings for 304 stainless steel,” *Corros. Sci.*, vol. 46, no. 1, pp. 75–89, 2004, doi: 10.1016/S0010-938X(03)00135-5.
- 28 L. S. Kasten, J. T. Grant, N. Grebasch, N. Voevodin, F. E. Arnold, and M. S. Donley, “An XPS study of cerium dopants in sol-gel coatings for aluminum 2024-T3,” *Surf. Coatings Technol.*, vol. 140, no. 1, pp. 11–15, May 2001, doi: 10.1016/S0257-8972(01)01004-0.
- 29 J. Mardel *et al.*, “The characterisation and performance of Ce(dbp)<sub>3</sub>-inhibited epoxy coatings,”

- Prog. Org. Coatings*, vol. 70, no. 2–3, pp. 91–101, Feb. 2011, doi: 10.1016/j.porgcoat.2010.10.009.
- 30 T. S. Lim, H. S. Ryu, and S. H. Hong, “Plasma electrolytic oxidation/cerium conversion composite coatings for the improved corrosion protection of AZ31 Mg alloys,” *J. Electrochem. Soc.*, vol. 160, no. 2, pp. C77–C82, 2013, doi: 10.1149/2.005303jes.
- 31 P. Visser, M. Meeusen, Y. Gonzalez-Garcia, H. Terryn, and J. M. C. Mol, “Electrochemical evaluation of corrosion inhibiting layers formed in a defect from lithium-leaching organic coatings,” *J. Electrochem. Soc.*, vol. 164, no. 7, pp. C396–C406, 2017, doi: 10.1149/2.1411707jes.
- 32 S. K. Poznyak *et al.*, “Novel inorganic host layered double hydroxides intercalated with guest organic inhibitors for anticorrosion applications,” *ACS Appl. Mater. Interfaces*, vol. 1, no. 10, pp. 2353–2362, 2009, doi: 10.1021/am900495r.
- 33 T. H. Muster *et al.*, “A combinatorial matrix of rare earth chloride mixtures as corrosion inhibitors of AA2024-T3: Optimisation using potentiodynamic polarisation and EIS,” *Electrochim. Acta*, vol. 67, pp. 95–103, Apr. 2012, doi: 10.1016/j.electacta.2012.02.004.
- 34 F. J. Presuel-Moreno, H. Wang, M. A. Jakab, R. G. Kelly, and J. R. Scully, “Computational modeling of active corrosion inhibitor release from an Al-Co-Ce metallic coating,” *J. Electrochem. Soc.*, vol. 153, no. 11, pp. B486–B498, 2006, doi: 10.1149/1.2335946.
- 35 A. Boag, A. E. Hughes, A. M. Glenn, T. H. Muster, and D. McCulloch, “Corrosion of AA2024-T3 Part I: Localised corrosion of isolated IM particles,” *Corros. Sci.*, vol. 53, no. 1, pp. 17–26, 2011, doi: 10.1016/j.corsci.2010.09.009.
- 36 Z. D. Dohcevic-Mitrovic *et al.*, “The size and strain effects on the Raman spectra of Ce<sub>1-x</sub>Nd<sub>x</sub>O<sub>2-δ</sub> (0 ≤ x ≤ 0.25) nanopowders,” *Solid State Commun.*, vol. 137, no. 7, pp. 387–390, 2006, doi: 10.1016/j.ssc.2005.12.006.
- 37 G. W. Graham, W. H. Weber, C. R. Peters, and R. Usmen, “Empirical method for determining CeO<sub>2</sub>-particle size in catalysts by raman spectroscopy,” *J. Catal.*, vol. 130, no. 1, pp. 310–313, 1991, doi: 10.1016/0021-9517(91)90113-I.
- 38 W. H. Weber, K. C. Hass, and J. R. McBride, “Raman study of CeO<sub>2</sub>: Second-order scattering, lattice dynamics, and particle-size effects,” *Phys. Rev. B*, vol. 48, no. 1, pp. 178–185, 1993, doi: 10.1103/PhysRevB.48.178.
- 39 J. Twu, C. J. Chuang, K. I. Chang, C. H. Yang, and K. H. Chen, “Raman spectroscopic studies on the sulfation of cerium oxide,” *Appl. Catal. B Environ.*, vol. 12, no. 4, pp. 309–324, 1997, doi: 10.1016/S0926-3373(96)00085-9.
- 40 I. Kosacki, V. Petrovsky, H. U. Anderson, and P. Colomban, “Raman Spectroscopy of Nanocrystalline Ceria and Zirconia Thin Films,” *J. Am. Ceram. Soc.*, vol. 85, no. 11, pp. 2646–2650, 2004, doi: 10.1111/j.1151-2916.2002.tb00509.x.
- 41 B. Yilmaz and N. Ediz, “The use of raw and calcined diatomite in cement production,” *Cem. Concr. Compos.*, vol. 30, no. 3, pp. 202–211, 2008, doi: 10.1016/j.cemconcomp.2007.08.003.

## 4.7. Supporting Information

### SI-4.1. Active inhibitor content of coating systems

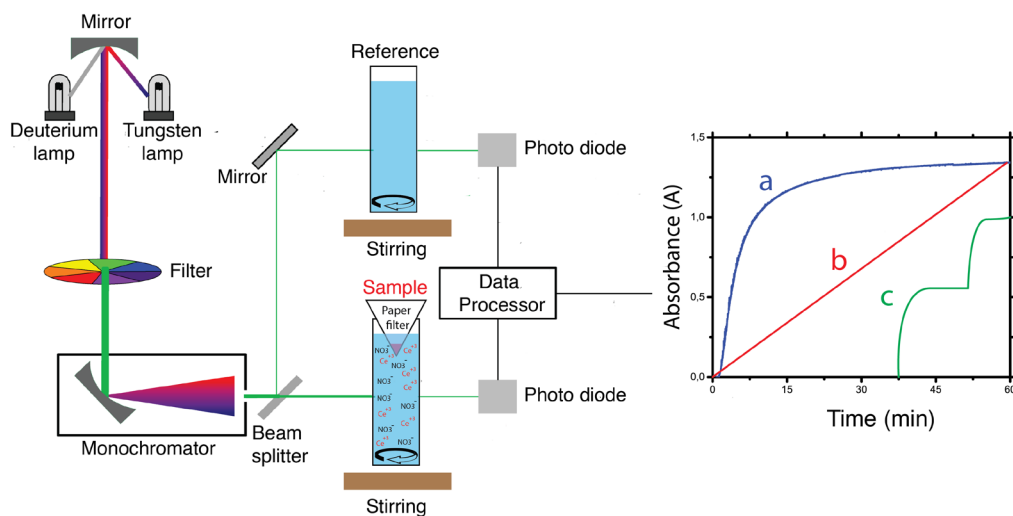
The active inhibitor content ( $X_{\text{inhibitor}}$ ) of the coating systems in moles per kg binder was calculated using equation 1;

$$X_{\text{inhibitor}} \left[ \frac{\text{mol}}{\text{kg binder}} \right] = \frac{C_{\text{inhibitor}} \left[ \frac{\text{g}}{\text{kg binder}} \right]}{M_{\text{inhibitor}} \left[ \frac{\text{g}}{\text{mol}} \right]} \quad \text{Eq. 1}$$

Where  $C_{\text{inhibitor}}$  is the content of active species per binder which was kept the same for all coating system at  $18 \text{ g kg}^{-1}$  binder.  $M_{\text{inhibitor}}$  is the molar weight of the inhibitor, which is  $434.22 \text{ g mol}^{-1}$  for  $\text{Ce}(\text{NO}_3)_3$  and  $294.19 \text{ k mol}^{-1}$  for  $\text{K}_2\text{Cr}_2\text{O}_7$ .

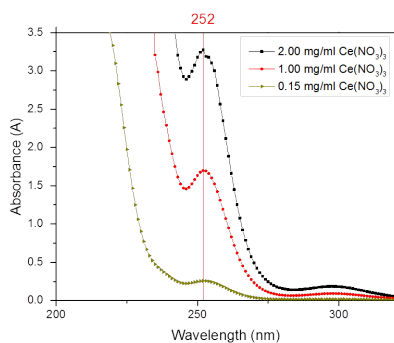
### SI-4.2. Modified UV/Vis for real-time release studies

Figure SI 4.1 illustrates the home-modified UV/VIS spectrometer setup used to measure the concentration of the  $\text{Ce}(\text{NO}_3)_3$  in solution. The setup consists of two devices; (i) a stirring device fitted inside the spectrometer, (ii) a semipermeable membrane (paper filter) fitted to the sample holder (tea-bag concept).



**Figure SI 4.1** schematic illustration of the UV/VIS setup.

Figure SI 4.2 illustrates the typical absorbance spectra for solutions containing  $\text{Ce}(\text{NO}_3)_3$ . The UV spectra for both pure  $\text{Ce}(\text{NO}_3)_3$  and released from Ce-DE containing samples showed corresponding Ce III peaks at 252 nm.



**Figure SI 4.2** UV/VIS Absorbance spectra for solutions containing  $\text{Ce}(\text{NO}_3)_3$  at three different concentrations.

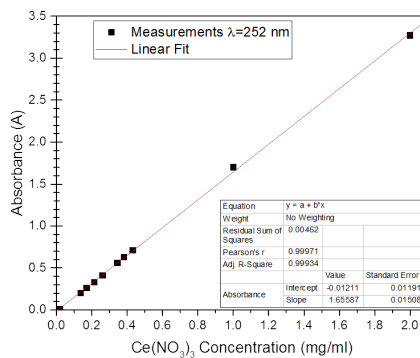
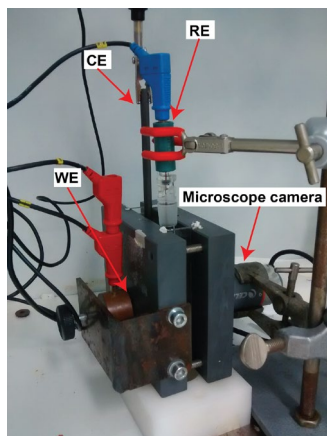


**Figure SI 4.3** calibration curve at 252 nm for  $\text{Ce}(\text{NO}_3)_3$  containing solutions based on solution ranging from 0.2 mg/ml to 2 mg/ml.

Figure SI 4.3 shows the UV/VIS calibration curve for solutions containing  $10^{-3}$  to  $10^{-5}$  M  $\text{Ce}(\text{NO}_3)_3$  based on 10 predefined inhibitor concentrations and measured at 252nm wavelength. The calibration curve was validated for both pure  $\text{Ce}(\text{NO}_3)_3$  and Ce-DE containing solutions using the real-time release UV/Vis cuvette setup as shown in Figure SI 4.1.

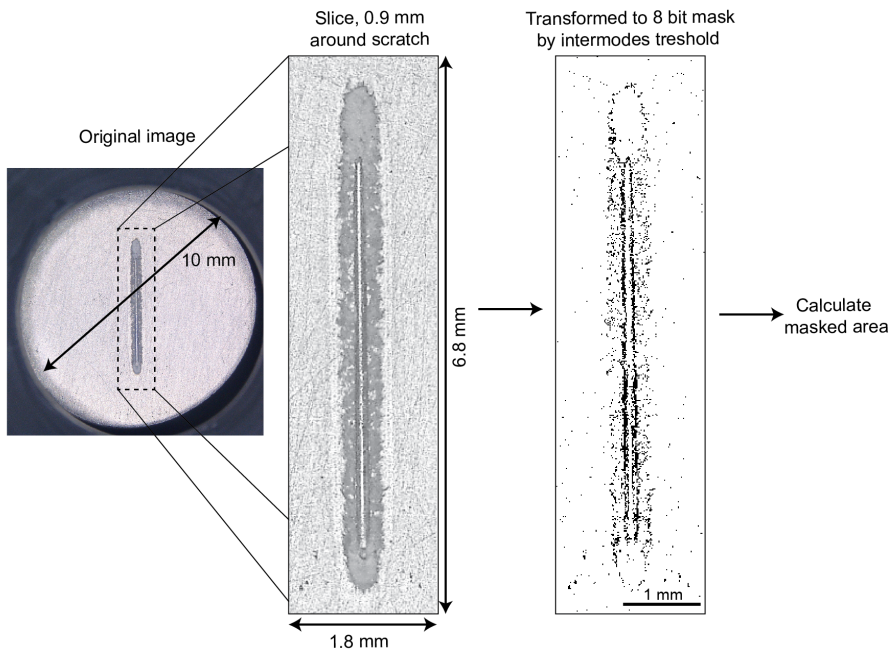
### SI-4.3. Optical-electrochemical set-up

Figure SI 4.4 shows a photograph of the optical-electrochemical setup. On the left, the red banana plugs of the potentiostat are connected to the analysed AA2024-T3 sample as working electrode (WE) and sensing electrode (S) held in vertical position by a copper block. The blue banana plug is connected to the Ag/AgCl reference electrode (RE) and the black banana plug to the counter electrode (CE). On the right side, a USB microscope camera is held in place in front of a transparent Plexiglas glass to observe the AA2024-T3 substrate while immersed inside the electrochemical cell.



**Figure SI 4.4** optical-electrochemical set-up used in the study. The analysed sample is visible on the left hand of the image and the microscope on the right hand.

The procedure analysing the degradation area based on the optical images is shown in Figure SI 4.5. For illustration purpose, the damaged epoxy coating after 6 h immersion in 0.05 M NaCl was selected in this figure.



**Figure SI 4.5** procedure on the optical analysis to investigate the degradation area.

Photos are recorded each hour, starting at the beginning of the measurement. These images are saved as jpeg files (960x1280 px.) and contain the entirely exposed surface of the coating including the 5 mm long scratch. All the degradation processes were detected within a 0.9 mm area around the centre, resulting in a total area ( $A_t$ ) of 12 mm<sup>2</sup>. This section of image was isolated from the rest and converted to 8-bit greyscale for further analysis using the intermodes threshold method with ImageJ image processing software. This threshold method locates a local maximum for the light background and a second local maximum for the dark area in the bimodal histogram, and converts the image to a binary mask. In the image immediately after immersion, the dark area (initial dark area) is caused by the presence of the scratch itself and in the case for the Cr coating also due to the presence of corrosion inhibitor inside the coating. In the subsequent images, the increase of the dark area over time with reference to the initial dark area is caused by the degradation of the coating and used to calculate the portion of degraded area over time ( $\Delta A_{\text{degraded}}$ ) by equation 2:

$$\Delta A_{\text{degraded}}(\%) = \frac{A_t - A_0}{A_s} * 100\% \quad \text{Eq 2.}$$

Where  $A_t$  is the degraded (dark) area at time  $t$ ,  $A_0$  the initial dark area and  $A_s$  the total studied area of 12 mm<sup>2</sup>.

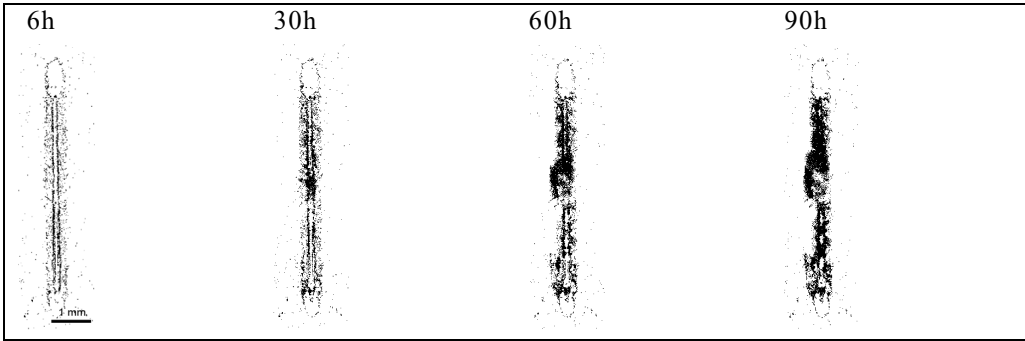


**Figure SI 4.6** 8-bit optical images of the damaged Epoxy coating immersed in 0.05 M NaCl.

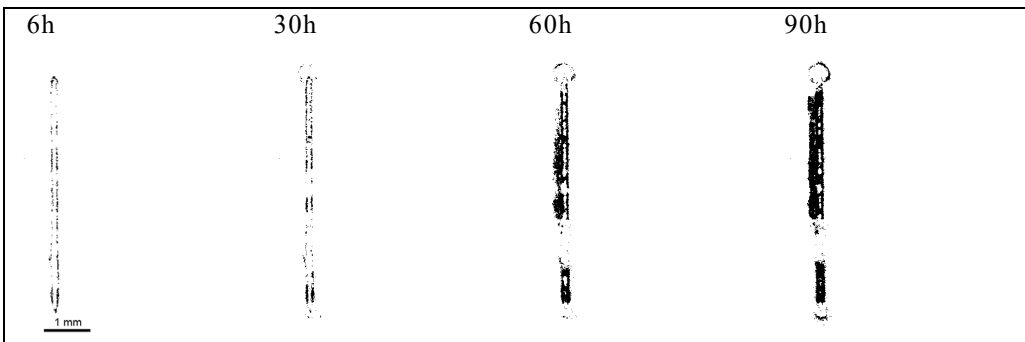


**Figure SI 4.7** 8-bit optical images of the damaged DE (1) coating immersed in 0.05 M NaCl.

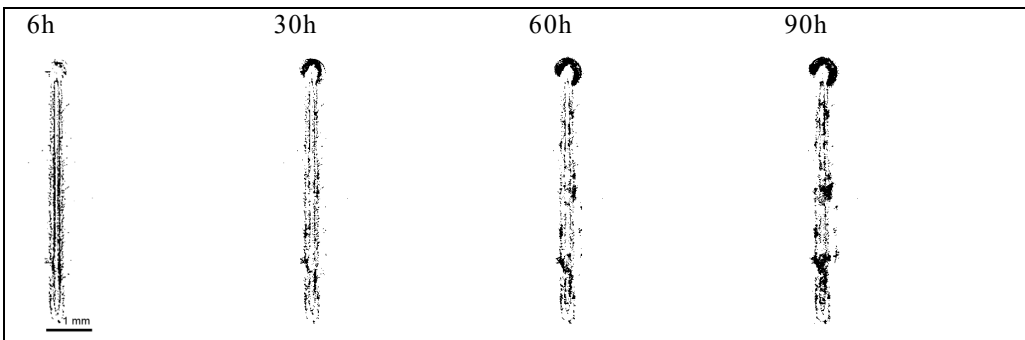


**Figure SI 4.8** 8-bit optical images of the damaged Ce (1) coating immersed in 0.05 M NaCl.

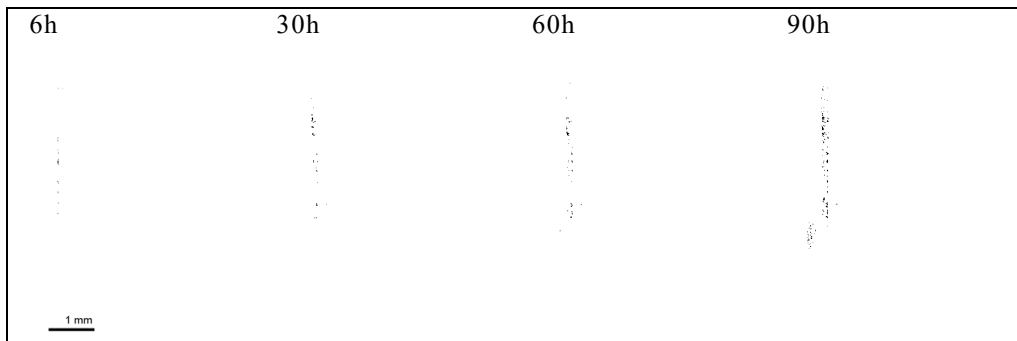


**Figure SI 4.9** 8-bit optical images of the damaged Ce-DE (1) coating immersed in 0.05 M NaCl.

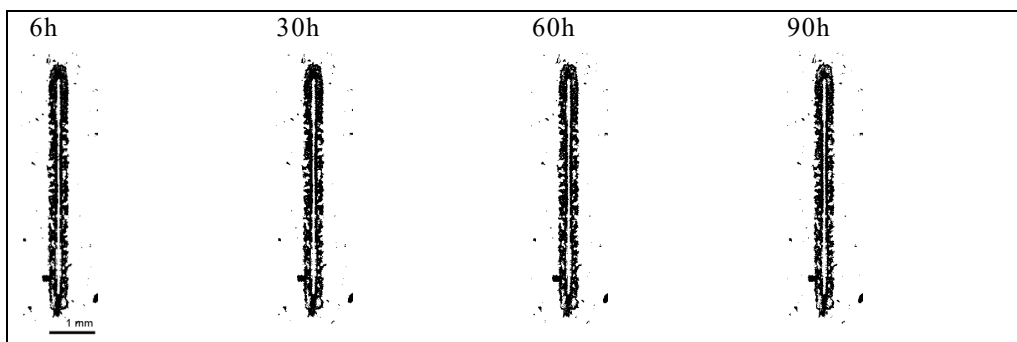


**Figure SI 4.10** 8-bit optical images of the damaged Cr coating immersed in 0.05 M NaCl.

#### ***SI-4.4. Effect of acid and alkali treatments on the cerium-doping of refined DE***

According to literature<sup>41</sup> the main impurities in the as received and refined diatomaceous earth are clay, volcanic glass, organic matter and inorganic oxides such as  $\text{Al}_2\text{O}_3$ ,  $\text{Fe}_2\text{O}_3$ ,  $\text{CaCO}_3$ ,  $\text{K}_2\text{O}$ ,  $\text{Na}_2\text{O}$  and  $\text{MgO}$ . These impurities could block the pores, thereby altering the surface area of the diatoms and thereby the doping. In order to remove the impurities present in the refined diatomaceous earth (DE), chemical treatments with acid and alkaline solutions have been explored.

For the acid treatment, 200 mg refined DE was dispersed in 20 ml solution of 3.0 M Sulfuric acid ( $\text{H}_2\text{SO}_4$ ) using a 50 ml flask fitted with a condenser and controlled at 100 in an oil bath. The flask was fitted with magnetic stirrer at around 200 rpm. After 16 hours the content was filtered using a Whatman® grade 595 paper filter. The acid treated product was repeatedly washed with water until the filtrate reached a pH of 7. The residue was removed from the filter and dried in a vacuum oven at 60°C for 24 hours to completely dry.

For the alkaline treatment, two batches were used. Namely, 200 mg refined DE for the first batch and 200 mg acid treated DE for the second batch. this was mixed with 5.0 ml of sodium hydroxide solution ( $\text{NaOH}$ ) having a pH of 11. The content was magnetically stirred for 1.5 hours at 200 rpm in a 50 ml flask. Finally the diatoms were filtered and water cleaned with the use of a Whatman® grade 595 paper filter until the filtrate reached a pH of 7. The residue was removed from the filter and dried in a vacuum oven at 60°C for 24 hours to completely dry.

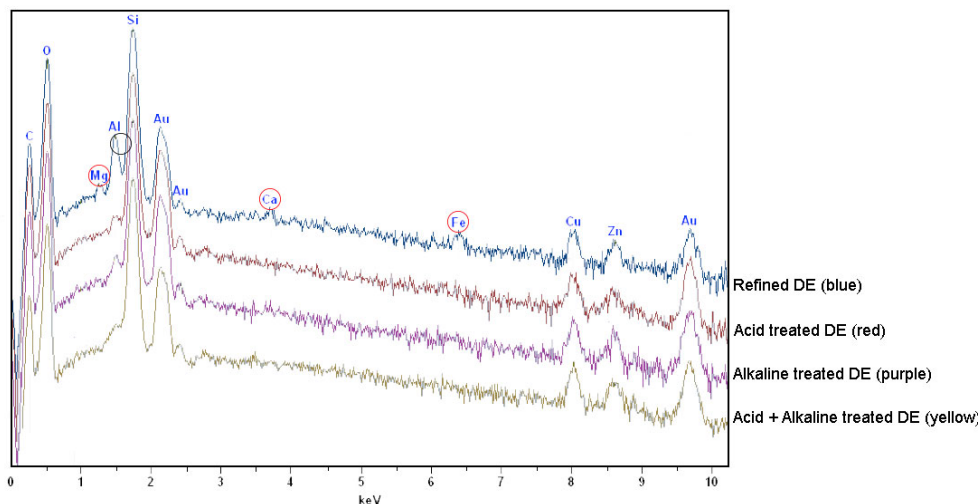


**Figure SI 4.11** SEM-EDS spectra of the DE treated by the 3 different chemical treatments (acid, alkaline and acid + alkaline) compared to the refined DE.

As can be seen in Figure SI 4.11, all the treatments lead to the disappearance of elements related to contaminant oxides (Fe, Ca, Mg) leaving only the pure silica ( $\text{SiO}_2$ ) diatom frustules available. Nevertheless, also a small peak related to Al remains. Yet, if the different chemical treatments are compared, it can be seen that the combined acid + alkaline treatment is the most effective in the removal of Al. Furthermore, a colour change of the diatom frustules from light brown to white was also noticeable after the acid treatment (not shown here), which is most probably due to the removal of organic matter.

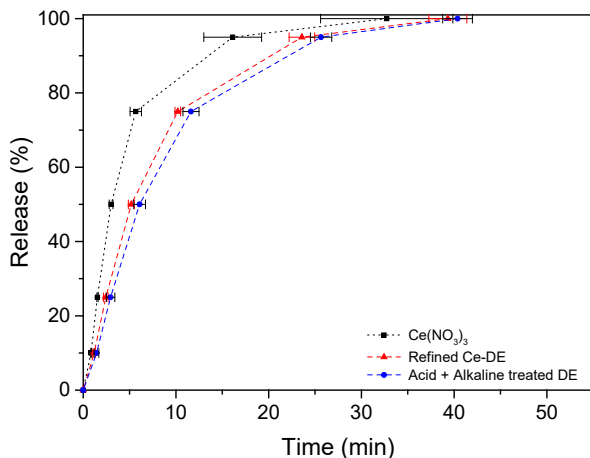


**Figure SI 4.12:** Release kinetics of  $\text{Ce}(\text{NO}_3)_3$  refined Ce-DE and Ce-DE treated by the acid + alkaline chemical treatment. Error-bars show the standard deviation created by threefold sampling and the lines are added for visualization purposes only.

From Figure SI 4.12 it can be seen that that the release of cerium from the acid + alkaline chemically treated DE has a slightly slower release compared to water separated frustules. However, the difference stays within the margin of error for the measurements and thereby suggests that the chemical treatment does not significantly change the release kinetics. Similar results were observed with the other chemical treatments (not shown here).

#### SI-4.5 Corrosion protection of Ce-DE on bare AA2024-T3

To study the release and corrosion protection by Ce-doped DE in solution, a 2 mm thick AA2024-T3 panel with lateral dimensions of 25 x 50 mm was manually sanded using silicon carbide paper down to grit 2000 followed by polishing with 3  $\mu\text{m}$  and 1  $\mu\text{m}$  diamond paste and finally degreased with acetone. 2 x 3 Polyethylene cylinders with an inner diameter and height of 6.2 x 5 mm were attached to the aluminium substrate with epoxy resin (Epikote™ 828) and amine crosslinker (Ancamine®2500) followed by curing in an oven at 60 °C for 24 hours. The cylinder wells were filled with 0.05 M NaCl solutions and covered with a cover slip to avoid evaporation while inspecting the aluminium surface with an optical microscope. Optical images of the coated and bare AA2024 substrates before, during and after immersion were obtained with a Keyence VHX-2000E using a wide-range resolution zoom lens (100x-1000x) in stitching mode.

Figure SI 4.13 shows optical micrographs of the surfaces of the samples before, during, and after 7 days of immersion in 0.05 M NaCl (a) without any corrosion inhibitor added to the solution, (b) 0.05 mM  $\text{Ce}(\text{NO}_3)_3$ , and (c) Ce-doped DE containing 0.05 mM  $\text{Ce}(\text{NO}_3)_3$ .

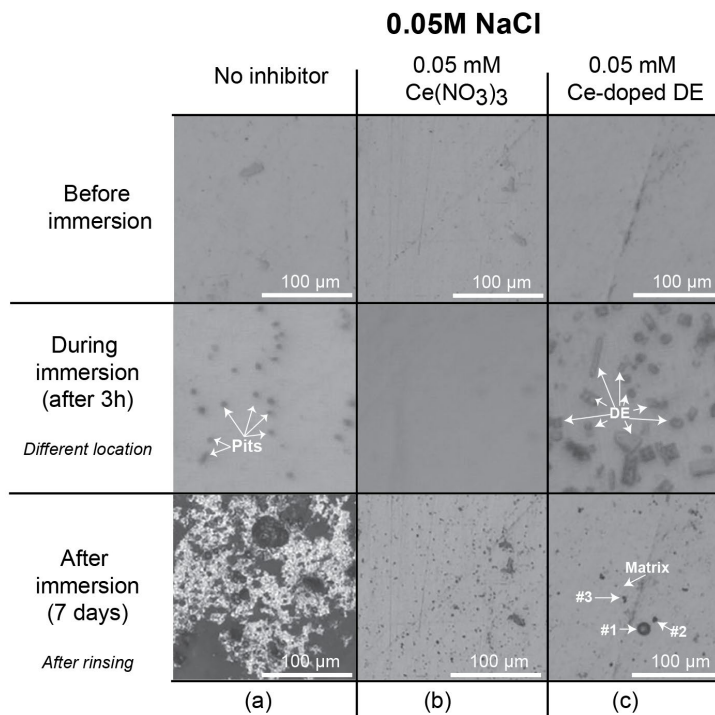


**Figure SI 4.13** Microscope images of polished AA2024-T3 before, during, and after 7 days of immersion in 0.05 M NaCl (a) without corrosion inhibitor (b) 0.05 mM  $\text{Ce}(\text{NO}_3)_3$  and (c) Ce-doped DE containing 0.05 mM  $\text{Ce}(\text{NO}_3)_3$ . Note, images during immersion do not represent real sizes due to the distortion by the solution.

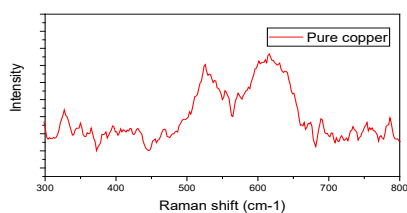
Figure SI 4.13(a) shows that pitting corrosion on AA2024 occurs within the first 3h of immersion in 0.05 M NaCl, indicating the susceptibility to localized corrosion in salt water for this alloy. The initiation of pitting did not occur when 0.05 mM  $\text{Ce}(\text{NO}_3)_3$  or Ce-doped DE was added, as shown in Figure SI 4.13(b-c), confirming that the Ce-doped DE is actively protecting the substrate. DE particles were visible at the aluminium surface during the immersion-test for the Ce-doped DE solution after 3h. Furthermore, several secondary phases became visible at the surface after 7 days of immersion and rinsing with water.

**Table SI 4.2.** EDS analysis showing relative atomic ratios of the elements at different points on AA2024 after 7 days immersion in 0.05 M NaCl with Ce-doped DE containing 0.05 mM  $\text{Ce}(\text{NO}_3)_3$ .

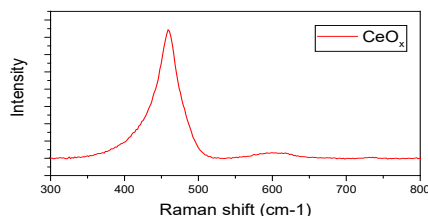
|         | Mg/Al | Si/Al | Cu/Al | Ce/Al |
|---------|-------|-------|-------|-------|
| #1 (DE) |       | 0.62  | 0.017 | 0.015 |
| #2 (IM) | 0.01  | 0.032 | 0.3   | 0.046 |
| #3 (IM) | 0.02  | 0.017 | 0.346 | 0.041 |
| Bulk    | 0.012 |       | 0.02  |       |

Table SI 4.2 shows the EDS analysis by relative atomic ratios of the elements at different locations as indicated in Figure SI 4.13(c). It shows the presence of silica (#1) caused by a diatom exoskeleton that was not properly rinsed away. Also the presence of cerium species at copper rich zones (#2 and #3) was detected at the secondary phases. From literature it is known that the inhibiting effect of cerium is due to the formation of cerium precipitates at the local cathodic regions.<sup>19</sup>

#### SI-4.6. Raman study

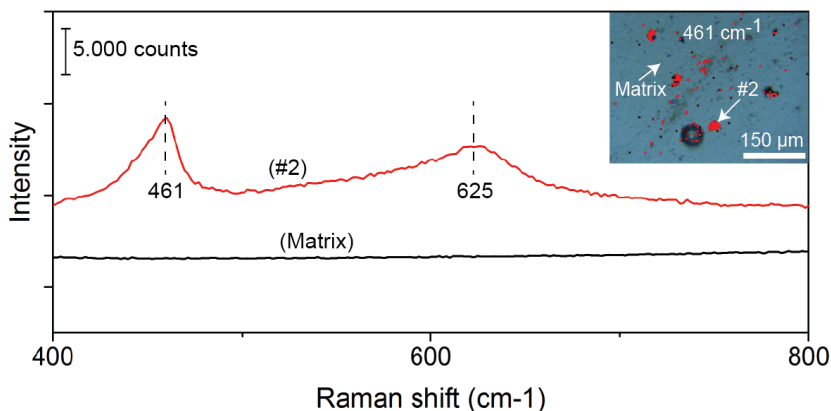


**Figure SI 4.14** Native oxide layer on pure copper



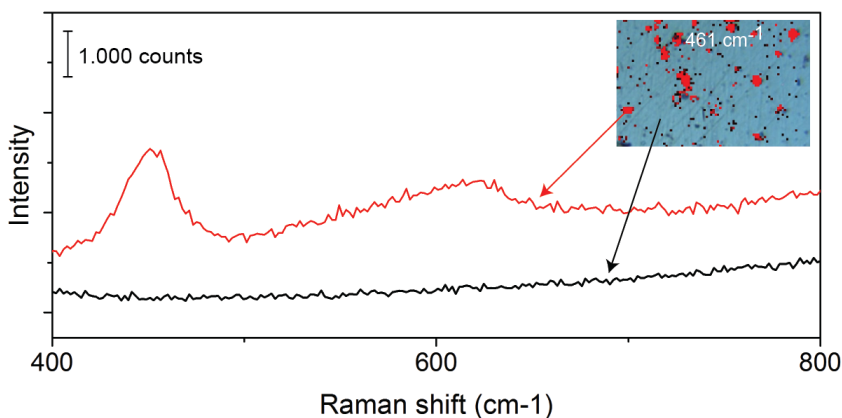
**Figure SI 4.15** Cerium oxide synthesized from  $\text{Ce}(\text{NO}_3)_3$

To further identify the location sites of Ce in relation to the metal surface composition of the secondary phases, Raman spectroscopy was performed on the systems as described in section 5. Figure SI 4.16 shows the analysis by Raman spectroscopy at the same locations as shown in Figure SI 4.13(c) after 7 days of immersion in 0.05 M NaCl containing Ce-DE particles dispersed in the electrolyte.

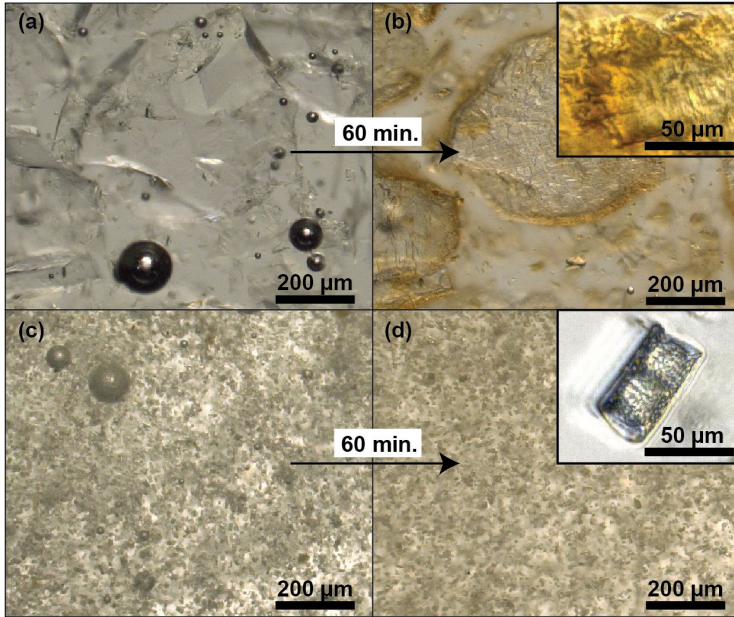


**Figure SI 4.16** Raman spectra on AA2024-T3 after 7 days of immersion in 0.05 M NaCl containing Ce-DE at the same location as shown in Figure SI4.13 (c). Black line corresponds to the matrix and red line to the local sites rich in Ce and Cu.

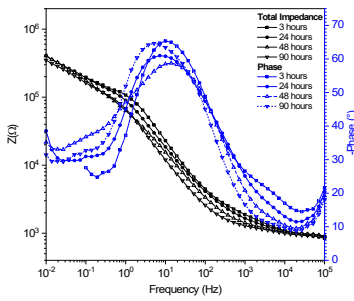
The intensity of signal at 463 cm<sup>-1</sup> was sufficient enough to generate a map (see inset of Figure SI 4.16) to illustrate that cerium has deposited only at the secondary phases. The same cerium deposits were also observed by SEM/EDS and Raman analysis on AA2024 exposed to Ce(NO<sub>3</sub>)<sub>3</sub> without the presence of DE as shown in Figure SI 4.17, which confirms sufficiently fast cerium release from the DE particles to prevent local corrosion by the formation of similar protective cerium precipitates at copper-rich phases.



**Figure SI 4.17** Bare AA2024, Ce(NO<sub>3</sub>)<sub>3</sub> without DE. Black line is for the bulk aluminium alloy and red line for the specific locations rich in copper.

*SI-4.7. Yellowing effect of cerium containing epoxy coatings*

**Figure SI 4.18** Microscope images of (a-b) Cerium Nitrate and (c-d) Ce-DE mixed with Ancamine®2500 just after mixing (a, c) and after 1 hour (b, d). Images illustrate the yellowing process in the case of the cerium salt –amine couple and its absence in the case of the Ce-DE amine one. Image confirms the strong reduction of the yellowing when the Ce-salt is included in an exoskeleton nanoporous microparticle.

**SI-4.8. Electrochemical Impedance Spectroscopy**

**Figure SI 4.19** Bode plot of the damaged Epoxy coating on AA2024-T4 after 3h, 24h, 48h, and 90h immersion in 0.05 M NaCl solutions.

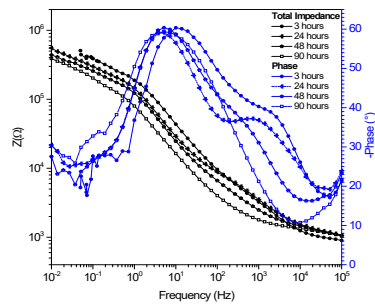


**Figure SI 4.20** Bode plot of the damaged DE (1) coating on AA2024-T4 after 3h, 24h, 48h, and 90h immersion in 0.05 M NaCl solutions.

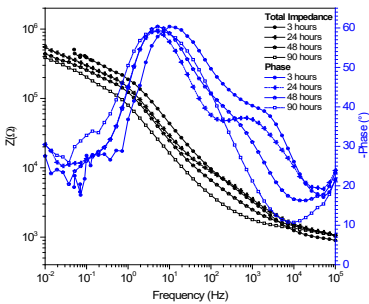


**Figure SI 4.21** Bode plot of the damaged Ce coating on AA2024-T4 after 3h, 24h, 48h, and 90h immersion in 0.05 M NaCl solutions.

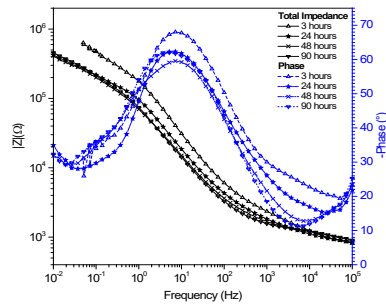


**Figure SI 4.22** Bode plot of the damaged Ce-DE (1) coating on AA2024-T4 after 3h, 24h, 48h, and 90h immersion in 0.05 M NaCl solutions.

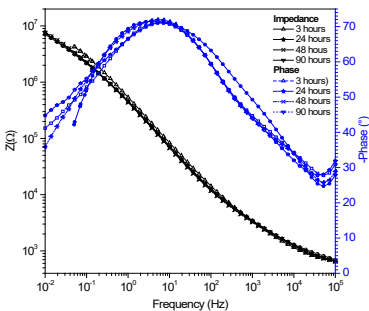


**Figure SI 4.23** Bode plot of the damaged Cr coating on AA2024-T4 after 3h, 24h, 48h, and 90h immersion in 0.05 M NaCl solutions.

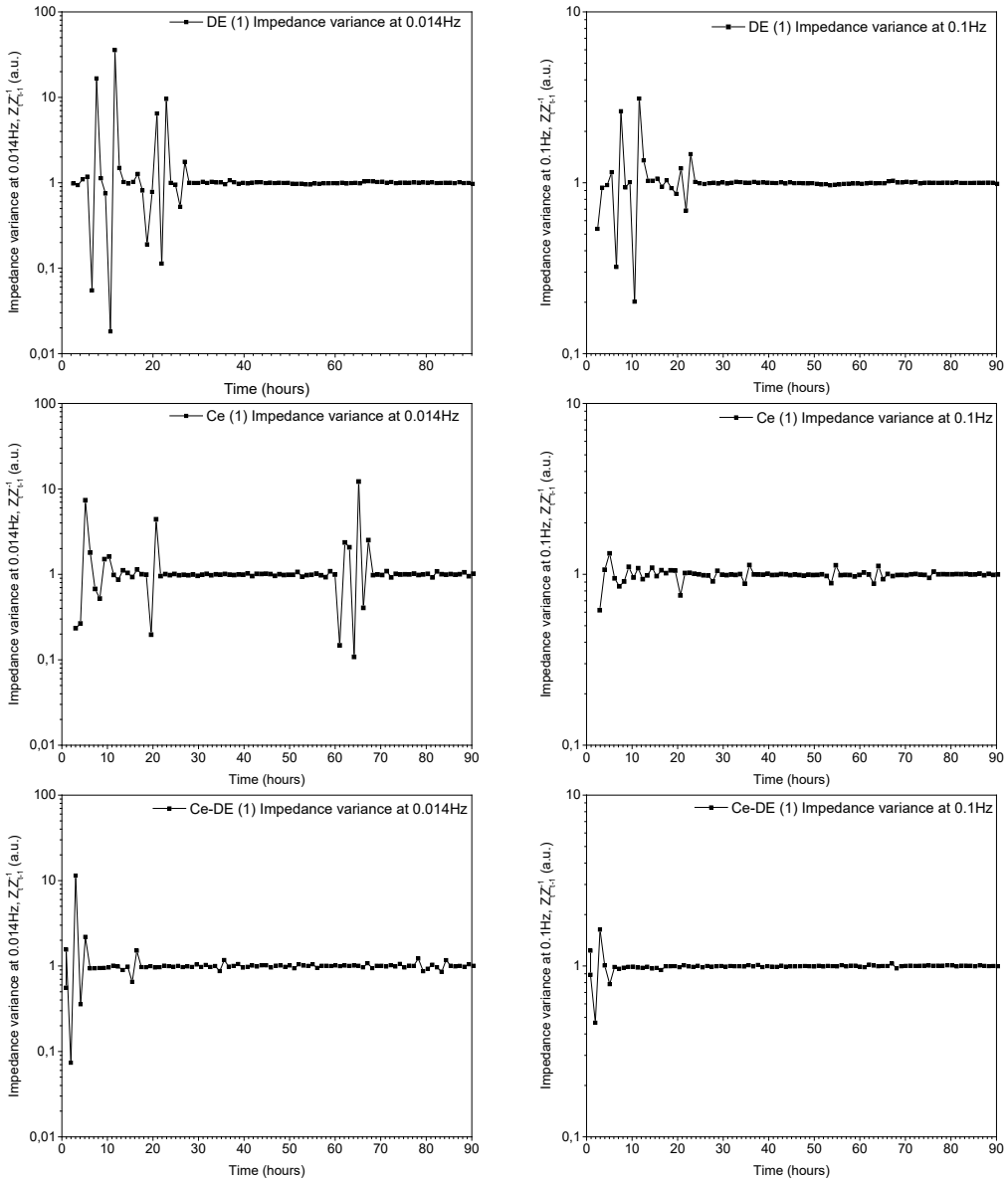


**Figure SI 4.24** Variation of the electrochemical impedance variance ( $Z_{nZ-1n-1}$ ) at frequencies 0.014 Hz, 0.1 Hz of three studied coating systems Ce(1), DE(1) and Ce-DE(1) during immersion in 0.05 M NaCl.

# 5

## **Corrosion inhibition at scribed locations in coated AA2024-T3 by cerium and DMTD loaded natural silica microparticles under continuous immersion and wet/dry cyclic exposure**

*Earlier studies on cerium-loaded naturally-occurring silica microparticles (i.e. diatomaceous earth) demonstrated the potential to efficiently protect small scratches in epoxy-coated AA2024-T3 panels during relatively short immersion times. The current work investigates the potential of such inhibitor-loaded microparticles to protect wide and deep scribes (up to 1 mm wide) in long-time immersion testing and during cyclic (wet/dry) conditions. For this, cerium nitrate and 2,5-dimercaptothiadiazole (DMTD) were used as inorganic and organic corrosion inhibitors. The corrosion protection was evaluated using a hyphenated real-time optics/electrochemistry method and two individual local techniques measuring oxygen concentration and electrochemical impedance (LEIM) inside the scribe. SEM/EDS was used to analyze the samples after exposure. The results show significant levels of corrosion protection at damaged locations at low cerium concentrations (3.7 wt.% Ce<sup>3+</sup> relative to the total coating mass) during 30 days immersion in salt solution. However, for a given scribe geometry the protection was found to be dependent on the electrolyte volume with larger electrolyte/exposed metal ratios leading to short protection time. A partial replacement of the Ce<sup>3+</sup> by DMTD in the microcarriers resulted in a higher degree of passivation than when DMTD was used alone. Wet/dry cyclic exposure tests showed that cyclic conditions can increase the build-up of stable inhibitor-containing layers in the case of cerium-loaded silica microparticles. This underlines the need for more research using wet/dry exposure conditions.*

This chapter has been published as:

P. J. Denissen, V. Shkirskiy, P. Volovitch, S. J. Garcia, Corrosion inhibition at scribed locations in coated AA2024-T3 by cerium and DMTD loaded natural silica microparticles under continuous immersion and wet/dry cyclic exposure, ACS Applied Materials & Interfaces, 2020.

## 5.1. Introduction

The wish and legal need to find less harmful but still efficient alternatives to carcinogenic hexavalent chromium salts as corrosion inhibitors in anticorrosive primers on aluminium aircraft alloys and other metals has triggered many studies in recent years.<sup>1,2</sup> Potentially acceptable alternatives such as lanthanide salts (e.g. Ce, Y, La, Pr and Nd)<sup>3-5</sup>, Li salts<sup>6-10</sup>, and organic compounds<sup>11-16</sup> have been identified and studied during the last decades. Nevertheless, these alternatives are generally less effective, work under limited environmental conditions (e.g. pH), and lose part of their efficiency when incorporated in polymeric matrices (coatings) due to unwanted physical/chemical inhibitor-coating interactions and uncontrolled release.<sup>16,17</sup> These challenges have been addressed by the development of numerous nano-sized encapsulation methods that reduce the unwanted inhibitor-coating interactions and allow for controlled release, from discrete use of nanoparticles to electrospun nanofiber mats.<sup>8,12,18-21</sup>

In our previous work we showed that naturally occurring nanoporous, hollow, silica microparticles (diatomaceous earth or DE) can also act as a container for corrosion inhibitors such as cerium nitrate ( $\text{Ce}(\text{NO}_3)_3$ ), an efficient corrosion inhibitor for Cu-rich aluminium alloys such as AA2024-T3.<sup>22</sup> When such loaded DE particles are mixed with an epoxy-amine, a coating with high corrosion inhibiting power was obtained. The degree of unwanted side reactions between the cerium-inhibitor in the containers and the matrix was lower than those observed for cerium salts directly added to epoxy/amine coatings. This allowed sufficient quantities of  $\text{Ce}^{3+}$  ions to diffuse to the metallic substrate at scribe locations to protect the metal in presence of corrosive electrolytes (0.05 M NaCl). This first study on DE particles as an effective containers for non-carcinogenic corrosion inhibitors served as a proof of principle. Nevertheless, the corrosion protection was just monitored for one inhibitor-carrier combination, small scratches (130  $\mu\text{m}$  wide scratches) and under continuous exposure to relatively large electrolyte volumes for short immersion times (up to 4 days).

The present work aims to expand this initial study and to investigate the effect of some other important parameters influencing the corrosion protection. Here we focus on the effect of: (i) large scale scribes (i.e. 1 mm wide and 300  $\mu\text{m}$  down below the coating layer), (ii) the use of an inorganic and an organic inhibitors, namely  $\text{Ce}(\text{NO}_3)_3$  (Ce) and 2,5-dimercaptothiadiazole (DMTD) loaded inside DE particles, (iii) the amount of the electrolyte volume to which a scribe is exposed during continuous (wet-) exposure up to 30 days immersion, and (iv) the corrosion protection in case of multiple wet/dry cycles. The latter, not very common in scientific reports, was prompted by past literature<sup>23-26</sup> showing that corrosion protection during continuous wet exposure can be quite different from that under cyclic wet/dry conditions. We monitored the evolution of the damaged coatings immersed in electrolyte and quantified the corrosion extent and kinetics, using a previously reported hyphenated real-time optics/electrochemistry method.

---

<sup>22,27,28</sup> To gain more information of the local corrosion processes we locally measured the time evolution of the oxygen concentration at the bottom of the scribe inspired by previous works<sup>29</sup> and performed electrochemical impedance mapping (LEIM) at the scribes.<sup>30,31</sup> SEM/EDS was used to analyse the samples after exposure and to obtain more information of the inhibitor-substrate interactions.

## 5.2. Experimental

### 5.2.1. Materials

Diatomaceous earth (DE) of the type Diafil 525, mainly belonging to the *Aulacoseiraceae* family was supplied by Profiltra Customized Solutions (NL). The DE was refined following the procedure reported elsewhere.<sup>22</sup> The resulting refined DE consisted primarily of intact hollow cylindrical micro-, and nano-porous amorphous silica structures with a mean particle size of 12  $\mu\text{m}$  with nanopores around 500 nm in diameter, evenly distributed around the wall structure.<sup>32</sup> Cerium nitrate hexahydrate ( $\text{Ce}(\text{NO}_3)_3 \cdot 6\text{H}_2\text{O}$ ) and 2,5-Dimercapto-1,3,4-thiadiazole (DMTD) were used as corrosion inhibitors. 3 mm thick industrial grade aluminium alloy 2024-T3 sheets were supplied by Kaizer Aluminium. The plates were cut in 200x250 mm panels, grinded using 320 grit SiC paper, degreased with acetone, sonicated for 30 min at 60 °C in ethanol and air dried. After drying, the panels were exposed to NaOH for 10s, rinsed with demi-water and dried under nitrogen for pseudoboehmite treatment prior to the coating application. Commercially available bisphenol-A based epoxy resin (Epikote™ 828) and amine crosslinker (Ancamine®2500) were supplied by AkzoNobel (NL) and used as-received to form the coating binder using xylene (99%) as solvent. Milipore® filtered water (electrical resistivity 18 M $\Omega$  cm) was employed in all steps requiring water.

### 5.2.2. Inhibitor loading and coatings preparation

#### 5.2.2.1. DE loading with inhibitors

Three batches of DE particles were prepared, namely: unloaded DE particles and inhibitor-loaded DE containing either  $\text{Ce}(\text{NO}_3)_3 \cdot 6\text{H}_2\text{O}$  or DMTD. A mixture of 5 g DE and 5 g inhibitor was added to 10 ml dimethylformamide (DMF,  $\geq 99.9\%$ ) and stirred for 24 h at 320 rpm using a shaking table. Next, the mixture was spread on a glass plate with a glass pipet and distributed with a 100  $\mu\text{m}$  spiral bar coater. Drying at 60 °C for 30 min led to a thin layer of dry DE particles loaded with corrosion inhibitors. The DE layer was removed from the plate with a spatula and the resulting powder was further dried for another 72 h at 60 °C and stored in a desiccator prior to use. As a result, DE particles with 50 wt.% inhibitor salt were obtained.

### 5.2.2.2. Coatings and controlled damages to the coated panels

Table 5.1 shows the different coating compositions used in this study. Besides the phr content of loaded DE particles, the table shows the derived (calculated) content of DE microcarrier and inhibitor in phr and the thereby resultant content of inhibiting active species in the coating in wt.%. The later was calculated based on the available inhibitor (in weight) in the container inside the coating but considering only the main inhibiting component of the salt in the (i.e.  $Ce^{3+}$  available in cerium salt). Details of the calculations can be found in the support information (SI-5.1).

**Table 5.1** Coatings formulation given as function of Epikote 828 resin (phr = parts per hundred epoxy resin in weight). Table includes the calculated inhibitor content in phr and the calculated content of inhibiting active component (DMTD or  $Ce^{3+}$ ) in wt.% of the total coating weight.

| Sample Name           | Inhibitor salt                             | Ancamine 2500 | DE particles | DE container | Inhibitor       | Inhibiting active component | Thickness  |
|-----------------------|--|---------------|--------------|--------------|-----------------|-----------------------------|------------|
|                       |  | (phr)         | (phr)        | (phr)        | (phr)           | (wt. %)                     | ( $\mu$ m) |
| Epoxy                 | -  | 58            | -            | -            | -               | -                           | 73 $\pm$ 5 |
| DE                    | -  | 58            | 48           | 48           | 0               | -                           | 65 $\pm$ 5 |
| DMTD-DE               | DMTD                                       | 58            | 48           | 24           | 24              | 11.5                        | 77 $\pm$ 5 |
| 0.5Ce-DE \ 0.5DMTD-DE | Ce(NO <sub>3</sub> ) <sub>3</sub> and DMTD | 58            | 48           | 24           | 12 Ce + 12 DMTD | 2.1 + 5.8                   | 50 $\pm$ 5 |
| Ce-DE                 | Ce(NO <sub>3</sub> ) <sub>3</sub>          | 58            | 48           | 24           | 24              | 3.7                         | 69 $\pm$ 5 |
| 0.50Ce-DE             | Ce(NO <sub>3</sub> ) <sub>3</sub>          | 58            | 24           | 12           | 12              | 2.1                         | 79 $\pm$ 5 |
| 0.16Ce-DE             | Ce(NO <sub>3</sub> ) <sub>3</sub>          | 58            | 8            | 4            | 4               | 0.8                         | 72 $\pm$ 5 |

A Roland EGX-350 engraver equipped with a conical cemented carbide tip of 0.25 mm in radius (ZECA-2025BAL) rotating at 15000 rpm was used to create controlled scribes on the coated panels. Scribes of 1.0 mm wide, 5.0 mm long and 0.35 mm deep (i.e. well into the metallic substrate) with respect to the coated surface were created without causing lateral delamination (Figure 5.1a). The resulting chips from the engraved zone were removed from the surface by air blowing. For the wet-dry cyclic test the TU Delft logo was engraved using the same set-up but with a smaller tip (0.13 mm in radius, ZECA-2013BAL) and a depth of 0.15 mm with respect to the coating surface (i.e. still well below the metal surface).

### 5.2.2.3. General characterization of the loaded DE particles and coatings

The inhibitor loaded microparticles were evaluated using a JEOL SJM-840 scanning electron microscope (SEM) coupled with energy dispersive X-ray spectroscopy (SEM-EDS) at 5 kV and a Renishaw inVia Confocal Raman spectrometer equipped with a 32 mW laser source at 532-

nm and a Leica objective of 50 $\times$  magnification and numerical aperture of 0.55. In the case of the Raman analysis an effective laser power of 10% was employed for 1 s excitation over 3 accumulations per point (i.e. 3 times 1s exposure).

Cross-sections of the as-prepared coatings were analysed by SEM-EDS at 5 kV after dry-grinding up to grit 4000 with SiC paper. The coatings were analysed for a second time after manual wet-polishing for 20 s to a final roughness of 1  $\mu\text{m}$ . A surface analysis of the scribes after exposure (immersion and wet/dry cycles) was performed using a JEOL JSM-IT100 SEM-EDS in backscattered electron mode (BSE) at 20 kV.

### 5.2.3. Corrosion tests

#### 5.2.3.1. Exposure to large electrolyte volumes (200 ml/cm<sup>2</sup>) and short immersion times

A recently developed 3D printed electrochemical cell combining electrochemical characterisation and real-time optics (Figure 5.1b) was used to monitor the corrosion behaviour at the scribes during continuous immersion (up to 4 days). The details of the hardware used for the testing and the protocol used to extract quantitative information from the under-immersion continuous imaging can be found elsewhere.<sup>27,28</sup> The exposed area to the electrolyte, including the scribe, was 0.5 cm<sup>2</sup> whereby 100 ml of 0.05 M NaCl aqueous solution was used (i.e. 200 ml/cm<sup>2</sup>). The samples were placed vertically with the long side of the scribes perpendicular to the base (Figure 5.1) to avoid the deposition of oxide and inhibitor products inside the scribe due to gravity. All experiments were conducted at room-temperature (20 $\pm$ 2  $^{\circ}\text{C}$ ) under ambient conditions.

A potentiostat Metrohm PGSTAT 302 and a Dino-Lite AM7915MZT USB-camera with a 5.0 megapixel CMOS sensor (2592 $\times$ 1944 pixels) were used for electrochemical tests and optical monitoring of the corrosion reactions. The camera and the electrochemical cell were both placed inside a Faraday cage to avoid external electrical interferences. A three-electrode setup was used consisting of a saturated Ag/AgCl reference electrode (RE), 6.6 mm diameter porous graphite rod as counter electrode (CE) and the scribed coated sample as working electrode (WE). This equipment allowed performing Electrochemical Impedance Spectroscopy (EIS) and Open Circuit Potential (OCP) measurements (i.e. global electrochemistry)<sup>27</sup> in parallel to the optical monitoring. EIS and OCP measurements, each taking 10 to 15 minutes, were performed every 60 minutes in case of stable OCP values ( $dE/dt < 0.1$  mV/s). EIS was performed in the frequency range 10<sup>5</sup>-10<sup>-2</sup> Hz at an amplitude of 10 mV root mean square (RMS) over OCP to minimize the influence of the test on the metal-coating system while still obtaining a reliable response. The potentiostat was controlled via an USB interface through the software package NOVA V1.11.1. A high resolution optical camera placed in front of the scribe and the DinoCapture 2.0 software

package allowed capturing images (1 pixel = 3  $\mu\text{m}$ ) of the scribe surface every 5 minutes while simultaneously performing the electrochemical tests.

The photographs of the scribes were further analysed using a previously reported optical analysis protocol.<sup>27,28,33</sup> This allowed obtaining highly space-temporally resolved quantitative information of the corrosion and inhibition processes in the form of ‘area changed as function of time’. This information is here presented in the form of colour maps of the scribes. To quantify the extent and kinetics of the optically detectable surface phenomena (e.g. pits, corrosion products and/or inhibitor deposition) the so called ‘changed surface area’ ( $S_{\text{changed}}$ ) parameter was calculated over time using equation (5.1):

$$S_{\text{changed}}|_t(\%) = \frac{N_t}{N} * 100 \% \quad (5.1)$$

where  $N_t$  is the number of changed pixels at time  $t$  and  $N$  the total amount of analysed pixels.

#### 5.2.3.2. Exposure to small electrolyte volumes (6.67 ml/cm<sup>2</sup>) and long immersion times

Local electrochemistry (namely LEIS/LEIM) and oxygen concentration measurements at the scribe were performed using a horizontally positioned 3D printed cell (Figure 5.1c). It is important to note that the horizontal position was necessary for the local measurements. The effect of the horizontal vs. vertical position on the overall inhibition should be studied in more detail in future works. Due to the configuration of the cell and the nature of local electrochemistry testing, the setup implied the exposure of a larger area than in the optical-electrochemical setup (3 cm<sup>2</sup>) but to a lower electrolyte volume (20 ml, 0.05 M NaCl) with a film thickness of 3 cm. This resulted in 6.67 ml/cm<sup>2</sup>, near 30 times less than in the optical-electrochemical setup.

Local concentrations of dissolved oxygen in solution were measured using an optical oxygen detector from PyroScience (OXB50) equipped with a 50-70  $\mu\text{m}$  bare fibre microsensor (OXB50) and external 4-wire PT100 temperature sensor. To offer some mechanical support and protection against accidental contact during mounting, the optical fibre was embedded in a glass microcapillary. The probe was positioned with a motorised stage from Sensolitics and located at the centre of the scribe, 50  $\mu\text{m}$  above the metal surface. The temperature-sensor was placed inside the electrolyte and used to calculate the oxygen signal under fluctuating temperatures between 21 $\pm$ 4  $^{\circ}\text{C}$  using the build-in software. The oxygen-levels were recorded every 3 s while the sample and probe were kept stationary to avoid the migration of electrolyte over a period of 15 h.

Local Electrochemical Impedance measurements were performed on a new batch of scribed coatings. A detailed description of the set-up can be found elsewhere.<sup>31</sup> An in-house-developed probe was placed and controlled in the x, y, z directions with the help of a Sensolitics system reaching precision of 1  $\mu\text{m}$  in each axis. The probe was positioned 100 $\pm$ 1  $\mu\text{m}$  above the coating surface. This was achieved by lowering the probe with 1  $\mu\text{m}$  steps until it reached the coating

surface and followed by a 100  $\mu\text{m}$  upwards displacement. Control measurements at heights 110 and 90  $\mu\text{m}$  showed that the obtained admittance values varied less than 1 % thereby showing the robustness of the method with height variations. The probe consists of two vertically displaced 200  $\mu\text{m}$  diameter Ag/AgCl wires allowing for higher spatial resolution compared to commercially available probes.<sup>34</sup> When scanning the sample surface the probe moved with a rate of 0.075 mm/s in x-direction and a step-size of 0.100 mm in the y-direction. The z-position was not changed during scanning. The measurements were performed using a standard 3-electrode setup combined with the probe connected to the auxiliary channels of a Solatron potentiostat XM IMS/s with FRA, under control of interfaced built-in OWISoft and XM-studio software. The three-electrode configuration consisting of a saturated Ag/AgCl reference electrode, platinum wire with a surface area of 50 mm<sup>2</sup> as counter electrode, and the scribed coated sample as working electrode. The measurements were performed using two different protocols: (i) Local Electrochemical Impedance Spectroscopy (LEIS) with the probe in stationarity position at the centre of the scribe while performing a traditional EIS measurement at a frequency range of 10<sup>5</sup>-10<sup>-2</sup> Hz whereby the points around 60 Hz were not taken into account because harmonics from external electrical equipment interfered with the measurements, and (ii) Local Electrochemical Impedance Mapping (LEIM) by moving the probe across a designated area of the scribed coating at a resolution of 0.075 x 0.100 mm per measured point while performing a an impedance measurement at a fixed excitation of 10 Hz. An amplitude similar to the global impedance (10 mV RMS) was found insufficient to obtain stable admittance values from the local probe at low frequencies. It was thereby decided to increase the admittance to 30 mV peak-to-peak while still obtaining a reliable and identical EIS response using the RE compared to 10 mV RMS.

The local potential difference between the wires of the LEI probe ( $\Delta V_{probe}$ ) were scaled to local current densities ( $i_{loc}$ ) through Ohm's law and used to calculate the local impedance per imposed frequency ( $\omega$ ). This involves the potential measured with respect to the reference electrode as shown in equation (5.2) and described in more detail elsewhere.<sup>34</sup>

$$Z(\omega) = \frac{\tilde{V}(\omega) - \Phi_{ref}}{i_{loc}(\omega)} = \frac{\tilde{V}(\omega)}{\Delta V_{probe}(\omega)} * \frac{d}{k} \quad (5.2)$$

Where  $\tilde{V}(\omega) - \Phi_{ref}$  represents the potential difference between the WE and the RE in the bulk solution,  $d$  the distance between the two probes and  $k$  the electrolyte conductivity of the electrolyte.

The calculations to re-construct the local impedance spectra and maps were performed with a dedicated Python script using the time-stamps from impedance measurements and the defined position of the probe from the positioning module.<sup>31</sup> The gradient and magnitude of the local admittance (inverse of impedance) was mapped as a function of x-, and y- position. Admittance

magnitudes were used rather than impedance so that the area of increased electrochemical activity generally appeared as peaks.<sup>31</sup>

### 5.2.3.3. *Wet/dry cyclic tests*

Wet/dry cyclic corrosion tests were performed on the best performing coating according to the long-term immersion testing. This allowed studying the stability of the inhibiting layer at the scribed site under discontinuous immersion conditions. For this the electrochemical cell with small electrolyte volumes (6.67 ml/cm<sup>2</sup>) was used. Each cycle (6 in total) consisted of: (i) exposure to 0.05 M NaCl electrolyte, (ii) electrolyte removal, coating washing with demineralised water and blowing with air, and (iii) drying under ambient conditions for 5 h. The exposure-time of each immersion step (wet) is shown in Table 5.2 and resulted in a total immersion-period of 13 days. After each wet exposure, photos of the scribes were taken with a Digital Microscope Keyence VHX-2000E using a VH-Z20R lens. At the end of the cyclic test the scribes were analysed by SEM/EDS.

**Table 5.2** Exposure time of each wet step during the wet/dry cyclic exposure

| Cycle | Immersion step duration in days |
|-------|---------------------------------|
| 1     | 2                               |
| 2     | 1                               |
| 3     | 2                               |
| 4     | 3                               |
| 5     | 1                               |
| 6     | 4                               |

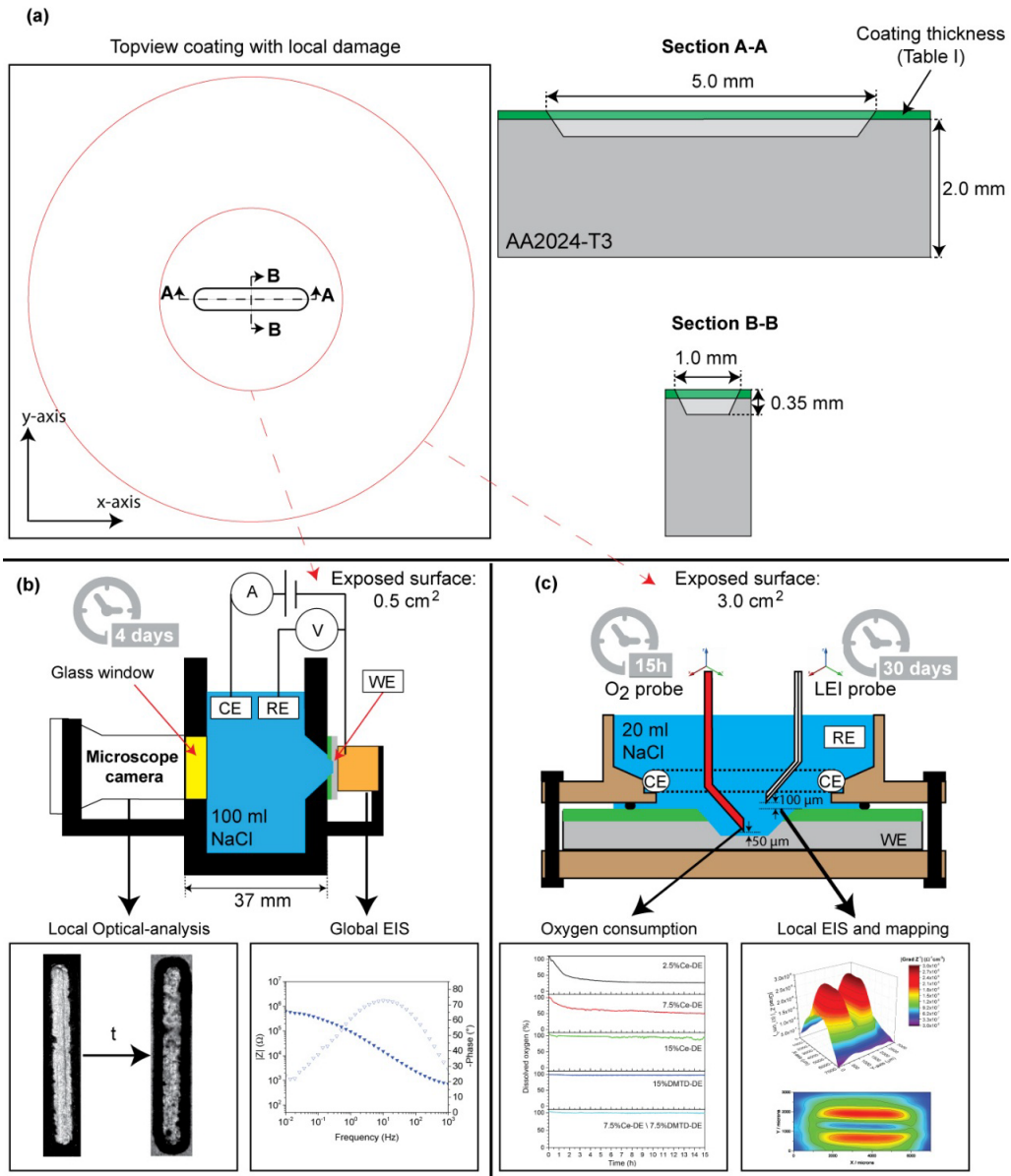


**Figure 5.1** (a) Schematics of local scribe dimensions and exposed areas used in the different cells shown in b and c; (b) optical-electrochemical cell with raw information obtained in the form of pictures and Bode plot; and (c) horizontal cell used for the local oxygen concentration and LEIS/LEIM tests.

### 5.3. Results and Discussion

#### 5.3.1. DE loading, release and coating evaluation

Figure 5.2 shows representative SEM images, EDS spectra and Raman results for the hollow diatomaceous earth (DE) microparticles before and after inhibitor loading with cerium salt and DMTD. A clearly visible layer with a high content of cerium is observed on the surface and pores of the Ce-loaded DE particles (Figure 5.2b and d). No inhibitor film around the particles surface was detected with SEM/EDS for the case of DMTD-modified DE (Figure 5.2c). Raman analysis (Figure 5.2e) on the other hand confirmed the presence of the DMTD by the detection of high intensity peaks corresponding to the vibrational signals of DMTD as reported elsewhere.<sup>35</sup> This suggests a higher loading inside the particles than in the case of the cerium loaded DE. Volumetric calculations on inhibitor-loaded microparticles indicates that less than 2 vol.% of the available internal volume is filled with inhibitor. This highlights that higher loadings per particle can be expected when using improved loading protocols.

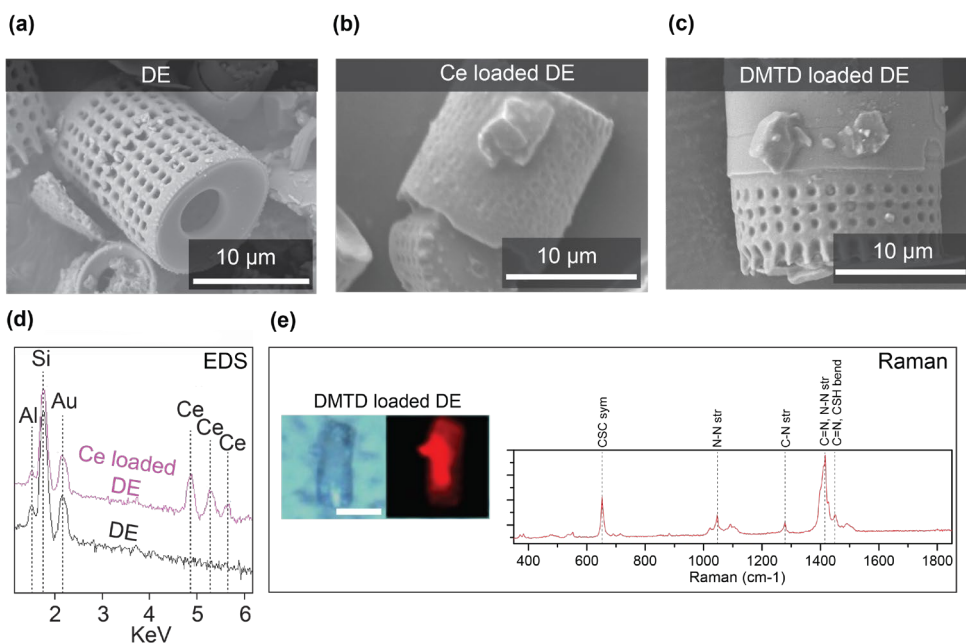


**Figure 5.2** SEM images of DE microparticles before (a) and after inhibitor loading with  $\text{Ce}(\text{NO}_3)_3$  (b) and DMTD (c). EDS spectra of the Ce loaded DE (d) and Raman results of the DMTD-loaded DE (e).

Figure 5.3 shows SEM/EDS micrographs of the epoxy coatings containing DE, Ce-DE, DMTD-DE and 0.5Ce-DE/0.5DMTD-DE after dry (Figure 5.3a) and wet-polishing (Figure 5.3b). The DE particles appear as silica clusters with a diameter between 5 and 30 μm distributed homogeneously over the entire cross-section of the coating in the case of the non-loaded DE,

and as highly agglomerated particles in the case of the Ce-DE. Higher levels of silica are detectable by EDS in the case of non-loaded DE than for the inhibitor-loaded ones. This is in good agreement with the higher DE microparticle loading in the case of the non-loaded DE coating (see Table 5.1, 48phr DE microparticles vs. 24 phr). Moreover, when wet polishing was used (Figure 5.3b), large open spaces appeared in and around the inhibitor-loaded DE particles. We attribute this effect to the local dissolution of cerium and DMTD salts and the removal of the surrounding coating matrix by the small amount of ethanol used during polishing. These results confirm that the inhibitors are located inside and around the DE particles after dispersion in the epoxy/amine coating.

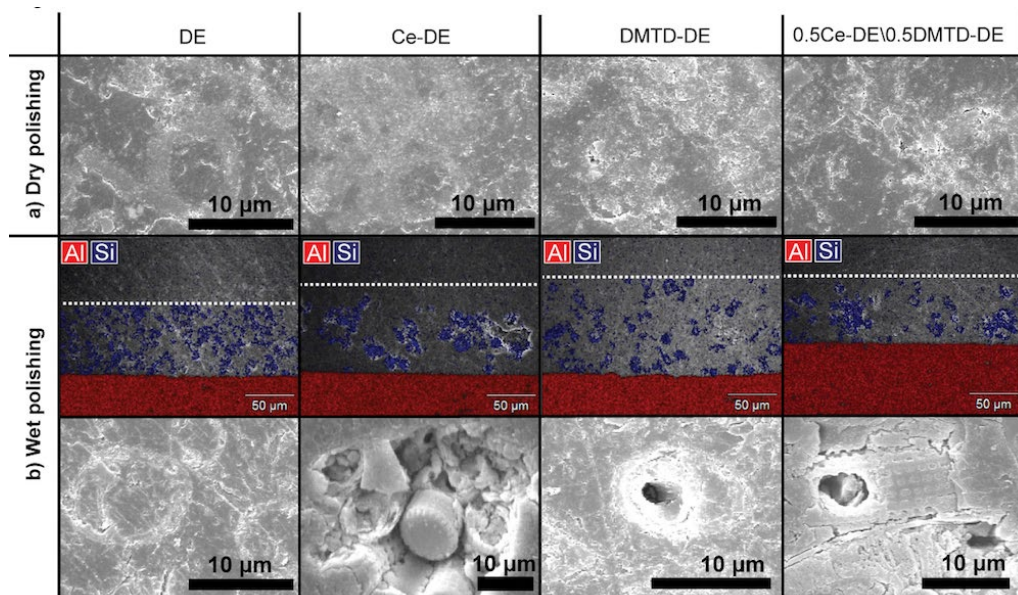


**Figure 5.3** SEM and SEM/EDS micrographs of the coating cross-sections after dry (a) and wet (b) polishing. The white dotted line highlights the interface between the coating and the casting resin. Blue regions indicate the presence of DE particles and the red regions indicate the AA2024-T3 substrate.

### 5.3.2. Global electrochemistry and spatially resolved real-time optics: exposure to large electrolyte volume per exposed damaged area

Figure 5.4 shows selected EIS Bode plots ( $|Z|$  and phase) of the studied coatings after 3 h (Figure 5.4a) and 90 h (Figure 5.4b) immersion obtained with the optical-electrochemical setup (Figure 5.1b). The corresponding Nyquist-plots can be found in the SI-5.2 The coating with unloaded DE is not shown since the results are comparable to those of the unloaded epoxy reference coating.

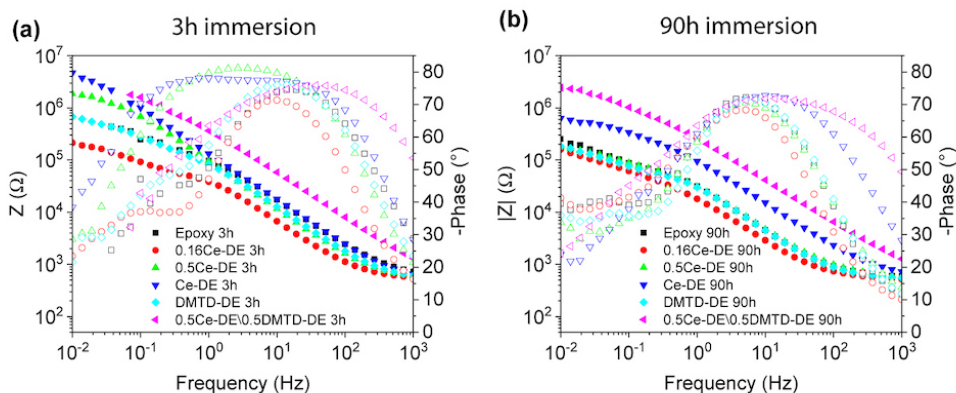


**Figure 5.4** Bode plots (total impedance and phase angle as function of frequency) of six scribed coatings after immersion in 200 ml/cm<sup>2</sup> 0.05 M NaCl for 3 h (a) and 90 h (b). Unstable points at low frequencies have been removed in accordance to large Kramers-Kronig residual errors.

At short immersion times (3 h, Figure 5.4a), the sample containing two inhibitors (0.5Ce-DE/0.5DMTD-DE) shows the highest total impedance. This is closely followed by the coating containing cerium at the same total inhibitor phr content but near two times more cerium in wt.%, namely Ce-DE, and the sample containing half the total inhibitor phr content (0.5Ce-DE). Interestingly, the phase angle for 0.5Ce-DE/0.5DMTD-DE is less broad and more located towards lower frequencies than the phase of Ce-DE and 0.5Ce-DE, which also show equally broad phase angle. The sample with the lowest cerium content (0.16Ce-DE) shows lower total impedance than the epoxy non-loaded coating, which in turn is similar to the total impedance of the sample containing only DMTD (DMTD-DE). This indicates a low degree of corrosion protection in these three samples. Despite the impedance loss over time in all cases (see SI-5.3, time evolution of impedance at 0.01Hz), the overall trend shown Figure 5.4b does not change during the 90 h immersion. As seen in Figure 5.4b, the 0.5Ce-DE/0.5DMTD-DE and Ce-DE coatings show significantly higher impedance values over the whole frequency range and the absence of pitting evidence at low frequencies based on the phase angle. These results confirm good corrosion protection under immersion conditions and are in agreement with our previously reported work with Ce-loaded DE.<sup>22</sup> While high impedance values at low and medium frequencies are often used to describe the degree of corrosion protection,<sup>16,36,37</sup> this assumption is not always valid for the inhibitors used in this work.<sup>27</sup> Highly resolved optical measurements during immersion help improving the interpretation of such signals.

Figure 5.5 shows optical micrographs and colour-gradient maps resulting from the image analysis at selected immersion times as obtained with the real-time optical-electrochemical set-up. The colour-gradient images allow visualizing the severity of the local surface changes over time (i.e. effect of pitting, de-alloying, inhibition, oxide formation), in which darker colours

relate to higher surface changes (i.e. higher degradation or oxide build up). The original images can be found in SI-5.4.

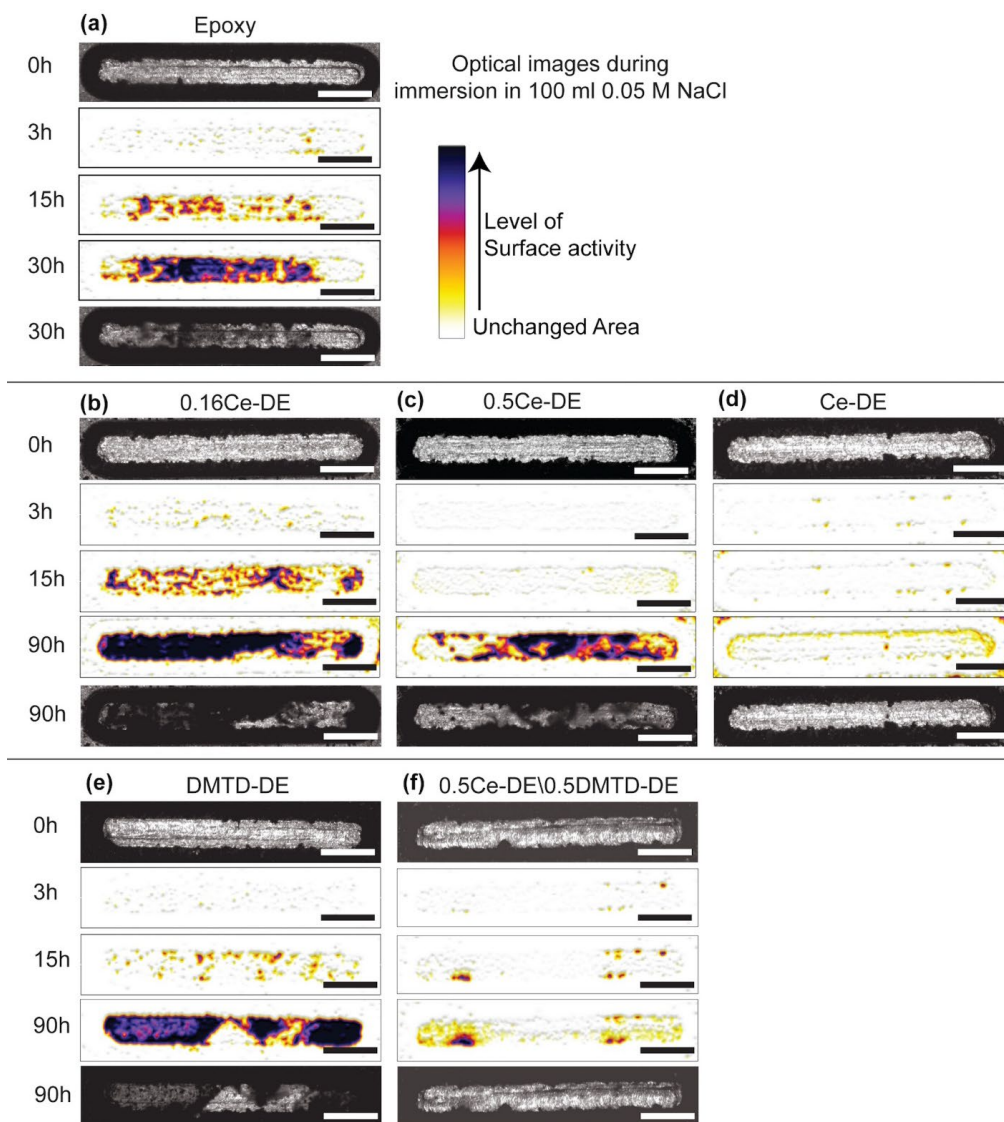


**Figure 5.5** Optical images of six coated systems obtained with the real-time optical-electrochemical set-up at 0, 3, 15 and 90 h immersion. Colour-images are the result of the implementation of the optical image analysis protocol. Scale bars represent 1mm.

At 3 h of immersion the non-inhibited epoxy coating (Figure 5.5a) already shows the presence of multiple grey and yellow spots with diameters between 5 and 50  $\mu\text{m}$  together with a couple of larger red-coloured spots with diameters above 50  $\mu\text{m}$ . The smaller grey-yellow locations can be related to initiation of local corrosion processes (e.g. intermetallic dissolution and

trenching),<sup>38</sup> while larger red areas relate to pitting and early-stage cooperative corrosion.<sup>39,40</sup> After 15 h immersion, large dark-purple and black spots surrounded by red and yellow rings become evident, indicative of oxide deposits. As the dimension of these features is larger than the reported mean intermetallic particle diameter (2-5  $\mu\text{m}$ ) their appearance can be related to the start of subsurface corrosion processes (i.e. intergranular corrosion).<sup>41,42</sup> The dominance of black and purple areas all over the exposed scribe at 30 h immersion is indicative of generalized subsurface corrosion and cooperative corrosion (i.e. advanced corrosion). In agreement with this, the large amount of corrosion products at the scribe location did not allow further optical analysis at longer immersion times for this sample. Comparable results were obtained for the coating with the lowest cerium concentration of (0.16Ce-DE, Figure 5.5b), well in agreement with the EIS results.

The samples with the higher cerium content (0.5Ce-DE (Figure 5.5c) and Ce-DE (Figure 5.5d)) showed a clear delay in the appearance of the first surface phenomenon related to corrosion (15 and 90 h respectively). At 90 h of immersion only the sample with the highest cerium content showed significant protection of the exposed metal surface based on the absence of detectable surface degradation in agreement with the EIS results.

Similarly to the Ce-containing samples, the DMTD containing coatings (DMTD-DE (Figure 5.5e) and 0.5Ce-DE/0.5DMTD-DE (Figure 5.5f)) show a clear delay in the appearance of surface degradation. The apparent inhibiting effect observed in the DMTD-DE sample at times below 15 h could not be easily extracted from the EIS results (Figure 5.4), highlighting the importance of the real-time optical inspection. The absence of protection at immersion times longer than 15 h suggests that DMTD is too instable at the surface or that there was insufficient DMTD release. On the other hand, the combination of cerium and DMTD (0.5Ce-DE/0.5DMTD-DE) shows significantly better results than the same amount of cerium alone (0.5Ce-DE) or higher contents of DMTD alone (DMTD-DE). Nevertheless, at 90 h immersion signs of local degradation can be seen. Interestingly, the EIS results ranked this sample as the best one despite the appearance of surface attack, while the Ce-DE sample showed less optically detectable surface attack and lower impedance, once more highlighting the need for in situ optics while electrochemical tests are being performed for a better understanding of the on-going degradation/protection processes.

Besides a qualitative analysis, the optical data can be used to obtain quantitative degradation kinetics. Figure 5.6 shows the percentage of changed area in time for the studied coatings.

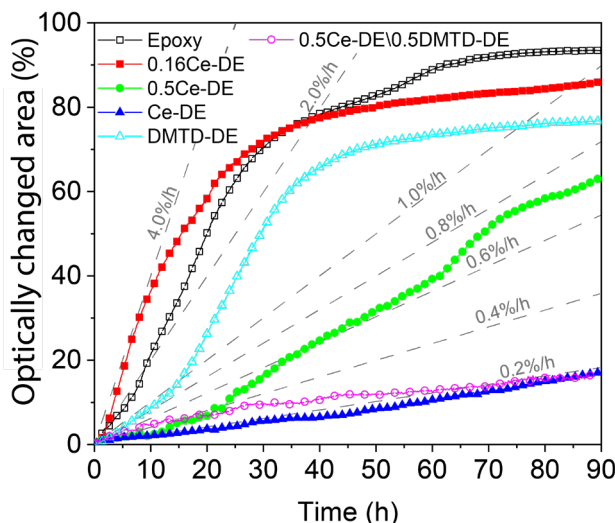


**Figure 5.6** Time evolution of the optically-detectable surface changes after image data treatment of the six coating systems. The grey dashed lines are added to give an impression of different degradation rates (%/h) so the reader can easily identify degradation rates for each coating during a specific exposure time.

As seen in Figure 5.6, the non-inhibited system and the coating with low cerium content (0.16Ce-DE) show fast degradation kinetics (2–4 %h<sup>-1</sup>), comparable to those previously reported for non-inhibited AA2024-T3 exposed to similar salt concentrations.<sup>22,27</sup> Despite the initial differences in degradation kinetics, both systems reached about 70 % changed area within 30 h immersion. The faster degradation for the 0.16Ce-DE sample suggests that very low inhibitor concentrations may promote corrosion processes such as pitting. Similar results were previously described for coatings containing chromates below a critical amount.<sup>43</sup>

The coatings with higher cerium content (0.5Ce-DE and Ce-DE) show one order of magnitude slower degradation kinetics (0.2–0.4 %h<sup>-1</sup>) during the first 20 h of immersion. Between 20 and 60 h immersion the changed-area growth kinetics for the 0.5Ce-DE tripled (0.6–0.8 %h<sup>-1</sup>) suggesting a drop in the inhibiting power of this coating. The sample with the highest cerium content (Ce-DE) maintained a constant and low changed-area growth kinetics during the whole immersion time (0.2%h<sup>-1</sup>).

The DMTD coatings (DMTD-DE and 0.5Ce-DE\0.5DMTD-DE) also have significantly slower changed-area growth kinetics (0.4–1.0 %h<sup>-1</sup>) during the first 15 h compared to the epoxy system, confirming that the local corrosion processes are inhibited during this period. After 15 h the kinetics increase for DMTD-DE reaching similar values to those of the unprotected coatings (2.5 %h<sup>-1</sup>). These results once more indicate that DMTD was released and inhibited the corrosion process during the first hours of immersion but that this effect was lost after 15 h most likely due

---

to insufficient release of DMTD and/or lack of stability at the metal surface. On the other hand, the coating with two inhibitors (0.5Ce-DE\0.5DMTD-DE) showed an interesting decrease in the degradation growth kinetics after 15 h (from 0.4 to 0.2 %h<sup>-1</sup>) thereby reaching values similar to the coating with twice the cerium content (Ce-DE). This highlights the synergy between the Ce and DMTD and is in good agreement with previous studies reporting on this effect.<sup>16,44</sup> It is nevertheless important to note that the actual mechanism for this synergy is not yet fully understood.

### 5.3.3. Spatial and temporally resolved local corrosion processes: exposure to small electrolyte volumes per exposed damaged area.

Figure 5.7 shows the oxygen concentration evolution during the first 15 h of immersion. A measurement on a coating without inhibitors (DE) is used as negative control and is shown as a grey dotted line in Figure 5.7. Although the tests were performed at the centre of the damage and they might therefore not be representative of the whole scratch, there was a very good agreement with the EIS results as discussed further on. These results reveal certain key differences as function of the inhibitor type and concentration used. Higher cerium contents (Ce-DE) lead to lower oxygen concentration depletion but also more instable signals after the first 6 h of immersion. When the organic inhibitor DMTD was used, with or without cerium (i.e. DMTD-DE and 0.5Ce-DE\0.5DMTD-DE), very stable high oxygen concentrations were measured.

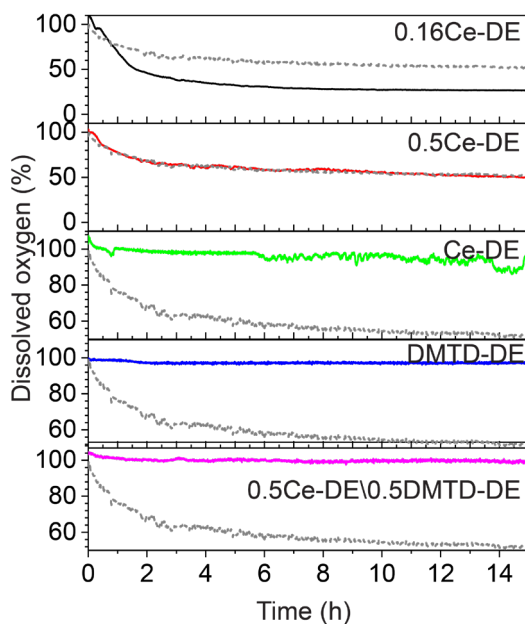


**Figure 5.7** Time-evolution of dissolved oxygen concentration at 50  $\mu\text{m}$  above the scribe during exposure to 20 ml 0.05 M NaCl. A measurement on a coating without inhibitors (DE) is used as negative control and shown as a grey dotted lines.

Low cerium concentrations (0.16Ce-DE) show a significant drop in  $\text{O}_2$  concentration with the immersion time, even sharper than the DE coating without inhibitors (grey dotted line). Such an  $\text{O}_2$  drop appeared faster (within the first 5 h) and more pronounced (reaching 25 %) for the lowest cerium content when compared to the drop observed at higher Ce contents or in the presence of DMTD thereby confirming that the sharp drop in oxygen consumption is related to the presence of redox processes related to corrosion. As shown in previous works<sup>29,45</sup>, this oxygen drop can

be related to the oxygen consumption in the cathodic reactions involved in the corrosion process, which, depending on the pH and thermodynamic local conditions, will mainly appear as reactions (5.3) and (5.4):



The level at which the oxygen concentration reaches an equilibrium can be directly related to the balance between the oxygen consumption due the redox reactions at the metal surface and the diffusion-driven oxygen replenishment from the electrolyte and surrounding air. Considering this, the oxygen measurement for 0.16Ce-DE is in perfect agreement with the results shown in Figure 5.5 and Figure 5.6 where the lowest cerium content led to faster degradation kinetics in the first hours of immersion compared to the coating without any inhibitor present (even when different samples were used). This suggests that cerium contents below a so far unspecified minimum can lead to increased corrosion rates. On the other hand, the coating with three times more cerium content (0.5Ce-DE) shows almost the same oxygen consumption compared to the coating without any inhibitors, while the results shown in Figure 5.5 and Figure 5.6 for this coating did show sign of inhibition. This indicates that the oxygen depletion rate due to the oxidation process has been reduced due to the presence of cerium and is similar to the oxygen replenishment rate, thereby indicating some inhibiting effect in good agreement with the EIS tests.

The coating with the highest level of cerium (Ce-DE) showed a sharp oxygen depletion peak during the first hour of immersion followed by full replenishment, which remained stable until 6 h of immersion. This first drop of oxygen and replenishment seems to be in good agreement with the protection mechanism of cerium ions, which have been reported to be efficient inhibitors after an initiation period of 30 to 180 min immersion.<sup>46-48</sup> After 6 h, reproducible oxygen fluctuations around the 80-100 % oxygen concentration appeared. These fluctuations are here attributed to processes related to corrosion initiation and inhibition such as: (i) sudden redox events related to local activation of intermetallic particles followed by immediate passivation, or/and (ii) the deposition of cerium ions at cathodic sites and passive film growth through the reaction (5.5),<sup>47</sup> followed by fast oxygen replenishment via diffusion:



The addition of DMTD highly hindered the oxygen depletion and led to very stable oxygen concentration profiles at the centre for the scribe thereby suggesting a strong effect of DMTD in hindering the redox reactions during the first 15 h of immersion in small electrolyte volumes, thus considering oxygen replenishment kinetics from solution and air.

Since the samples with low cerium content showed significant corrosion already during the first 4 days of immersion in all previous experiments, it was decided to monitor the local electrochemical signal distribution only for the best performing samples and one reference. The set-up shown in Figure 5.1c allowed measuring global EIS as well as local EIS. Both methods led to comparable results, see Bode and Nyquist plots in SI-5.5, which validate the impedance measurements near the metal surface as opposite to other local techniques such as SVET.<sup>49</sup> It was decided to perform the local impedance mapping (LEIM) at 10 Hz frequency in good agreement with literature where this frequency is used to validate comparably damaged coating with LEIM.<sup>30</sup> At this frequency the impedance values reflect the kinetics of charge transfer at the metal/electrolyte interface. Therefore, the measured impedance values should be proportional to the corrosion current through Stern-Geary relation and thereby be a direct relation to the inhibition power of the different systems.<sup>50</sup> Moreover, this frequency is representative for the detection of different behaviours between samples, as can be seen in the Nyquist plots (SI-5.5). Figure 5.8 shows a selection of the obtained LEIM results after 4, 10, 24 and 30 days and their related optical micrographs. All the obtained original LEIM maps (including measurements performed at different days of immersion) can be found in SI-5.6.

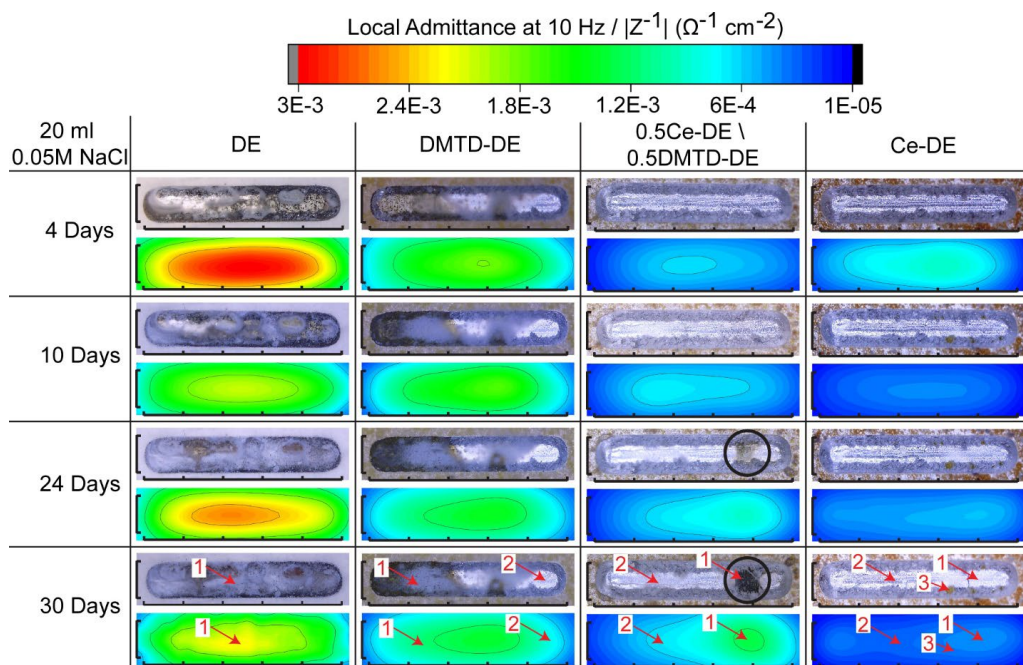


**Figure 5.8** Representative LEIM results (admittance modulus  $|Z^{-1}|$  maps) obtained at 10 Hz and 100  $\mu\text{m}$  above the scribed coating and the corresponding in-situ optical images as function of the immersion-time. LEIM maps resolution is 0.075 x 0.100 mm with 0.1 mm step size (960 points per map). The probe-to-sample distance was identical in all cases (100 $\pm$ 1  $\mu\text{m}$  above the coating). Arrows and numbers indicate the locations where post-exposure SEM/EDS analysis was performed. Distance between ticks in the x-axis of the images correspond to 1 mm.

When the LEIM tests were finished (30 days immersion) an SEM-EDS analysis of the scribes was performed. The main locations of interest are marked with arrows and numbers in Figure 5.8. Figure 5.9 and Table 5.3 show backscattered SEM images and the composition by EDS in atom.%, respectively of these locations.

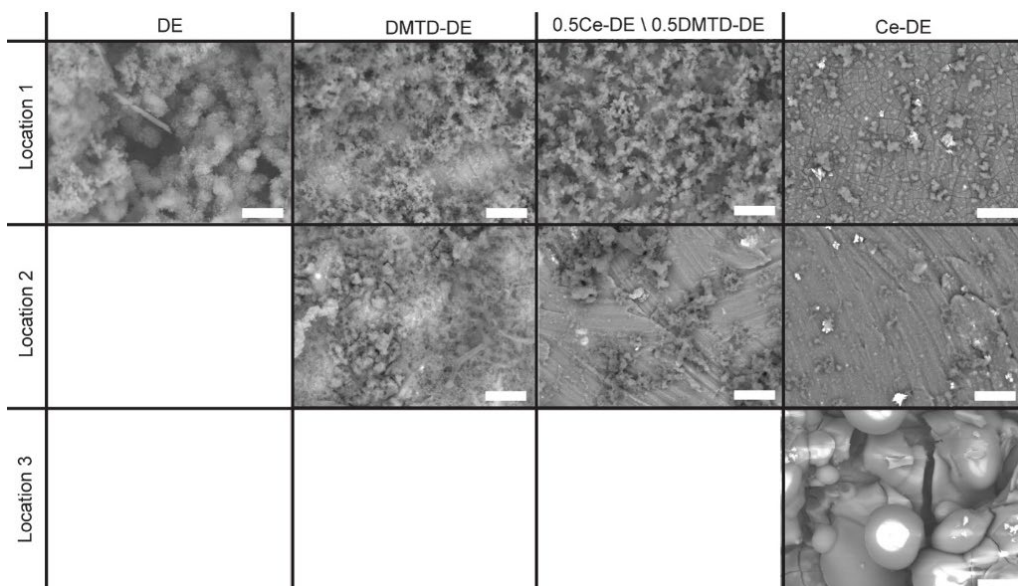


**Figure 5.9** SEM micrographs in BSE mode after 30 days immersion at the locations marked with arrows and numbers in Figure 5.8. Scale bar represents 10  $\mu\text{m}$ .

**Table 5.3** EDS analysis of the marked locations in Figure 5.8 and shown in Figure 5.9. Results are shown in atom.%.

| Sample – location           | O    | Al    | Cu   | Zn  | Mg  | Cl  | S   | Ce  |
|-----------------------------|------|-------|------|-----|-----|-----|-----|-----|
| DE – 1                      | 70.9 | 26.2  | -    | 2.5 | -   | -   | -   | -   |
| DMTD-DE – 1                 | 73.9 | 24.1  | -    | -   | -   | -   | 1.3 | -   |
| DMTD-DE – 2                 | 35.3 | 61.9  | 1.4  | -   | 1.1 | -   | -   | -   |
| 0.5Ce-DE/<br>0.5DMTD-DE – 1 | 70.4 | 24.4  | -    | -   | -   | 1.2 | -   | 3.4 |
| 0.5Ce-DE/<br>0.5DMTD-DE – 2 | 56.7 | 38.13 | 1.5  | -   | -   | -   | -   | 3.5 |
| Ce-DE – 1                   | 61.4 | 25.0  | 13.7 | -   | -   | -   | -   | -   |
| Ce-DE – 2                   | 75.3 | 25.0  | -    | -   | -   | -   | -   | -   |
| Ce-DE – 3                   | 56.0 | 39.1  | -    | -   | 1.3 | -   | -   | -   |

\*Table shows the elements that were detected above 1 atom %

As can be seen in Figure 5.8, after 4 days of immersion clear oxides are visible in the DE and DMTD-DE samples accompanied by high admittance values (red and green colours). These results under small electrolyte volumes are similar to the previous optical and electrochemical

results in large electrolytes (Figure 5.4, Figure 5.5, and Figure 5.6) showing high surface activity and low impedance values well before 4 days immersion. As can be seen in the optical images, the amount of oxide products in the non-inhibited DE sample kept increasing with the immersion time to grow as a thick heterogeneous layer containing  $\text{Al}_2\text{O}_3$  and traces of  $\text{ZnO}$  (Figure 5.9 and Table 5.3), which is in good agreement with previous long-term exposure measurements to 0.05 M NaCl for AA2024-T3.<sup>48</sup> At 10 days of immersion the thick aluminium oxide layer already masked the metal surface to the local probe resulting in a slight decrease of the local admittance.

Interestingly, the DMTD sample did not show this massive oxide growth. These findings combined with no oxygen concentration drop during the first hours (Figure 5.7) suggest that DMTD-loaded DE are able to partially protect the metal surface during the first hours of immersion. At longer times nevertheless (beyond one day immersion) the protection is deactivated and corrosion is initiated. However, the formed oxides remained stable at least between 10 and 30 days of immersion limiting further degradation in a not-yet fully understood process. The SEM-EDS analysis of the samples after 30 days immersion (Figure 5.9) confirmed the presence of thin granular structures primarily containing Al and O (location 1 and 2) with traces of sulphur from the DMTD (location 1), copper (location 2) and magnesium (location 2). Even when considering the quantification limitations of EDS, at location 2, an area that remained bright during the 30 days immersion, the amount of detected oxygen resulted below the stoichiometric values for pure aluminium oxides or hydroxides, thereby suggesting lower levels of oxidation (i.e. a thinner layer) and a positive effect of the corrosion inhibitor.

The coating containing both cerium and DMTD loaded DE (0.5Ce-DE\0.5DMTD-DE) shows a significantly lower amount of surface changes (optical images) together with low admittance values (blue colours) in time. This is a clear sign of high levels of active corrosion protection at large scribes. Despite the obvious good performance, at 24 days immersion, a region showing optically detectable changes was observed (marked with a black circle in Figure 5.8). This area slowly but steadily became darker and bigger with the immersion time. At the end of the immersion period, the SEM-EDS analysis of this area (location 1) confirmed the presence of oxide features comparable to those observed in the DMTD-DE sample, although with a significant amount of detectable cerium (>3 atom.%). A different location apparently not attacked by corrosion (location 2 for this sample in Figure 5.8) showed a significantly lower amount of oxygen, comparable cerium content and traces of copper (Table 5.3). Considering the metal-oxygen atomic ratios of  $\text{Ce}_2\text{O}_3$ ,  $\text{Ce}(\text{OH})_3$ ,  $\text{Al}_2\text{O}_3$ , and  $\text{Al}(\text{OH})_3$  these results suggest the presence of a cerium oxide layer at these locations. The absence of sulphur traces could be due to the inhibitor being below the detection limit of SEM-EDS. Considering the limited corrosion protection levels achieved with the samples 0.5Ce-DE (Figure 5.6 and Figure 5.7) and DMTD-DE (Figure 5.8), the results are a clear indication of a significant synergetic effect between DMTD and cerium, at least when present in DE containers.

A more remarkable result was obtained for Ce-DE sample. This coating remained stable with no obvious sign of degradation at the scribe during the whole duration of the experiment (30 days). Only small changes in admittance (off-centred local maxima) were measured at long immersion times as indicated by arrows in Figure 5.8. The SEM-EDS analysis at this location (location 1 in the Figure 5.8 for this sample) showed an homogenous but cracked thin layer similar to those of cerium conversion layers<sup>51</sup> and for excessive growth of Ce-containing precipitates.<sup>52</sup> Nevertheless, no clear signs of cerium was detected by SEM-EDS or Raman. The compositional analysis at this location showed a composition close to  $\text{Al}(\text{OH})_3$  with higher copper levels than expected for AA2024-T3 (i.e. max 5 wt.%), thereby suggesting the deposition from de-alloyed copper-rich intermetallic particles. The EDS analysis at other two locations (location 2 and 3) also did not confirm the presence of cerium despite the clear smooth surface at location 2. Location 3 on the other hand showed significant amounts of Mg which together with the low amount of oxygen could indicate formation of a Mg-Al oxide. It should be noted that the low corrosion activity at the scribe was accompanied by the absence of delamination during the whole immersion period as indicated by the stability of the admittance local maxima (SI-5.6) and the different optical images. To the best of our knowledge, and despite the lack of evidence of the presence of cerium at the scribe, these remarkably high levels of protection of large scribes (1 mm wide and 0.35 mm deep) for such long immersion times ( $\geq 30$  days) have only been reported for Cr(VI) containing coatings such as commercial coatings containing significantly higher amounts of inhibitor (e.g. 16 wt.%  $\text{SrCrO}_4$ ).<sup>30</sup>

#### 5.3.4. Effect of electrolyte volume per exposed area on the corrosion protection

The optical-electrochemical analysis using large volume-to-exposed area ratios ( $200 \text{ mL}/\text{cm}^2$ ) as exposed in Figure 5.6 shows that higher content of cerium-loaded particles or the partial replacement of cerium by DMTD lead to higher levels of corrosion inhibition. It should be noted that the remarkable protection at large damages in the case of the best performing coatings, Ce-DE and 0.5Ce-DE/0.5DMTD-DE, is achieved at very low active inhibitor contents (Table 5.1). Nevertheless, the continuous increase of optically detectable surface changes measured during the first 4 days immersion suggests that the protective effect will eventually be (partially) lost as it is not enough to fully stop the degradation growth (corrosion) in the presence of large electrolyte volumes. Interestingly, the oxygen measurements and LEIM tests performed under smaller ratios of electrolyte ( $6.67 \text{ mL}/\text{cm}^2$ ) showed efficient protection at longer immersion times. Under small electrolyte ratios, DMTD-DE showed a good degree of protection during the first 15h immersion while Ce-De and 0.5Ce-DE/0.5DMTD-DE maintained their high levels of protection well beyond 4 days of immersion. Despite the good results when exposed to low volumes, the two best performing samples also start showing some signs of protection loss at around 30 days immersion. The eventual loss of protection with the immersion time suggests an insufficient inhibitor supply at the damaged site to cope with the apparent stability loss of the

inhibiting layer on the metal surface, these effect being more identifiable when large electrolytes are used. The results show that further studies are required to better understand the effect of electrolyte volume and inhibiting layer stability on the long term protection while highlight the need of continuous inhibitor supply.

### 5.3.5. Performance during wet/dry cyclic test

In the above sections the potential of inhibitor-loaded exoskeletons to protect coated metals at large scribed sites for long immersion times was demonstrated with remarkable results. Nevertheless, most applications are expected to work under wet-dry cyclic exposure which may affect the inhibiting behaviour of anticorrosive coatings. In this last section we performed a preliminary study of the effect of wet/dry cycles during the immersion period and compared the behaviour to the continuous immersion results obtained for the best performing system (Ce-DE). Figure 5.10 shows the optical images taken right after the drying step following the protocol exposed in the experimental section.

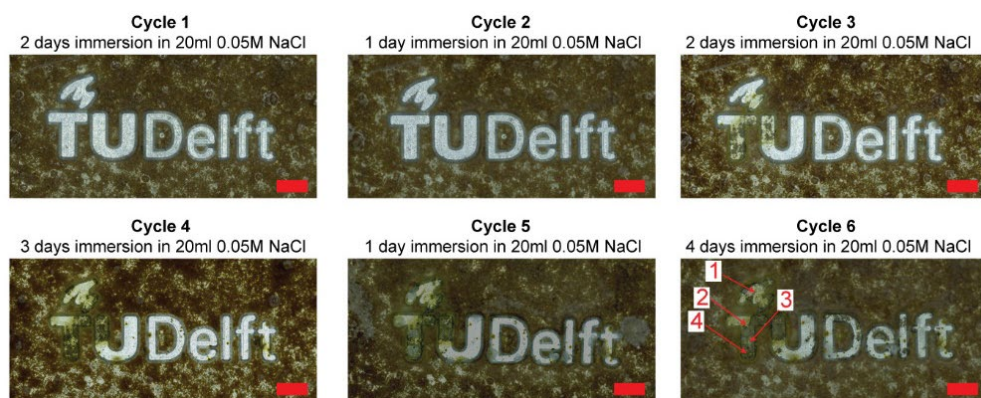


**Figure 5.10** Optical images of the best performing coating according to continuous immersion (Ce-DE) with the “TU Delft” logo engraved. Micrographs show the evolution with the wet/dry cycles. For each immersion period fresh 20 ml 0.05 M NaCl electrolyte solutions were used. Locations marked with arrows and numbers were analysed by SEM-EDS. Scale bars represent 1mm.

In Figure 5.10 it can be seen that the Ce-DE coating was able to protect the exposed aluminium surface (i.e. TUDelft logo) completely during the first 2 wet-dry cycles. After the second drying step followed by 3 days immersion (third cycle) the first optical changes in the logo can be seen, roughly 25 % of the exposed surface and mainly located at the widest scribed sites (letters T and U). Subsequent wet/dry cycles led to more surface changes until the test was stopped. After the cyclic test roughly 50 % of the metal surface (TUDelft logo) remained as bright as the non-exposed substrate. Interestingly, with the immersion time, the exposed metal area became yellowish, a clear indication of cerium oxide being formed on the surface.<sup>53,54</sup>

In order to identify the nature of the deposits visible in Figure 5.10, a number of SEM-EDS analysis were performed at the locations marked with arrows and numbers in Figure 5.10. The SEM micrographs and the EDS results can be seen in Figure 5.11 and Table 5.4 respectively.

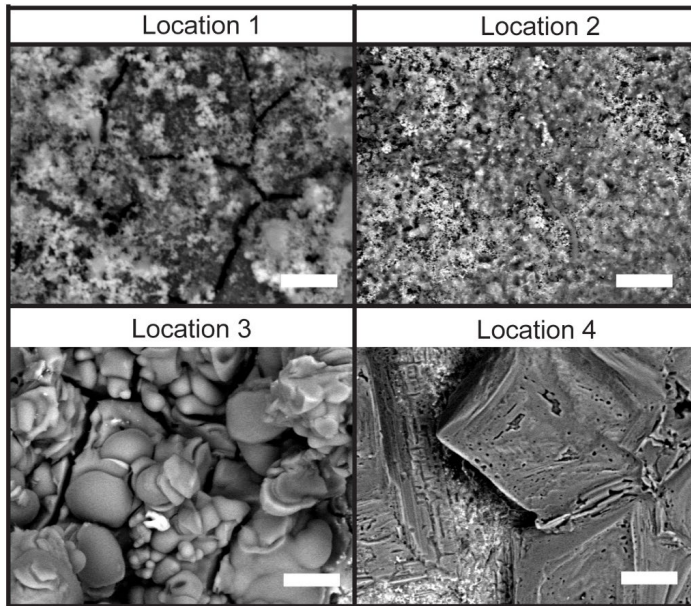


**Figure 5.11** SEM micrographs in BSE mode for the Ce-DE coating after 6 wet/dry cycles. Locations correspond to those marked in Figure 5.10. Scale bar represents 10  $\mu\text{m}$ .

**Table 5.4** EDS analysis for the locations shown in the SEM-BSE images in Figure 5.11. Results are in atom%.

| Location | O    | Al   | Cu  | Cl   | Ce  |
|----------|------|------|-----|------|-----|
| 1        | 42.7 | 17.3 | 2.9 | 4.8  | 4.1 |
| 2        | 60.3 | 29.1 | -   | 6.6  | -   |
| 3        | 47.3 | 15.7 | -   | 32.1 | 4.3 |
| 4        | 10.6 | -    | -   | 87.9 | 1.0 |

\*Table shows the elements that were detected above 1 atom %

As seen in Figure 5.11, comparable features as those observed in the Ce-DE sample exposed to continuous immersion during 30 days (Figure 5.9) are observed for locations 1 to 3 during wet/dry cycles. Nevertheless, the cyclic wet/dry test also led to the formation of a thicker and more pronounced, presumably protective, layer with significant traces of cerium at different locations (Table 5.4). Locations 1 and 3 can be considered comparable in terms of composition although considerably higher levels of Cl, not measured during the continuous immersion tests, are detected at location 3. Despite these results the most surprising structures are found in

location 4. At this location no Al was detected while relatively big crystalline structures containing chlorine, cerium and oxygen were observed. These crystalline structures remained after washing the exposed surface with demi-water several times, thereby demonstrating their high stability. Notwithstanding the darkening and yellowing, the relatively low Al contents in all the locations together with the high levels of oxygen and cerium suggests, at least, some partial stable passivation of the exposed metal surface by the cerium released from the Ce-DE particles. It is important to note that for these tests the precise procedure, such as additional rinsing steps between the wet-dry exposure, can have an effect on the degree of protection. Our results do however confirm a significantly different behaviour when dry cycles are included in the exposure protocol and highlight the need for more dedicated studies including so called wet/dry cycles.

## 5.4. Conclusions

Corrosion protection by inhibitor-loaded naturally occurring silica microparticles (i.e. diatomaceous earth) to protect wide and deep scribes (up to 1 mm wide and 350  $\mu\text{m}$  deep) was studied. The diatomaceous earth particles were loaded with cerium nitrate and 2,5-dimercaptothiadiazole (DMTD). The corrosion inhibition performance of epoxy-amine coatings containing different amounts of loaded particles and corrosion inhibitors was then evaluated under continuous immersion and during cyclic (wet/dry) conditions using in-situ real-time optical electrochemical setup and local electrochemistry.

It was found that even when the loading of corrosion inhibitor in the diatomaceous earth is far from optimized (i.e. containing large free volumes), corrosion protection was achieved for at least 30 days immersion in salt solution with coatings containing as low as 3.7 wt. % active inhibiting component (i.e.  $\text{Ce}^{3+}$ ). The coatings loaded only with an organic inhibitor (DMTD) did not result in significant corrosion protection possibly due to insufficient inhibitor release. Nevertheless, the use of a limited amount of DMTD together with cerium led to a remarkable increase in the efficiency while coatings containing similar cerium content were unable to protect the damages for long times. This points at the synergy between the two inhibitors when loaded into diatomaceous earth. Nevertheless, the corrosion protection significantly reduces in terms of immersion time when the samples are exposed to larger electrolyte volumes. Finally, wet/dry cyclic tests showed that drying steps and cumulative supply of fresh electrolyte can increase the build-up of stable inhibitor-containing layers compared to more commonly performed immersion testing. The long-term protection show the potential of this technology as well as the need for tests other than continuous immersion to better understand the limitations and potential of upcoming novel anticorrosive concepts.

## 5.5. References

- 1 Surface Engineering Association, “REACH and the impact of Hexavalent Chromium,” *Surface Engineering Association*, 2019. <https://www.sea.org.uk/blog/reach-and-the-impact-of-hexavalent-chromium/> (accessed Mar. 01, 2020).
- 2 E. Eichinger, J. Osborne, and T. Van Cleave, “Hexavalent chromium elimination: An aerospace industry progress report,” *Met. Finish.*, vol. 95, no. 3, pp. 36–41, 1997, doi: 10.1016/S0026-0576(97)86771-2.
- 3 M. A. Jakab, F. Presuel-Moreno, and J. R. Scully, “Critical concentrations associated with cobalt, cerium, and molybdenum inhibition of AA2024-T3 corrosion: Delivery from Al-Co-Ce(-Mo) alloys,” *Corrosion*, vol. 61, no. 3, pp. 246–263, 2005, doi: 10.5006/1.3280634.
- 4 H. Shi, E. H. Han, and F. Liu, “Corrosion protection of aluminium alloy 2024-T3 in 0.05M NaCl by cerium cinnamate,” *Corros. Sci.*, vol. 53, no. 7, pp. 2374–2384, Jul. 2011, doi: 10.1016/j.corosci.2011.03.012.
- 5 K. A. Yasakau, M. L. Zheludkevich, S. V. Lamaka, and M. G. S. Ferreira, “Mechanism of corrosion inhibition of AA2024 by rare-earth compounds,” *J. Phys. Chem. B*, vol. 110, no. 11, pp. 5515–5528, Mar. 2006, doi: 10.1021/jp0560664.
- 6 J. Gui and T. M. Devine, “Influence of lithium on the corrosion of aluminum,” *Scr. Metall.*, vol. 21, no. 6, pp. 853–857, 1987, doi: 10.1016/0036-9748(87)90336-X.
- 7 C. M. Rangel and M. A. Travassos, “The passivation of aluminium in lithium carbonate/bicarbonate solutions,” *Corros. Sci.*, vol. 33, no. 3, pp. 327–343, 1992, doi: 10.1016/0010-938X(92)90064-A.
- 8 C. D. Dieleman, P. J. Denissen, and S. J. Garcia, “Long-Term Active Corrosion Protection of Damaged Coated-AA2024-T3 by Embedded Electrospun Inhibiting Nanonetworks,” *Adv. Mater. Interfaces*, vol. 5, no. 12, 2018, doi: 10.1002/admi.201800176.
- 9 P. Visser, M. Meeusen, Y. Gonzalez-Garcia, H. Terryn, and J. M. C. Mol, “Electrochemical evaluation of corrosion inhibiting layers formed in a defect from lithium-leaching organic coatings,” *J. Electrochem. Soc.*, vol. 164, no. 7, pp. C396–C406, 2017, doi: 10.1149/2.1411707jes.
- 10 J. S. Laird, P. Visser, S. Ranade, A. E. Hughes, H. Terryn, and J. M. C. Mol, “Li leaching from Lithium Carbonate-primer: An emerging perspective of transport pathway development,” *Prog. Org. Coatings*, vol. 134, pp. 103–118, Sep. 2019, doi: 10.1016/j.porgcoat.2019.04.062.
- 11 W. Chen, H. Q. Luo, and N. B. Li, “Inhibition effects of 2,5-dimercapto-1,3,4-thiadiazole on the corrosion of mild steel in sulphuric acid solution,” *Corros. Sci.*, vol. 53, no. 10, pp. 3356–3365, 2011, doi: 10.1016/j.corosci.2011.06.013.
- 12 M. Abdolah Zadeh, J. Tedim, M. Zheludkevich, S. van der Zwaag, and S. J. Garcia, “Synergetic active corrosion protection of AA2024-T3 by 2D- anionic and 3D-cationic nanocontainers loaded with Ce and mercaptobenzothiazole,” *Corros. Sci.*, vol. 135, pp. 35–45, 2018, doi: 10.1016/j.corosci.2018.02.018.
- 13 D. Chadwick and T. Hashemi, “Electron spectroscopy of corrosion inhibitors: Surface films formed by 2-mercaptobenzothiazole and 2-mercaptobenzimidazole on copper,” *Surf. Sci.*, vol. 89, no. 1–3, pp. 649–659, 1979, doi: 10.1016/0039-6028(79)90646-0.
- 14 E. L. Ferrer, A. P. Rollon, H. D. Mendoza, U. Lafont, and S. J. Garcia, “Double-doped zeolites for corrosion protection of aluminium alloys,” *Microporous Mesoporous Mater.*, vol. 188, pp. 8–15, Apr. 2014, doi: 10.1016/J.Micromeso.2014.01.004.
- 15 G. Williams, A. J. Coleman, and H. N. McMurray, “Inhibition of Aluminium Alloy AA2024-T3 pitting corrosion by copper complexing compounds,” *Electrochim. Acta*,

- vol. 55, no. 20, pp. 5947–5958, Aug. 2010, doi: 10.1016/j.electacta.2010.05.049.
- 16 D. Snihirova, S. V. Lamaka, P. Taheri, J. M. C. Mol, and M. F. Montemor, “Comparison of the synergistic effects of inhibitor mixtures tailored for enhanced corrosion protection of bare and coated AA2024-T3,” *Surf. Coatings Technol.*, vol. 303, no. Part B, pp. 342–351, 2016, doi: 10.1016/j.surfcoat.2015.10.075.
- 17 R. L. Twite and G. P. Bierwagen, “Review of alternatives to chromate for corrosion protection of aluminum aerospace alloys,” *Prog. Org. Coatings*, vol. 33, no. 2, pp. 91–100, 1998, doi: 10.1016/S0300-9440(98)00015-0.
- 18 X. Shi, T. A. Nguyen, Z. Suo, Y. Liu, and R. Avci, “Effect of nanoparticles on the anticorrosion and mechanical properties of epoxy coating,” *Surf. Coatings Technol.*, vol. 204, no. 3, pp. 237–245, 2009, doi: 10.1016/j.surfcoat.2009.06.048.
- 19 P. Loison, V. Debout, H. Groult, J. Creus, and S. Touzain, “Incorporation of silica nanocontainers and its impact on a waterborne polyurethane coating,” *Mater. Corros.*, vol. 70, no. 10, pp. 1884–1899, 2019, doi: 10.1002/maco.201910809.
- 20 R. Sharmila, N. Selvakumar, and K. Jeyasubramanian, “Evaluation of corrosion inhibition in mild steel using cerium oxide nanoparticles,” *Materials Letters*, vol. 91. Elsevier B.V., pp. 78–80, Jan. 15, 2013, doi: 10.1016/j.matlet.2012.09.051.
- 21 D. Borisova, H. Möhwald, and D. G. Shchukin, “Influence of embedded nanocontainers on the efficiency of active anticorrosive coatings for aluminum alloys part I: Influence of nanocontainer concentration,” *ACS Appl. Mater. Interfaces*, vol. 4, no. 6, pp. 2931–2939, 2012, doi: 10.1021/am300266t.
- 22 P. J. Denissen and S. J. Garcia, “Cerium-loaded algae exoskeletons for active corrosion protection of coated AA2024-T3,” *Corros. Sci.*, vol. 128, no. September, pp. 164–175, Nov. 2017, doi: 10.1016/j.corsci.2017.09.019.
- 23 A. M. Homborg *et al.*, “Application of transient analysis using Hilbert spectra of electrochemical noise to the identification of corrosion inhibition,” *Electrochim. Acta*, vol. 116, pp. 355–365, Jan. 2014, doi: 10.1016/j.electacta.2013.11.084.
- 24 X. Ma *et al.*, “The inhibition effect of polyaspartic acid and its mixed inhibitor on mild steel corrosion in seawater wet/dry cyclic conditions,” *Int. J. Electrochem. Sci.*, vol. 11, no. 4, pp. 3024–3038, 2016, doi: 10.20964/110403024.
- 25 P. Visser, H. Terryn, and J. M. C. Mol, “On the importance of irreversibility of corrosion inhibitors for active coating protection of AA2024-T3,” *Corros. Sci.*, vol. 140, pp. 272–285, Aug. 2018, doi: 10.1016/j.corsci.2018.05.037.
- 26 V. Saini *et al.*, “Superabsorbent polymer additives for repeated barrier restoration of damaged powder coatings under wet-dry cycles: A proof-of-concept,” *Prog. Org. Coatings*, vol. 122, pp. 129–137, Sep. 2018, doi: 10.1016/j.porgcoat.2018.05.019.
- 27 P. J. Denissen and S. J. Garcia, “Reducing subjectivity in EIS interpretation of corrosion and corrosion inhibition processes by in-situ optical analysis,” *Electrochim. Acta*, vol. 293, pp. 514–524, 2019, doi: 10.1016/j.electacta.2018.10.018.
- 28 P. J. Denissen, A. M. Homborg, and S. J. Garcia, “Interpreting electrochemical noise and monitoring local corrosion by means of highly resolved spatiotemporal real-time optics,” *J. Electrochem. Soc.*, vol. 166, no. 11, pp. C3275–C3283, 2019, doi: 10.1149/2.0341911jes.
- 29 M. G. Taryba, M. F. Montemor, and S. V. Lamaka, “Quasi-simultaneous Mapping of Local Current Density, pH and Dissolved O<sub>2</sub>,” *Electroanalysis*, vol. 27, no. 12, pp. 2725–2730, 2015, doi: 10.1002/elan.201500286.
- 30 A. S. Nguyen and N. Pébère, “A local electrochemical impedance study of the self-healing properties of waterborne coatings on 2024 aluminium alloy,” *Electrochim. Acta*, vol. 222, pp. 1806–1817, 2016, doi: 10.1016/j.electacta.2016.11.152.
- 31 V. Shkirskiy, A. Krasnova, T. Sanchez, A. Amar, V. Vivier, and P. Volovitch,

- “Development of anodic and cathodic blisters at a model Zn/epoxy interface studied using local electrochemical impedance,” *Electrochem. commun.*, vol. 111, Feb. 2020, doi: 10.1016/j.elecom.2019.106633.
- 32 M. S. Aw, M. Bariana, Y. Yu, J. Addai-Mensah, and D. Losic, “Surface-functionalized diatom microcapsules for drug delivery of water-insoluble drugs,” *J. Biomater. Appl.*, vol. 28, no. 2, pp. 163–174, 2013, doi: 10.1177/0885328212441846.
- 33 P. Thévenaz, U. E. Ruttimann, and M. Unser, “A pyramid approach to subpixel registration based on intensity,” *IEEE Trans. Image Process.*, vol. 7, no. 1, pp. 27–41, 1998, doi: 10.1109/83.650848.
- 34 V. M. Huang, S. L. Wu, M. E. Orazem, N. Pébre, B. Tribollet, and V. Vivier, “Local electrochemical impedance spectroscopy: A review and some recent developments,” *Electrochim. Acta*, vol. 56, no. 23, pp. 8048–8057, 2011, doi: 10.1016/j.electacta.2011.03.018.
- 35 N. Maiti, R. Chadha, A. Das, and S. Kapoor, “Surface selective binding of 2,5-dimercapto-1,3,4-thiadiazole (DMTD) on silver and gold nanoparticles: A Raman and DFT study,” *RSC Adv.*, vol. 6, no. 67, pp. 62529–62539, 2016, doi: 10.1039/c6ra10404e.
- 36 M. Schem *et al.*, “CeO<sub>2</sub>-filled sol-gel coatings for corrosion protection of AA2024-T3 aluminium alloy,” *Corros. Sci.*, vol. 51, no. 10, pp. 2304–2315, Oct. 2009, doi: 10.1016/j.corsci.2009.06.007.
- 37 S. V. Lamaka, M. L. Zheludkevich, K. A. Yasakau, M. F. Montemor, and M. G. S. Ferreira, “High effective organic corrosion inhibitors for 2024 aluminium alloy,” *Electrochim. Acta*, vol. 52, no. 25, pp. 7231–7247, 2007, doi: 10.1016/j.electacta.2007.05.058.
- 38 A. Boag, A. E. Hughes, A. M. Glenn, T. H. Muster, and D. McCulloch, “Corrosion of AA2024-T3 Part I: Localised corrosion of isolated IM particles,” *Corros. Sci.*, vol. 53, no. 1, pp. 17–26, 2011, doi: 10.1016/j.corsci.2010.09.009.
- 39 A. Hughes *et al.*, “Co-operative corrosion phenomena,” *Corros. Sci.*, vol. 52, no. 3, pp. 665–668, 2010, doi: 10.1016/j.corsci.2009.10.021.
- 40 A. E. Hughes *et al.*, “Corrosion of AA2024-T3 Part II: Co-operative corrosion,” *Corros. Sci.*, vol. 53, no. 1, pp. 27–39, 2011, doi: 10.1016/j.corsci.2010.09.030.
- 41 A. M. Glenn *et al.*, “Corrosion of AA2024-T3 Part III: Propagation,” *Corros. Sci.*, vol. 53, no. 1, pp. 40–50, 2011, doi: 10.1016/j.corsci.2010.09.035.
- 42 A. E. Hughes, N. Birbilis, J. M. C. Mol, S. J. Garcia, X. Zhou, and G. E. Thompson, “High Strength Al-Alloys: Microstructure, Corrosion and Principles of Protection,” *Recent Trends Process. Degrad. Alum. Alloy.*, pp. 223–262, 2011, doi: 10.5772/18766.
- 43 K. F. Khaled, “Electrochemical Evaluation of Environmentally Friendly Cerium Salt as Corrosion Inhibitor for Steel in 3.5 % NaCl,” *Int. J. Electrochem. Sci.*, vol. 8, pp. 3974–3987, 2013, Accessed: Apr. 08, 2020. [Online]. Available: [www.electrochemsci.org](http://www.electrochemsci.org).
- 44 D. Snihirova, M. Taryba, S. V. Lamaka, and M. F. Montemor, “Corrosion inhibition synergies on a model Al-Cu-Mg sample studied by localized scanning electrochemical techniques,” *Corros. Sci.*, vol. 112, pp. 408–417, 2016, doi: 10.1016/j.corsci.2016.08.008.
- 45 M. G. Taryba, K. Van den Bergh, J. De Strycker, O. Dolgikh, J. Deconinck, and S. V. Lamaka, “Novel use of a micro-optode in overcoming the negative influence of the amperometric micro-probe on localized corrosion measurements,” *Corros. Sci.*, vol. 95, pp. 1–5, 2015, doi: 10.1016/j.corsci.2015.02.037.
- 46 N. C. Rosero-Navarro *et al.*, “Electrochemical techniques for practical evaluation of corrosion inhibitor effectiveness. Performance of cerium nitrate as corrosion inhibitor for AA2024T3 alloy,” *Corros. Sci.*, vol. 52, no. 10, pp. 3356–3366, Oct. 2010, doi:

- 10.1016/j.corsci.2010.06.012.
- 47 I. I. Udoh, H. Shi, F. Liu, and E. H. Han, "Synergistic Effect of 3-Amino-1,2,4-triazole-5-thiol and Cerium Chloride on Corrosion Inhibition of AA2024-T3," *J. Electrochem. Soc.*, vol. 166, no. 6, pp. C185–C195, 2019, doi: 10.1149/2.0621906jes.
- 48 S. J. Garcia, T. A. Markley, J. M. C. Mol, and A. E. Hughes, "Unravelling the corrosion inhibition mechanisms of bi-functional inhibitors by EIS and SEM-EDS," *Corros. Sci.*, vol. 69, pp. 346–358, 2013, doi: 10.1016/j.corsci.2012.12.018.
- 49 V. Upadhyay and D. Battocchi, "Localized electrochemical characterization of organic coatings: A brief review," *Prog. Org. Coatings*, vol. 99, pp. 365–377, 2016, doi: 10.1016/j.porgcoat.2016.06.012.
- 50 D. Snihirova, S. V. Lamaka, and M. F. Montemor, "'SMART' protective ability of water based epoxy coatings loaded with CaCO<sub>3</sub> microbeads impregnated with corrosion inhibitors applied on AA2024 substrates," *Electrochim. Acta*, vol. 83, pp. 439–447, 2012, doi: 10.1016/j.electacta.2012.07.102.
- 51 R. G. Buchheit, S. B. Mamidipally, P. Schmutz, and H. Guan, "Active corrosion protection in Ce-modified hydrotalcite conversion coatings," *Corrosion*, vol. 58, no. 1, pp. 3–14, 2002, doi: 10.5006/1.3277303.
- 52 L. B. Coelho, D. Cossement, and M. G. Olivier, "Benzotriazole and cerium chloride as corrosion inhibitors for AA2024-T3: An EIS investigation supported by SVET and ToF-SIMS analysis," *Corros. Sci.*, vol. 130, pp. 177–189, Jan. 2018, doi: 10.1016/j.corsci.2017.11.004.
- 53 D. R. Arnott, N. E. Ryan, B. R. W. Hinton, B. A. Sexton, and A. E. Hughes, "Auger and XPS studies of cerium corrosion inhibition on 7075 aluminum alloy," *Appl. Surf. Sci.*, vol. 22–23, no. PART 1, pp. 236–251, 1985, doi: 10.1016/0378-5963(85)90056-X.
- 54 E. A. Matter, S. Kozhukharov, M. Machkova, and V. Kozhukharov, "Comparison between the inhibition efficiencies of Ce(III) and Ce(IV) ammonium nitrates against corrosion of AA2024 aluminum alloy in solutions of low chloride concentration," *Corros. Sci.*, vol. 62, pp. 22–33, Sep. 2012, doi: 10.1016/j.corsci.2012.03.039.

## 5.6. Supporting Information

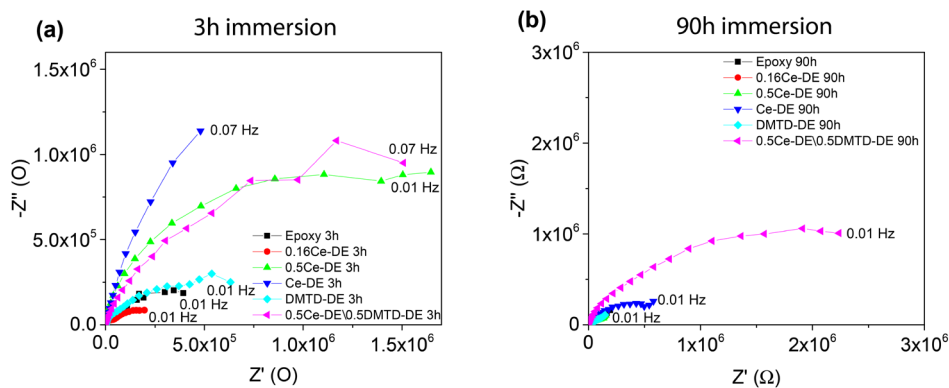
### SI-5.1. Active inhibitor component inside the coating

$$m_{active\ inhibitor} = \frac{m_{inhibitor} * \left( \frac{MW_{active\ component}}{MW_{inhibitor}} \right)}{m_{coating}} * 100\ %$$

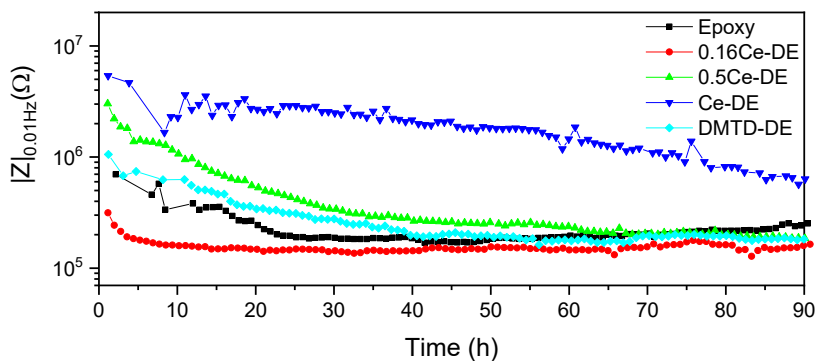
Where;

- $m_{active\ inhibitor}$  is the active inhibitor component (wt.%),
- $m_{inhibitor}$  is the total weight of inhibitor added to the coating (g),
- $m_{coating}$  is the total weight of the final coating composition (g),
- $MW_{active\ component}$  is the molecular weight of the active component for the inhibitor (u),
- $MW_{inhibitor}$  is the molecular weight of the inhibitor (u).

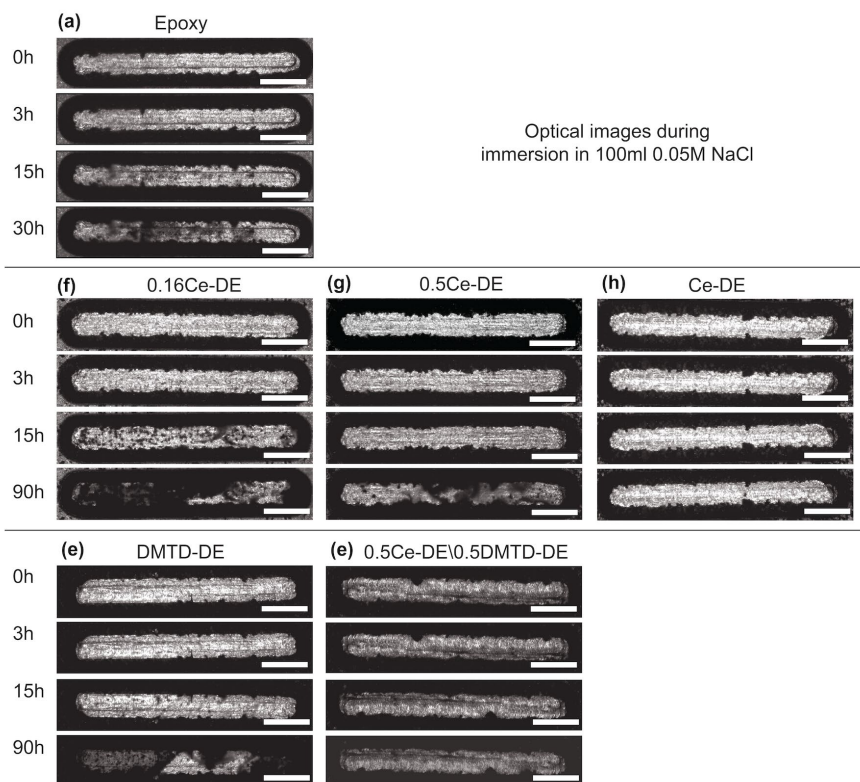
### SI-5.2. Optical-electrochemical study: Nyquist plots



**Figure SI 5.1** Nyquist plots of six scribed coatings after immersion in 200 ml/cm<sup>2</sup> 0.05 M NaCl for 3 h (a) and 90 h (b). Instable points at low frequencies have been removed in accordance to large Kramers-Kronig residual errors.

**SI-5.3. Optical-electrochemical study: Evolution of impedance**

**Figure SI 5.2** Nyquist plots of six scribed coatings after immersion in 200 ml/cm<sup>2</sup> 0.05 M NaCl for 3 h (a) and 90 h (b). Instable points at low frequencies have been removed in accordance to large Kramers-Kronig residual errors.

**SI-5.4. Optical-electrochemical study: Optical images**

**Figure SI 5.3** Optical images of six coated systems obtained with the real-time optical-electrochemical set-up at 0, 3, 15, and 90 h immersion.

### SI-5.5. Local electrochemical impedance spectra

Figure SI 5.4 shows the simultaneously obtained global and local EIS data as Bode and Nyquist plots after 4 days immersion.

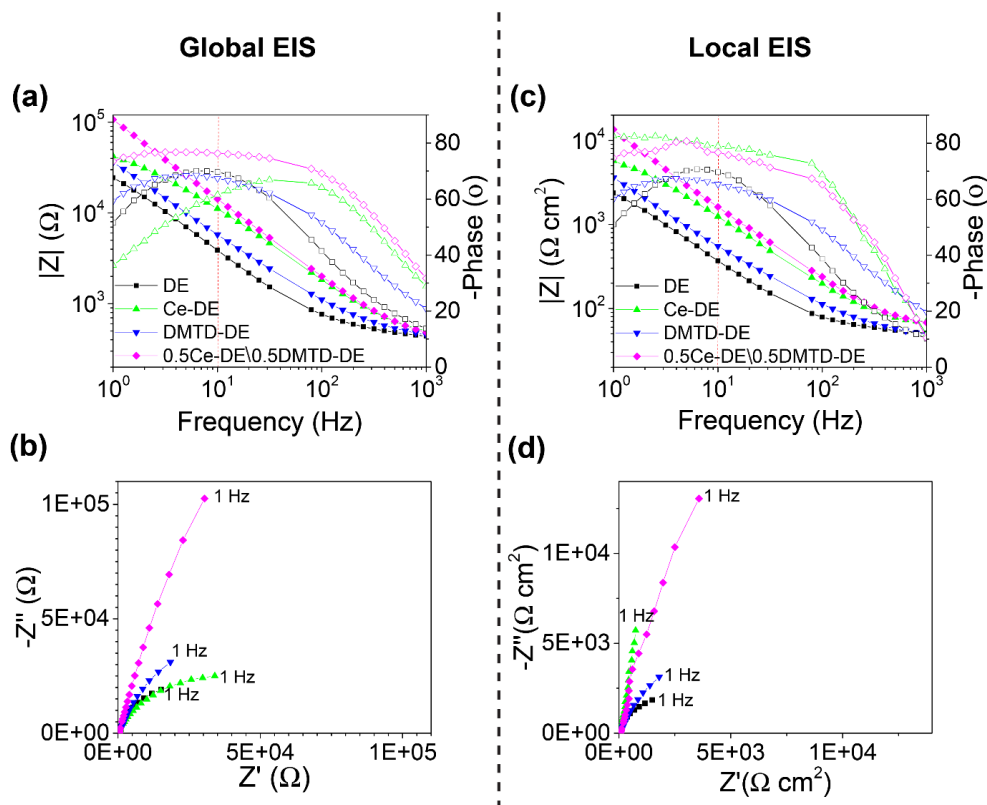


**Figure SI 5.4** Simultaneously obtained global EIS (a,b) and local EIS (c,d) as Bode plot (a,c) and Nyquist plot (b,d) in the frequency range of  $10^3$  Hz - 1 Hz after 4 days immersion. Local EIS was measured at 100  $\mu\text{m}$  above the surface of the coating in the centre of the damage. The frequency of 10 Hz is indicated in the bode plot by the red dotted line.

The Local EIS data shows similar results as conventional EIS. It is important to note that quantitative comparison between local and global EIS measurements is nevertheless impossible since only the radial component of current lines are sensed by LEIS.

### SI-5.6. Local electrochemical impedance spectra

Figure SI 5.6 show 3D contour map of the gradient of the admittance modulus  $|\text{Grad } Z^{-1}|$  for the damaged coatings (i.e. DE, Ce-DE, DMTD-DE, and 0.5Ce-DE/0.5DMTD-DE) after 4, 10, 24 and 30 days. The local admittance values show the biggest gradients (i.e. highest local maxima indicated in red) exactly at the boundary between the bare metal and the coated metal (i.e. at the edge of the coating).

From these results the average gradient of the admittance is calculated by averaging over all the slices in x-direction over the 5 mm long damage. Figure SI 5.5 shows the average gradient of the admittance and it can be seen that the local maxima stays at the same position in the y-axis (1 mm width of the damage) for all the tested coatings, indicating that no apparent widening of the damage has taken place during the 30

days of immersion. The height of the local maxima in the average gradient of the admittance is directly proportional to the difference in admittance between the coating and the exposed metal surface. Figure SI 5.5 thereby shows that the highest gradients are reached for DE ( $2.5 \times 10^{-6} \Omega^{-1} \text{cm}^{-3}$ ) followed by DMTD-DE ( $1.5 \times 10^{-6} \Omega^{-1} \text{cm}^{-3}$ ) at all immersion times, which is in good accordance with the low impedance values at the damage. The samples with the highest impedance (Ce-DE and 0.5Ce-DE\0.5DMTD-DE) show lower local maxima after 4 days around  $1 \times 10^{-6} \Omega^{-1} \text{cm}^{-3}$  and  $0.5 \times 10^{-6} \Omega^{-1} \text{cm}^{-3}$ , respectively. After 10 days the local maxima for Ce-DE decreases further toward  $0.5 \times 10^{-6} \Omega^{-1} \text{cm}^{-3}$  while the opposite occurs after 24 days for 0.5Ce-DE\0.5DMTD-DE. This suggests that the combined release of Ce and DMTD results in faster protection that is less stable over time compared to the release of Ce alone, which shows an increase in stability by the reduction of admittance gradient.

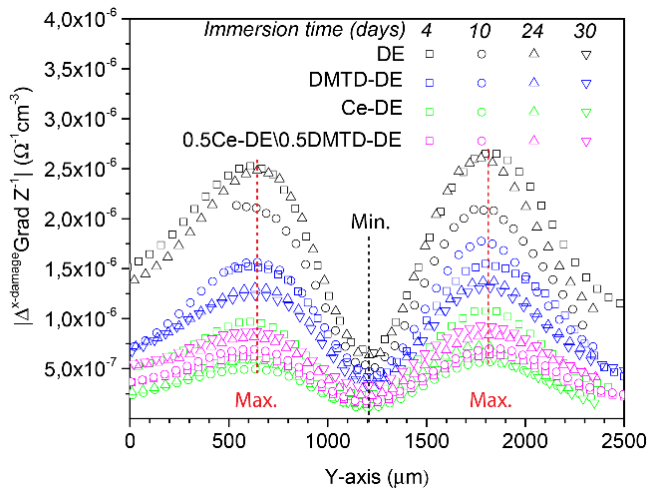


**Figure SI 5.5** LEIM results obtained at 10 Hz and 100  $\mu\text{m}$  above the damaged coating at different immersion-times showing the average gradient of the admittance modulus  $|\Delta^{x\text{-damage}} \text{Grad } Z^{-1}|$  over all the recorded slices in x-direction over the 5 mm long damage for different immersion-times. Dashed lines show the local minima and maxima.

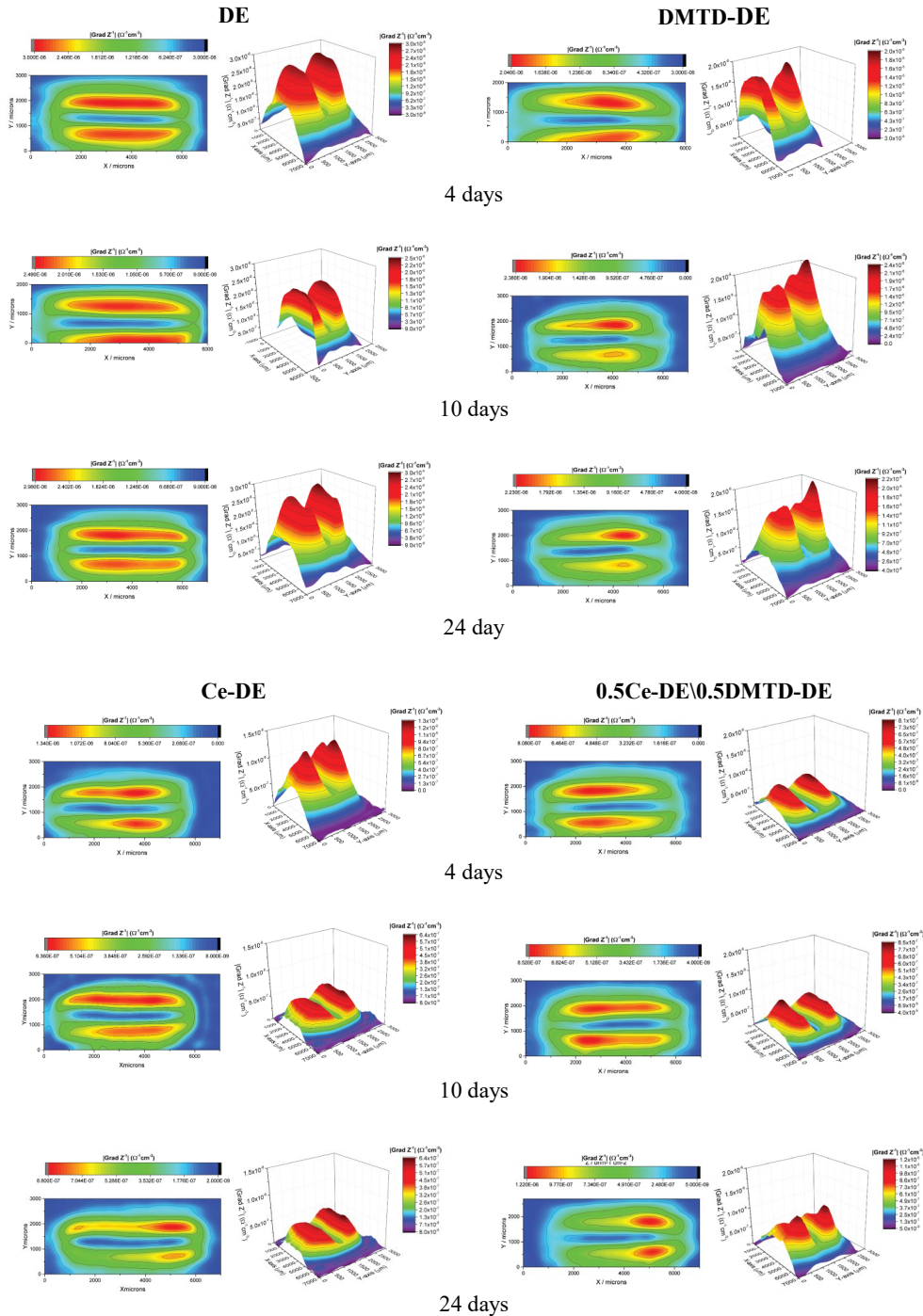


Figure SI 5.6 Gradient of admittance  $|\text{Grad } Z'|$  during immersion in 0.05 M NaCl

# 6

## **A simulation-based guideline for the design of anticorrosive primers based on inhibitor-loaded carriers**

*In this work a diffusion-driven inhibitor transport model for locally damaged coatings under immersion conditions is used as a guideline for the design of anti-corrosion primers based on inhibitor-loaded carriers. The effect of the inhibitor diffusivity, coating thickness and damage dimensions are simulated to determine the minimal inhibitor release rate necessary to reach the required inhibitor concentrations for corrosion protection of the exposed metal. Kinematic and mass conservation laws are used as first-order approximations to study the effect of the characteristics of inhibitor-loaded nano-, or micro-particles embedded in an organic coating on the inhibitor release rate. The simulated results are validated experimentally using epoxy coatings containing cerium-loaded zeolites and diatomaceous earth as nano-, and micro-carriers respectively. A dedicated opto-electrochemical setup with high spatial and temporal resolution in combination with coinciding electrochemical potential noise measurement is used to validate the model. Immersion of the damaged coatings in a 0.05 M NaCl electrolyte shows that the nano-particles are only able to protect relatively small damages. Micron-sized carriers on the other hand allow sufficient release to protect larger damages, even at low pigment volume concentrations. Simulation and experimental results show that a sufficiently fast inhibitor dissolution and rapid electrolyte diffusion pathways inside the coating play an important role in sustained inhibitor release and corrosion protection at local damages.*

## 6.1. Introduction

Organic coatings have the primary function to protect metal surfaces from aggressive environmental conditions by a well-adhering passive barrier layer<sup>1,2</sup>. This layer stops or significantly hinders the transport of aggressive species, thereby preventing corrosion processes occurring at the metal substrate.<sup>3,4</sup> Nevertheless, environmental factors (e.g. mechanical stresses, thermal cycles, and moisture) can cause micro- and macroscopic defects in the coating, resulting in a local loss of protection.<sup>5-7</sup>

Corrosion inhibitors are incorporated in the coatings to provide additional protection in case of local through-coating damages or after barrier loss. Under such circumstances the inhibitor leaches from the coating surrounding the damaged site towards the exposed metal and protects it by blocking anodic and/or cathodic active regions. Hence, the ideal coating should reduce the diffusion of aggressive species while, in case of failure, allow a sufficiently fast transport of enough inhibitor through the coating for active protection.<sup>8,9</sup>

Over the past decades a few studies have shown that particle networks and connectivity are important factors for the transport of leachable inhibitors through the coating. Tomography techniques showed that inhibitor release in Strontium chromate ( $\text{SrCrO}_4$ ) containing primers is dependent on the creation of large clusters of chromate micro-particles via void pathways.<sup>10,11</sup> Other studies involving inhibitor salts have shown the importance of the coating composition and pigment volume concentration (PVC)<sup>12-15</sup> and modelled the effects of inhibitor diffusion through the coating<sup>16-20</sup> and as function of pH<sup>17-20</sup> and damage size.<sup>18-20</sup>

Studying the release from coatings containing other types of corrosion inhibitors is also relevant for alternative strategies to replace the much debated carcinogenic and environmentally hazardous chromates. Examples are organic inhibitors,<sup>21</sup> lanthanides<sup>22</sup> and, more recently, lithium salts.<sup>23</sup> Several new strategies have been proposed to increase their sustained or triggered release at the damage site using discrete carriers (e.g. zeolites,<sup>24</sup> clays,<sup>25,26</sup> hollow nanoparticles,<sup>27</sup> diatomaceous earth micro-particles<sup>28</sup>) or inhibiting nanonetworks.<sup>29,30</sup> The required characteristics of inhibitor release from the coating or the effect of interconnected pathways inside the coatings are still not fully understood for systems based on inhibitor containing nano- or micro-sized carriers, while these conditions could be important factors in the protection of local damages.

Modelling of inhibitor release from the coating walls at through-thickness damage locations is complex when all involved factors are considered. This is due to the large amount of unknowns involved such as the rates of electrochemical reaction at the metal surface involving local inhibitor deposition, equilibrium conditions at the metal surface, local swelling and hydrolysis in the coating, the release and transport of inhibiting species through the various interfaces and

finally the homogeneity of the coating.<sup>31,32</sup> For this reason studies in the field include clearly defined boundary conditions set by a number of assumptions to simplify the problem yet allowing for relevant information to be retrieved. The transport of inhibitors from the coating-damage interface under immersion conditions, sometimes referred to as the chemical throwing power<sup>18</sup>, has been described as a diffusion-driven process based on Fick's law.<sup>18,33</sup> On the other hand, several other studies have shown that non-Fickian diffusion models are required to accurately describe the inhibitor transport inside the coating.<sup>31,32,34,35</sup>

In the present work the inhibitor diffusion through a coating towards a damage location is modelled using a multi physics finite elements method (FEM). For simplification, the minimum local inhibitor concentration for corrosion protection is considered without taking the actual corrosion and deposition reactions at the metal-electrolyte interface into account due to their fast reaction speeds in comparison with the other steps in the process. The obtained parameters are used to calculate the transport of inhibiting species from the coating towards the electrolyte interface by mass conservation, assuming a homogeneous system with random dispersion of inhibiting species (located initially in the discrete carriers) and charge neutrality of the solution. The effects of the inhibitor diffusion coefficient, coating thickness and damage diameter on the minimum inhibitor concentration at the damage to obtain corrosion protection are investigated. To validate the results from the model, a range of epoxy coatings with compositions and damage dimensions comparable to the systems modelled are prepared and tested using a recently developed opto-electrochemical setup. Cerium is used as inhibitor and stored following previously reported procedures using both nano-particles<sup>24</sup> and micro-particles.<sup>28</sup> The effects of damage diameter, particle size, PVC and connecting inhibitor pathways on the degree of corrosion protection is studied for the case of epoxy-coated AA2024-T3, damaged and immersed in 0.05 M NaCl.

## 6.2. Experimental

### 6.2.1. Damaged coating under immersion conditions used in simulation and corrosion experiments

Figure 6.1 illustrates the geometry of the coating system with the damage dimensions and the electrolyte volume it was exposed to. The same geometry parameters were used for the simulations and corrosion experiments.

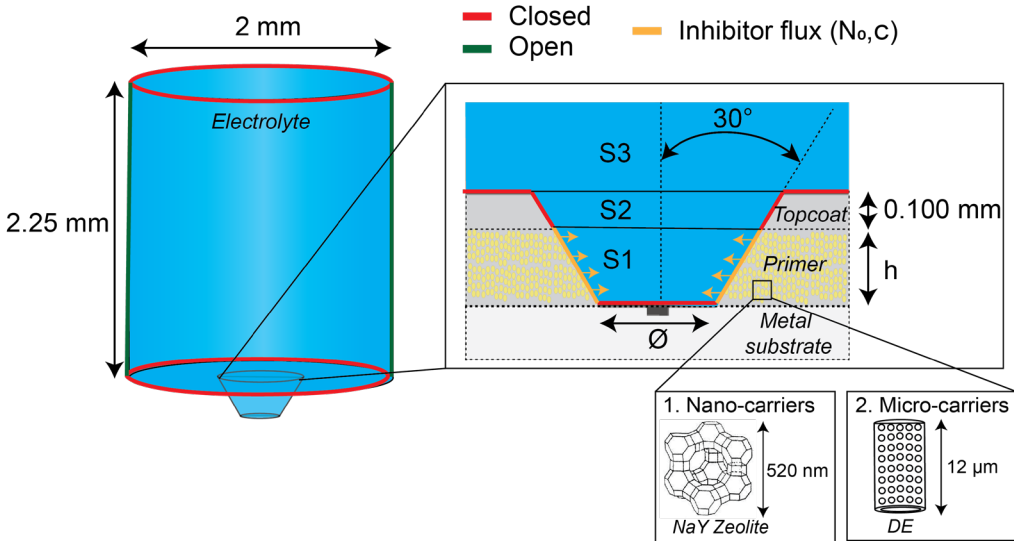


**Figure 6.1** Graphical illustration of the 3D model representing the anticorrosion coating with its damage (i.e. circular hole) and the electrolyte volume it is exposed to.

The electrolyte is shown in Figure 6.1 in blue and is bounded by three interfaces, namely cone-shaped S1 (linking the electrolyte to the primer) and S2 (linking the electrolyte to the topcoat) with an apex angle of  $30^\circ$  and a larger cylinder S3 (setting the dimensions of the electrolyte on top of the coating) on top. The primer contains homogeneously distributed NaY zeolites or diatomaceous earth (DE) as either nano-, or micro-carriers at a defined pigment volume concentrations (PVC) and inhibitor loading levels ( $\gamma_i$ ), the diameter of the damage at the metal surface ( $\emptyset$ ), the primer thickness ( $h$ ) and the coating composition are varied for the simulations and experiments. In the simulations this exposed metal surface is considered to be inert (i.e. no local release or uptake of the inhibitor species) and a minimum accumulated inhibitor concentration at this surface is considered as the governing condition for protection. The boundaries at the side walls of S1 represent the damaged coating primer surface (shown in orange in Figure 6.1). From this boundary a flux of diluted inhibitor species is assumed (i.e. dissolved inhibitors moving from the coating boundary toward the centre of the electrolyte). S2 represents the electrolyte volume enclosed by the topcoat walls above S1 and below the open electrolyte

above the damage (S3). S2 has a fixed height of 100  $\mu\text{m}$  with closed external boundaries (no release or uptake by the topcoat). S3 is the modelled electrolyte volume above the coating. In this case, the sides of the cylinder are open in order to simulate the exposure of the damage to a larger electrolyte field similar to the experimental conditions. The top of the modelled domain is the electrolyte surface located 2.25 mm above the metal surface. The same coating and damage dimensions are used in the simulation and the validating experimental tests as explained in the materials and test set-up sections.

### 6.2.2. Diffusion-limited model for inhibitor transport in the electrolyte

A 3D finite element model (FEM) is built in COMSOL Multiphysics® 5.4 (build: 225) to predict the concentration gradients of inhibitor species in the electrolyte (in S1, S2, and S3) as a result of the diffusional flux through the primer walls at the damage location (shown by orange arrows in Figure 6.1). The 3D CAD model of the electrolyte (Figure 6.1) is built in CATA V5R20 and imported as a solid step file into COMSOL with an absolute tolerance of  $1.0 \times 10^{-5}$  mm. In these simulations the dissolution and diffusion of the inhibitor through the coating is not considered. Hence, the transport of diluted inhibitors in the electrolyte is modelled given the boundary conditions as explained in the previous section. The transport is assumed to be concentration driven diffusion-limited; that is, convection and migration by an electric field in the electrolyte are not taken into account. The model also assumes that the inhibitor species are dilute at the coating/electrolyte interface. These conditions are assumed to be realistic as only a limited amount of highly soluble inhibitors is already in a dissolved stage when they cross the coating-electrolyte interface, allowing the inhibitor concentration to remain below the solubility limit. Under these conditions the electrolyte properties (i.e. density and viscosity) containing dissolved inhibitors can be assumed to be equal to those of the solvent ( $\text{H}_2\text{O}$ ).<sup>36</sup> The following mass flow equation (6.1) is used to describe the diffusion of inhibitor  $i$  in the electrolyte:

$$\frac{\partial c_i}{\partial t} + \nabla \cdot J_i = R_i \quad (6.1)$$

Where  $c_i$  is the concentration of the species ( $\text{mol}/\text{m}^3$ ),  $J_i$  the mass flux relative to the averaged velocity ( $\text{mol}/(\text{m}^2\text{s})$ ), and  $R_i$  the mass flow reaction rate expression for the species ( $\text{mol}/(\text{m}^3\text{s})$ ).

In this case the mass flux is based on the diffusion of molecular species through Fick's law as shown in equation (6.2):

$$J_i = -D_c \nabla c_i \quad (6.2)$$

Where  $D_c$  is the inhibitor diffusion coefficient ( $\text{m}^2/\text{s}$ ), which can be varied in the simulations under isotropic conditions at 293.15 K.

The initial conditions of the model assumes that there are no inhibitor species present at the start ( $t = 0$ ;  $C_{\text{bulk}} = 0$ ) and that there is a constant release flux ( $N_{0,c}$  in  $\text{mol}/(\text{m}^2\text{s})$ ) of a predefined number of inhibitor species ( $\mathbf{n}$ ) at the primer-coating boundary as shown in Figure 6.1 and equation (6.3):

$$N_{0,c} = -\mathbf{n} \cdot \mathbf{J}_i \quad (6.3)$$

For the simulations a standard mesh is used, consisting out of 7292 elements with an average quality of 0.66. The time-dependent calculations are executed with a step-size of 1 s on 7931 internal and 1501 external degrees of freedom within the mesh. The release-flux, inhibitor diffusion coefficient and damage size ( $\emptyset$  and  $h$  indicated in Figure 6.1) are varied during the different simulations to investigate their effect on the inhibitor concentration profiles at and near the damage location over a period of 10 ks after initial exposure.

### 6.2.3. Inhibitor depletion from carriers at the primer-electrolyte interface

The amount of released inhibitor from the carriers embedded inside the coating can be calculated using a kinematic model whereby the inhibitor release flux ( $N_{0,c}$ ) from the diffusion-limited model for the electrolyte is coupled to a representative damage geometry and coating composition. The inhibitor mass flow reaction rate ( $R_i$ ) taking place at the coating-electrolyte interface over a period of time ( $t$ ) can be obtained from the diffusion rate using the principle of mass conservation:

$$\frac{dR_i}{dt} = N_{0,c} = m_i \frac{\pi \emptyset h}{\cos(30^\circ)} t \quad (6.4)$$

Where  $m_i$  is the available inhibitor species (molar) that can be released from the coating interface.

As a first order approximation, the calculations on the coating are described in terms of homogeneously distributed inhibiting species from the carriers without taking transport properties (i.e. linearization) and electro-migration of the electrolyte into consideration. The coating-side of the interface is shown in more detail in Figure 6.2 and schematically depicts the inhibitor release from the coating for two carrier/network configurations.

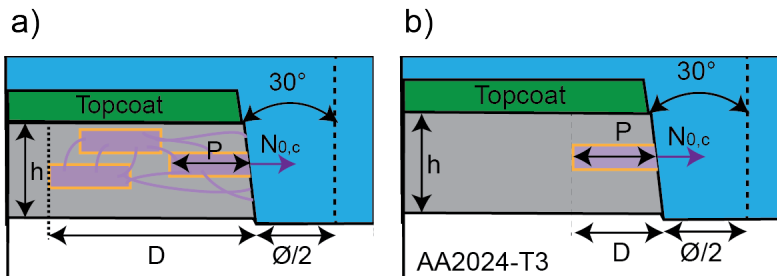


**Figure 6.2** Graphical illustration of the damaged coating to study inhibitor release for (a) single carriers directly exposed to the electrolyte interface and (b) interconnected network of particles.

In the first configuration (Figure 6.2a) it is assumed that the inhibitors are released from the particles with size (P) located at a distance (D) from the coating-electrolyte interface, whereby  $0 < D \leq P$ . In the second configuration it is assumed that the inhibitors are also released from particles located inside the coating with inhibitor transport through an interconnected diffusive network ( $D > P$ ). The inhibitor mass (molar) can be calculated for both configurations through the following kinematic equation assuming the release is limited by the distance of inhibitor from the damage, D:

$$m_i = \frac{\pi \left(\frac{\emptyset}{2} + D\right)^2 h}{\cos(30^\circ)} - \frac{\pi \left(\frac{\emptyset}{2}\right)^2 h}{\cos(30^\circ)} \frac{PVC \cdot \rho_c \cdot \gamma_i}{Mw_i} \quad (6.5)$$

Where  $\rho_c$  is the coating density ( $\text{g}/\text{m}^3$ ),  $\gamma_i$  the inhibitor concentration loaded inside the carriers, and  $Mw_i$  the molecular weight of the inhibitor ( $\text{g}/\text{mol}$ ).

Considering equations (6.4) and (6.5) the maximum release-rate ( $N_{\max}$ ) that can be reached over a period of time (t) before the particles are completely depleted at a distance from the crack. This can be expressed using equation (6.6), whereby the penetration distance (D) is the only geometrical variable for a given coating composition and damage geometry:

$$N_{\max} = \frac{\rho_c \cdot PVC \cdot \gamma_i}{Mw_i} \left( \frac{D^2}{\emptyset} + D \right) t \quad (6.6)$$

The model can also be used to describe the depletion time as the moment when the inhibitor species are completely depleted from their carriers in combination with the inhibitor release flux ( $N_{0,c}$ ) from the diffusion-limited model in equation (6.7):

$$t_{\text{depletion}} = \frac{\rho_c \cdot PVC \cdot \gamma_i}{Mw_i \cdot N_{0,c}} \left( \frac{D^2}{\emptyset} + D \right) \quad (6.7)$$

## 6.2.4. Materials and samples preparation for experimental validation

### 6.2.4.1. Materials

NaY zeolites (CBV 100) with a  $\text{SiO}_2/\text{Al}_2\text{O}_3$  mole ratio of 5.1 and a particle size of  $520 \pm 50$  nm are purchased from Zeolyst International and used as received. Diatomaceous earth (Diafil 525) is supplied by Profiltra Customized Solutions (NL). After cleaning the diatomaceous earth following a procedure reported elsewhere,<sup>28</sup> a mixture of cylinder shaped micro- to nano-porous amorphous silica particles with a mean particle size of  $12 \pm 5$   $\mu\text{m}$  is obtained. Cerium nitrate hexahydrate ( $\text{Ce}(\text{NO}_3)_3 \cdot 6\text{H}_2\text{O}$ ) and dimethylformamide (DMF,  $\geq 99.9\%$ ) are used in the inhibitor

loading process. 2 mm thick bare copper-rich aluminium alloy 2024-T3 (AA2024-T3) panels are supplied by Kaizer Aluminium and used as substrate. Commercially available bisphenol-A based epoxy resin (Epikote™ 828 with 184-190 g/eq. epoxy) and amine crosslinker (Ancamine®2500 with 105-110 g/eq. H<sup>+</sup>) are supplied by AkzoNobel (NL) and used as-received to form the coating binder. Xylene (99%) is used as solvent in the coating formulation. Milipore® Elix 3 UV filtered water is employed in all steps requiring water.

#### 6.2.4.2. Loading nano- and micro-carriers with inhibitor

The cerium-loading of the zeolite and diatomaceous earth is carried out following previously reported procedures through ion exchange<sup>24</sup> and local precipitation by controlled solvent evaporation,<sup>28</sup> respectively. After loading, the resulting Ce-loaded zeolites (CeY) contain 12±0.5 wt.% Ce<sup>3+</sup> cations in their structure, while the Ce-loaded diatomaceous earth (CeDE) contain 50 wt.% Ce(NO<sub>3</sub>)<sub>3</sub>·6H<sub>2</sub>O, which is equivalent to 16 wt.% Ce<sup>3+</sup> cations.

#### 6.2.4.3. Coatings formulation and application

Coupons of 200x250 mm<sup>2</sup> are cut from the same 2 mm thick AA2024-T3 panel, ground using a 320 grit SiC paper to remove the native oxide layer, degreased with acetone and sonicated in ethanol at 60°C for 30 min. After air drying, a pseudo-boehmite treatment is performed on the coupons to increase the amount of reactive hydroxyl groups on the surface by 10 s immersion in 2 M NaOH followed by a 30 s immersion in distilled water and drying with nitrogen. The coupons are then stored in a dry and clean environment prior to coating for a maximum of 15 min.

Four different coating compositions are prepared (namely, REF, CeY, CeDE1 and CeDE2), as listed in Table 6.1. The coating binder formulation, identical for all coatings, is prepared using the g/eq. provided by the resins manufacturer for a stoichiometric epoxy reaction. In the presence of xylene as solvent, the weight-ratio used is 2.70:1.57:1.06 (epoxy:amine:solvent). The binder formulation is mixed for 5 min using a high-speed mixer at 2400rpm and then left to pre-cure at room temperature for 30 min. After adding the inhibitor loaded carriers, the coating formulation is manually stirred for 5 minutes and then applied onto the metal coupons using a doctor blade with wet thicknesses of 10/50/100 µm depending on the coating layer to be deposited. After a flash-off period of 30 minutes the samples are cured at 60°C for 24h to achieve full crosslinking and solvent evaporation. The dry coating thicknesses are measured using an eddy current probe and results are indicated in Table 6.1. The samples are stored in a desiccator and taken out to acclimatize 30 min before damaging and corrosion testing.

**Table 6.1** Composition and layer thicknesses of the 4 coating systems tested

| Name  | Single layer | Carrier type | Carrier loaded with inhibitor | Dry thickness |        | $\rho$               | PVC <sup>1</sup> |
|-------|--------------|--------------|-------------------------------|---------------|--------|----------------------|------------------|
|       |              |              | (phr)                         | (μm)          |        | (g/cm <sup>3</sup> ) | (%)              |
| REF   | Primer       | -            | -                             | 100±20        |        | 1.20                 | -                |
| CeY   | Primer       | CeY          | 142                           | 45            | 145±20 | 0.90                 | 30               |
|       | Topcoat      | -            | -                             | 100           |        | 1.20                 | -                |
| CeDE1 | Primer       | CeDE         | 32                            | 45            | 145±20 | 1.12                 | 10               |
|       | Topcoat      | -            | -                             | 100           |        | 1.20                 | -                |
| CeDE2 | Primer 1     | -            | -                             | 10            | 155±20 | 1.20                 | -                |
|       | Primer 2     | CeDE         | 140                           | 45            |        | 0.98                 | 30               |
|       | Topcoat      | -            | -                             | 100           |        | 1.20                 | -                |

$$^1 PVC = \frac{V_{inhibitor} + V_{carrier}}{(V_{inhibitor} + V_{carrier} + V_{binder})} * 100\% ; \text{ where } V_{binder} \text{ is the dry volume}$$

#### 6.2.4.4. Controlled damages on coated panels

A Roland EGX-350 engraver equipped with a conical cemented carbide tip is used to create well-controlled circular damages to the coated panels prior to immersion in electrolyte for the corrosion studies. The engraving process stopped immediately after the first contact with the metallic surface, as detected using an LED and a closed electric circuit between the tip and the substrate. The engraving proceeded in steps of 10 μm in the z-direction perpendicular to the sample surface until the electric circuit closed (i.e. LED is ON). Damages with two different dimensions are created depending on the tip used: (i) 50 μm diameter damage with an AC125-BAL-PRO-002 with a tip-angle of 30° ; and (ii) 300 μm diameter damage with a ZECA-2025BAL with a tip-angle of 30°.

### 6.2.5. Corrosion evaluation with an in-situ optical and electrochemical set-up

All electrochemical tests are performed using the optical-electrochemical setup shown in Figure 6.3. The setup is placed on an optical table equipped with active isolators and a damping breadboard. The table is then covered with a Faraday cage to avoid interferences from external electrical sources. The working principle of the set-up is identical to the one described in our previous works.<sup>37,38</sup> Main difference with past works is that in the present work a commercial cell for Raman-electrochemistry studies from redox.me® (Figure 6.3) is used. The cell has a volume of 4.5 ml, an aperture opposite to a 1 mm thick quartz glass window of 3.5 cm<sup>2</sup> (i.e. exposed area of the studied sample to the electrolyte) and an optical path of 2.25 mm (i.e. distance between the sample and the quartz window). The cell is placed vertically on top of a manual

translation stage that allowed positioning the damage in the field of view of the camera. This design of the Raman-cell can be regarded as an evolution of the cells described in earlier work,<sup>37,38</sup> as it has a shorter optical path required for high magnification recording and is easier in handling and focussing the sample relative to the camera. A high-magnification USB camera from Dino-Lite, model AM7515MT4A (415-470x) with a 5.0 megapixel CMOS sensor (2592x1944 pixels) and an 8-LED ring-light is placed parallel to the glass window to monitor and illuminate the exposed area. The camera is controlled with DinoCapture 2.0 and programmed to record with a time interval of 1 minute, simultaneously with the electrochemical measurements.

The electrochemical signals are recorded with an Ivium Compactstat controlled by IviumSoft V2.86. Following past works using electrochemical noise, it is decided to follow the surface response to the electrolyte (0.05 M NaCl) by monitoring the electrochemical potential noise (EPN) between the working electrode (WE) and a saturated Ag/AgCl reference electrode (RE) using a potential-range setting of 1 V in a 2-electrode configuration. A sampling frequency of 20 Hz is used to record rapid occurring fluctuations while a low-pass filter of 10 Hz is applied to avoid aliasing on the recorded signal.

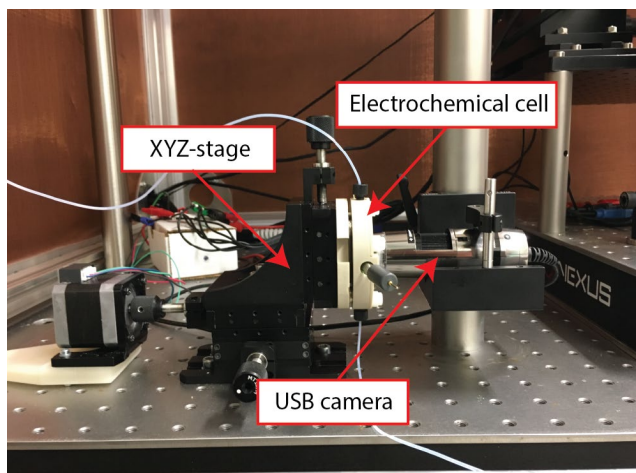


**Figure 6.3** Image of the optical-electrochemical setup placed on an optical table inside a Faraday cage.

### 6.2.5.1. Analysis of the optical images

Highly resolved optical information at a resolution of 3 pixels/ $\mu\text{m}$  is obtained through an automated image analysis procedure present in ImageJ software. After a recursive repositioning procedure the exposed metal surface is isolated from the surrounding coating by cropping, resulting in two sets of images. The images of the exposed metal surface are analysed using the previously described analysis method to calculate the surface fraction having undergone optical changes.<sup>37,38</sup> A new time-resolved method is used on both sets of images to obtain the optical activity at the metal surface and at the surrounding coating separately. This is obtained by subtracting the intensity of each pixel in x and y direction at time n ( $i_n$ ) from the intensity at time n+k ( $i_{n+k}$ ) from the recursively repositioned images, whereby k is the step-size as shown in equation (6.8).

$$i_{\text{Difference}}(x, y) = |i_{n+k}(x, y) - i_n(x, y)| \quad (6.8)$$

With this procedure, a pixel that changes its recorded intensity within the period (k) will be classified as an “active pixel” whereby the extent of activity for this pixel is obtained through its intensity-value. All processed images are converted to 8-bit (256 bin grey-scale, bin 0 for black and bin 255 for white). For the exposed metal surface a static thresholding bin-limit of 15 is used while the surrounding coating requires a lower thresholding limit of 7 due to the occurrence of smaller intensity changes. The statistical outliers and random fluctuations are removed using a 1 px filter. The step size (k) is set to 300 s in order to quantify the occurring processes at the metal in the graphs, whereby the pixels are converted to a percentage of active area based on the size of the exposed metal surface. The step size (k) is set to 2 ks for the shown illustrations, indicating the degree and type of changes at the coating and surrounding coating in a colour-plot in which the grey-value of each active pixel is transposed to a colour-gradient (Fire-LUT). Pixels related to inactivity are indicated white, while all other pixels are coloured from yellow to black according to their degree of activity. Such an approach allows the identification of changes in activity that are difficult to observe from the original images.

### 6.2.5.2. Analysis of the electrochemical data

Under open-circuit conditions the local time-frequency behaviour of the EPN provides information about the corrosion kinetics, and so, the nature of the underlying physical-electrochemical processes.<sup>39-41</sup> The EPN signals are studied with a Hilbert-Huang transform through Matlab from Mathworks® based on a publicly available procedure from Rilling et al.<sup>42,43</sup> This was combined with the use of published EPN spectra of the AA2024-T3 corrosion and inhibition by cerium under immersion conditions in a similar electrolyte.<sup>44</sup> In the present work, the described approach is used to identify localized corrosion, inhibition or passivation regimes as a function of the immersion time. Examples of the Hilbert-Huang identification procedure can be found in SI-6.1.

### 6.3. Results and Discussion

Simulated and experimental results are obtained for damaged epoxy coatings containing cerium loaded carriers. The coatings are applied on AA2024-T3 and exposed to electrolyte containing 0.05 M NaCl. Based on the available literature it is known that AA2024-T3 shows the first signs of local corrosion around intermetallic particles within 100 s after immersion.<sup>45,46</sup> Several studies show that the presence of  $\text{Ce}^{3+}$  in the electrolyte can stop or significantly reduce local corrosion by the formation of a thin passivation layer.<sup>47-50</sup> A few studies reported that cerium concentrations as low as  $10^{-5}$  M already give protection but the cerium concentration should preferentially be between  $10^{-4}$  and  $10^{-3}$  M and not higher than  $10^{-2}$  M.<sup>22,37,48,51</sup> In this work a minimum local concentration of  $10^{-5}$  M after 100 s immersion will be considered as sufficient to avoid any over-estimation on the simulated minimum required inhibitor release rate.

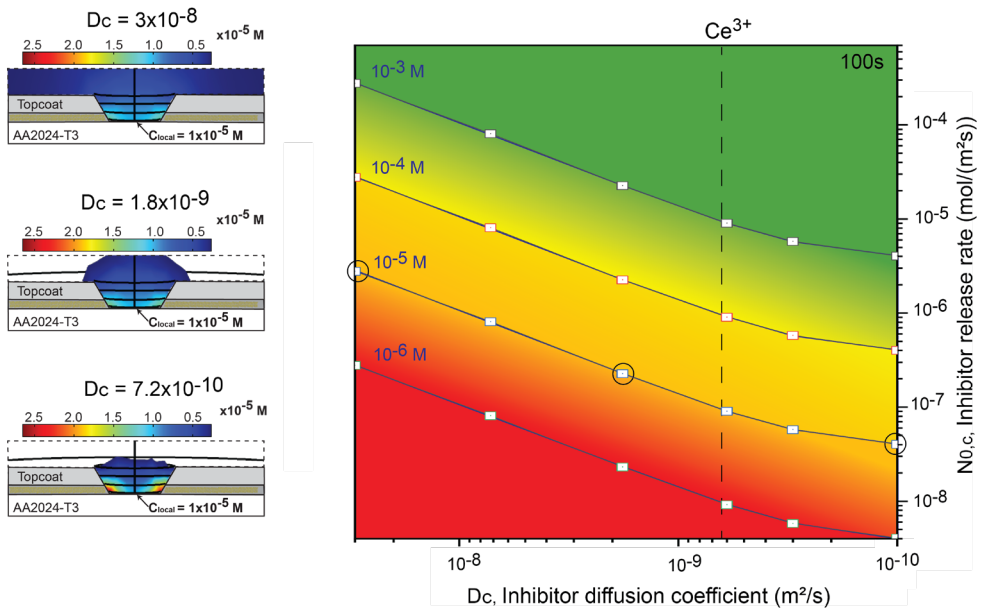
#### 6.3.1. Diffusion-limited inhibitor release simulations

The following section discusses the effect of several coating and damage properties on the minimum required inhibitor release from anti-corrosive coatings containing homogeneously dispersed inhibitor in the primer. The results are obtained using a diffusion limited model of the electrolyte in combination with mass-conservation laws for the damaged coating system as explained in the experimental section.

##### 6.3.1.1. Inhibitor diffusivity

The typically reported inhibitor diffusion coefficients ( $D_c$ ) in aqueous solutions are in the range of  $10^{-10}$  to  $10^{-9}$   $\text{m}^2/\text{s}$  at room temperature (e.g.  $6.0 \times 10^{-10}$   $\text{m}^2/\text{s}$  for  $\text{Cr}^{3+}$ ,  $6.2 \times 10^{-10}$   $\text{m}^2/\text{s}$  for  $\text{Ce}^{3+}$ , and  $1.0 \times 10^{-9}$   $\text{m}^2/\text{s}$  for  $\text{Li}^+$ ).<sup>52-54</sup> Figure 6.4 shows the effect of inhibitor diffusivity on the minimum required release rate for protection, which can be used as guideline for inhibitor selection.

In this simulation a range of inhibitor release rates at the interface is investigated, resulting in concentration gradients in the electrolyte. The Figure therefore shows the direct relation between inhibitor diffusion coefficient value and the inhibitor release rate, together with the derived inhibitor concentration obtained at the centre of the damage site after 100 s exposure using a primer of 45  $\mu\text{m}$  thickness and a damage size of 300  $\mu\text{m}$  diameter. The local inhibitor concentration at the centre of the damage is shown through iso-contour lines and by means of a colour code. Insufficient concentration for protection (e.g.  $10^{-6}$  M) is shown in red, the minimum required inhibitor concentration (e.g.  $10^{-5}$  M) in orange and a sufficient concentration for inhibition (e.g.  $10^{-3}$  M) in green. Representative diffusion models obtained during the simulation are shown on the left side of the graph at the minimum required concentration for protection ( $10^{-5}$  M) for three  $D_c$  values:  $3 \times 10^{-8}$ ,  $1.8 \times 10^{-9}$ , and  $7.2 \times 10^{-10}$   $\text{m}^2/\text{s}$ .



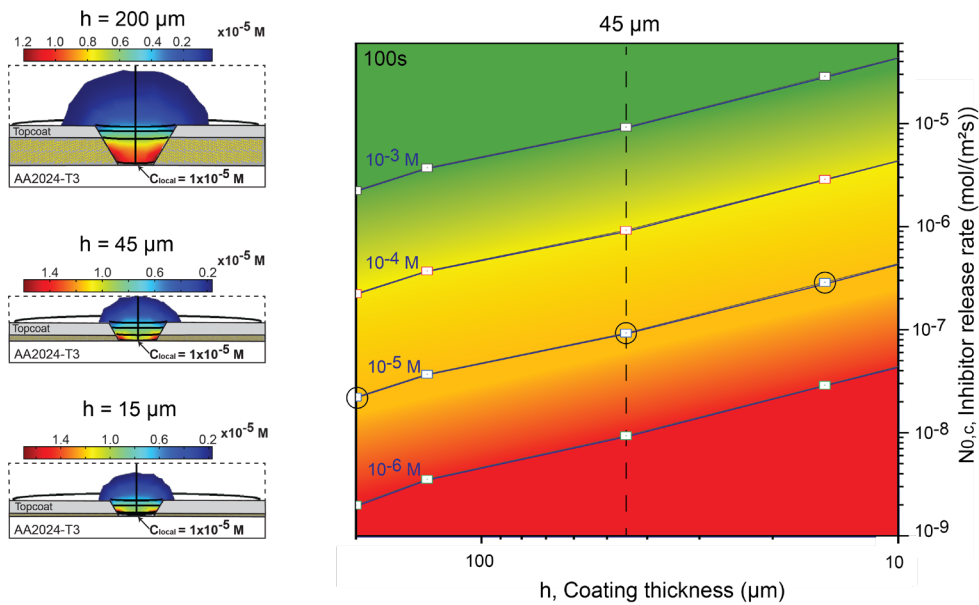
**Figure 6.4** Graphs show the effect of the inhibitor diffusion coefficient ( $D_c$ ) on the required inhibitor release rate ( $N_{0,c}$ ) after 100 s exposure. The colour gradient and inner lines show the local inhibitor concentration at the centre of the damage where  $10^{-6} \text{ M}$  (red) is insufficient inhibitor concentration to protect and  $10^{-5} \text{ M}$  (orange) is the minimum required amount. Schemes show the 2D cross-sections from the diffusion model at  $10^{-3} \text{ M}$ . Coating variable parameters used in this simulation:  $h = 45 \text{ }\mu\text{m}$ ,  $\varnothing = 300 \text{ }\mu\text{m}$ .

Figure 6.4 shows that inhibitors with lower diffusion coefficient values in the electrolyte (e.g.  $\text{H}_2\text{O}$ ) require higher release rates from the coating to protect the metal (i.e. faster inhibitor transport from the coating) considering first corrosion signs are visible after 100 s immersion. From the 2D models it can be observed that a lower diffusion coefficient values results in a larger concentration gradient at the damage, while higher diffusion gradients result in the dissipation of species towards the electrolyte bulk above the damage location, thereby increasing the possibility of inhibitor loss before reaction with the substrate.

In general, slow inhibitor release rates are favourable to avoid more inhibitor to be released from the damaged coating than required for protection. However, the diffusion coefficient needs to be sufficiently high to allow the substrate protection at the entire damaged location in a desirable time (e.g. 100 s). Considering that the diffusion coefficient for  $\text{Ce}^{3+}$  is reported to be around  $6.2 \times 10^{-10} \text{ m}^2/\text{s}$  at  $25^\circ\text{C}$  in aqueous solutions as denoted with a dashed line in Figure 6.4, according to the simulation results a minimum inhibitor release rate of  $7 \times 10^{-7} \text{ mol}/\text{m}^2 \cdot \text{s}$  would be necessary to protect this damage.

### 6.3.1.2. Coating thickness

In this section the effect of the coating thickness ( $h$ ) on the inhibitor release rate after 100 s exposure is studied using cerium as inhibitor ( $D_c(\text{Ce}^{3+}) = 6.2 \times 10^{-10} \text{ m}^2/\text{s}$ ). Considering that the dry film thickness of primers is usually between 5 and 200  $\mu\text{m}$  depending on the application and used standards,<sup>21,55</sup> the results shown in Figure 6.5 can be used as guideline to evaluate if the selected coating thickness is appropriate to achieve the minimum required inhibitor concentration for protection. Representative diffusion models are shown on the left side of the graph for three different thicknesses ( $h = 200, 45$  and  $15 \mu\text{m}$ ).



**Figure 6.5** Graphs show the effect of primer thickness ( $h$ ) on the required inhibitor release rate ( $N_{0,c}$ ) after 100 s exposure. The colour gradient and inner lines show the local inhibitor concentration at the centre of the damage where  $10^{-6} \text{ M}$  (red) is insufficient inhibitor concentration to protect and  $10^{-5} \text{ M}$  (orange) is minimum required amount. Schemes show the 2D cross-sections from the diffusion model at  $10^{-5} \text{ M}$ . Model parameters:  $\varnothing = 300 \mu\text{m}$ ,  $D_c(\text{Ce}^{3+}) = 6.2 \times 10^{-10} \text{ m}^2/\text{s}$ .

As expected, Figure 6.5 shows that thicker coatings require lower release rates to reach similar local inhibitor concentrations at the centre of the damage as thin coatings. This effect is linear and caused by the larger exposed surface of the coating to the electrolyte at the damaged location in the case of thicker coatings. Considering most primers used to protect aerospace alloys range between 15 and 50  $\mu\text{m}$ ,<sup>21</sup> due to weight restrictions and taking into account the experimental conditions to validate the model (Table 6.1) it is decided to fix the thickness to 45  $\mu\text{m}$  (dotted line) for the remainder of the work.

### 6.3.1.3. Damage size

The above simulations have been done for a specific damage dimension. Nevertheless, in real applications the thickness of the primer and the diffusion rate of the pigment are fixed while the damage size can vary. In line with this, Figure 6.6 shows the effect of the damage diameter ( $\varnothing$ ) on the minimum required inhibitor release rate needed for protection after 100 s exposure. Representative diffusion models to reach at  $10^{-5}$  M at the centre of the damage are shown on the left side of Figure 6.6 for  $\varnothing = 1000, 300$  and  $50 \mu\text{m}$ .

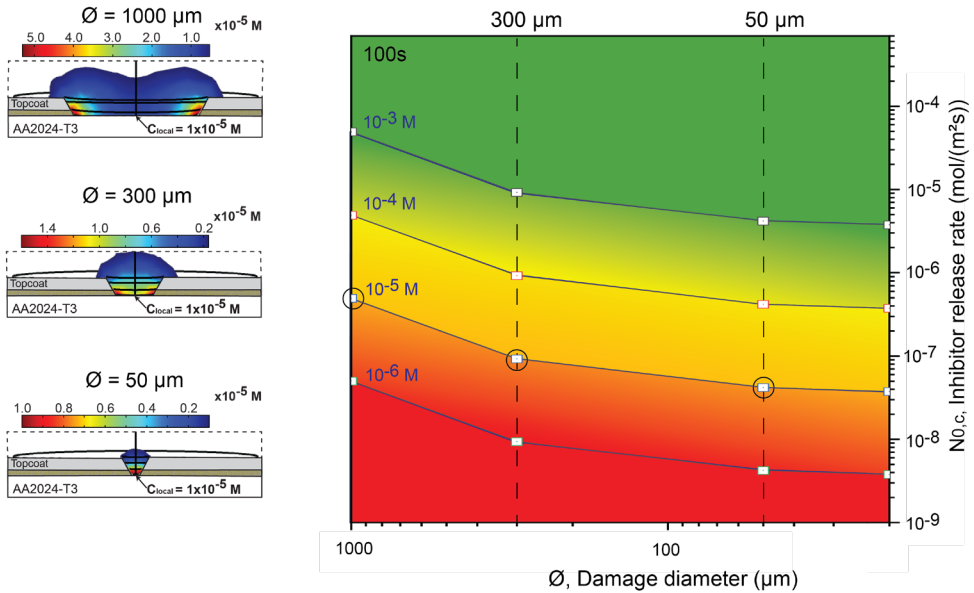


**Figure 6.6** Graph shows the effect of damage diameter ( $\varnothing$ ) on the required inhibitor release rate ( $N_{0,c}$ ) after 100 s exposure. The colour gradient and inner lines show the local inhibitor concentration at the centre of the damage where  $10^{-6}$  M (red) is insufficient inhibitor concentration to protect and  $10^{-5}$  M (orange) is minimum required amount. Schemes show the 2D cross-sections from the diffusion model at  $10^{-5}$  M. Model parameters:  $h = 45 \mu\text{m}$ ,  $D_c(\text{Ce}^{3+}) = 6.2 \times 10^{-10} \text{ m}^2/\text{s}$ .

The results in Figure 6.6 show that slightly higher release-rates are required to protect larger damages (i.e. to provide sufficient inhibitor concentration all over the damage after 100 s exposure). This is due to the larger diffusion path that the inhibitor needs to cover within the damage electrolyte which requires larger diffusion gradients from the coating walls at the damage towards the centre of the metal surface. The required release-rate shows a quadratic growth with the damage diameter as diffusion gradients towards the bulk solution above the damage increase. The simulations show that a minimum release rate of  $4.2 \times 10^{-8} \text{ mol}/(\text{m}^2\text{s})$  for  $\varnothing = 50 \mu\text{m}$  and of  $9.3 \times 10^{-8} \text{ mol}/(\text{m}^2\text{s})$  for  $\varnothing = 300 \mu\text{m}$  are required.

### 6.3.1.4. Carrier-size and PVC

When the inhibitors are localized at carriers instead of homogeneously dissolved in the coating, as in the previous cases, the model needs to take into account the inhibitor depletion from the particles. The inhibitor depletion for the particles located at the coating-electrolyte interface can be calculated using equation (6.6) based on the inhibitor release rate simulations and the mass conservation laws. For these calculations it is assumed that the required inhibitor release rate and local inhibitor concentration at the damage wall (as calculated in the previous sections) can be sustained over a period of 1000 s immersion by inhibitor diffusion from the bulk to the damage location. Figure 6.7 shows the simulated maximum inhibitor release rates ( $N_{max}$ ) that can be achieved during this period for a damaged coating whereby the carrier-size (P) and PVC are varied.

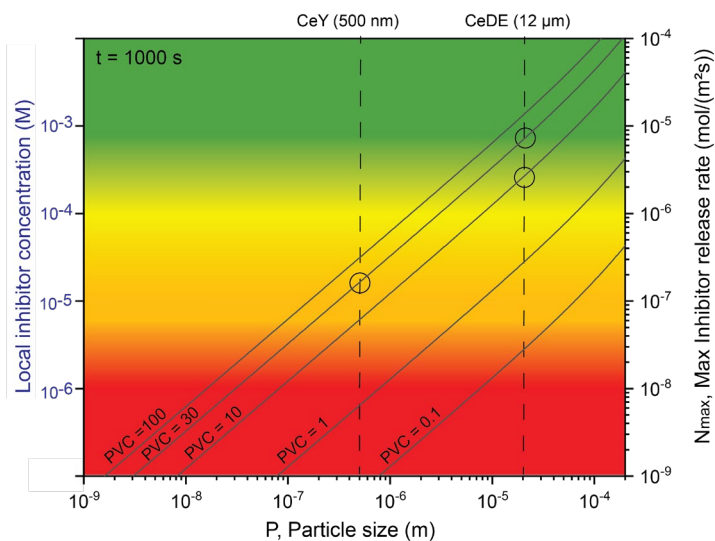


**Figure 6.7** Graph shows effect of particle size (P) and PVC on the maximum reachable inhibitor release rate ( $N_{max}$ ) maintained for 1000 s exposure. The colour gradients show the local inhibitor concentration at the centre of the damage where  $10^{-6}$  M (red) is insufficient inhibitor concentration to protect and  $10^{-5}$  M (orange) is minimum required amount. Model parameters:  $\varnothing = 300 \mu\text{m}$ ,  $\gamma_i = 15\%$   $\text{Ce}^{3+}$  inside the carriers.

Figure 6.7 shows that a higher inhibitor release rate can be achieved by adding more loaded carriers inside the coating (i.e. increasing the PVC) or by using carriers with a larger particle size. The Figure shows that increasing the PVC above 30% does not result in a significantly higher release rate while using larger carriers does improve the behaviour, even at lower PVC. To validate the simulated results, the corrosion protection under immersion conditions is tested experimentally (and shown in 3.2) for damaged coatings containing: (i) 30 PVC nano-particles (CeY), (ii) 10 PVC micro-particles (CeDE1) and (iii) 30 PVC micro-particles (CeDE2).

### 6.3.1.5. Inhibitor pathways through the coating

In the previous section only the particles located at the coating-electrolyte interface are taken into account to study the maximum inhibitor release that can be sustained during 1000 s immersion. This scenario ultimately results in the depletion of inhibitor species from the nearest particles over longer immersion times. Figure 6.8 shows the calculated time-dependent depletion (length within the coating without inhibitor from the damage). In the Figure the yellow zone represents the  $Ce^{3+}$  depletion in time from a single-particle. The green zone represents the depletion length in time considering that inhibitor pathways within the coating were created and calculated using equation (6.7).

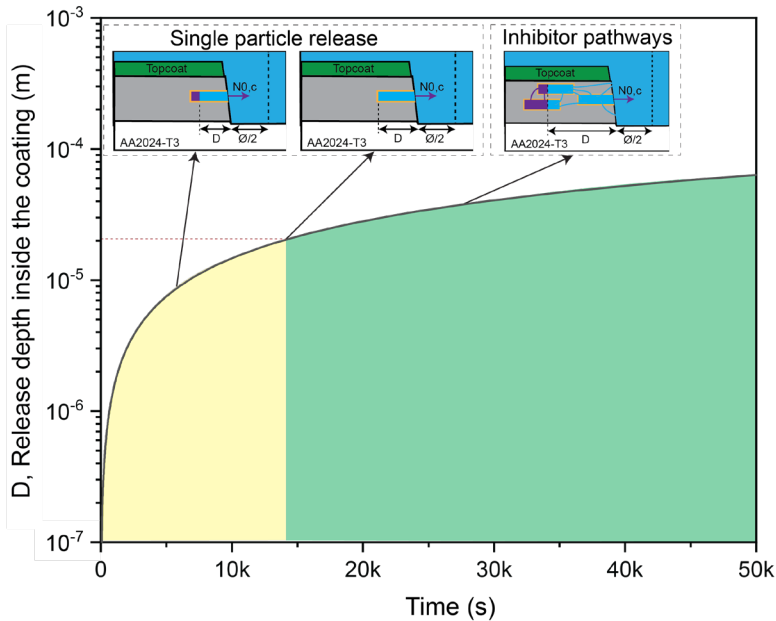


**Figure 6.8** Calculated time-dependent inhibitor release from CeDE particles located at the coating damage surface (yellow) and the release from an interconnected network of particles (green). Model parameters:  $\varnothing = 300 \mu\text{m}$ ,  $C_{\text{local}} = 5 \times 10^{-5} \text{ M}$ ,  $(\text{PVC} \cdot \gamma_i) \propto N_{0,c}$ .

Figure 6.8 shows that single particles are depleted after 14000 s (<3.9h) immersion whereby the PVC and inhibitor content are assumed to be directly proportional to the release rate. The release time, and therefore amount of inhibitor being released in time, can be increased when interconnected paths between particles, i.e. networks, are created (green area in Figure 6.8). Such connection paths enable the release and diffusion of  $Ce^{3+}$  ions located at large distances from the damage. It should be noted that in this case, the inhibitor diffusion from particles further away towards the damage edge has to take place before the particles at the coating-electrolyte interface are completely depleted in order to have a sufficient inhibiting power.

### 6.3.2. Validation through optical-electrochemical experiments

The following section discusses the optical and electrochemical results obtained from the corrosion experiments for conditions similar to the simulation results (section 6.3.1.). In this way the experimental results are used to validate the model results and their generic guidelines for the design of anticorrosive coatings based on carrier systems.

#### 6.3.2.1. Corrosion of coated AA2024-T3 in 0.05 M NaCl

Figure 6.9 shows the experimental results for epoxy coatings without inhibitors applied on AA2024-T3 and used as reference system (REF). The coatings were evaluated in 0.05 M NaCl solutions and after performing damages of  $\varnothing = 50 \mu\text{m}$  (small damage) or  $\varnothing = 300 \mu\text{m}$  (large damage). Figure 6.9 a-b show the raw EPN signals. The background colour of these Figures indicates the classification on the basis of Hilbert-Huang spectra (HHS) as described in the experimental procedure shown in SI-6.1. The colours vary between grey (corrosion), green (inhibition) and yellow (passivation). Figure 6.9 c-d show the untreated original optical images under immersion and (e-f) the temporal resolved optical changes that take place in a 2 ks interval whereby the degree of activity is indicated by the colour bar. Figure 6.9 g-h show the corresponding quantitative information derived from the activity inside the damage in steps of 300 s (black columns), as well as the cumulative affected area over time (red line).

The EPN signal (Figure 6.9 a-b) shows a fluctuating potential around -500 mV vs Ag/AgCl. The kinetic information contained in these signals, as well as the HHS analysis, can be regarded as typical for the corrosion of AA2024-T3 under these conditions.<sup>44</sup> Hence, the grey background colour used indicates a stable localised corrosion process throughout the measurement. The optical results (Figure 6.9 c-d) show that pits appear at the metal surface in combination with oxide formation around the edge of the damage (i.e. top-right corner for the small damage). The processed images (Figure 6.9 e-f) show that the activity is localised as spots with a size below  $10 \mu\text{m}$  in radius (shown in red and purple) at the exposed metal and at the boundary with the coating, while no activity is observed at or underneath the coating itself (i.e. no delamination). After 4 ks the activity is localised around those pits that were already active in the first stage when the coating was still stable (i.e. no activity outside the damaged metal). The quantitative optical analysis (Figure 6.9 g-h) shows a clear activity at the AA2024-T3 surface (black columns). It is important to mention that the larger damage site results in a lower amount of activity yet more evenly distributed over the time compared to the activities in the small damage site. This is attributed to local compositional fluctuations of the exposed AA2024-T3 combined with a more averaged optical evaluation of the local activity when the surface-area is increased. The cumulative rate of affected surface area (shown in red) is nevertheless comparable in both cases and close to those values previously reported for bare AA2024-T3 (red dotted line, 0.003 %/s).<sup>38</sup> This indicates the occurrence of similar corrosion-related phenomena (i.e. localised corrosion) in both cases and are in good agreement with previously reported co-operative

corrosion processes (i.e. subsurface corrosion and oxide formation) on AA2024-T3 at long immersion times.

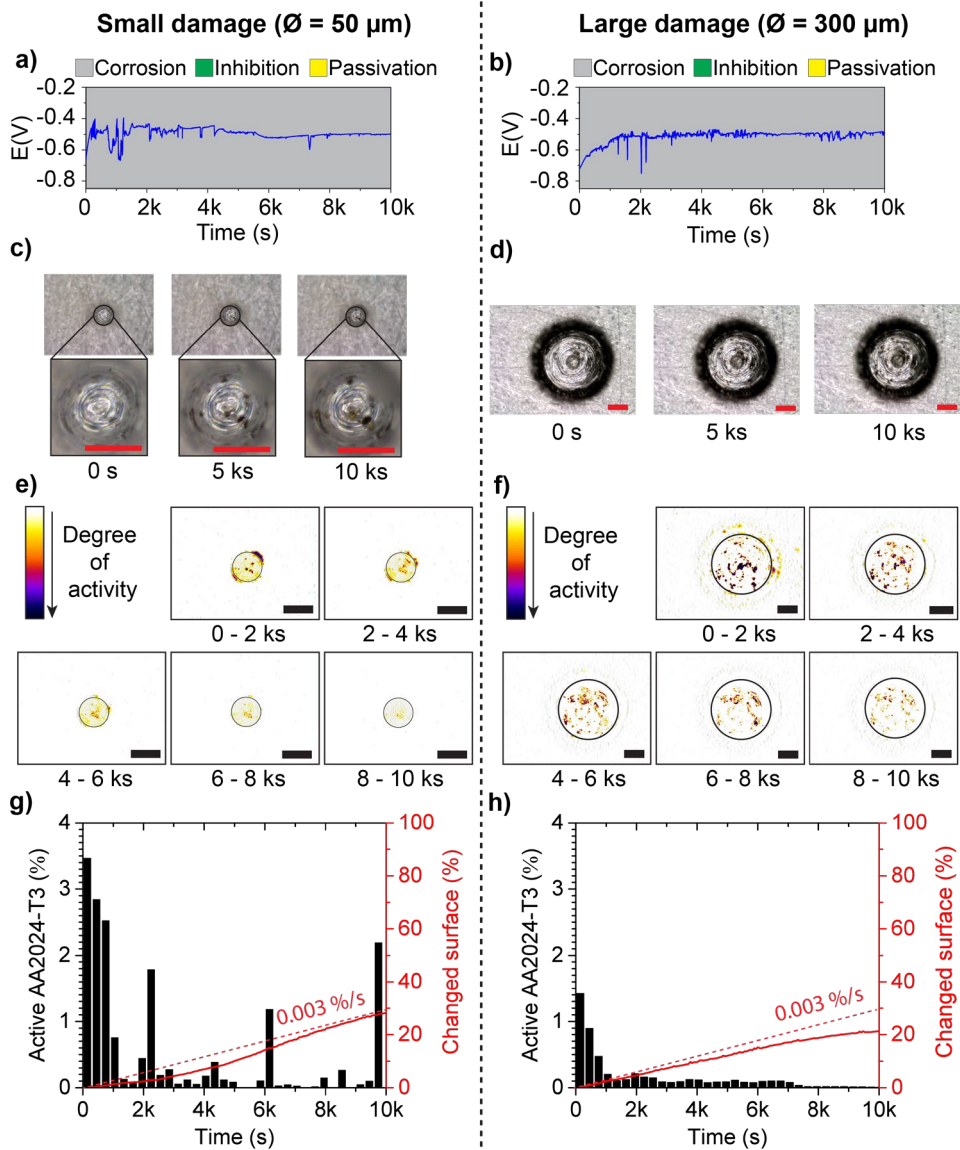


**Figure 6.9** Optical and electrochemical results for epoxy coatings during immersion in 0.05 M NaCl over a period of 10 ks containing a small damage (left) and a large damage (right). Indicated as (a-b) the raw EPN signals, (c-d) the original images, (e-f) the optically detected degree of activity, and (g-h) the quantitative optical analysis inside the damage where bars indicate variations in a specific period of time (300 s) and red lines the cumulative variation, including the reported values from literature<sup>38</sup> (red dashed line). Scale bar represents 50 and 100  $\mu\text{m}$  for the small and large damage, respectively.

## 6.3.2.2. The effect of damage size

Figure 6.10 shows the optical and electrochemical results during immersion in 0.05 M NaCl for epoxy coatings containing cerium-loaded nano-particles (CeY coating) in the presence of small ( $\varnothing = 50 \mu\text{m}$ ) and large damages ( $\varnothing = 300 \mu\text{m}$ ).

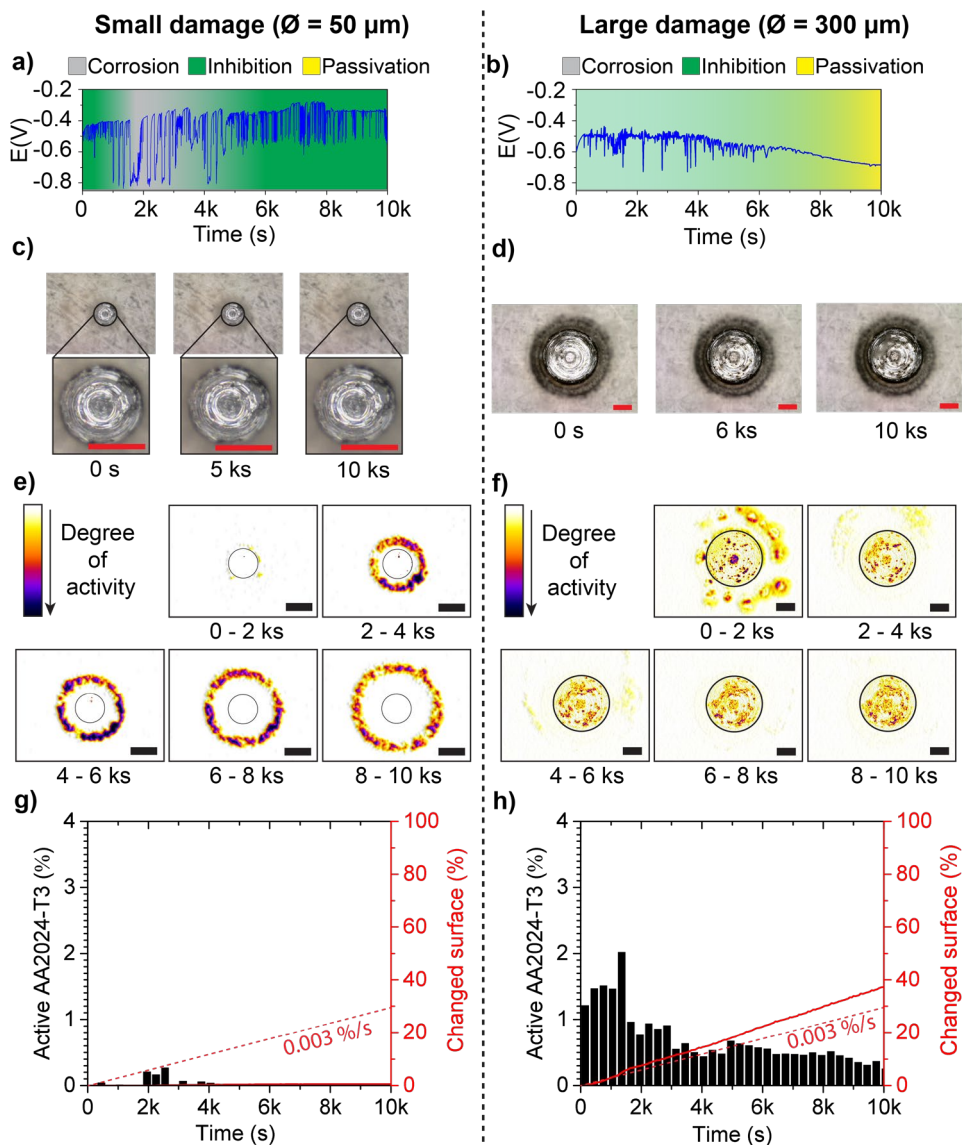


**Figure 6.10** Optical and electrochemical results for CeY coatings during immersion in 0.05 M NaCl over a period of 10 ks containing a small damage (left) and a large damage (right). Indicated as (a-b) the raw EPN signals, (c-d) the original images, (e-f) the optically detected degree of activity, and (g-h) the quantitative optical analysis inside the damage where bars indicate variations in a specific period of time (300 s) and red lines the cumulative variation, including the reported values from literature<sup>38</sup> (red dashed line). Scale bar represents 50 and 100  $\mu\text{m}$  for the small and large damage, respectively.

The results for the CeY coatings with a small damage show that the EPN signal (Figure 6.10a) fluctuates continuously between -400 mV and -800mV, indicative of a fast occurring activity with significant energy. HHS analysis indicates initial inhibitor activity (shown in green), followed by limited corrosion activity around 2 ks (shown in grey), finally followed by inhibition activity again for the rest of the measurement. The optical images (Figure 6.10c) and processed images (Figure 6.10e) show that the exposed metal (inside the black circle) does not show any sign of corrosion during the immersion period. The quantitative optical analysis (Figure 6.10g) shows almost no activity or visible surface changes on the AA2024-T3 (inside the black circle) for most of the immersion time. An almost isolated event at around 2 ks coincides with the 'corrosion' period identified in the EPN analysis.

Another remarkable result is observed in the analysis of the micrographs. These reveal the presence of a high activity ring around the black circle (i.e. the damage) as seen in Figure 6.10e. This outside ring moves away from the damage centre with the immersion time, especially after 2 ks. This process coincides with the kinetic information obtained from the HHS analysis when inhibitive action at the metal is restored. The optical activity at the coating is likely to be the result of a change in the refractive index of the coating as observed in previous works.<sup>29</sup> This can be caused by one or a combination of different processes such as water ingress, inhibitor release, delamination and/or the formation of corrosion products underneath the coating. Unfortunately, the image analysis is yet unable to discern which of these is predominant. Nevertheless, the obvious corrosion protection at the exposed metal, the EPN signals and the symmetry of the ring suggest that this is most likely due to water uptake through diffusion pathways inside the coating. Such process may allow for the release of  $\text{Ce}^{3+}$  relatively far away from the damage site. Based on the optical analysis, the large EPN transient amplitudes and their typical characteristics, similar to EPN signals for bare AA2024 exposed to cerium ions, can be explained by the action of the corrosion inhibitor at the exposed metal. These results confirm that the exposed metal surface is significantly less active than the coating without inhibitors (Figure 6.9), indicating effective corrosion protection.

When the large damage is investigated, the EPN signal (Figure 6.10b) starts at around -600 mV only to increase during the first few hundred seconds towards -500 mV. This is followed by large transients similar as those observed in the EPN signal for the small damage (Figure 6.10a), although with decreasing amplitudes, until the potential becomes stable after 6 ks, which is followed by a downward drift towards -700 mV. In the first stage from 0-7 ks, HHS analysis shows limited corrosion activity alternated with inhibitive action (shown in grey/green), followed by passivity (shown in yellow). The optical images (Figure 6.10d) show that pits and oxides have formed inside the damage and the processed images (Figure 6.10f) show that the activity at the metal is localised and occurs at high intensity (purple and red spots with sizes between 1 and 20  $\mu\text{m}$  in radius). Additionally, the coating shows localised spots of activity

during the first 2 ks located around the damage. It is important to note that for longer immersion-times ( $t > 2$  ks) the activity at the surrounding coating (activity ring as that one observed for the small damage) is most likely located outside the field of view. The optical analysis quantification (Figure 6.10h) reveals a significant amount of activity at the metal initiated right after immersion combined with a rate of surface changes above 0.003 %/s, which is slightly higher than the REF coating (Figure 6.9). These results show that this anticorrosion coating is not effectively protecting the exposed metal surface due to a too limited action of the corrosion inhibitor.

The optical-electrochemical results are in very good agreement with the diffusion-limited release model (Figure 6.6). The experimental results confirm that a very effective coating (e.g. CeY) in the protection of relatively small damages ( $\varnothing = 50 \mu\text{m}$ ) may be insufficient to protect large damages ( $\varnothing = 300 \mu\text{m}$ ) due to an insufficient inhibitor release rate as indicated by the model.

#### 6.3.2.3. *The effect of particle size and PVC*

Figure 6.11 shows the processed optical-electrochemical results for CeDE1 and CeDE2 coatings containing a large damage ( $\varnothing = 300 \mu\text{m}$ ) during immersion in 0.05 M NaCl. In addition, the CeDE2 coating contains a thin  $10 \pm 5 \mu\text{m}$  pure epoxy layer between the metal and the inhibitor-loaded epoxy to prevent optical changes underneath the coating possibly caused by delamination or undercoating processes. In this case all the optical activity observed outside the damage can only be related to electrolyte and/or inhibitor transport inside the inhibitor-containing layer. The EPN signal for both coatings (Figure 6.11 a-b) shows a potential starting at around -700 mV and slowly drifting towards -500 mV with an increasing transient density over time. The HHS analysis shows inhibition activity in both measurements (shown in green), with limited corrosion activity at the end of the exposure for the case of 10 PVC (shown in grey). This corrosion activity may only be caused by a single location that becomes slightly active over a relatively short time span. The optical images (Figure 6.11 c-d) and the processed images (Figure 6.11 e-f) for both coatings confirm the lack of activity. This indicates a clear metal protection against corrosion without significant water ingress in the coating (absence of ring at the coating around the damage as observed in Figure 6.10). The image analysis quantification (Figure 6.11 g-h) confirms the effective damage protection with around 2 % area changed at the end of the exposure time and a degradation rate significantly lower than the reference 0.003 %/s.

When comparing CeY coating shown in Figure 6.10 (i.e. PVC=30) with the CeDE2 (same PVC and inhibitor loading) the results clearly suggest the benefit of using larger particles: CeDE2 shows clear effective corrosion protection while CeY for large damage sites does not. Nevertheless, since the zeolite system relies on ion exchange and the DE relies on dissolution for the release of the inhibitor, it is not possible to discard the influence of the binding type between the carrier and the inhibitor on the effective corrosion protection. Size and/or binding type exert such a large influence on the inhibition that coatings with significantly lower PVC

(CeDE1) still show significantly higher levels of protection than the coating with 30 PVC nanocarriers. These results are in any case in good agreement with the model (Figure 6.7) which indicates that a higher release rate can be achieved with larger particles. Similar results are obtained for the CeDE coating containing a small damage ( $\varnothing = 50 \mu\text{m}$ ), shown in SI-6.2.

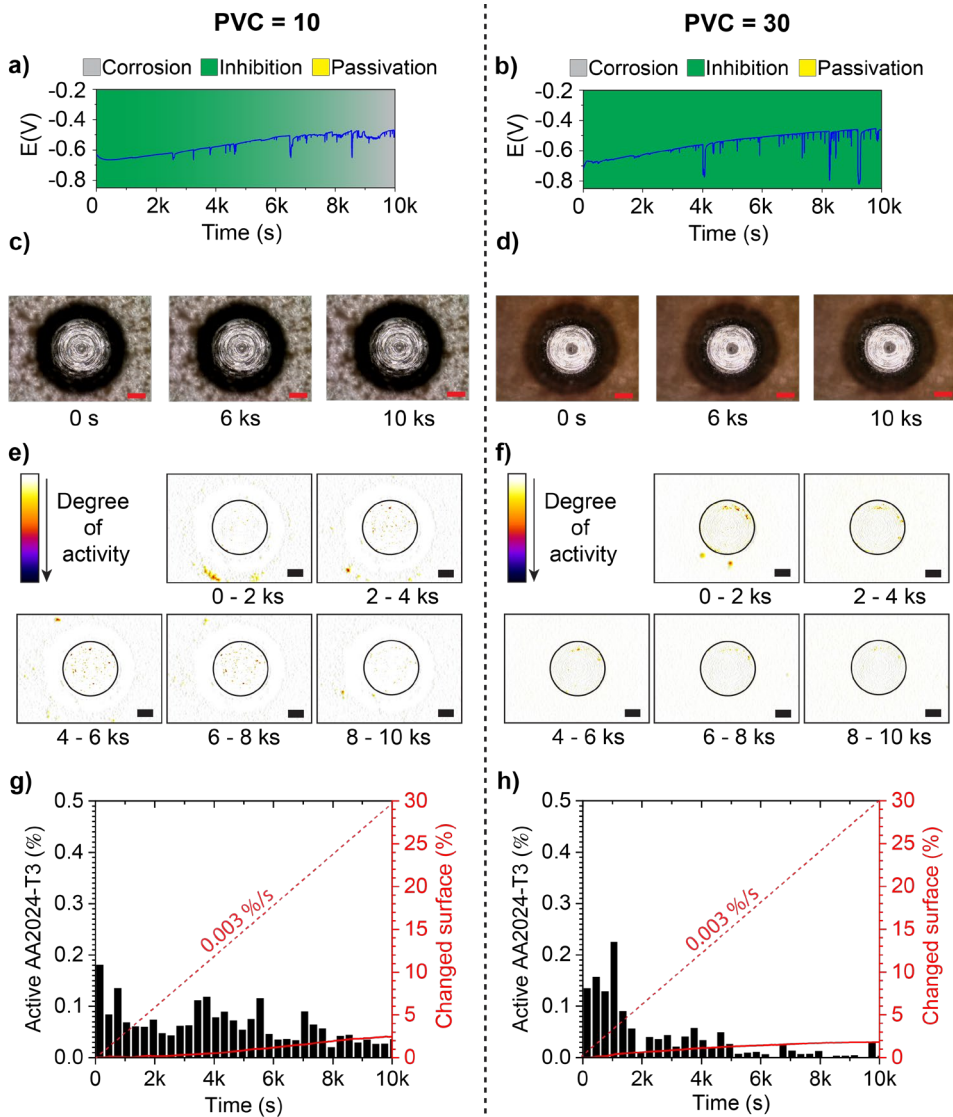


**Figure 6.11** Optical and electrochemical results for CeDE coatings during immersion in 0.05 M NaCl over a period of 10 ks containing 10 PVC (left) and 30 PVC (right) micro-carriers. Indicated as (a-b) the raw EPN signals, (c-d) the original images, (e-f) the optically detected degree of activity, and (g-h) the quantitative optical analysis inside the damage where bars indicate variations in a specific period of time (300 s) and red lines the cumulative variation, including the reported values from literature<sup>38</sup> (red dashed line). Scale bar represents 100  $\mu\text{m}$ .

#### 6.3.2.4. *The effect of inhibitor pathways*

The experimental results in Figure 6.11 show that both 10 and 30 PVC CeDE particles provide sufficient protection for a short period of time (i.e. <10 ks). Also the model shown in Figure 6.8 suggests that for this time-period (< 3 h) the release of inhibitors from particles located at the particle-electrolyte interface would be sufficient to yield protection. Nevertheless, to reach an extended protection time the model suggests that the creation of inhibitor pathways is important. The diffusion within the coating can be promoted by increasing the PVC (i.e. shorter particle-particle distance). In this section the effect of diffusion pathways on the corrosion protection is investigated for the CeDE coatings containing 10 and 30 PVC at relatively long immersion times (50 ks) for small and large damages. Figure 6.12 shows the optical results for a small damage (left side) and a large damage (right side) during immersion in 0.05 M NaCl.

The EPN signal and HHS analysis for the small damage in 10 PVC (Figure 6.12a) starts with inhibitor activity (shown in green). Subsequently, from 8 to 20 ks, some limited localized corrosion is detected (shown in grey). At immersion times >20 ks a passive state is detected (shown in yellow). When the damage is larger (Figure 6.12b), the same coating of 10 PVC shows inhibiting activity only during the first 7.3 ks. After this initial inhibition, corrosion gradually becomes more dominant with very characteristic transients for AA2024-T3 in an NaCl solution. The optical images and analysis for 10 PVC (Figure 6.12 c-d) suggest surface activity at long immersion times. This is more evident when the treated images are observed (Figure 6.12 e and f). The small damage (Figure 6.12 c and e) shows darkening of the exposed metal surface in combination with several black spots (local corrosion) and very high activity in the analysed colour plot. Similar darkening of the entire surface is observed in control samples in which the REF coating system was damaged and then immersed in 0.05 M NaCl containing 10<sup>-6</sup> M cerium nitrate, which is below the minimum required for corrosion protection (SI-6.3). This control test suggests that 10 PVC is unable to release sufficient Ce<sup>3+</sup> over longer immersion-times (>10 ks). Additionally, the large damage (Figure 6.12 d and f) shows local activity (i.e. pits and cooperative corrosion) and high local activity at the metal surface similar to the REF coating, however to a lesser extent and appearing after longer immersion-times.

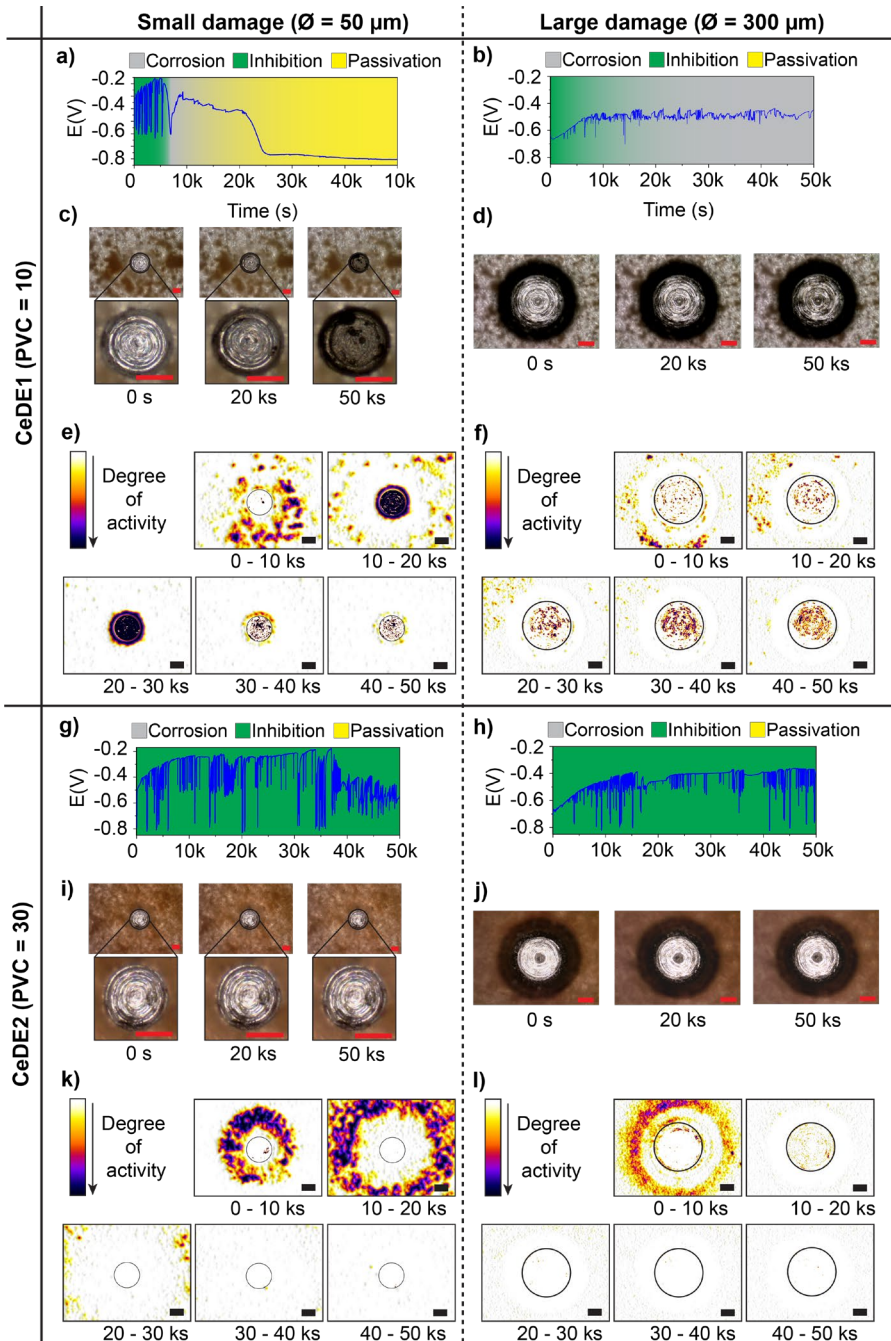


**Figure 6.12** Optical and electrochemical results for coatings containing CeDE particles at 10 PVC and 30 PVC during immersion in 0.05 M NaCl over a period of 50 ks. Coatings contain a small damage (left) and a large damage (right). Scale bar represents 50 and 100  $\mu\text{m}$  for the small and large damage, respectively.

For 30 PVC however, the EPN signals from the small as well as the large damage (Figure 6.12 g-h) contain time domains with variable transient densities and amplitudes. The HHS analysis indicates that these transients are associated with inhibitor activity in both cases. The optical images for 30 PVC (Figure 6.12 i-j) show the total absence of signs related to corrosion over the period of 50 ks in both cases. These results are a clear indication that higher PVCs results in a longer protection-period. The optically detected degree of activity (Figure 6.12 k-l) shows a significant amount of activity at the coating near the damage (ring) moving away from the damage centre during the first 20 ks and 10 ks for the small and large damage, respectively. This very process was observed for the CeY coating containing a similar PVC (Figure 6.10) yet at much shorter times (<10 ks) and is non present in the case of coatings without inhibitors or at lower PVC. This, together with the high degree of protection observed, support the idea that the coating optical changes (ring) are related to the electrolyte diffusion in the coating due to the particle interconnections induced by a sufficiently high PVC. This electrolyte path can then result in the dissolution of  $Ce^{3+}$  and its diffusion towards the damage location. This results confirm the underlying idea shown by the model (Figure 6.8) and previous experimental work that the creation of inhibitor diffusion pathways within the coating is of utmost relevance to facilitate efficient corrosion protection for long immersion times.

## 6.4. Conclusions

In this work, diffusion-driven inhibitor transport simulations based on kinematic mass-conservation laws are used to design of anticorrosive coatings containing inhibitor loaded particles with specific protection characteristics. The simulations are linked to validation experiments performed on epoxy coating containing either zeolites as nanocarriers or diatomaceous earth as microcarriers, loaded with cerium salt as inhibitor. The coatings are applied on AA2024-T3 and contain through-thickness damages that are exposed to 0.05 M NaCl solutions to promote local corrosion and active inhibition. Based on the simulated results, the following designing guidelines are formulated for the design of anticorrosive coatings containing inhibitor loaded carrier particles:

- Higher diffusion coefficient values ( $D_c$ ) for the selected corrosion inhibitor will allow faster inhibitor exposure at the entire metal surface.
- The required inhibitor release rate decreases linearly with increasing coating thickness.
- Larger damages require higher inhibitor release rates. Experimental results confirmed that inhibitor-loaded nano-particles are only able to protect small damages of 50  $\mu\text{m}$  in diameter and not larger damages of 300  $\mu\text{m}$  in diameter.
- An increase in the size of the inhibitor carriers (e.g. from 1  $\mu\text{m}$  to 15  $\mu\text{m}$ ) will result in significantly higher inhibitor release rates and therefore protection in time, even at lower PVC. This was experimentally proven when comparing coatings with 10 PVC of loaded micro particles with coatings containing 30 PVC inhibitor-loaded nano-particles.
- Interconnected networks of inhibitor diffusion pathways inside the coating can prolong the release and protection-time of small and large damages. Experimental results showed that higher PVC can be used to achieve this desired behavior.
- The inhibitor-carrier binding state may significantly influence the release rate and the impact of interconnected networks strategies on the corrosion protection. Nevertheless, the model did not take this into account and the experimental results could only suggest this might be a factor to consider in future works.

## 6.5. References

- 1 J. M.-J. O. C. Chem'Assoc and undefined 1949, "The mechanism of the protective action of an unpigmented film of polystyrene."
- 2 A. A. Roche and J. Guillemet, "Mechanical and chemical properties of organic coatings applied to metallic sheet substrates," *Thin Solid Films*, vol. 342, no. 1, pp. 52–60, Mar. 1999, doi: 10.1016/S0040-6090(98)01340-6.
- 3 J. E. O. Mayne, "How paints prevent corrosion," *Anti-Corrosion Methods and Materials*, vol. 1, no. 8, pp. 286–290, Aug. 01, 1954, doi: 10.1108/eb018973.
- 4 W. Funke and H. Haagen, "Empirical or Scientific Approach to Evaluate the Corrosion Protective Performance of Organic Coatings," *Ind. Eng. Chem. Prod. Res. Dev.*, vol. 17, no. 1, pp. 50–53, Mar. 1978, doi: 10.1021/i360065a014.
- 5 X. F. Yang, C. Vang, D. E. Tallman, G. P. Bierwagen, S. G. Croll, and S. Rohlik, "Weathering degradation of a polyurethane coating," *Polym. Degrad. Stab.*, vol. 74, no. 2, pp. 341–351, 2001, doi: 10.1016/S0141-3910(01)00166-5.
- 6 F. Deflorian, S. Rossi, L. Fedrizzi, and C. Zanella, "Comparison of organic coating accelerated tests and natural weathering considering meteorological data," *Prog. Org. Coatings*, vol. 59, no. 3, pp. 244–250, Jun. 2007, doi: 10.1016/j.porgcoat.2006.09.036.
- 7 F. X. Perrin, C. Merlatti, E. Aragon, and A. Margailan, "Degradation study of polymer coating: Improvement in coating weatherability testing and coating failure prediction," *Prog. Org. Coatings*, vol. 64, no. 4, pp. 466–473, Mar. 2009, doi: 10.1016/j.porgcoat.2008.08.015.
- 8 S. B. Lyon, R. Bingham, and D. J. Mills, "Advances in corrosion protection by organic coatings: What we know and what we would like to know," *Progress in Organic Coatings*, vol. 102, Elsevier B.V., pp. 2–7, Jan. 01, 2017, doi: 10.1016/j.porgcoat.2016.04.030.
- 9 A. E. Hughes, I. S. Cole, T. H. Muster, and R. J. Varley, "Designing green, self-healing coatings for metal protection," *NPG Asia Mater.*, vol. 2, no. 4, pp. 143–151, 2010, doi: 10.1038/asiamat.2010.136.
- 10 A. E. Hughes *et al.*, "The application of multiscale quasi 4D CT to the study of SrCrO4 distributions and the development of porous networks in epoxy-based primer coatings," *Prog. Org. Coatings*, vol. 77, no. 11, pp. 1946–1956, 2014, doi: 10.1016/j.porgcoat.2014.07.001.
- 11 A. E. Hughes *et al.*, "Revelation of intertwining organic and inorganic fractal structures in polymer coatings," *Adv. Mater.*, 2014, doi: 10.1002/adma.201400561.
- 12 S. G. R. Emad *et al.*, "How pigment volume concentration (PVC) and particle connectivity affect leaching of corrosion inhibitive species from coatings," *Prog. Org. Coatings*, vol. 134, pp. 360–372, Sep. 2019, doi: 10.1016/j.porgcoat.2019.05.008.
- 13 M. T. Rodríguez, S. J. García, J. J. Gracenea, K. A. Habib, and J. J. Suay, "Influencia de la concentración de pigmento en volumen (CPV) en las propiedades de una imprimación epoxi," *Rev. Metal.*, vol. 41, no. Extra, pp. 202–207, 2005, doi: 10.3989/revmetalm.2005.v41.iextra.1025.
- 14 M. T. Rodríguez, J. J. Gracenea, J. J. Saura, and J. J. Suay, "The influence of the critical pigment volume concentration (CPVC) on the properties of an epoxy coating: Part II. Anticorrosion and economic properties," *Prog. Org. Coatings*, vol. 50, no. 1, pp. 68–74, 2004, doi: 10.1016/j.porgcoat.2003.10.014.
- 15 A. Kalendová, D. Veselý, I. Sapurina, and J. Stejskal, "Anticorrosion efficiency of organic

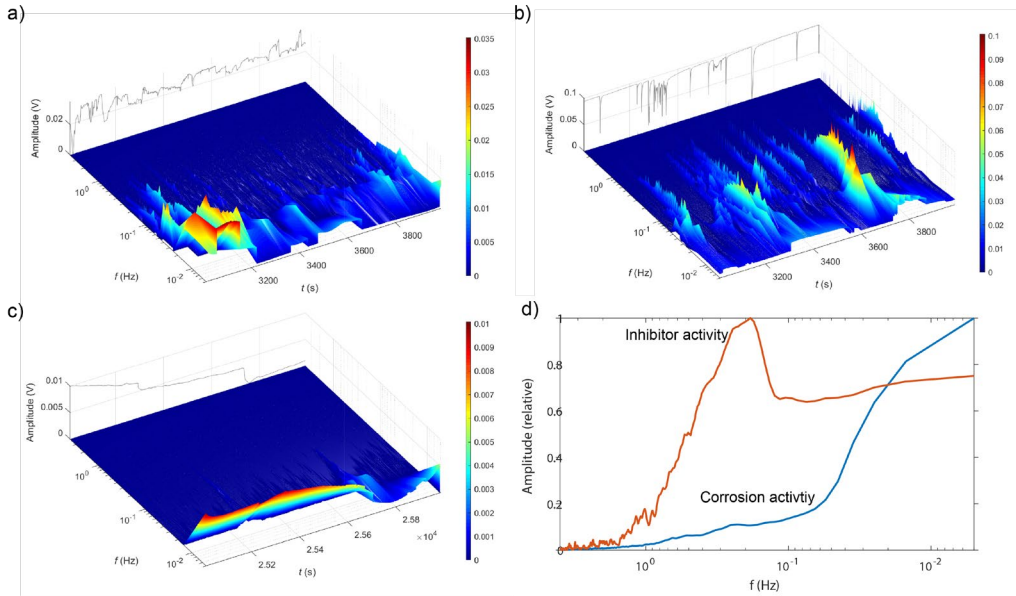
- coatings depending on the pigment volume concentration of polyaniline phosphate,” *Prog. Org. Coatings*, vol. 63, no. 2, pp. 228–237, 2008, doi: 10.1016/j.porgcoat.2008.06.005.
- 16 T. Prosek and D. Thierry, “A model for the release of chromate from organic coatings,” *Prog. Org. Coatings*, vol. 49, no. 3, pp. 209–217, Apr. 2004, doi: 10.1016/j.porgcoat.2003.09.012.
- 17 H. Wang, F. Presuel, and R. G. Kelly, “Computational modeling of inhibitor release and transport from multifunctional organic coatings,” *Electrochim. Acta*, vol. 49, no. 2, pp. 239–255, Jan. 2004, doi: 10.1016/j.electacta.2003.08.006.
- 18 F. J. Presuel-Moreno, H. Wang, M. A. Jakab, R. G. Kelly, and J. R. Scully, “Computational modeling of active corrosion inhibitor release from an Al-Co-Ce metallic coating,” *J. Electrochem. Soc.*, vol. 153, no. 11, pp. B486–B498, 2006, doi: 10.1149/1.2335946.
- 19 F. Thébault, B. Vuillemin, R. Oltra, K. Ogle, and C. Allely, “Investigation of self-healing mechanism on galvanized steels cut edges by coupling SVET and numerical modeling,” *Electrochim. Acta*, vol. 53, no. 16, pp. 5226–5234, Jun. 2008, doi: 10.1016/j.electacta.2008.02.066.
- 20 R. Oltra and F. Peltier, “Influence of mass transport on the competition between corrosion and passivation by inhibitor release after coating breakdown,” *Prog. Org. Coatings*, vol. 92, pp. 44–53, Mar. 2016, doi: 10.1016/j.porgcoat.2015.11.024.
- 21 R. L. Twite and G. P. Bierwagen, “Review of alternatives to chromate for corrosion protection of aluminum aerospace alloys,” *Prog. Org. Coatings*, vol. 33, no. 2, pp. 91–100, 1998, doi: 10.1016/S0300-9440(98)00015-0.
- 22 M. A. Jakab, F. Presuel-Moreno, and J. R. Scully, “Critical concentrations associated with cobalt, cerium, and molybdenum inhibition of AA2024-T3 corrosion: Delivery from Al-Co-Ce(-Mo) alloys,” *Corrosion*, vol. 61, no. 3, pp. 246–263, 2005, doi: 10.5006/1.3280634.
- 23 J. S. Laird, P. Visser, S. Ranade, A. E. Hughes, H. Terryn, and J. M. C. Mol, “Li leaching from Lithium Carbonate-primer: An emerging perspective of transport pathway development,” *Prog. Org. Coatings*, vol. 134, pp. 103–118, Sep. 2019, doi: 10.1016/j.porgcoat.2019.04.062.
- 24 M. Abdolah Zadeh, J. Tedim, M. Zheludkevich, S. van der Zwaag, and S. J. Garcia, “Synergetic active corrosion protection of AA2024-T3 by 2D- anionic and 3D-cationic nanocontainers loaded with Ce and mercaptobenzothiazole,” *Corros. Sci.*, vol. 135, pp. 35–45, 2018, doi: 10.1016/j.corsci.2018.02.018.
- 25 L. V. Gorobinskii, G. Y. Yurkov, and D. A. Baranov, “Production of high porosity nanoparticles of cerium oxide in clay,” *Microporous Mesoporous Mater.*, vol. 100, no. 1–3, pp. 134–138, 2007, doi: 10.1016/j.micromeso.2006.09.047.
- 26 X. Shi, T. A. Nguyen, Z. Suo, Y. Liu, and R. Avci, “Effect of nanoparticles on the anticorrosion and mechanical properties of epoxy coating,” *Surf. Coatings Technol.*, vol. 204, no. 3, pp. 237–245, 2009, doi: 10.1016/j.surfcoat.2009.06.048.
- 27 P. Loison, V. Debout, H. Groult, J. Creus, and S. Touzain, “Incorporation of silica nanocontainers and its impact on a waterborne polyurethane coating,” *Mater. Corros.*, vol. 70, no. 10, pp. 1884–1899, 2019, doi: 10.1002/maco.201910809.
- 28 P. J. Denissen and S. J. Garcia, “Cerium-loaded algae exoskeletons for active corrosion protection of coated AA2024-T3,” *Corros. Sci.*, vol. 128, no. September, pp. 164–175, Nov. 2017, doi: 10.1016/j.corsci.2017.09.019.
- 29 C. D. Dieleman, P. J. Denissen, and S. J. Garcia, “Long-Term Active Corrosion Protection of

- Damaged Coated-AA2024-T3 by Embedded Electrospun Inhibiting Nanonetworks,” *Adv. Mater. Interfaces*, vol. 5, no. 12, 2018, doi: 10.1002/admi.201800176.
- 30 P. J. Rivero, A. Iribarren, S. Larumbe, J. F. Palacio, and R. Rodríguez, “A Comparative Study of Multifunctional Coatings Based on Electrospun Fibers with Incorporated ZnO Nanoparticles,” *Coatings*, vol. 9, no. 6, p. 367, Jun. 2019, doi: 10.3390/coatings9060367.
- 31 E. Javierre, S. J. Garcia, J. M. C. Mol, F. J. Vermolen, C. Vuik, and S. van der Zwaag, “Tailoring the release of encapsulated corrosion inhibitors from damaged coatings: Controlled release kinetics by overlapping diffusion fronts,” *Prog. Org. Coatings*, vol. 75, no. 1–2, pp. 20–27, 2012, doi: 10.1016/J.Porgcoat.2012.03.002.
- 32 E. Javierre, “Modeling self-healing mechanisms in coatings: Approaches and perspectives,” *Coatings*, vol. 9, no. 2, 2019, doi: 10.3390/COATINGS9020122.
- 33 J. R. Scully, N. Tailleart, and F. Presuel-Moreno, *Tunable multifunctional corrosion-resistant metallic coatings containing rare earth elements*. Woodhead Publishing Limited, 2014.
- 34 S. A. Furman, F. H. Scholes, A. E. Hughes, and D. Lau, “Chromate leaching from inhibited primers. Part II: Modelling of leaching,” *Prog. Org. Coatings*, vol. 56, no. 1, pp. 33–38, May 2006, doi: 10.1016/j.porgcoat.2006.01.016.
- 35 A. Nazarov, D. Thierry, T. Prosek, and N. Le Bozec, “Protective action of vanadate at defected areas of organic coatings on zinc,” *J. Electrochem. Soc.*, vol. 152, no. 7, pp. B220–B227, Jul. 2005, doi: 10.1149/1.1924067.
- 36 “Chemical Reaction Engineering Module User’s Guide,” 1998. Accessed: Mar. 24, 2020. [Online]. Available: [www.comsol.com/blogs](http://www.comsol.com/blogs).
- 37 P. J. Denissen and S. J. Garcia, “Reducing subjectivity in EIS interpretation of corrosion and corrosion inhibition processes by in-situ optical analysis,” *Electrochim. Acta*, vol. 293, pp. 514–524, 2019, doi: 10.1016/j.electacta.2018.10.018.
- 38 P. J. Denissen, A. M. Homborg, and S. J. Garcia, “Interpreting electrochemical noise and monitoring local corrosion by means of highly resolved spatiotemporal real-time optics,” *J. Electrochem. Soc.*, vol. 166, no. 11, pp. C3275–C3283, 2019, doi: 10.1149/2.0341911jes.
- 39 A. M. Homborg *et al.*, “Novel time-frequency characterization of electrochemical noise data in corrosion studies using Hilbert spectra,” *Corros. Sci.*, vol. 66, pp. 97–110, 2013, doi: 10.1016/j.corsci.2012.09.007.
- 40 S. J. García, H. R. Fischer, and S. Van Der Zwaag, “A critical appraisal of the potential of self healing polymeric coatings,” *Prog. Org. Coatings*, vol. 72, no. 3, pp. 211–221, 2011, doi: 10.1016/j.porgcoat.2011.06.016.
- 41 A. Aballe, M. Bethencourt, F. J. Botana, and M. Marcos, “Wavelet transform-based analysis for electrochemical noise,” *Electrochem. commun.*, vol. 1, no. 7, pp. 266–270, 1999, doi: 10.1016/S1388-2481(99)00053-3.
- 42 P. Flandrin, G. Rilling, and P. Gonçalves, “Empirical mode decomposition as a filter bank,” *IEEE Signal Processing Letters*, vol. 11, no. 2 PART I, pp. 112–114, Feb. 2004, doi: 10.1109/LSP.2003.821662.
- 43 G. Rilling, P. Flandrin, and P. Gonçalves, “ON EMPIRICAL MODE DECOMPOSITION AND ITS ALGORITHMS.”
- 44 A. M. Homborg *et al.*, “Application of transient analysis using Hilbert spectra of electrochemical

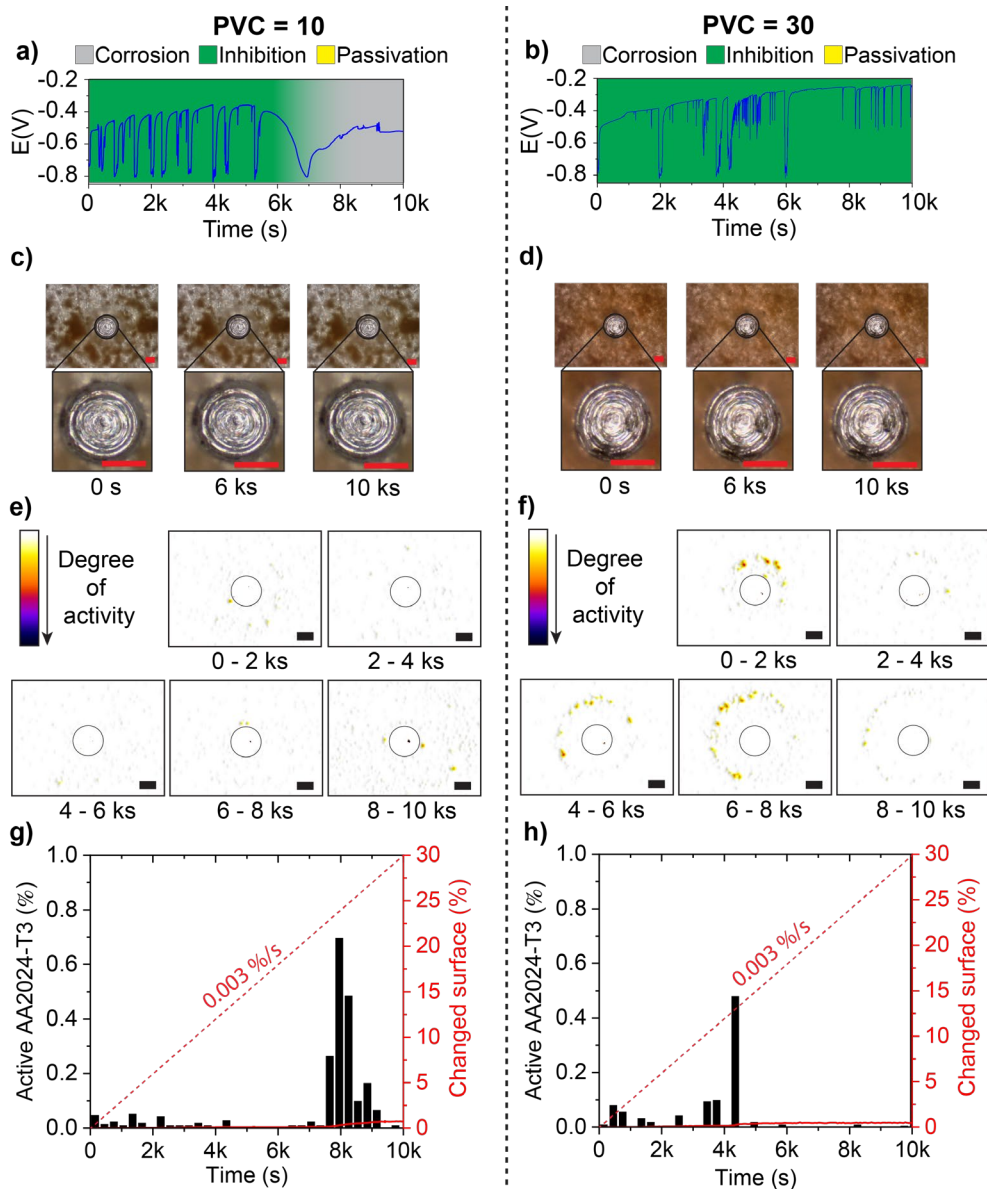
- noise to the identification of corrosion inhibition,” *Electrochim. Acta*, vol. 116, pp. 355–365, Jan. 2014, doi: 10.1016/j.electacta.2013.11.084.
- 45 A. Boag, A. E. Hughes, A. M. Glenn, T. H. Muster, and D. McCulloch, “Corrosion of AA2024-T3 Part I: Localised corrosion of isolated IM particles,” *Corros. Sci.*, vol. 53, no. 1, pp. 17–26, 2011, doi: 10.1016/j.corsci.2010.09.009.
- 46 X. Zhang, T. Hashimoto, J. Lindsay, and X. Zhou, “Investigation of the de-alloying behaviour of  $\theta$ -phase (Al<sub>2</sub>Cu) in AA2024-T351 aluminium alloy,” *Corros. Sci.*, vol. 108, pp. 85–93, 2016, doi: 10.1016/j.corsci.2016.03.003.
- 47 S. Szunerits and D. R. Walt, “Aluminum surface corrosion and the mechanism of inhibitors using pH and metal ion selective imaging fiber bundles,” *Anal. Chem.*, vol. 74, no. 4, pp. 886–894, 2002, doi: 10.1021/ac0108257.
- 48 T. H. Muster *et al.*, “A rapid screening multi-electrode method for the evaluation of corrosion inhibitors,” *Electrochim. Acta*, vol. 54, no. 12, pp. 3402–3411, 2009, doi: 10.1016/j.electacta.2008.12.051.
- 49 S. J. García *et al.*, “The influence of pH on corrosion inhibitor selection for 2024-T3 aluminium alloy assessed by high-throughput multielectrode and potentiodynamic testing,” *Electrochim. Acta*, vol. 55, no. 7, pp. 2457–2465, 2010, doi: 10.1016/j.electacta.2009.12.013.
- 50 L. Paussa, F. Andreatta, N. C. Rosero Navarro, A. Durán, and L. Fedrizzi, “Study of the effect of cerium nitrate on AA2024-T3 by means of electrochemical micro-cell technique,” *Electrochim. Acta*, vol. 70, pp. 25–33, May 2012, doi: 10.1016/j.electacta.2012.02.099.
- 51 E. A. Matter, S. Kozhukharov, M. MacHkova, and V. Kozhukharov, “Electrochemical studies on the corrosion inhibition of AA2024 aluminium alloy by rare earth ammonium nitrates in 3.5% NaCl solutions,” *Mater. Corros.*, vol. 64, no. 5, pp. 408–414, 2013, doi: 10.1002/maco.201106349.
- 52 F. H. Spedding, R. A. Nelson, and J. A. Rard, “Conductances, Transference Numbers, and Activity Coefficients of Some Aqueous Terbium Halides at 25°,” *J. Chem. Eng. Data*, vol. 19, no. 4, pp. 379–381, 1974, doi: 10.1021/je60063a029.
- 53 B. Fourest, J. Duplessis, and F. David, “Comparison of Diffusion Coefficients and Hydrated Radii for some Trivalent Lanthanide and Actinide Ions in Aqueous Solution,” *Radiochim. Acta*, vol. 36, no. 4, pp. 191–196, 1984, doi: 10.1524/ract.1984.36.4.191.
- 54 F. Martelli, S. Abadie, J. P. Simonin, R. Vuilleumier, and R. Spezia, “Lanthanoids(III) and actinoids(III) in water: Diffusion coefficients and hydration enthalpies from polarizable molecular dynamics simulations,” *Pure Appl. Chem.*, vol. 85, no. 1, pp. 237–246, 2013, doi: 10.1351/PAC-CON-12-02-08.
- 55 H. M. Hajar, M. J. Suriani, M. G. M. Sabri, M. J. Ghazali, and W. B. W. Nik, “Corrosion Performance of Coating Thickness in Marine Environment,” *Biosci. Biotechnol. Res. ASIA*, vol. 12, no. 1, pp. 71–76, 2015, doi: 10.13005/bbra/1637.

## 6.6. Supporting Information

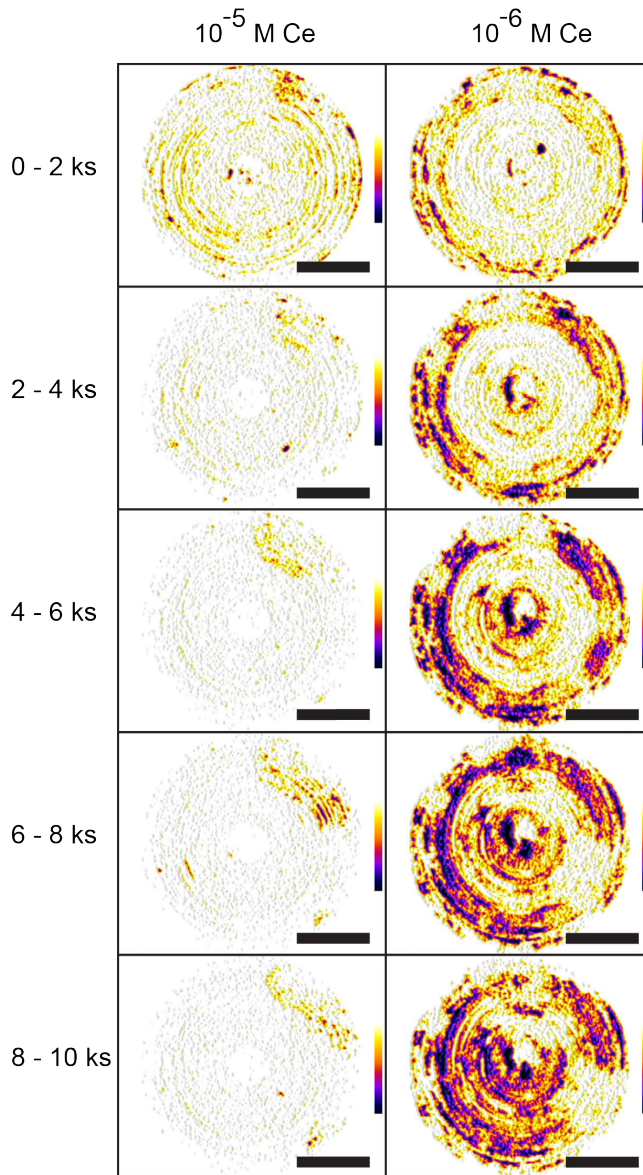
### SI-6.1 HHS analysis of the EPN signal



**Figure SI 6.1** HHS analysis of the EPN signal for a) damaged epoxy coating showing corrosion activity, b) damaged CeDE1 coating showing inhibitor activity, c) damaged CeDE coating showing passivation, and d) the two-dimensional comparison between inhibitor- and corrosion activity.

**SI-6.2. Optical and electrochemical results for CeDE (small damage)**

**Figure SI 6.2** Optical and electrochemical results for CeDE coatings during immersion in 0.05 M NaCl over a period of 10 ks containing 10 PVC (left) and 30 PVC (right) micro-carriers. Indicated as (a-b) the raw EPN signals, (c-d) the original images, (e-f) the optically detected degree of activity, and (g-h) the quantitative optical analysis inside the damage where bars indicate variations in a specific period of time (300 s) and red lines the cumulative variation, including the reported values from literature<sup>38</sup> (red dashed line). Scale bar represents 100  $\mu$ m.

*SI-6.3. Processed optical analysis on two epoxy coatings for cerium in solution*

**Figure SI 6.3** Processed optical analysis on two epoxy coatings on AA2024-T3 containing a circular damage immersion in 0.05 M NaCl containing cerium nitrate in solution at  $10^{-5}$  and  $10^{-6}$  M. Scale bar represents 50  $\mu\text{m}$ .

## Acknowledgements

While a PhD degree signifies the contribution of knowledge by conducting independent research, these two pages of the dissertation will show that this journey is everything except a solo mission.

First of all, thank you Santiago Garcia. I could not have wished for a better promotor and you really spoiled me by your continuous support, constructive contributions and your personal interest in my life. I learned from you in numerous ways and this helped me to advance my scientific knowledge and insight while giving me all the freedom to walk my own paths. I also want to thank Sybrand van der Zwaag for all the support and guidance through your broad knowledge and advice on all aspects, priceless. Santiago and Sybrand, thank you once more for creating this wonderful experience!

During my PhD I also had the opportunity to visit Paris for 4 months, and I want to thank Polina Volovich who made it possible for me to join the laboratory of Interfaces, Electrochemistry and Energy (I2E) at École Nationale Supérieure de Chimie de Paris. In particular, I would like to thank Viacheslav for his knowledge, beautiful scientific mind-set and climbing skills. Also not to forget are Alina, Xuejie, Cyril, Ine, Abdelilah, Jeff, Anna, Perrine, Thomas, Diego for the fun time during the breaks and social events, thanks!

It was a pleasure for me to work together with many incredible minds on different projects during my PhD. Thank you Axel Homborg for the nice projects we have worked on together, it was always a pleasure when you passed by in Delft. A special mention to Pierre, having another PhD candidate around you working on an almost identical subject is rare for NovAM, and your short visit to our group really enlightened me. I would also like to mention Christian, Angelique, Clara, Pierre, Cong, Matteo, and Olga, for the work you did on relevant corrosion-related research-subjects. The synergy of working together on different aspects really inspired me and I learned a great deal from all of you.

I would also like to thank the people that helped me in numerous different ways. Especially Shanta for always being able to organise everything, I still do not know your secret on this matter,

probably never will! I would also like to thank Frans, Durga, Berthil, Marlies, Johan and all the others from the Delft Aerospace structures and Materials Laboratory for their help inside and around the instrumentation, these would have been worthless without your guidance and positive problem-solving mind-sets.

Talking about a good atmosphere, this is what all my colleagues at NovAM made possible, truly. Not only my office-buddies Johan, Hongli, Dimosthenis and my screaming companion Monti, but also Atsushi, Pim, Theo, Antonio, Marianella, Reza, Tadhg, Anton, Arijana, Casper, Daniella, Hamideh, Hao, Hugo, Jimmy, Mariana, Martino, Mina, Nan, Satya, Vincent, Wouter<sup>2</sup>, Zekja Niels, Amber, Bert, Cleopatra, Kevin, Linda, Max, Michael, Paula, Petter, Ruben, Sil, Silvia, Taylor, and all other NovAM Colleagues, students and adopted NovAM'ers. Your presence during day and night resulted in many hilarious moments, taking for granted the less hilarious mornings the day after.

Ellen, I would like to thank you for all the love and support you gave me during these years. I cannot imagine a better way to enjoy life than together with you, at home on the couch or at our unlimited traveling expeditions around the world to explore new wonderful places and people!

Finally and most importantly, I want to thank my parents, sister and Nora for all the support and family time. We are roughly 1000 km apart from each-other, but the moments we are not are also the most memorable in my life!

# List of publications

## Journal publications

1. P. J. Denissen, A. M. Homborg, S. J. Garcia  
*A simulation-based guideline for the design of anticorrosive primers based on inhibitor-loaded carriers*  
To be submitted, **2020**
2. P. J. Denissen, V. Shkirskiy, P. Volovitch, S. J. Garcia  
*Corrosion inhibition at scribed locations in coated AA2024-T3 by cerium and DMTD loaded natural silica microparticles under continuous immersion and wet/dry cyclic exposure*  
ACS Applied Materials & Interfaces, **2020**, 12 (20), 23417-23431
3. P. J. Denissen, A. M. Homborg, S. J. Garcia  
*Interpreting Electrochemical Noise and Monitoring Local Corrosion by Means of Highly Resolved Spatiotemporal Real-Time Optics*  
Journal of The Electrochemical Society **2019**, 166 (11), C3275-C3283
4. P. J. Denissen, S. J. Garcia  
*Reducing subjectivity in EIS interpretation of corrosion and corrosion inhibition processes by in-situ optical analysis*  
Electrochimica Acta **2019**, 293, 514-524
5. C. D. Dieleman, P. J. Denissen, S. J. Garcia  
*Long-Term Active Corrosion Protection of Damaged Coated-AA2024-T3 by Embedded Electrospun Inhibiting Nanonetworks*  
Advanced Materials Interfaces **2018**, 5 (12), 1800176
6. P. J. Denissen, S. J. Garcia  
*Cerium-loaded algae exoskeletons for active corrosion protection of coated AA2024-T3*  
Corrosion Science **2017**, 128, 164-175

Conference contributions

1. M. Olgiati, P. J. Denissen, A. M. Homborg, S. J. Garcia  
*Oral presentation: Effect of stability and instability of cerium oxide layers on the protection of AA2024-T3*  
European Corrosion Congress, Online, September 2020
2. P. J. Denissen, S. J. Garcia  
*Oral presentation: Real-time visualizing and quantifying corrosion*  
Nederlands Lucht- en Ruimtevaartcentrum, Corrosie workshop, Marknesse, The Netherlands, November 2019
3. P. J. Denissen, S. J. Garcia  
*Oral presentation: Towards long term corrosion protection: from nano- to micro-carriers*  
European Corrosion Congress, Sevilla, Spain, September 2019
4. P. J. Denissen, A. M. Homborg, S. J. Garcia  
*Oral presentation: Visualizing and quantifying early stage corrosion: a combination of real time optics and electrochemical noise*  
European Corrosion Congress, Sevilla, Spain, September 2019
5. P. J. Denissen, S. J. Garcia  
*Oral presentation: Exploring long-term protection at large damage sites in aerospace coatings using inhibitor and carrier synergies*  
European Corrosion Congress, Warsaw, Poland, September 2018
6. P. J. Denissen, S. J. Garcia  
*Oral presentation: Monitoring corrosion and corrosion protection in bare and coated aluminium by optical-electrochemical hyphenated tools*  
European Technical Coatings Congress, Amsterdam, The Netherlands, June 2018
7. P. J. Denissen, S. J. Garcia  
*Oral presentation: Hand-in-hand development of new protective coatings and evaluation technologies: an algae-based inhibitor release system*  
SURFAIR, Biarritz, France, May 2018
8. P. J. Denissen, R. K. Bose, A. Susa, S. van der Zwaag, S. J. Garcia  
*Poster presentation: New imaging techniques to analyse self-healing coatings*  
6<sup>th</sup> International Conference on Self-Healing Materials, Friedrichshafen, Germany, June 2017
9. P. J. Denissen, S. J. Garcia  
*Oral presentation: Cerium loaded algae exoskeletons for active corrosion protection of coated AA2024-T3*  
European Corrosion Congress, Prague, Czech Republic, September 2017

10. P. J. Denissen, S. J. Garcia  
*Poster presentation: Hyphenated opto-electrochemistry for the development of self-healing coatings*  
European Corrosion Congress, Prague, Czech Republic, September 2017
11. P. J. Denissen, S. J. Garcia  
*Oral presentation: Diatoms as new bio-based carrier for active corrosion protection of AA2024*  
12<sup>th</sup> Coatings Science International Conference (CoSi), Noordwijk, The Netherlands, June 2016

### Patents

1. S. J. Garcia, P. J. Denissen, 2018, *Diatoms as natural carriers for controlled release for metal protection and coatings*, WO2018169397

Creativity award for the poster “Diatoms as new bio-based carrier for active corrosion protection of AA2024”, 12<sup>th</sup> Coatings Science International Conference (CoSi), Noordwijk, The Netherlands, June 2016

SURFAIR award by a jury of high-level experts recognized in the Aeronautics & Aerospace industry for the presentation “Hand-in-hand development of new protective coatings and evaluation technologies: an algae-based inhibitor release system” SURFAIR, Biarritz, France, May 2018

Participation Grant from the Dutch Association of Paint Technicians (NVVT) and the Federation of Associations of Technicians for Industry of Paints in European Countries (FATIPEC) to present at the European Technical Coatings Congress (ETCC) 2018

Young Scientist Grant from the European Federation of Corrosion (EFC) at the European Corrosion Conference (EURCORR) in 2018 for an internship at École Nationale Supérieure de Chimie de Paris in France within the laboratory of Interfaces, Electrochemistry and Energy (I2E) supervised by Polina Volovitch



## About the Author

Paul Denissen was born in April of 1990 and grew up in the province Zeeland (the Netherlands) where he finished high-school in 2007. He then went to Delft where he followed the Bachelor of Aeronautical Engineering at the University of Applied Sciences INHOLLAND. During this period he completed his compulsory 6 months internship in China where he worked on computational fluid dynamics at the Northwestern University Xian. In 2013 he finished his graduation thesis dedicated to the design, production and installation of a new support structure for the ATLAS detector at CERN (Switzerland). Paul also worked as a software developer and co-founded a student Dreamteam “Human Power Team Delft and Amsterdam” with the aim to break the human powered speed record (<http://www.hptdelft.nl/>). Here he acted as project-leader in a team of 6 full-time and 14 part-time members. In 2013 Paul started his master at the Delft University of Technology in the field of Material Science and Engineering. He finished his graduation thesis in the Novel Aerospace Materials group at the faculty of Aerospace Engineering where he worked on the development of new carrier systems for corrosion inhibitors in order to enhance their kinetic properties when applied as anti-corrosion coatings on metals. From 2016 Paul continued his research as a PhD candidate working on the development of new anticorrosive coatings and corrosion monitoring technologies under the supervision of Dr. Santiago J. Garcia and Prof. dr. ir. Sybrand van der Zwaag. The coatings are based on the use of algae exoskeletons for the encapsulation of corrosion inhibitors as a route to replace Cr(VI). The new evaluation technologies are based on the development of new combined optical-electrochemical techniques to study corrosion processes. After finishing the PhD dissertation, Paul started to create the company Correlimage (<http://www.correlimage.com>) to commercialise his work on new optical and electrochemical techniques to monitor and evaluate local corrosion processes under industrial conditions.

